NTNU
Norwegian University of
Science and Technology

A study of highly oxidized, high-grade metamorphic sedimentary rocks

A geochemical and petrophysical study of rocks from the Modum Complex, South Norway

Hedda Garshol Jensen

Geology
Submission date: May 2017
Supervisor: Suzanne McEnroe, IGP

Norwegian University of Science and Technology
Department of Geoscience and Petroleum

Abstract

The Modum Complex is a part of the Kongsberg Sector, located west of the Oslo Graben in southern Norway. It is made up of arenaceous, argillaceous and calcareous rocks, in addition to volcanites and intrusives. Regionally, the rocks have been exposed to amphibolite facies metamorphism, and aeromagnetic surveys have shown numerous negative anomalies in the area. The investigated rocks are a part of the Høgås anticline, and are of a chemical composition that has not been investigated commonly in the past.

In order to investigate the rare chemical space and possible sedimentary protoliths of these rocks, varied laboratory work has been done. Microscopy, EPMA and XRF were performed to explore mineralogy and geochemistry, presenting Fe-Mg-rich rocks, low in Al, Na, Ca and K. Using rock chemistry and mineral assemblages, two compositional groups were recognized; one kyanite/sillimanite-bearing group including talc with rare NaAl-substitution, and one amphibole-bearing groups, displaying higher amounts of Ca.

The tourmalines in the amphibole-rocks display higher Ca-content than the tourmalines in the kyanite-rocks, and these are interpreted to be formed in early stages of metamorphism. This reflects that the chemical differences in the rocks are due to differences in the original iron-rich sediments. To find a suitable protolith, the XRF-results are compared to chemical compositions of sedimentary rocks found in various literature. The rocks are possibly derived from a hematite-rich, Al-poor, silty pelite with components of volcanic ash and/or evaporite chemistry. The protoliths are interpreted to be originally oxidized, owing to an oxidizing, alkaline, shallow marine environment with absence of organic carbon.

The magnetic properties were explored by measuring NRM and susceptibility, in addition to temperature dependent susceptibility and demagnetization behavior. These investigations point out titanohematite as the primary remanence carrier. Again, two groups were recognized, displaying higher NRM and susceptibility for the kyanite-bearing rocks, along with higher contents of titanohematite. Demagnetization measurements indicate presence of two oxide phases, possibly owing to nanoscale exsolution lamellae of ilmenite in the titanohematite.

Sammendrag

Modumkomplekset er en del av Kongsbergsektoren, lokalisert vest for Oslo Graben i Sør-Norge. Det består av sandige, leirige og kalkholdige bergarter, i tillegg til vulkanitter og intrusjoner. Regionalt har steinene blitt utsatt for metamorfose opp til amfibolitt-facies, og aeromagnetiske undersøkelser har vist en rekke negative anomalier i området. De undersøkte bergartene er en del av Høgås antiklinal, og har en kjemisk sammensetning som ikke har blitt undersøkt i stor grad tidligere.

For å undersøke det sjeldne kjemiske området og mulige sedimentære protolitter til disse bergarter, har variert laboratoriearbeid blitt utført. Mikroskopi, EPMA og XRF ble utført for å undersøke mineralogi og geokjemi, og dette viste Fe-Mg-rike bergarter, fattige på Al, Na, Ca og K. Ved å bruke bergkjemi og mineralselskaper ble to typer sammensetning gjenkjent; en kyanitt/sillimanittbærende gruppe som inkluderer talk med sjelden NaAl-substitusjon, og en amfibolbærende gruppe, som inneholder høyere mengder Ca.

Turmalinene i amfibol-bergartene viser høyere Ca-innhold enn turmalinene i kyanitt-bergartene, og disse er tolket til å ha blitt dannet i tidlige stadier av metamorfose. Dette gjenspeiler at de kjemiske forskjellene i bergartene skyldes forskjeller i de originale jernrike sedimentene. For å finne en passende protolitt, sammenlignes XRF-resultatene med kjemiske sammensetninger av sedimentære bergarter, funnet i forskjellig litteratur. Bergartene er muligens dannet fra en hematittrik, Al-fattig, siltig pelitt med komponenter av vulkansk aske og/eller evaporittkjemi. Protolittene tolkes for å være opprinnelig oksiderte, grunnet et oksiderende, alkalisk, grunt havmiljø med fravær av organisk karbon.

De magnetiske egenskapene ble undersøkt ved å måle NRM og susceptibilitet, i tillegg til temperaturavhengig susceptibilitet og demagnetiseringsadferd. Disse undersøkelsene peker på titanohematitt som den primære bærer av bergartenes remanens. Igjen ble to grupper gjenkjent, som viste høyere NRM og susceptibilitet for de kyanittbærende bergartene, sammen med høyere innhold av titanohematitt. Demagnetiseringsmålinger indikerer tilstedeværelse av to oksidfaser, muligens på grunn av utfellingslameller i nanoskala av ilmenitt i titanohematitt.

Acknowledgements

This thesis has been carried out at the (IGP) at the Norwegian University of Science and Techology (NTNU) as a part of my Master of Science degree. I would like to give a huge thanks to my supervisor Suzanne McEnroe, for giving me specific tasks to work with and helpful comments on my text. I am immensely grateful for the opportunity to participate and present my own poster at the Castle Meeting conference in Dinant, Belgium, August 2016, which can be found in appendix C.

I would like to thank Peter Robinson at NGU, which I have learned so much from and who has always been available to answer my questions. Thanks to Nathan Church, Gertjee Ter Maat, Alexander Michels and Marianne Floen Stange for help with magnetic measurements and great company during the Castle Meeting conference in Belgium. Thanks to Kjetil Eriksen for making thin sections, Yingda Yu for teaching me how to work the SEM-machine, Torill Sørløkk for guidance with XRF preparation and Morten Peder Raanes for performing the EPMA analyses. A special thanks to Anette Utgården Granseth for helping words when I have been stuck and assisting in the final editing of my thesis.

Finally, I would like to thank my classmates for all the great memories we have collected throughout these years, and the gang at the study hall for "grøt-fredag" and moral support in times of frustration.

Hedda Garshol Jensen

Trondheim, 27.05.17

Table of content

Abstract……..……..……..……..……..iii

Sammendrag……..……..……..……..v

Acknowledgements……..……..……..……..…vii

List of figures……..……..……..……...…..xiii

List of tables……..……..……..……..……..xv

Abbreviations……..……..……..……xvii

1. Introduction……..……..……..……1

1.1 Background……..……..……..…..……1

1.2 Previous work……..……..……3

2. Aim of study……..……..……..……..……..……..7

3. Location, geological setting……..……..……..……9

3.1 Regional geology……..……..……..……..……..9

3.2 The Modum Complex……..……..……..……..……..9

3.3 Mining history and mineralizations……..……..……....……12

4. Petrological theory……..……..……..……..……..……13

4.1 Metamorphism……..……..……..……..……..…..…13

4.2 Metamorphic facies……..……..……..……..……13

4.2.1 Amphibolite facies……..……..……..……..…14

4.2.2 Barrovian zones……..……..……..……..……16

4.3 Element theory……..……..……..……..……..……..16

4.4 Hydrothermal alteration……..……..……..……17

4.4.1 Solubility……..……..……..……..……..17

4.4.2 Redox potential……..……..……..……..……19

4.4.3 Metasomatism……..……..……..…..……..……20

4.5 Chemographic diagrams……..……..……..…..……..……21

5. Geomagnetic theory……..……..……..……..……23

5.1 Earth magnetism……..……..……..……..……..23

5.2 Rock magnetism……..……..……..……..……..…24

5.2.1 Remanent magnetism……..……..……..……..…25

5.2.2 Induced magnetisation and susceptibility……..……..……25

5.2.3 Köenigsberg ratio……..……..……..……..……26

5.3 Types of magnetism……..……..……..……..……27

5.3.1 Diamagnetism……..……..……..……..……27

5.3.2 Paramagnetism……..……..……..……..……27

5.3.3 Ferromagnetism……..……..……..……..……28

5.3.4 Ferrimagnetism and antiferromagnetism……..……..……28

5.4 Hematite-ilmenite solid solution……..……..……..……..……29

5.4.1 Hematite……..……..……..……..…….30

5.4.2 Ilmenite……..……..……..……...31

5.4.3 Lamellar magnetism……..……..……..….31

6. Methods……..……..……..……..……..……..……33

6.1 Optical microscopy of thin sections……..……..……33

6.2 Scanning Electron Microprobe (SEM) ……..……..……..……33

6.3 Electron microprobe analysis (EMPA) ……..……..……..……34

6.4 XRF……..……..……..……..……..……..……..35

6.5 Density measurements……..……..……..……..……36

6.6 Susceptibility measurements……..……..……..……..…36

6.6.1 Temperature dependent susceptibility……..……..…….37

6.7 NRM measurements……..……..……..……..……37

6.7.1 Demagnetization measurements……..……..……..……37

6.8 Sources of error……..……..……..……..……..…38

7. Petrology……..……..……..……..……..……..…39

7.1 Rock and thin section descriptions……..……..……..……39

*7.1.1 MOD35 - Phlogopite-talc-hematite schist with sillimanite-albite clusters*40

7.1.2 MOD36 – Sillimanite-hematite rock with talc, phlogopite and albite……41

7.1.3 MOD37- Layered quartz-oligoclase-phlogopite rock with talc, amphibole and coarse-grained oligoclase lumps……..……..……..…..42

7.1.4 MOD38 - Layered quartz-oligoclase-phlogopite rock with talc, amphibole and coarse-grained oligoclase lumps……..……..……...…...43

7.1.5 MOD39 - Layered oligoclase-phlogopite rock with talc, amphibole and coarse-grained oligoclase lumps. Graded beds in outcrop.……..……44

7.1.6 MOD40 – Chlorite-talc-kyanite-hematite schist with quartz and phlogopite……..45

7.1.7 MOD41 - Quartz-hematite granulite……..……..……..…..46

7.1.8 HJ002 - Metasedimentary rock from near pyroxene-hornblendite……..46

7.1.9 HJ003 - Pyroxene-hornblendite……..……..……..……47

7.1.10 MODHJK – Quartz-feldspar granulite……..……..……...48

7.2 Mineralogy……..……..……..……..……..……49

7.2.1 Quartz……..……..……..……..……..…49

7.2.2. Feldspar……..……..……..……..……..49

7.2.3 Phlogopite/biotite ……..……..……..……..……56

7.2.4 Talc……..……..……..……..……..……62

7.2.5 Amphibole……..……..……..……..…….67

7.2.6 Chlorite……..……..……..……..……..72

7.2.7 Tourmaline……..……..……..……..……75

7.2.8 Kyanite/Sillimanite……..……...…..……..……...…77

7.2.9 Apatite……..……..……....…..……..……...…78

7.2.10 Unknown mineral……..……..……..……..……80

7.2.11 Accessory minerals……..……..……..……..82

7.2.11.1 Paragonite……83

7.2.12 Oxides……..……..……..……..……83

7.3 XRF……..……..……..……..……..……..88

8. Petrophysical properties……..……..……....……..……..95

8.1 Densities……..……..……..……..……..……95

8.2 Susceptibility values……..……..……..……..……96

8.3 NRM intensities……..……..……..……..……..……96

8.4 Köenigsberg ratio (Q-value) ……..……..……..……..……..…98

8.5 AF demagnetization……..……..……..……..……99

8.6 Temperature dependent susceptibility……..……..……..……..…104

9. Discussion……..……..……..……..……..……..……109

9.1 Related assemblages and phase relations……..……..……..……109

9.1.1 Rocks with kyanite/sillimanite……..……..……..……..109

9.1.2 Rocks with amphibole……..……..……..……113

9.1.3 Quartz-hematite rock…..……..……..…….....114
9.2 Chemography……..……....……..……....……..……114
9.3 Possible protoliths……..……..……..……..…….117
9.4 Oxidized protolith……..……....……..……....……...121
9.5 Discussion of petrophysical properties……..……..……..……...122
9.5.1 Oxide content and petrophysical properties……..……..……123
9.5.2 Amount, size and types of exsolutions……..……..……..124
9.6 Suggestions for further work……..……..……..……..….125
10. Conclusions……..……..……..……..……..……127
11. References……..……..……..……..……..……..129

Appendix A – Magnetic properties

Appendix B – AF demagnetization

Appendix C – Castle Meeting conference poster

List of figures

Figure 1.1: Bedded, metasedimentary sedimentary rock at MOD39 with dark lumps, containing diffuse, fine titanohematite……..……1

Figure 1.2: The negative anomaly of the Høgås fold, with the sample locations……2

Figure 1.3: Structural measurements near the Høgås negative anomaly. a) 5 poles to foliation and calculated fold axis. b) Five foliations plotted directly. c) Lineations measured on foliation planes ……..3

Figure 1.4: Airborne magnetic data of the Kongsberg lithotectonic unit. b) Combined lithotectonic and structural map of the Kongsberg lithotectonic unit and adjacent units (Scheiber et al., 2015) ……..……...……4

Figure 1.5: Aeromagnetic survey map over the Mesoproterozoic basement of the Modum Complex, south Norway (Robinson et al., 2014) ……6

Figure 3.1: Sketch tectonic map of Scandinavia highlighting the areas affected by the Sweconorwegian orogeny (Scheiber et al., 2015)……9

Figure 3.2: Aeromagnetic map over the sample area (NGU database) ……11

Figure 4.1. Temperature-pressure diagram showing the generally accepted limits of the various facies (Winter, 2010) ……14

Figure 4.2: shows solubility of Si and Al as a function of pH (Robb, 2005) ……18

Figure 4.3: Diagram over Eh and pH limits of some natural environments (Robb, 2005)……20

Figure 4.4: Hypothetical three-component chemographic compatibility diagram illustrating the positions of different stable mineral coexisting under given P-T conditions (Nelson, 2011) ...22

Figure 5.1: Bar magnet. Field lines showing the magnetic field of a magnet. The lines converge at the poles, thus the field will be strongest here (Reynolds, 2011) ……23

Figure 5.2: The field due to an inclined geocentric dipole (Reynolds, 2011) ……24

Figure 5.3: vector sum of induced and remanent intensities of magnetisation, J (Reynolds, 2011) ……...25

Figure 5.4: The total magnetization, J_{tot}, of a rock is the sum of the induced magnetization J_i and the remanent magnetization J_r (McEnroe et al., 2009a) …….……26

Figure 5.5: Examples of disordered and ordered magnetic structures. Arrows represent the direction of atomic moments (Harrison and Feinberg, 2009) ……28

Figure 5.6: Showing the titanomagnetite and hematite-ilmenite solid-solution (redrawn after Dentith and Mudge, 2014) ……30

Figure 7.1: Photomicrographs of quartz……50

Figure 7.2: Photomicrographs of feldspar……..……51

Figure 7.3: Ternary feldspar diagram of the compositional differences. Figure based on Deer et al. (1992) ……..……52

Figure 7.4: Photomicrographs of phlogopite……57

Figure 7.5: Fe/(Fe+Mg) plotted versus Total Al. Diagram for classification of biotite, where Al is based on content of Al in tetrahedral position from the general structural formula…….……58

Figure 7.6: Ternary phlogopite diagram of the compositional differences in the various sections……..…58

Figure 7.7: Photomicrographs of talc……62

Figure 7.8: Ternary talc diagram of the compositional differences in the various sections…..66

Figure 7.9: Plot of Na in A site versus Al for talc. Al is based on content of Al in tetrahedral position from the general structural formula……..……66

Figure 7.10: Fe/(Fe+Mg) plotted versus Al for talc. Al is based on content of Al in tetrahedral position from the general structural formula……..……67

Figure 7.11: Photomicrographs of amphibole……...……68

Figure 7.12: Classification diagram for amphibole based on Leake et al (1978). The diagram parameters are $Ca_B > 1.50$; $(Na+K)_A < 0.50$. This does not fit for HJ003, where $(Na+K)_A > 0.50$……69

Figure 7.13: Amphibole quadrilateral showing the compositional differences compared to standard amphiboles. Figure based on quadrilateral from Putnis (1992)……69

Figure 7.14: Tetrahedral Al plotted versus Na in A site for amphiboles……70

Figure 7.15: Photomicrographs of chlorite....……...……72

Figure 7.16: Chlorite diagram showing the compositional differences, where Fe/(Fe+Mg) is plotted versus Al/(Al+Si). Fe is plotted as Fe_{tot}……73

Figure 7.17: Photomicrographs of tourmaline……..……75

Figure 7.18: Ternary tourmaline diagram showing compositional differences……76

Figure 7.19: Photomicrographs of kyanite and sillimanite…….....……77

Figure 7.20: Photomicrographs of apatite…….……78

Figure 7.21: Photomicrographs of the unknown mineral....…….……80

Figure 7.22: Ternary diagram showing composition of mystery mineral compared to chlorite and talc……..……81

Figure 7.23: Photomicrographs of oxide phases……85

Figure 7.24: Harker diagrams showing the whole rock chemistry, wt.% of SiO2 plotted against the other main elements in the samples…….……90

Figure 7.25: ACF diagrams with XRF main element chemistry for amphibolite facies and greenschist facies……...91

Figure 7.26: Showing weathering trends, closer to Al_2O_3 means more advanced weathering. After Rollinson (1993) ……..93

Figure 7.27: Discriminant function diagram for the provenance signatures of sandstone-mudstone suites using major elements. After Rollinson (1993) ……..……93

Figure 7.28: The classification of terrigenous sandstones using log(Na_2O/K_2O) vs log(SiO_2/Al_2O_3). After Rollinson (1993) ……..……94

Figure 7.29: Classification of terrigenous sandstones and shales using log(Fe_2O_3/K_2O) vs log(SiO_2/Al_2O_3). After Rollinson (1993) ……..……94

Figure 8.1: Density values (g/cm^3) plotted versus susceptibility values (SI) ……96

Figure 8.2: Density values (g/cm^3) plotted versus NRM values (A/m) ……..……97

Figure 8.3: Plot of directions of the NRM intensities……98

Figure 8.4: Log-log plot of NRM (A/m) vs induced magnetization J_i (A/m). Q-value diagonals indicate the distribution of Q-values for each specimen……...……99

Figure 8.5: AF demagnetization curves for selected samples……...100-101

Figure 8.6: Zijderveld diagrams from AF demagnetization for selected samples. Note that b. MOD36-1a and j. MODHJK-1a are not oriented! ……102-103

Figure 8.7: NRM plotted versus M(50%); field intensity where 50% of the magnetization is lost……...…104

Figure 8.8: Temperature dependent susceptibility curves from all samples……106-107

Figure 9.1: Ternary diagram showing that talc-kyanite breaks down to chlorite-quartz in MOD40. Based on figure from Kulke and Schreyer (1973) …….……..110

Figure 9.2: Showing biotite, talc and chlorite found in MOD36 and MOD41 plotted together with Mg-paragonite…….112

Figure 9.3: Microphotograph from MOD39, showing talc replacing biotite……113

Figure 9.4: The Na-rich volume……..116

Figure 9.5: Ca-rich volume……..116

Figure 9.6: Tetrahedron showing the chemical spaces……117

List of tables

Table 4.1. Overview over Barrovian zones and associated mineral assemblages..……16

Table 4.2: Metamorphic minerals, their possible precursors and original hydrothermal materials (Pirajno, 2009) ……..……17

Table 6.1: Standards used for EPMA…….……35

Table 6.2: Detection limits and maximum concentration for various elements……36

Table 7.1: Summary of modal amounts of minerals in each thin section, estimated by optical microscopy……39

Table 7.2a-c: Feldspar analyses and structural formulae……..……53-55

Table 7.3a-c: Biotite analyses and structural formulae……..…59-61

Table 7.4a-b: Talc analyses and structural formulae……64-65

Table 7.5a-b: Amphibole analyses and structural formulae……..……70-71
Table 7.6: Chlorite analyses and structural formulae……74
Table 7.7: Apatite analyses and structural formulae……..……79
Table 7.8: Comparison of the mystery mineral with kulkeite…….……81
Table 7.9: Comparison of the mystery mineral with AK6, mineral found in kimberlites……..82
Table 7.10: EPMA results and structural formulae of the dioctahedral mica/Mg-paragonite....83
Table 7.11a-b: Titanohematite analyses, cation formulae and end-members……...…86-87
Table 7.12: Ilmenite analyses, cation formulae and end-members……87
Table 7.13: XRF results, main elements……...88
Table 7.14: XRF results, trace elements……...89
Table 8.1: Summary of magnetic properties……..……95
Table 8.2: Results from thermoremanent susceptibility measurements……..……105
Table 9.2: Typical chemical composition for various rocks (Goldschmidt and Muir, 1954)…118

Abbreviations

Ab	Albite
Act	Actinolite
AF demag	Alternating field demagnetization
Amp	Amphibole
Ap	Apatite
An	Anorthite
Ath	Anthophyllite
BSD	Backscatter Electron Diffusion imaging
Bt	Biotite
CAF	Canted antiferromagnetic
Cc	Chalcocite
Chl	Chlorite
EDS	Energy Dispersive Spectrometry
EPMA	Electron Probe Microanalysis
Ep	Epidote
Fsp	Feldspar
Gr	Garnet
Ged	Gedrite
Hem	Hematite
Hbl	Hornblende
Ilm	Ilmenite
Kfs	K- feldspar
Ky	Kyanite
Mu	Muscovite
NGU	Geological Survey of Norway
Phl	Phlogopite
Pl	Plagioclase
Ppl	Plane polarized light
Ppm	Parts per million
Px	Pyroxene
Qz	Quartz
Rut	Rutile
SEM	Scanning Electron Microscope
Ser	Sericite
Sil	Sillimanite
SS	Solid solution
Tlc	Talc
Tur	Tourmaline
Xpl	Cross polarized light
XRF	X-ray fluorescence
Zr	Zirconium

1. Introduction

1.1 Background

During spring 2015, the author was provided some samples to do initial magnetic measurements, with the aim of learning the instruments in the magnetometry lab. These investigations proved to be quite interesting, and as a result, the decision was made to proceed with these samples for a master's thesis. The samples were collected in July 2013, during field work on the Høgås fold in the Modum Complex. Back then, the rocks were believed to be mainly bedded metamorphosed, sedimentary rocks with titanohematite. Figure 1.1 is a photograph from the sample called MOD39, showing dark lumps of what was then guessed to be cordierite. Talc was suspected from the hand specimens and confirmed present by Bjørn Eske Sørensen, using XRD. The talc has a fibrous habit, with fibers parallel to the lineations, in turn parallel to the fold axis. It was therefore proposed that the talc might be pseudomorphous after orthoamphibole. In addition, small amounts of colorless amphibole were found.

Figure 1.1: Bedded, metamorphosed sedimentary rock at MOD39 with dark lumps, containing diffuse, fine titanohematite. During initial field work, these lumps were suspected to be cordierite, and this mistake was extended by discovery of small amounts of colorless amphibole assumed to be anthophyllite. The present study shows that the lumps are oligoclase and the amphiboles are NaAl-substituted actinolite.

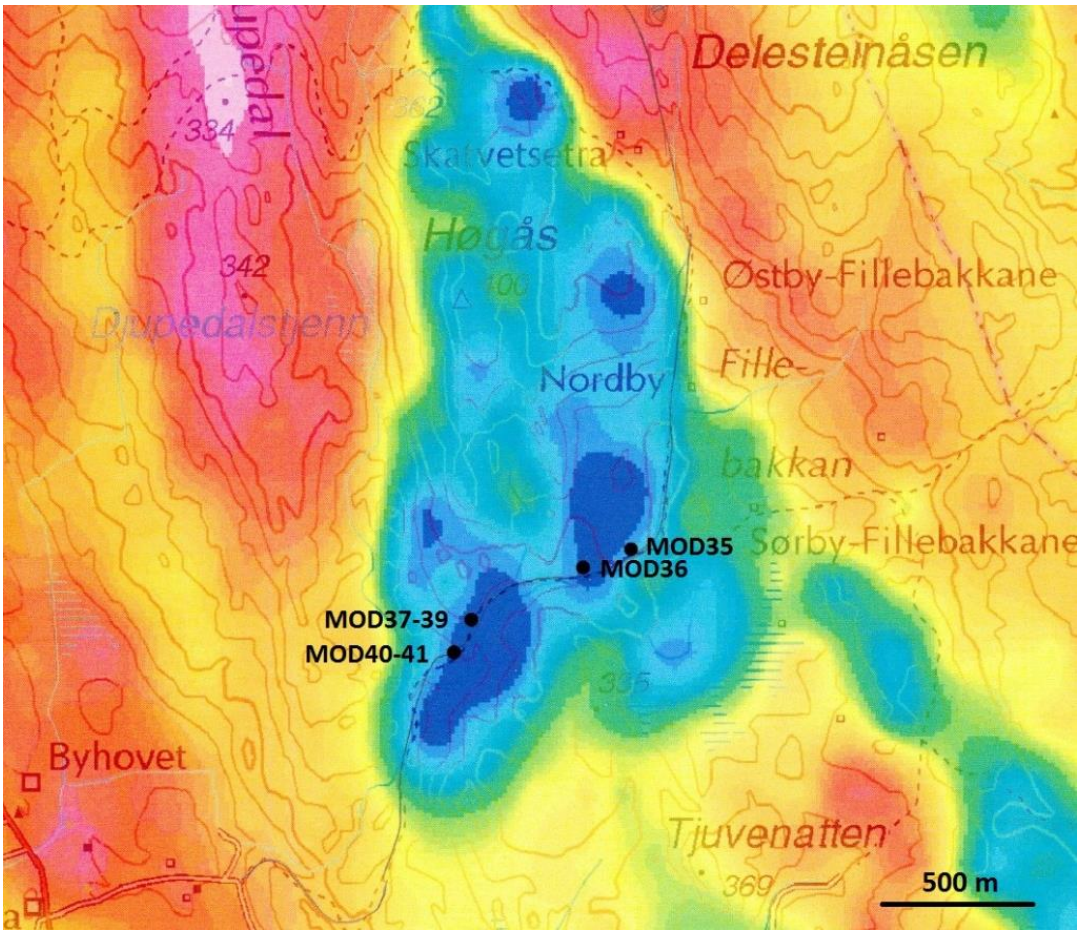

Figure 1.2: The negative anomaly of the Høgås anticline, with the sample locations.

The area that has been investigated in this thesis is located about 10 km west of the Oslo Graben, in southern Norway. Recent high-resolution aeromagnetic surveys have shown numerous negative anomalies in the area, resulting from remanent magnetism. The remanent anomalies in the area range to nearly 2000 nT below background, as mapped in ground magnetic traverses (McEnroe et al., 2016). Samples from seven locations from a small area of metamorphosed sedimentary rocks around the Høgås fold have been the main focus of this thesis, and these have been compared with samples from four other locations in the Modum Complex. The area of the Høgås fold with the sample locations are shown in figure 1.2. MOD35-MOD36 are located in the east limb of the fold, while MOD37-MOD41 are from the west limb. HJ002-HJ003 are located approximately 7 km N-E of the Høgås fold. Structural measurements on the Høgås fold in 2013 are shown in figure 1.3, including foliations, lineations, and a calculated fold axis.

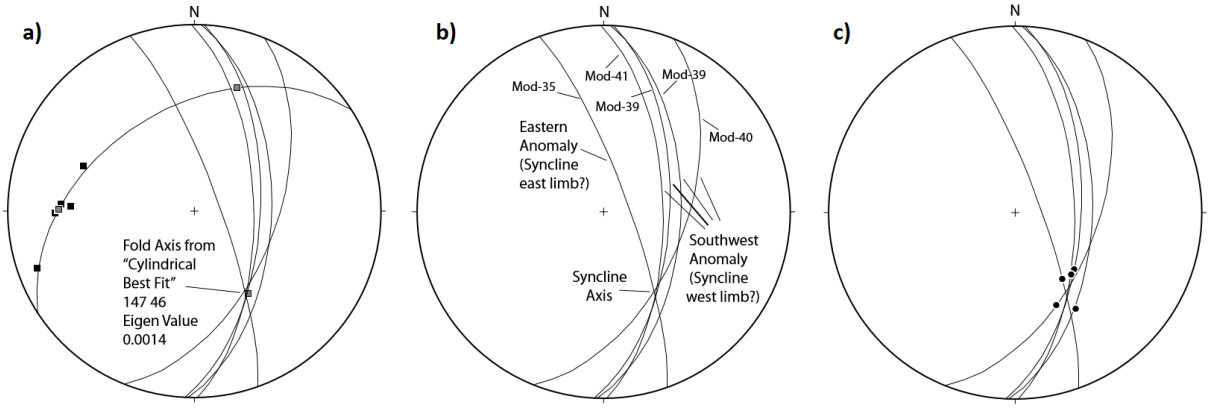

Figure 1.3: Structural measurements near the Høgås negative anomaly. a) 5 poles to foliation and calculated fold axis, measured on four oriented blocks extracted for paleomagnetic studies, June 1., 2013. b) Five foliations plotted directly. One additional measurement not on extracted block (dark tag). Foliation is quasi-parallel to bedding, including top-E (?) graded bedding near MOD39. c) Lineations measured on foliation planes on four oriented blocks extracted for paleomagnetic studies and one additional measurement, June 1., 2013. Lineation is parallel to inferred syncline axis, plunging 46° southeast.

1.2 Previous work

The Bamble and Kongsberg sectors have been thoroughly investigated in earlier studies. this area has been part of a long-term argument beginning between Victor M. Goldschmidt and Tom Barth about the importance of metasomatism, and whether it is a regional or local process. Still, regional metasomatism is the most widespread theory, and the majority of the previous work supports this theory. Bugge wrote about geological and petrographic investigations in the Kongsberg-Bamble formation in 1943, describing the rock material. He also analyzed the metamorphic and metasomatic processes and the changes induced in the rocks. Here, the publication is divided into the Old Complex, comprising metamorphic arenaceous, argillaceous, and calcareous sediments, volcanites and basic intrusives, and the Younger Complex, formed during or after a migmatization period. Detailed description of the geology of the Modum Complex are given by Jøsang (1966), and Starmer did extensive work in the Kongsberg sector in the 70's and 80's. Among other things, Starmer suggested that a N-S mylonite zone separated two areas of very different geology, reflecting an up-thrusting of the eastern Modum block. Jøsang performed detailed mapping of the Modum area, describing and discussing the rocks and metasomatic processes. He also described tectonic features and set up a stratigraphy, which he interpreted to be of sedimentary origin. In Waque's master thesis (1996), he stated that

Modum is dominated by Early- to Mid-Proterozoic quartz-rich metasedimentary rocks that have been metamorphosed to sillimanite grade during the Kongsberg orogeny (1500 Ma).

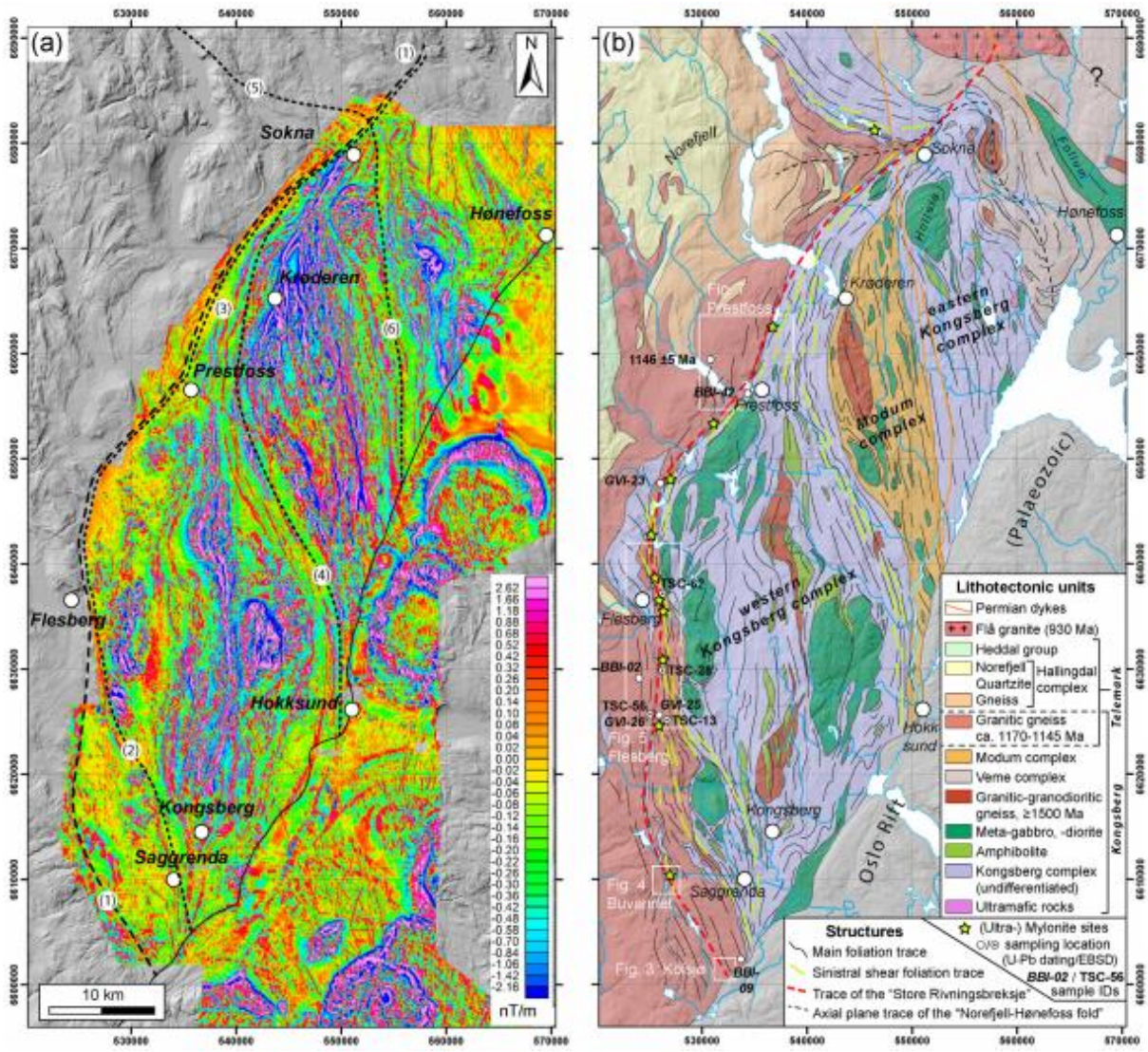

Figure 1.4: a) Airborne magnetic data of the Kongsberg lithotectonic unit. b) Combined lithotectonic and structural map of the Kongsberg lithotectonic unit and adjacent units (Scheiber et al., 2015).

Jacobsen and Heier published a paper in 1978, summarizing the sequence of events in the Kongsberg Sector, as follows: a) Deposition of sodic volcanics, with major and trace element chemistry similar to present day island-arc tholeiite series and some sedimentary rocks. b) Intrusion of calc-alkaline gabbroic to dioritic rocks, together with deformation, folding and metamorphism. This produced a series of quartzo-feldspathic gneisses interlayered with amphibolites. c) Intrusion of gabbros. d) Intrusion of batholitic gneisses, deformation, and a new round to metamorphism up to amphibolite facies. The paper also states that quartzo-

feldspathic gneisses are the most abundant rocks and, together with interlayered amphibolites and mica schists, represents the oldest part of the gneiss complex.

Ingrid Anne Munz has also written several papers about the Modum area. In 1995, she published a paper together with Tom Andersen about LILE and other trace elements, mobilized by metamorphic fluids during the Sveconorwegian orogeny at 1.25-0.9 Ga. They found that LILE and chalcophile element depletion was related to granulite-facies metamorphism as well as albitization and other metasomatic processes at lower grade of metamorphism. Munz et al. (1995) also found that veins occurring in association with albitization of metagabbros and metasediments contained fluid inclusions of hydrocarbon fluids and aqueous fluids with variable salinities. They described retrogradation and alteration due to late stage fluid infiltration and hydrothermal activity in contact zones between metagabbros and metasediments. A few years earlier, a paper on orthoamphibole-cordierite rocks was published (Munz, 1990). These rocks occur as meter wide lenses or bands in areas of extensive albitization. Orthoamphibole was characterized by rosettes of amphibole needles, and the mineral assemblage talc-kyanite was also found in various places in these rocks. This assemblage has been related to the special whiteschist rocks, defined by Schreyer (1974). These rocks are commonly found together with albitites in contact zones between metagabbros and supracrustals, formed due to extensive hydrothermal activity. The paper suggests that orthoamphibole-cordierite rocks break down to whiteschists.

In 2008, Bingen et al. published a paper on the Sveconorwegian orogeny, recognizing four deformational phases. The Arendal phase (1140-1080 Ma) represents the collision between the Idefjorden and Telemarkia terranes, producing the Bamble and Kongsberg tectonic wedges. This caused high-grade metamorphism and deformation. At 1050-980 Ma, the Agder phase led to burial and exhumation of the Idefjorden Terrane and crustal thickening of the Telemarkia Terrane. The Falkenberg phase at 980-970 Ma reflects final convergence in the belt followed by divergence, and the Dalane phase at 970-900 Ma led to gravitational collapse of the belt. Scheiber et al. (2015) recently published a paper revisiting the boundary between the Kongsberg and Telemark lithotectonic units, describing multiple phases of reactivation and strain localization which led to the formation of complex fault patterns, extensive quartz vein networks and an enormous brittle fault zone that locally juxtaposes different blocks.

Extensive work has also been done with respect to the magnetism of the area. Numerous negative remanent anomalies have been found in the area. Fabian et al. (2008) found sillimanite-rocks from the Modum Complex with a stable NRM of ~1 A/m with an upward pointing

magnetic vector at steep angle to the present field direction and with very low susceptibility (0,00016 SI). McEnroe et al. (2009a) proved that exchange bias can be linked to lamellar magnetism. They showed that negative remanent magnetization came from rocks containing metamorphic titanohematite with abundant nanoscale exsolution of ilmenite. In 2014, a paper was published by Robinson et al. Here, they found that negative anomalies were derived from rocks containing ilmenite with hematite exsolution. Three types of exsolution was found; spinel plates, rutile blades, and lamellae that were too fine for EPMA analyses. An aeromagnetic map from this article can be seen in figure 1.5. These rocks were found to have a NRM with declination of 276° and inclination of -67°, reflecting the late Mesoproterozoic time of remanence acquisition.

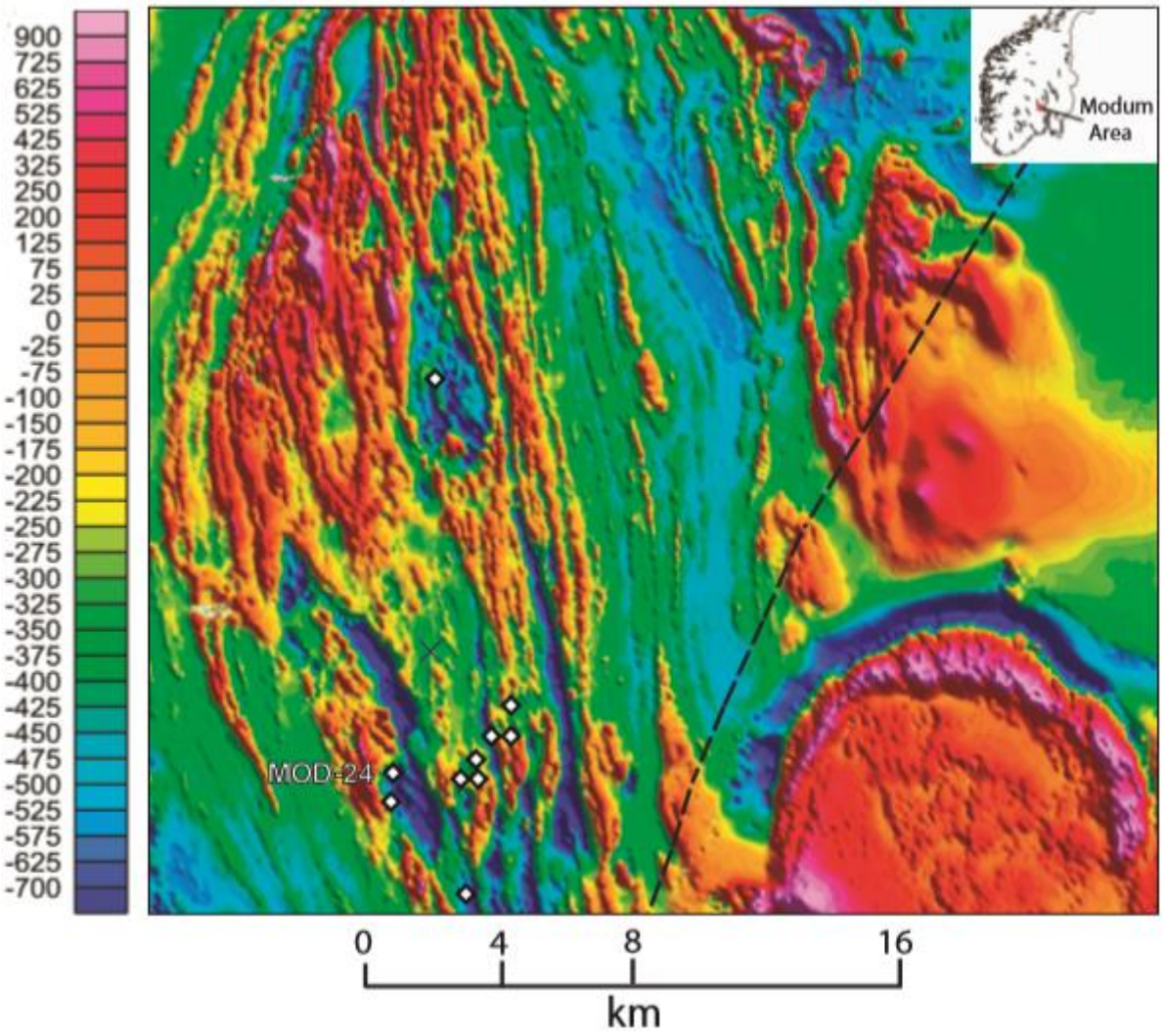

Figure 1.5: Aeromagnetic survey map over the Mesoproterozoic basement of the Modum Complex, south Norway. To the southeast is the Permian Oslo Rift, with black line indicating the western boundary (map by Giulio Viola, Robinson et al., 2014).

2. Aim of study

Through diverse petrographic and magnetic laboratory work, the aim of this thesis is to answer the following questions:

- How do these rocks plot geochemically?
- Is it possible to decide what the sedimentary protoliths were and why the rocks are so oxidized?
- What is causing the negative anomalies?

The petrology of the rocks has been investigated through XRF analyses and the use of 10 thin sections. Mineral chemistry was obtained through EPMA analyses. To investigate the magnetic minerals and properties, 72 samples have been investigated for density, susceptibility and NRM, and for selected samples, demagnetization curves and temperature-dependent susceptibility curves have been obtained.

3. Geological setting

3.1 Regional geology

The continental crust of southern Norway is a part of the Scandinavian Domain of the Baltic Shield (Andersen and Munz, 1995). In this area, there is a Sveconorwegian orogenic belt, which is a result of the collision between Fennoscandia and another major plate at the end of the Mesoproterozoic era (Bingen et al., 2008). This event is similar to the Grenville orogeny, which was an orogenic event during the assembly of the supercontintent called Rodinia. The Sveconorwegian belt divides into a Paleoproterozoic Eastern Segment and four Mesoproterozoic terranes. These are the Idefjorden, Kongsberg, Bamble and Telemarkia terranes. Bamble and Kongsberg are tectonic wedges after collision between Idefjorden and Telemarkia terranes, and probably formed a continuous terrane in the Precambrian (Grorud, 1997). Two phases of metamorphism are recognised in the area. Most of the Bamble and Kongsberg terrains are metamorphosed to middle and upper amphibolite facies during the Kongsberg orogeny around 1500 Ma (Andersen and Munz, 1995). Granulite-facies rocks are sporadically found. A map over the area can be seen in figure 3.1. Bamble and Kongsberg terranes are now separated by the Oslo Graben. The Kongsberg sector can be subdivided into the western Kongsberg complex, the Modum complex and the eastern Kongsberg complex (Andersen and Grorud, 1998).

3.2 The Modum Complex

Resent aeromagnetic surveys over Southern Norway have showed numerous remanent anomalies in the Modum area (McEnroe et al., 2016). In the Modum complex, supracrustal rocks are dominant. The Modum complex is the core of an antiformal structure, exposing quartzites and sillimanite-bearing rocks, which is not found in other places in the Kongsberg sector. They are surrounded by overlying hornblende-plagioclase-biotite-quartz gneisses lying in synforms (Waqué, 1996). According to Jøsang (1966), Munz (1990), Munz et al. (1994) and Munz et al. (1995), the Modum complex consists of several different rock types. Sedimentary rocks include mica gneisses and schists with sillimanite, quartzites and marbles, while intrusives include granitic and dioritic gneisses, metagabbros and amphibolites. In addition, metamorphic rocks like orthoamphibole-cordierite rocks, whiteschists and albitites are found. This was claimed to result from large-scale interaction between rocks and aqueous fluids. In addition, pegmatites and ultramafic bodies are found, together with calcite veins, cobalt mineralization and dykes and veins of various ages.

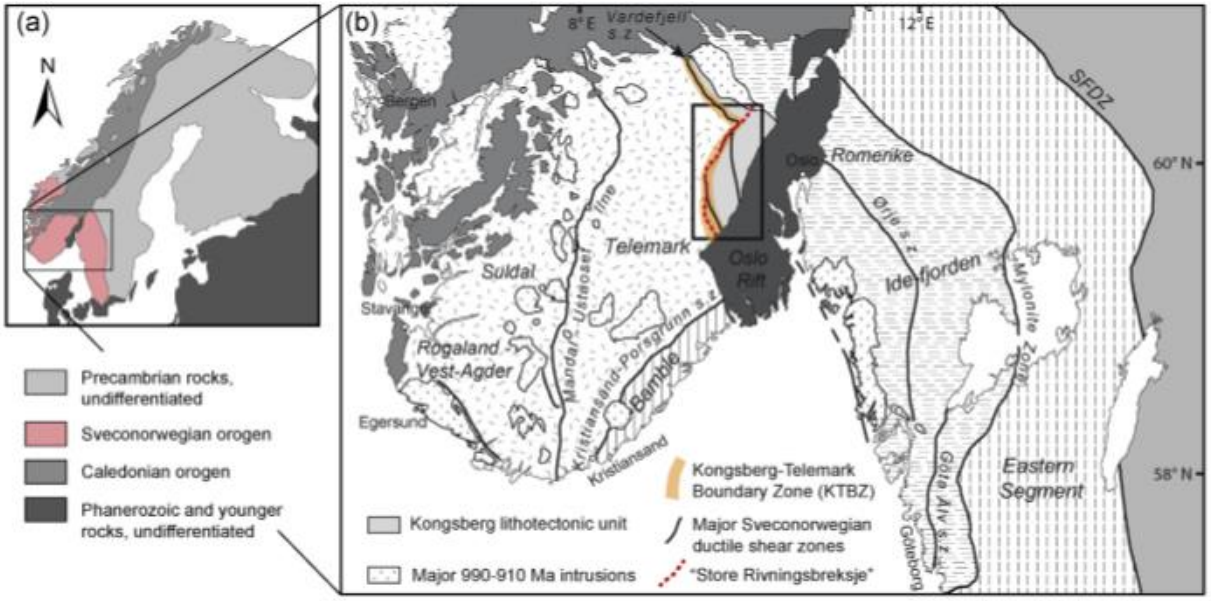

Figure 3.1: a) Sketch tectonic map of Scandinavia highlighting the areas affected by the Sweconorwegian orogeny. b) Map of the Sveconorwegian orogen showing units, major ductile shear zones, Sweconorwegian plutons and the Kongsberg-Telemark boundary zone. Framed in black are the Kongsberg sector (Scheiber et al., 2015).

Approximately 60 % of the Modum complex is made up of metamorphosed sedimentary rocks. These beds are steeply dipping and isoclinally folded, and are intruded by subsequently metamorphosed gabbro and amphibolite bodies (Andersen and Grorud, 1998). The gabbros intruded the metasediments near the onset of the Sveconorwegian high-grade metamorphism, with penetrative deformation and regional foliation around 1224 Ma. The peak amphibolite-facies metamorphism was in the sillimanite stability field. According to Starmer (1980), the Modum Complex is separated from the western part of the Kongsberg terrane by a major shear zone, so that no granulite facies assemblage is present in Modum. This has recently been studied extensively by Scheiber et al. (2015). They found that the oldest part of the boundary zone between Kongsberg and Telemark (KTBZ) formed during the Sveconorwegian orogenic cycle (1140-900 Ma), within and at the margin of a granitic belt formed by intrusions between 1170 and 1146 Ma. Mylonitic shear zones formed within this belt, followed by later folding and exhumation of the Telemark lithotectonic unit in the footwall of the KTBZ. This zone has been repeatedly reactivated in a brittle fashion, forming complex fault patterns, extensive quartz vein networks and a 100 km long brittle fault zone.

Munz (1990) states that the rocks may be subdivided into three major units: (1) Supracrustal rocks consisting of quartzites, micaschists, sillimanite-bearing gneisses and calc-silicates. (2) Metamorphosed gabbros/amphibolites. (3) Hydrothermally formed rocks including the M(F)ASH rocks, albitites, scapolite and calcite veins. In some locations, the gabbros are altered to amphibolites, and garnet coronas have been found. Munz and Morvik (1991) determined P-T ranges of 7-10 kbar and 600-800°C for corona formation, locally related to hydrothermal alteration in the contact zones between the gabbros and surrounding rocks that occurred both before, during and after peak metamorphism. The hydrothermal activity has also led to formation of lenses of orthoamphibole-cordierite rocks, cobalt sulphide/arsenide mineralizations, and veins and dykes of scapolite, albite and calcite.

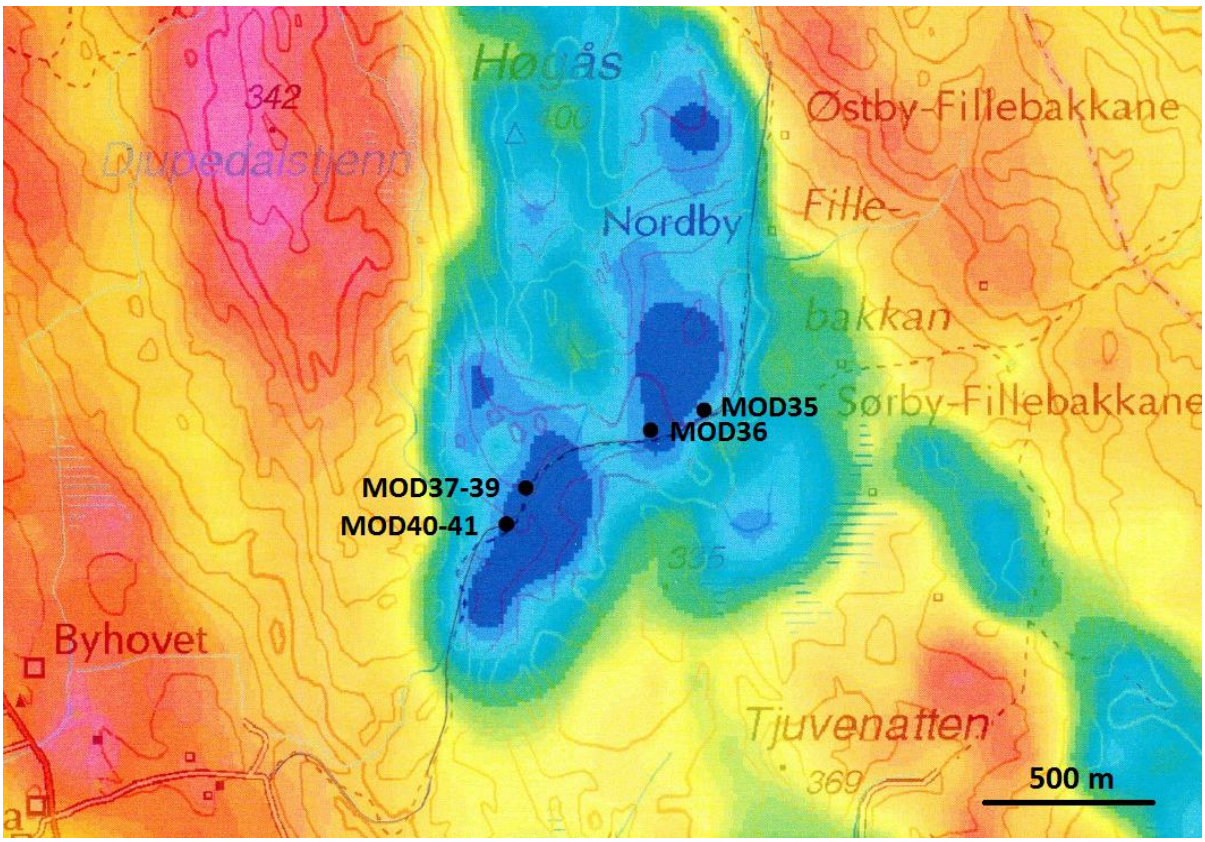

Figure 3.2: Aeromagnetic map over the sample area (NGU database)

3.3 Mining history and mineralizations

The metamorphosed sedimentary rocks in the Modum Complex contain concordant, sulphide-rich zones, called fahlbands. These are strongly radioactive, due to the presence of uraninite. These bands are too abundant to be classified as accessory minerals, but too sparse to be massive ores (Gammon, 1966; as cited in Andersen and Grorud, 1998). Two of these contain cobalt minerals. From 1776 to 1898, the Skutterud Cobalt Mines was operated by the Modum

Blaafarveværk Company (Grorud, 1997). This locality is of cobalt triarsenide skutterudite, and is mostly nickel-free. How this cobalt ore formed is not known, but one theory includes fluids emanating from mafic intrusions. Another theory is that the formation is related to the formation of albitites during Sveconorwegian metasomatism. The thermal maximum in the area was around 1.2-0.9 Ga, but it is also unknown whether the cobalt minerals are results from primary precipitation or remobilization. The timing of this ore deposition is important to understand the crustal evolution in Southern Norway, because it can say something about the lower age limit for the clastic sedimentation in the Kongsberg sector (Andersen and Grorud, 1998).

4. Petrological theory

4.1 Metamorphism

Metamorphism is a process by which rocks can change their texture, mineralogy, and locally chemical composition. These changes are driven by changes in temperature, pressure, stress and fluid migration (Winter, 2010). Temperature is the most important factor, and it is common to put the upper and lower boundaries of metamorphism at 200 and 1000°C respectively. Lithostatic pressure is dependent on the density and volume of the overlying rocks. For instance, the pressure can increase during orogeny, because the crust can become thicker.

Dependent on the composition of the rock, increasing temperatures will lead to some minerals breaking down and recrystallizing into new minerals. This is called prograde metamorphism, and commonly involves devolatilization reactions where the hydrous and carbonate minerals lose their volatiles (Winter, 2010). Later, the temperature and pressure will decrease, and if fluids are available, new changes can occur, called retrograde metamorphism. It may be possible to track these changes by identifying points where mineral assemblages were in equilibrium, and make a P-T-t path (pressure-temperature-time path) for the rocks in a limited area.

Metamorphism can be classified in several types, like regional, local and hydrothermal metamorphism (Smulikowski et al., 2003). This thesis will focus on regional metamorphism. It can also be divided into types based on how the temperature and pressure conditions were at the time of metamorphism, like low-temperature or ultra-high pressure metamorphism. This is related to metamorphic facies, which is a concept first introduced by Eskola in 1915. According to IUGS/SCMR, a metamorphic facies is a set of metamorphic mineral assemblages related to different metamorphic conditions, in particular temperature and pressure (Smulikowski et al., 2003). Another metamorphic concept is metamorphic zones, also called Barrovian zones. Here, the zones are divided based on the appearance of a new mineral, called index minerals, in a metamorphosed pelitic rock as metamorphic grade increases (Winter, 2010).

4.2 Metamorphic facies

The mineral assemblages in rocks are related to different metamorphic conditions, where many variables, like pressure, temperature and activity of fluids such as H_2O and CO_2 is important (Smulikowski et al., 2003). Hence, facies can be used to decide what pressure and temperature

the rock was subjected to during metamorphism based on prior experience. Facies can also be defined separately for rocks of different bulk composition (Winter, 2010). Eskola (1920) defined eight facies; greenschist, epidote-amphibolite, amphibolite, pyroxene-hornfels, sanidinite, granulite, glaucophane-schist and eclogite. Later, a zeolite facies and a prehnite-pumpellyite facies have been added. Figure 4.1 shows a pressure-temperature diagram with facies limits. In this thesis, the amphibolite facies is the focus.

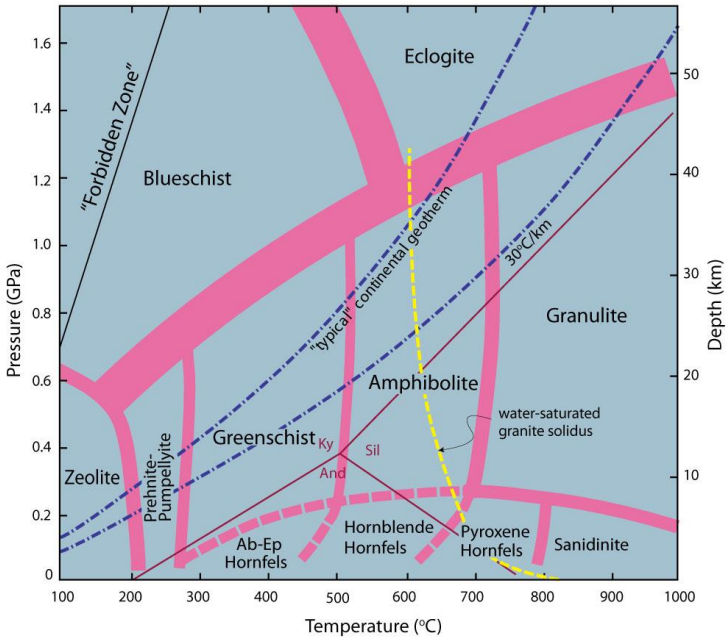

Figure 4.1. Temperature-pressure diagram showing the generally accepted limits of the various facies. Also included are the average geotherm, the 30°C/km geothermal gradient, the minimum melting curve for H_2O-saturated granite and the stability range for the three Al_2SiO_5 polymorphs (Winter, 2010).

4.2.1 Amphibolite facies

Each facies has diagnostic mineral assemblage occurring in metamorphosed rocks, most commonly based on rocks of basaltic composition, because basaltic rocks occur in practically all orogenic belts around the world (Winter, 2010). But, there are major mineralogical differences between basaltic and sedimentary rocks. The amphibolite facies for basaltic rocks are mostly based on the occurrence of rocks which consist of more than 75% of a combination of hornblende and plagioclase more calcic than An_{17} (Smulikowski et al., 2003). Where other minerals are present (>5%), a prefix should be added, e.g. quartz-amphibolite (Coutinho et al., 2007). Pelitic rocks (metamorphosed shales) are generally more sensitive to changes in the P-T conditions, leading to several assemblages in each facies. An amphibolite from a sedimentary protolith is called para-amphibolite, though it can be hard to determine the nature of the

protolith (Coutinho et al., 2007), and many layered amphibolites are in fact layered basaltic ash and lavas. The facies can be divided into types based sequences of P-T conditions, where greenschist, epidote-amphibolite, amphibolite and granulite belongs to the medium P-T type (Smulikowski et al., 2003).

Pelites are fine-grained mature clastic sediments derived from mudstones and shales. They undergo extensive changes during progressive metamorphism, and tend to form mica schists with porphyroblasts of e.g. chlorite, biotite, garnet, staurolite, cordierite, sillimanite, and kyanite. The chemistry is dominated by high Al and K, like clays, mica, and chlorite. These may also contain quartz, feldspar and iron oxides (Winter, 2010). Rocks in the amphibolite facies commonly show chemical evidence of hydrothermal alteration, which again is most common in igneous rocks where the alteration occurred in or near the original igneous environment. As many reactions involve devolatilization, H_2O and CO_2 is important. In metamorphic rocks, it is commonly difficult to see what textural and mineralogical relationships are pre- or post-metamorphic. If the rocks have been retrograded, this complicates the matter even further (Pirajno, 2009). In such situations, it is important to investigate whole-rock and mineral geochemistry.

In basaltic rocks, Mg-rich rocks in the greenschist facies tend to be composed of act + chl + ab + ep + qz ± (bt, mu). Fe-rich rocks in the epidote-amphibolite facies contain hbl + ab + ep + qz + bi ± (gr, chl) (Graham et al., 1983). Metasedimentary, non-calcareous rocks contain qz + ab + mu + chl + rut ± (bt, gt, cc, tur, ep), while in more Ca-rich sediments, rutile is commonly replaced by titanite. In high-temperature, hydrous assemblages, chlorite is absent. At temperatures of amphibolite facies and above, intermediate plagioclase is stable (Yardley et al., 2013). Chlorite and/or talc can be products from plagioclase breakdown, and if they are present below 600°C, this is of major importance for the formation of amphibolite-facies shear zones. This also have implication of the exhumation of lower-crustal rocks and further fluid infiltration (Bach et al., 2013).

It is also possible to say something about the origin of the fluids by its composition, e.g. low content of Na and K in the bulk rock indicates an acid-sulphate alteration zone (Pirajno, 2009, Pirajno et al., 2013). Unusual cordierite + anthophyllite rocks may be present in the amphibolite facies. These have very high values of Mg and low values of Ca, which are unlike other known sedimentary or igneous rocks (Winter, 2010). These changes are proposed to be due to hydrothermal alteration by hot recirculating brines as near mid-ocean ridges that occurred long before regional metamorphism. Munz et al. (1995) showed that fluid inclusions in albitized

rocks from amphibolites in Modum contained low values of K, Na-Ca-Cl brines with a Ca/Na-ratio below 1, and Br/Cl-ratios like seawater. This means that sea water can be trapped in rocks without necessarily leading to rock transformation by fluid influx.

The transition from amphibolite to granulite facies occurs between 650 and 850°C, where pelitic and quartzo-feldspathic rocks start to melt if a aqueous fluid is present in granitoid rocks (Winter, 2010). This transition is recognized by the loss of hornblende, muscovite and biotite, at the same time as orthopyroxene and garnet appear (Touret and Nijland, 2013).

4.2.2 Barrovian zones

Sandstones usually show inconspicuous changes across an area, in contrast to pelitic rocks. Pelitic rocks were originally shales, and that can be divided into zones based on appearances of index minerals (Winter, 2010). The zones, called Barrovian zones, are divided by isograds, which represent fields of similar metamorphic grade. Table 4.1 gives an overview over the different zones with associated index minerals.

Table 4.1. Overview over Barrovian zones and associated mineral assemblages.

Barrovian zone	**Mineral assemblage**
Chlorite	Chlorite, muscovite, quartz, albite
Biotite	Biotite, chlorite, muscovite, quartz, albite
Garnet	Garnet, biotite, chlorite, muscovite, quartz, albite/oligoclase
Staurolite	Staurolite, biotite, muscovite, quartz, garnet, plagioclase. Some chlorite may persist.
Kyanite	Kyanite, biotite, muscovite, quartz, plagioclase, usually garnet and staurolite.
Sillimanite	Sillimanite, biotite, muscovite, quartz, plagioclase, garnet, staurolite. Some kyanite may persist.

4.3 Element theory

Geochemistry is about quantifying elements to classify rocks and it can be possible to find the origin and evolution of a magmatic system. Elements can be divided into major, minor and trace elements. Major elements are elements that make up more than 1 wt.% of a rock. These are usually presented as oxides, like SiO_2, Al_2O_3, MgO, FeO (or sometimes Fe_2O_3), CaO, Na_2O and K_2O. These eight elements compose 98.5 wt.% of the crust, and are decisive for the mineral

assemblage in the rocks (Winter, 2010). Major elements can be used in rock classification, construction of variation diagrams, and to compare rock compositions with experimentally determined melt compositions (Rollinson, 2013). Together with trace elements, major elements can be used to identify the tectonic settings of igneous rocks. Trace elements constitute less than 0.1 wt.% of the rock concentration, and are usually given as a single element and in ppm, where 1000 ppm equals 0.1 wt.% (Best, 2009). These elements substitute for other major and minor elements. Minor elements make up between 1 and 0.1 wt.% of a rock, and can also substitute for major elements, and locally, where they reach saturation level, form their own mineral phase. Examples are P and Ca, that can form minerals like apatite and titanite (Winter, 2010). These minerals are usually called accessory minerals.

4.4 Hydrothermal alteration

In any study of chemical changes in metamorphic rocks, weathering and/or diagenetic alteration of the protolith must be considered (Bebout, 2013). Weathering is the alteration of rocks at or near the Earth's surface, due to atmospheric agents (Winter, 2010). Chemical weathering is when rock materials are dissolved and aqueous solutions transport soluble ions and molecules (Robb, 2005). Clay and oxides are common residual weathering products, together with other unaltered residual material with low solubility, like silica and alumina. Table 4.2 shows an overview of metamorphic minerals and their possible precursors. The ionic potential is the ratio of ionic charge to ionic radius, and cations with low ionic potential are easily hydrated and become mobile. This happens under a range of conditions, but under alkaline conditions, these will precipitate and be adsorbed into clay particles. The same principle is valid for anions with high ionic potential, which will form soluble complexes and dissolve easily.

Table 4.2: Metamorphic minerals, their possible precursors and original hydrothermal materials (Pirajno, 2009).

Metamorphic minerals	Possible precursors	Possible origin
Chlorite	Montmorillonite	Altered volcanic glass
Muscovite	Illite	Diagenetic illite derived from kaolinite, or epithermal alteration
Almandine garnets	Chamosite	Hydrothermal sediments, oolites
Sillimanite, kyanite, and alusite	Kaolinite, alumino-silicate clays	Acid leaching of sulphate-bearing solutions, epithermal systems

4.4.1 Solubility

Different elements have different solubility, influencing which elements can exchange with each other in aqueous solutions. There is a hierarchy of mobility in the surficial environment: Ca>Na>Mg>Si>K>Al=Fe (Robb, 2005). In ground waters, alkaline and alkali elements are typically the most soluble, while Al and ferric Fe are relatively immobile. In clay minerals, Si^{4+} can replace Al^{3+}, leading to negative surface charge. This is then neutralized by adsorption of cations on the surface of the clay minerals. Since Al is mostly immobile during weathering, it is a good measure of the degree of rock weathering (Pirajno et al., 2013).

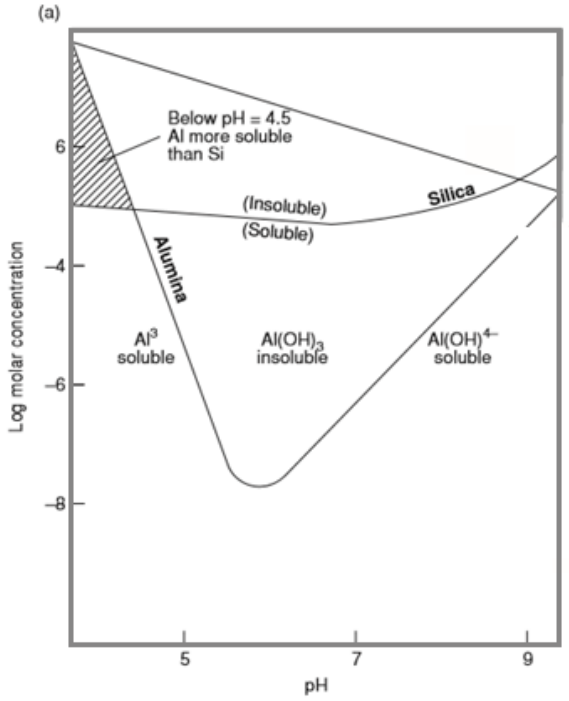

Figure 4.2: Shows solubility of Si and Al as a function of pH (Robb, 2005).

Shown in figure 4.2, Al is more soluble than Si when the pH is below 4.5, in so-called acidic conditions. Therefore, the resultant soils are typically silica-enriched and depleted in Al and Fe (Robb, 2005). The solubility of Si increases with pH, while Al is most soluble at either very low, or high pH. Key minerals like chlorite and muscovite, and the ratio of Fe/Mg can say something about the hydrothermal environment (Pirajno et al., 2013). Widespread alkali exchange has been documented in sandstones altered by diagenesis (Bebout, 2013). During diagenesis and metamorphism, oxide grains grow and turn coarser. Increasing concentrations of Cl and/or temperature in the fluid will increase the solubility of several transition metals like Fe, Mn, Pb and Zn (Yardley et al., 2013).

Hydrothermal alteration is an important mechanism in metamorphism, particularly at shallow levels where rock fracturing allows openings for fluid migration. When low temperature, highly oxidizing, meteoric fluids meet and mix with less oxidizing, magmatic fluids with reduced sulphur, this will cause precipitation of metal sulphides and iron oxides (Robb, 2005).

4.4.2 Redox potential

Oxidation is the transfer of electrons by oxygen present in air or in water (Robb, 2005). Iron is the most common oxidized element, and is the only common element that occurs widely in two different valence states (Winter, 2010). Iron goes from ferrous (Fe^{2+}) to ferric (Fe^{3+}) valence state by loss of electrons. Redox is an abbreviation for reduction and oxidation, and the redox potential is an important parameter for characterising aqueous solutions and the oxidizing and reducing conditions in geological environments (Pirajno et al., 2013).

Hydrothermal alteration depends on chemical potential, which indicates the capacity of one compound to react with another, and fugacity, which is a measure of the escaping tendency of a vapour or gas and its departure from ideal behaviour (Winter, 2010). Oxygen fugacity, f_{O2}, is a variable controlling oxidation potential in terms of partial pressure of oxygen. This relates to the potential of Fe to occur in a more oxidised or reduced state, where the ratio of Fe^{3+}/Fe^{2+} increases with increasing oxygen fugacity. At the lowest f_{O2}, Fe is in its native state, while at higher f_{O2}, it occurs as FeO in various minerals. At higher f_{O2}, some Fe^{2+} become Fe^{3+}, allowing stability of magnetite while at still higher f_{O2}, ferric Fe forms hematite through the reaction

$$Fe^{2+}{}_4Fe^{3+}{}_8O_4 + O_2 \leftrightarrow 6Fe_2O_3$$

Magnetite Hematite

In this reaction, the four Fe^{2+} ions in magnetite are oxidized to Fe^{3+} in hematite, while O_2-ions compensate and maintain electrical neutrality (Winter, 2010).

Oxygen fugacity can also help determine the composition of fluids (Pirajno et al., 2013), and will help decide where and in what state the iron will be incorporated. This also affects the stability of the minerals. In rocks with relatively high oxygen fugacities, the Fe^{3+} will be concentrated in oxides, and these rocks will therefore have less Fe^{2+} available for the silicates (Winter, 2010). This is important in ferrous minerals like biotite. When the Fe^{2+} in the biotite lattice is weathered and oxidized, biotite will get a charge imbalance, and is destabilized.

Eh and pH also influence the geological conditions and iron state. Fe is least mobile as ferrous iron at high Eh and pH (Robb, 2005). In an oxidizing system, the Eh is high (Pirajno et al.,

2013), and in figure 4.3, this relationship is shown. If aqueous solutions containing Fe^{2+} in a reduced system are introduced into an oxidizing system, this will lead to precipitation of Fe^{3+} and concentration of iron (Robb, 2005). This can form e.g. BIF, banded iron formations, where the major components Fe and Si appear to come from the oceans and not a continental source. Oxidation is hence an important tool to decide original geological conditions, but it can also cause confusion. Studies have shown that small changes in oxidation ratio can lead to changes in mineral mode and compositions, complicating the estimation of metamorphic conditions (Boger et al., 2012).

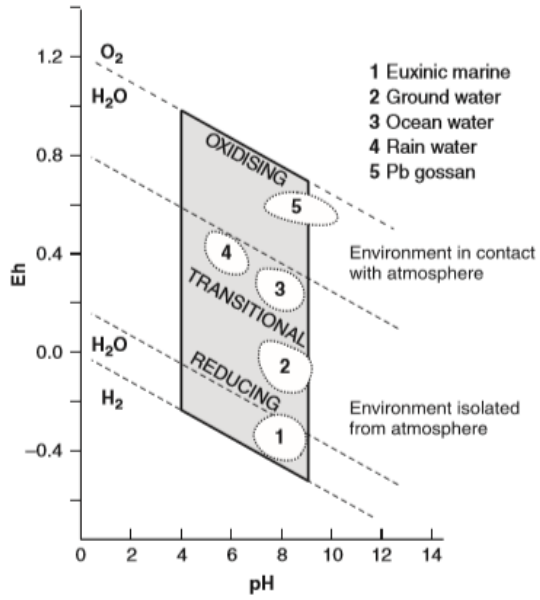

Figure 4.3: Diagram over Eh and pH limits of some natural environments (Robb, 2005).

4.4.3 Metasomatism

Metasomatism is a term that has been under continued discussion over many decades. The largest question is uncertain whether the process can extend to large areas, or if it is more of a local process. The process is related to hydrothermal metamorphism (Smulikowski et al., 2003), although aqueous solutions are not the only medium through which the process is alleged to take place. The definition is "a metamorphic process by which the chemical composition of a rock or rock portion is altered in a pervasive manner and which involves the introduction and/or removal of chemical components as a result of the interaction of the rock with aqueous fluids" (Zharikov et al., 2006). Is may also occur where there are chemical gradients between rocks of different composition, without the participation of a fluid. During metasomatism, the rock remains in a solid state. This means that fluids interact with the rock to add or deplete the rock

with different chemical components. Metasomatism as thus defined usually happens along shear zones, fractures, faults and in permeable lithologies (Yardley et al., 2013).

A hydrothermal fluid can be defined as a hot aqueous solution, and may have the ability to change the rocks they circulate through (Pirajno, 2009). This is most practical when there is a large fluid/rock ratio. When such a ratio is small, the fluid composition is likely to be controlled by the rock. The main factors controlling the alteration process are the nature of the rock, composition of the fluids, and concentration, activity, chemical potential of the fluid components, and the fluid/rock ratio. The most abundant sources of metasomatic fluids are sedimentary basin brines and magmatic fluids, like NaCl-brines derived by dissolution of halite, or Br/Ca-rich brines evolved from the brines remaining after halite precipitation. This can commonly lead to e.g. albitisation (Yardley, 2013). Magmatic fluids are dependent on the composition of the initial magma, and are released during magma cooling and crystallization (Yardley et al., 2013). These fluids can contain B and F volatiles derived from melt. Other types of fluid are e.g. sea water, which typically has a salinity of 3.5 wt.% (Robb, 2005). This can come from i.e. black smokers and weathering of continental crust. Common components of sea water are cations like Na^+, K^+, Mg^{2+}, Ca^{2+}, or anions like Cl^-, HCO_3^- and SO_4^{2-}. Meteoric water has been in contact with the atmosphere, and refers to groundwater that has infiltrated into the upper crust (Robb, 2005). This can be especially related to ore deposits characterized by low-temperature transport and precipitation, but can also penetrate deep into the crust and become heated and mineralized (Pirajno, 2009). Connate/formational water refers to water that is included within the interstitial pore spaces of sediments (Robb, 2005). This becomes less relevant with depth, as the pore fluid is likely to be expelled by burial, at the same time as the temperature and fluid pressure of the water increases. Metamorphic fluids include water from dehydration and decarbonation reactions through rising pressure and temperature (Pirajno, 2009). One example is the prograde reaction when muscovite and chlorite react to form biotite at around 400°C, producing H_2O (Robb, 2005).

Because volatiles are so easily mobilized during metamorphism, metasomatism is mostly redistribution of volatiles. When a fluid is introduced into rocks without being in equilibrium with the host rock, exchange can occur (Winter, 2010). This occurs as an attempt to reach equilibrium between the new fluid and host rock, and can happen on large or small scales. The greatest changes happen when rocks of large composition contrasts are adjacent, and the elements can move easily. One example is when lenses with contrasting composition undergoes metamorphism, like igneous intrusions in sediments (Winter, 2010).

4.5 Chemographic diagrams

Chemographic diagrams can be excellent tools to show the relationship between chemical compositions in rocks and stable mineral assemblages (Winter, 2010). They are usually limited to a small range of P-T conditions, and can be based on atomic, molar, or weight ratios. Phases that coexist at equilibrium in a rock are connected by tie-lines (Nelson, 2011). The diagrams explain why rocks that are in equilibrium at the same metamorphic grade can have different mineral assemblages. Figure 4.4 demonstrates the principle of these diagrams, also showing why some mineral pairs cannot coexist. Most petrologists would agree that this happens at least on a small scale in rocks containing fluid components, rather than on a regional scale. Many high-grade rocks contain local preserved evidence of steep chemical equilibrium. This disequilibrium can occur even in rocks containing such minerals as biotite containing a volatile component (Robinson, pers. comm., 2017).

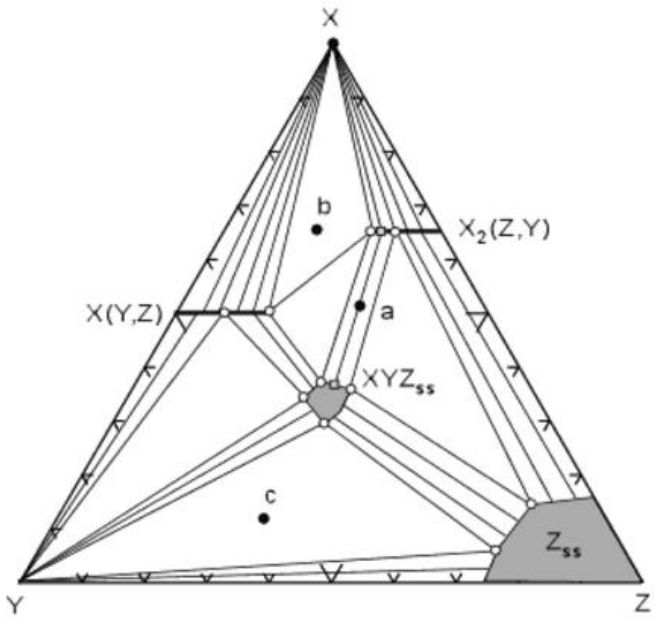

Figure 4.4: Hypothetical three-component chemographic compatibility diagram illustrating the positions of different stable mineral coexisting under given P-T conditions (Nelson, 2011).

It is common to use triangular chemographic diagrams, but most metamorphic rocks contain more than three components. Various methods can be used to solve this problem, like ignoring some components, combine components or using projections (Nelson, 2011). In projections, we assume that a component is always present in the system, projecting all other phases from this. Projections makes it possible to plot more components in the same diagrams, but also leads to complications because some compositions will plot at negative values in the diagram.

5. Geomagnetic theory

The principles of magnetism can be described with help of a bar magnet. Magnetic poles are the fundamental element of magnetism (Dentith and Mudge, 2014). They have either positive or negative polarity, referred to as respectively north or south poles. Magnetic poles of equal strength but opposite polarity are known as magnetic dipoles, and occur as pairs. A bar magnet consists of many much smaller bar magnets, or dipoles. They are all aligned parallel to the long axis of the whole bar magnet (Reynolds, 2011). The north and south poles will cancel each other out, except at the end faces of the whole magnet. The greater concentration of free poles, the higher will be the intensity of magnetization. The field of a magnet, or a magnetic dipole, interacts with the field of the Earth, which leads to the north pole of the magnet being attracted towards geographic north.

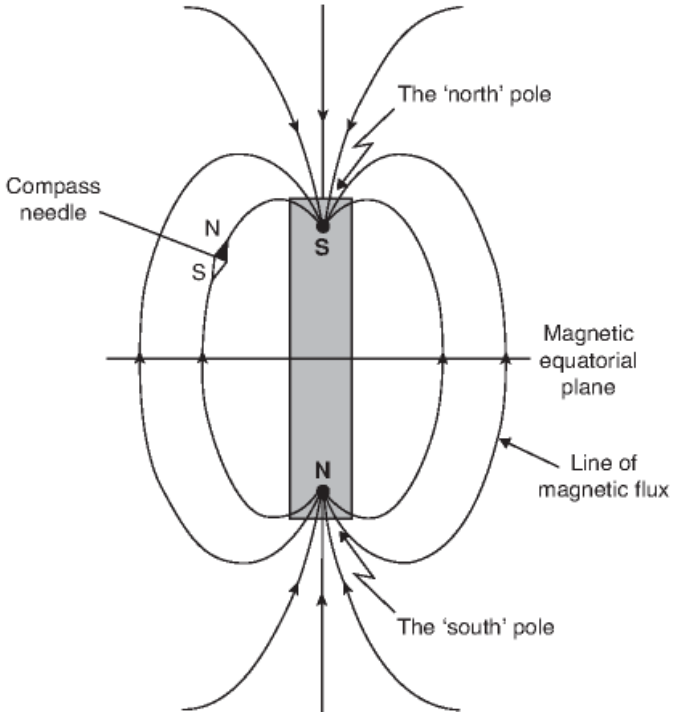

Figure 5.1: Bar magnet. Field lines showing the magnetic field of a magnet. The lines converge at the poles, thus the field will be strongest here (Reynolds, 2011).

5.1 Earth magnetism

The Earth has a magnet field H, originating from within and around the Earth's core (Reynolds, 2011). The geomagnetic field is not produced by a bar magnet within the Earth, but the shape of the field is approximated to a magnetic dipole with the south pole actually placed in the

northern hemisphere (Basavaiah, 2011). The magnetic north and south poles do not coincide with the geographic poles, but are inclined 11.5° to the Earth's rotation axis (Dunlop and Özdemir, 1997). The geomagnetic poles are changing its location with time, moving approximately 50 km/yr. in NW direction. A geomagnetic field can be described with declination, D, which is the deviation from true north, inclination, I, which is the deviation from the horizontal, and the total magnetic force, F, which is the resultant vector of D and I. The magnetic intensity varies from 30,000 nT to 60,000 nT.

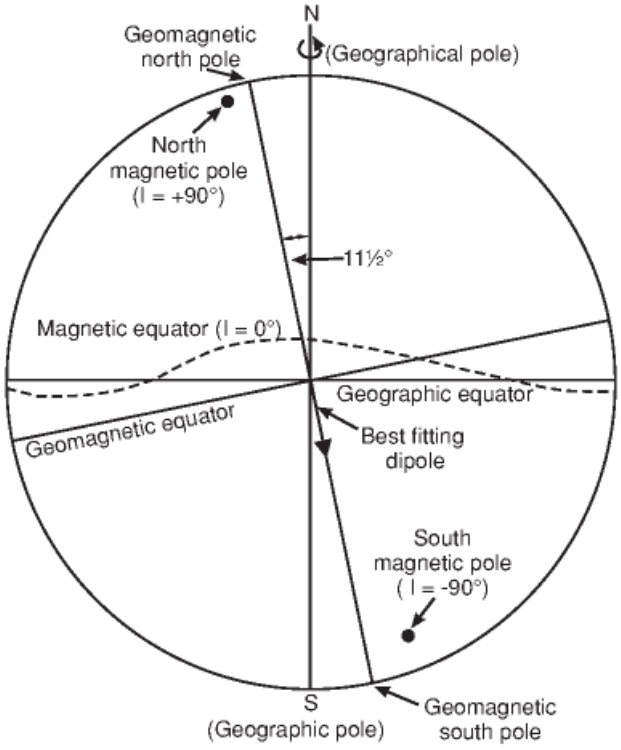

Figure 5.2: The field due to an inclined geocentric dipole (Reynolds, 2011).

5.2 Rock magnetism

Magnetic methods measure spatial variations in the Earth's magnetic field (Dentith and Mudge, 2014). Changes in the magnetic field are caused mostly by variations in a rock's magnetism, due to abundance and configuration of magnetic atoms. The fundamental law of electromagnetism states that a moving electrical charge creates a magnetic field (Basavaiah, 2011). Each electron has a magnetic moment, which acts in either of the two opposing directions, making it behave like a tiny magnet. If a magnetic substance is placed in a magnetic field, H, all the magnetic atoms will align (Dunlop and Özdemir, 1997). This behavior is called

magnetization, J. In various literature, this is also called M. Magnetism can be inherently possessed in a material, or it can be induced by an external magnetic field, like the Earth's magnetic field (Dentith and Mudge, 2014). This is called remanent magnetization, J_r, or induced magnetization, J_i, respectively. The total magnetization of a body is the vector sum of these components (fig. 5.3).

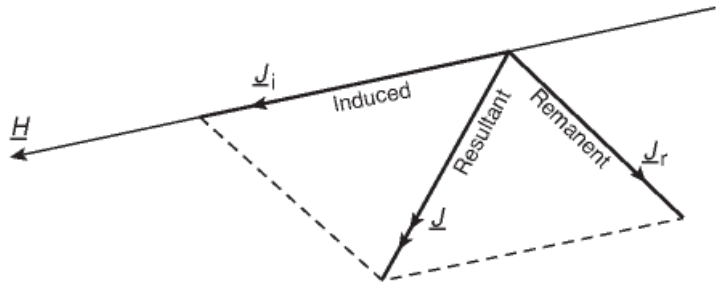

Figure 5.3: Vector sum of induced and remanent intensities of magnetization, J (Reynolds, 2011).

5.2.1 Remanent magnetization

The remanent, or permanent, magnetization is sustained by the internal strength due to permanently magnetic particles (Reynolds, 2011). These materials have the ability to retain magnetization in the absence of a field, or in the presence of a different magnetic field (Musset and Khan, 2000). Generally, the strength and orientation of this magnetism is related to how the external field was at the field the rock was formed and abundance of magnetic minerals in the rock. Only ferromagnetic grains can contribute to remanence (Dentith and Mudge, 2014), so the natural remanent magnetization are affected by factors like magnetic grain size and microstructures. The NRM is the vector sum of all the different possible components of magnetization acquired over its history (Moskowitz, n.d.),

5.2.2 Induced magnetization and susceptibility

Magnetic susceptibility is a fundamental property of a rock. Susceptibility is the ratio of magnetization to magnetic field, or, as Dentith and Mudge (2014) describes it, the "ratio of the strength of the induced magnetism to the strength of the field that caused it". It is given by $\kappa = J_i/H$ and is dimensionless. Susceptibility is hence a measure of how magnetizable a substance can become as a magnetic field is applied (Moskowitz, n.d.). The induced field is approximately parallel to the field that caused it, and the stronger the susceptibility, the stronger the induced magnetism generated by the body will be.

5.2.3 Köenigsberg ratio

Köenigsberg ratio, also called Q-value, gives the relative importance of remanent and induced magnetization. This ratio is given by $Q= J_r/J_i$, where J_r is the values of NRM and J_i is the values of susceptibility times the local field value. Q-values of >>1 indicates that remanence dominates, and Q-values of <<1 indicates that induced magnetization dominates. The Q-value can also say something about the susceptibility, e.g. a very high Q-value can indicate low susceptibilities. The directions of each component significantly influence the resultant overall magnetism (Dentith and Mudge, 2014). Köenigsberg ratio can vary within a single rock type, however the ratio can also say something about cooling rates. Slowly cooled plutonic rocks usually have coarse-grained multi-domain magnetite and small Q-values, while rapidly chilled igneous rocks tend to have fine-grained titanomagnetite and large Q-values (Nagata, 1961, as cited in Reynolds, 2011). This generalization based on Q-values indicate that when rocks are cooled from high temperatures to low temperatures, they will get higher remanence.

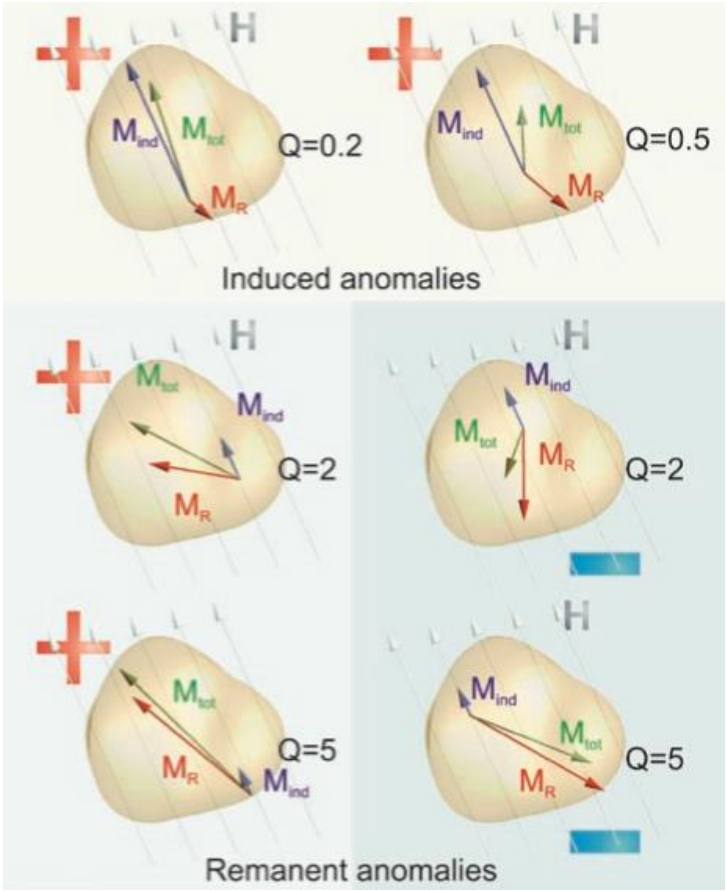

Figure 5.4: The total magnetization, J_{tot}, of a rock is the sum of the induced magnetization J_i and the remanent magnetization J_r. Induced anomalies are always positive, while remanent anomalies can have either sign, depending on their remanence direction (McEnroe et al., 2009a).

5.3 Types of magnetism

The origin of magnetism lies in the orbital and spin motions of electrons and how the electrons interact with one another (Moskowitz, n.d). For most atoms and ions, the magnetic effect of these cancel each other out, so that the atom or ion is non-magnetic. In atoms where they don't cancel, the atoms have a magnetic dipole forming the material's spontaneous magnetization (Dentith and Mudge, 2014). The main distinction between magnetic minerals is that in some materials there is no collective interaction of atomic magnetic moments, while in other materials there is a very strong interaction.

5.3.1 Diamagnetism

Although diamagnetism is usually very weak, it is a fundamental property of all materials. Here the atomic electron spins align so that their magnetic dipoles oppose an external magnetic field. These materials have zero magnetization when the field is removed and a characteristic weak negative, temperature independent susceptibility (Dentith and Mudge, 2014), and are composed of atoms which have no net magnetic moment. This is because all the orbital shells of the atoms are filled so there are no unpaired electrons (Moskowitz, n.d.). These minerals do not exhibit magnetism until they are placed in an external magnetic field, H. Then, a force is exerted on the electrons, which slows the electrons down, leading to slight change in magnetic property (Basavaiah, 2011). Quartz, feldspar, calcite, and water are examples of diamagnetic minerals.

5.3.2 Paramagnetism

Paramagnetic minerals have positive, relatively weak, field-independent susceptibility. This is because some of the atoms or ions in the material have a net magnetic moment due to unpaired electrons in partly filled orbitals (Moskowitz, n.d.). In these materials, the electron spins align so that their magnetic dipoles align with an external field (Dentith and Mudge, 2014). It has zero magnetization when the field is removed, because the individual magnetic moments of the atoms are assumed to be non-interacting (Dunlop and Özdemir, 1997).

The paramagnetic susceptibility increases with decreasing temperature, known as the Curie Law. In normal conditions the susceptibility is independent of applied field, and is mainly dependent on Fe-concentration. Most iron-bearing sulphides, carbonates and silicates are paramagnetic, and have 10-100 times greater susceptibility than diamagnetic minerals.

5.3.3 Ferromagnetism

The atomic moments in ferromagnetism minerals exhibit very strong interactions, unlike in paramagnetic minerals, produced by electronic exchange forces which result in a parallel or antiparallel alignment of atomic moments. The exchange forces are so large that they would be equivalent to a field in the order of 1000 Tesla (Moskowitz, n.d.). In these materials, the atomic dipoles are magnetically coupled, and the nature of the coupling determines the material's magnetic properties. In a ferromagnet, the magnetic dipoles are parallel and the material has a strong intrinsic magnetism and high susceptibility (Dentith and Mudge, 2014). These are the minerals we think of as magnetic.

At 0 Kelvin, the magnitude of the magnetization is dependent on the spin magnetic moments of electrons. The saturation magnetization, J_s, is the maximum induced magnetic moment that can be obtained in a magnetic field H, so the magnetization will not exceed this (Moskowitz, n.d.). J_s is independent of particle size, but dependent on temperature. Ferromagnetic minerals have a magnetic ordering temperature, called Curie temperature (T_c). At temperatures above T_c, the thermal agitation causes the spontaneous alignment to the destroyed so that the material becomes paramagnetic. This temperature is an intrinsic property and can be used for mineral identification.

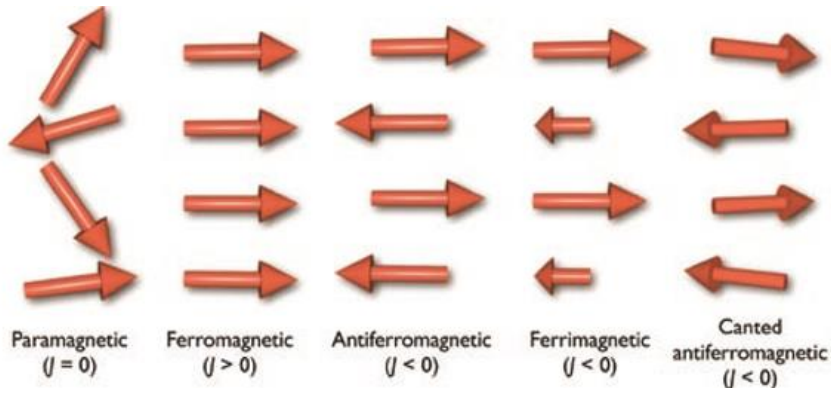

Figure 5.5: Examples of disordered and ordered magnetic structures. Arrows represent the direction of atomic moments (Harrison and Feinberg, 2009).

5.3.4 Ferrimagnetism and antiferromagnetism

Ferrimagnetism and antiferromagnetism are variants of ferromagnetism. Ferrimagnets have magnetic structure composed of two magnetic sublattices separated by oxygen. Exchange interactions are mediated by oxygen anions, called super exchange interactions (Moskowitz, n.d.). This results in antiparallel magnetic moments of different magnitudes so the sum in one

direction is larger than in the opposite direction (Basavaiah, 2011). These have high positive susceptibility and can acquire remanent magnetism. Examples are cubic oxides of magnetite and maghemite, which exhibit all the same behaviors as ferromagnetic minerals.

Antiferromagnetism have sublattice moments that are exactly equal, but opposite. This results in zero net moment. They also have zero remanence and no hysteresis, but a small positive susceptibility that varies with temperature (Moskowitz, n.d.). At temperatures above 0 Kelvin, local thermal rotations of the magnetic moments of the sublattices result in a small susceptibility, which increases until the temperature increases (Dunlop and Özdemir, 1997). At a specific temperature, the Néel temperature (T_N), the ordering temperature of antiferromagnets is reached, and the susceptibility follows the Curie-Weiss law for paramagnets. If the anti-parallelism is not exact, and neighboring spins are slightly tilted, a very small net magnetization can be produced (Moskowitz, n.d.). This is called canted antiferromagnetism, and hematite is one example. These minerals exhibit many of the typical magnetic characteristics of ferromagnets.

5.4 Hematite-ilmenite solid solution

The ferromagnetic iron-titanium oxide minerals comprise a solid solution series (fig. 5.6). With increasing degree of oxidation and at low Ti/Fe ratio, it goes from wüstite (FeO) to hematite (Fe_2O_3), and to rutile (TiO_2) with increasing titanium content (Dentith and Mudge, 2014). The hematite-ilmenite solid solution series ($Fe_{2-x}Ti_xO_3$; $0 < x < 1$) have hematite (αFe_2O_3) and ilmenite ($FeTiO_3$) as endmembers. The solid solution is complete only at high temperatures, above 1050°C (Deer et al., 1992). Depending on the magnetic structure, and/or degree of exsolution, the remanent response of the hematite-ilmenite SS can even dominate an aeromagnetic signature (McEnroe et al., 2004b). Exsolved rhombohedral oxides can be found in both in igneous and metamorphic rocks.

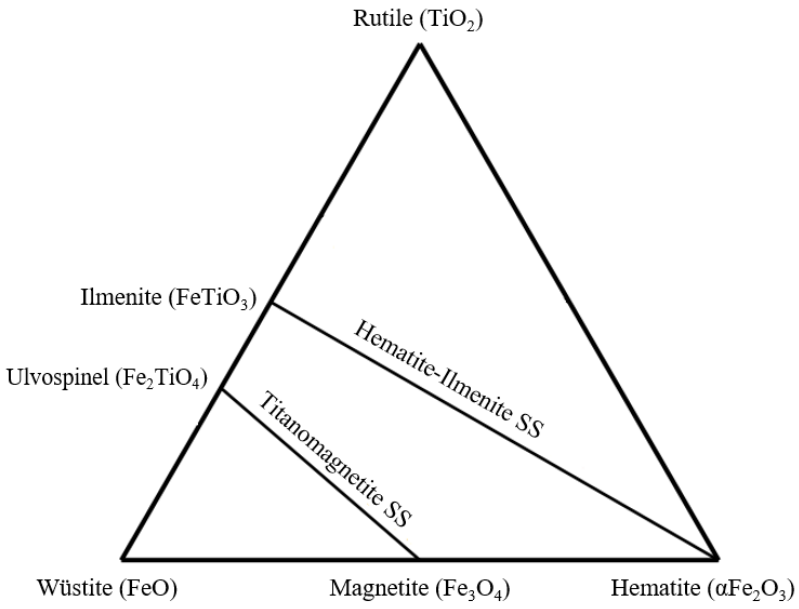

Figure 5.6: Showing the titanomagnetite and hematite-ilmenite solid-solution (redrawn after Dentith and Mudge, 2014).

5.4.1 Hematite

Hematite has a rhombohedral structure and is nominally antiferromagnetic. It can still carry weak ferromagnetism, and the sublattice magnetizations have a slight deviation from antiparallelism, called spin canting. Hematite is regarded as a weakly "parasitic" ferromagnetic mineral (Basavaiah, 2011). Hematite can also have defects or impurity atoms in the crystalline lattice which can produce a magnetic moment. It has low susceptibility, a high coercivity, and T_c of ~675°C. At -15°C pure hematite goes through a structural transition called Morin transition, where the directions of preferred spin orientation lead to loss of spin canting, so that the weak ferromagnetism disappears. Hematite is opaque in transmitted light, appears bright greyish white in reflected light, and it is common to find red internal reflections (Pilpotts, 2003). It is strongly anisotropic, and in electron backscatter microphotographs, hematite is light grey. Small amounts of the defect spinel-structured Fe_2O_3, called maghemite, can sometimes retain the spinel-structure, influencing the apparent magnetism of hematite (Deer et al, 1992).

A large proportion of hematite is not of igneous origin; found in soils and in weathering products from iron-bearing minerals (Deer et al, 1992). It is rare in igneous rocks, but abundant in iron ores produced from metamorphosed sediments. Hematite can form by deuteric high-temperature oxidation of titanomagnetite during cooling of a melt, or as an inversion product of titanomaghemite during later reheating of a rock (Dunlop, 1990). It also occurs as a product

of prolonged oxidation of magnetite at ordinary temperatures, and as products of dehydration of weathering products like goethite (αFeOOH).

5.4.2 Ilmenite

Like hematite, ilmenite is rhombohedral. It is not magnetic in room temperature, but becomes antiferromagnetic at -216°C, and cannot be used to determine the natural magnetization (Basavaiah, 2011). Exsolved ulvospinel tends to be oxidized to ilmenite if dissociated water is present, producing deuteric oxidation (Dentith and Mudge, 2014). In thin section, it appears opaque in transmitted light, and brownish grey with a pink tint in reflected light. It reflects less light than hematite and has a stronger, brownish bireflectance, but is equally anisotropic (Pilpotts, 2003). In backscatter electron microphotographs, ilmenite is darker grey than hematite. In very thin grains in transmitted light, hematite appears red and ilmenite brown.

5.4.3 Lamellar magnetism

McEnroe and Brown (2000), McEnroe et al. (2001, 2002, 2009a) and Robinson et al. (2004) showed that lamellar magnetism in ilmeno-hematite can carry strong remanent magnetism and even cause magnetic anomalies. Robinson et al. (2002, 2004, 2006) claim that mixed-valence contact layers between paramagnetic ilmenite and canted antiferromagnetic hematite reduces local ionic charge imbalance (as cited in McEnroe et al., 2009a). This means that lamellar magnetism occurs because the fine exsolution lamellae are magnetically aligned. McEnroe et al. (2004b) states that in lamellar magnetism, ferrimagnetism is coupled to the principal antiferromagnetic moments of hematite. Lamellar magnetism is created at the same temperature as the temperature when chemical exsolution happens, which makes lamellar magnetism a chemical remanent, rather than thermal remanent magnetization (Robinson et al., 2004). Lamellar magnetism is thermally very stable and very resistant to alternating field demagnetization. Therefore, presence of hemo-ilmenite or ilmeno-hematite is likely to generate ancient crustal magnetic anomalies.

6. Methods

6.1 Optical microscopy of thin sections

An optical microscope can be used on polished thin sections to identify minerals, and observe mineral textures, alteration, particle shapes and mineral associations, determine mineral proportions and measure grain sizes (Petruk, 2000). By combining reflected and transmitted light, polished-, thin- and polished-thin sections can be studied with the same microscope. Different minerals will then get different optical characteristics, which can be used to identify the minerals. In isotropic specimens, no light will be transmitted, and reflected light must be used. The minerals are identified by the amount of light they reflect, and their reflected color.

All thin sections were prepared at the thin section laboratory at the Department of Geology and Mineral Resources Engineering at the Norwegian University of Science and Technology (NTNU). Four sections were made in 2013, six were made in October 2016 and one in December 2016. All sections are polished thin sections. Some have a size of 28x48 mm and some are rounded because they were cut from drill cores, and all sections have a thickness of ~30 µm. Petrographic work was performed on an optical Leica DM2500P microscope, and all images were captured by camera mounted on the microscope. An Epson Perfection v600 Photo Scanner with polarizing film was used.

For a first-hand identification of the mineral phases, transmitted and reflected light were used. Plane- and cross-polarized light (resp. ppl and xpl) was used to determine optical properties like color, interference color and cleavage. To identify the different minerals, the book by Deer et al. (1992) was used, together with unpublished notes from microscopy classes at NTNU.

6.2 Scanning Electron Microprobe (SEM)

In SEM, the light source in regular microscopes is replaced by an electron source which scans the surface. This gives a much higher resolution, because the SEM uses an invisible beam of electrons. With the additional BSD, the electron beam penetrates deeper into the material, instead of only scanning the surface. EDS gives an element assembly for a given point. For this thesis, SEM, BSD, and EDS was used as a preparation for further work on the electron microprobe, mainly to determine which elements to analyze at the EPMA. In addition, the instruments were used to confirm or reject assumptions made in optical microscopy, e.g. whether a specific grain was cordierite or feldspar.

The work was performed on a FESEM, Zeiss Ultra 55 limited edition, with Backscatter Detection (BSD) and Electron Dispersive Spectroscopy (EDS) at the Department of Materials Science and Engineering, NTNU. The thin sections were coated with carbon before the analysis with an Agar Turbo Carbon Coater. This is because the epoxy mounting material in the thin sections is a poor electrical conductor, which causes charging problems (Guo et al., 2013). When the sections are coated with carbon, this prevents the beam from charging the minerals. At the same time, this leads to problems with analyzing the carbon content in the minerals. The investigations were made with 10 mm working distance, and acceleration voltage of 10 kV. The aperture size was set to 120 µm diameter.

6.3 Electron microprobe analysis (EMPA)

The electron microprobe (EPMA) is a microbeam instrument. Wavelength spectrometers are used to detect X-ray counts from the sample surface, and is used to determine the quantitative compositions of minerals in polished sections (Petruk, 2000). The thin sections that were used in the optical microscope were also investigated in the microprobe. Because only one point can be analyzed at a time, the sections had to be prepared with accurate points that should be measured. EPMA can be used to investigate zoning, alteration, and mineral liberation. The machine can also perform line scans, giving an element map of an area. This can show compositional variations in zoned minerals. The analyses were performed on a JEOL JXA-8500F Electron Probe Micro Analyzer by Morten Raanes.

The EMPA investigations were performed in four sessions. A list was prepared for examining all the silicates, with Na, Mg, K, Al, Ca, Mn, Si, Ti, Fe, Ba, P, F, Cl, V and Cr. The oxides were examined with the same list. Two reference standards were used for different elements, which can be seen in table 6.1. Detections limits for the elements are also shown. With the aid of Peter Robinson, mineral formulas were calculated and mineral compositions were plotted in chemographic diagrams. Unfortunately, after the third session, a mechanical error was discovered, revealing that the Si-contents were most likely underestimated in the previous sessions. Because of time constraints, all the previous work could not be redone, but the fourth session was used to control how erroneous the results were. The results from this session showed no major changes, but in the mineral formulae in chapter 7, the results from the last session is marked in italic writing instead of bold.

Table 6.1: Standards used for EPMA.

	Biotite	Plagioclase	Element	Detection limit (ppm)
Na2O	0.045	4.351	**Na**	186
F	0	0	**F**	200
Cl	0.017	0.03	**Cl**	106
V2O3	0.033	0	**V**	189
MgO	19.809	0.072	**Mg**	161
K2O	9.848	0.347	**K**	157
Cr2O3	0.03	0.024	**Cr**	196
Al2O3	14.766	28.308	**Al**	160
CaO	0	11.863	**Ca**	164
MnO	0.129	0	**Mn**	164
SiO2	38.493	53.609	**Si**	281
TiO2	1.797	0.081	**Ti**	288
FeO	10.601	0.386	**Fe**	175
BaO	0.247	0	**Ba**	464
P2O5	0	0	**P**	426
Total	95.811	99.043		

6.4 XRF

X-ray fluorescence spectroscopy is a method for chemical analysis of elements in a sample. When appropriate X-ray excitation techniques are used, all elements emit characteristic X-ray radiation. This is used to identify elements and estimate the concentrations. The intensities of the fluorescent X-rays are compared with the intensity of those from a known standard to determine the elements.

For an XRF analysis, the powder must be ground as fine as possible. Two different samples must be prepared, one for main elements and one for trace elements. For the trace elements analysis, 9.6 g powder was mixed with 2.4 g wax and put in a tube. A glass bullet was put in the tube, before the tube was stirred to mix the powder with the wax. The mix was then pressed together at 200 kN to make a powder pill. The trace element analyses were run on this powder pill, and takes around 38 min. For the main elements analysis, the loss on ignition was measured. Approximately 2.5 g powder was measured accurately, burned, and the weight was measured accurately after ignition. This loss on ignition was then reversed after the analysis, and concentrations were recalculated. Exactly 5 g lithium tetraborate/metaborate (66/34) and 0.5 g powder was mixed, and 60 µl lithium iodide was added. This was melted into a glass pill, and the main elements analyses were run. The analyses were run on a S8 Tiger 4 kW X-ray

spectrometer. One sample from each location was tested, in addition to one scapolite-bearing Modum-sample collected in a previous study.

Table 6.2: Detection limits and maximum concentration for various elements using XRF at NTNU.

Analyte	Detection limit [ppm]	Max concentr. [ppm]	Analyte	Detection limit [ppm]	Max concentr. [ppm]
Sc	1.6	60	**Y**	6.5	800
TiO2		2.60 %	**Zr**	4.9	550
V	1.4	340	**Nb**	0.6	700
Cr	3.3	24000	**Mo**	1	700
MnO		1.30 %	**Sn**	3.1	1300
Fe2O3		25.70 %	**Sb**	1.7	122
Co	2.2	700	**Cs**	4.7	260
Ni	1.5	2640	**Ba**	5	4000
Cu	4.7	5400	**La**	5.2	1340
Zn	3.8	1310	**Ce**	4	2230
Ga	0.7	400	**Pb**	1.5	5500
As	2.9	330	**Th**	12.6	1003
Rb	0.9	1300	**U**	1.5	650
Sr	0.9	1650			

6.5 Density measurements

Density and volume can be calculated by measuring dry and wet weight of a sample. 72 samples were soaked in water for at least 24 hours prior to the measurements to limit error in volume calculation due to porosity. Excess water was removed before measuring mass and density. Volume was then calculated using:

$$\text{volume } (cm^3) = \frac{mass\ (g)}{density\ (\frac{g}{cm\text{^}3})}$$

6.6 Susceptibility measurements

Susceptibility was measured for all 72 samples on a AGICO Kappabridge at the Department of Geology and Mineral Resources Engineering at NTNU. The instrument was calibrated and corrected for the holder prior to measuring the rock samples. The values were then volume corrected and used together with NRM in a Q-plot. All samples were measured for room-

temperature susceptibility, and one sample from each location was measured for low-temperature and high-temperature susceptibility.

6.6.1 Temperature dependent susceptibility

An AGICO Kappabridge equipped with CS-3 Furnace and CS-L Cryostat was used for measuring temperature-dependent susceptibility. One specimen from each location was crushed to powder, weighted, and put into a narrow test tube, together with a thermometer. For all samples, a low-temperature curve and a high-temperature heating and cooling curves were measured. In addition, another low-temperature run was done. To avoid contamination, the equipment was thoroughly cleaned after each measurement.

For low-temperature measurements, liquid nitrogen was used to lower the temperature of the sample to -192°C. For the high-temperature measurements, the test tube was placed into a furnace, heated up to 700°C, and cooled back down to room temperature. All measurements were run in air. The data were processed in IgorPRO, where a correction for the holder was done. Finally, Ti-amounts of the hematites were calculated based on the Curie temperatures.

6.7 NRM measurements

Measurements of natural remanent magnetization (NRM) were performed on all 72 samples on a AGICO JR-6 Spinner Magnetometer at the Department of Geology and Mineral Resources Engineering at NTNU. Samples from MOD36 and MODHJK were not oriented. The samples were placed in the instrument, which produces an oscillating magnetic field due to the rotating magnetic moment of the samples (Butler, 2004). All measurements were recorded in the program Remasoft30, which gave values for mean declination, inclination and α95. The directions were then plotted in the program Stereonet8, given by the inclination and declination of the magnetization for each sample. Positive and negative inclination are distinguished by using different plot symbols. This can give indications as to whether the remanent magnetism formed e.g. before or after folding. The NRM-values was inserted into Excel, and then volume-corrected, to be used together with susceptibility in a Q-plot. For this, a local field of 40.6 A/m was used.

6.7.1 Demagnetization measurements

As a part of the author's special syllabus during spring 2016, stepwise measurements of alternating field (AF) demagnetization were performed on 49 samples on an AGICO alternating

field demagnetizer. 10 representative curves were selected to be a part of this thesis and to use for further discussion.

6.8 Sources of error

SEM is an easy and quick method to get an overview over what elements are present in the minerals. When working with the SEM, one must take into consideration that some element peaks may overlap, so it is important to think through what elements are most likely to cause the peaks. This problem can be solved using EPMA.

The microprobe is considered as a good method, usually giving accurate quantitative results. The results from the EPMA should sum up to 100 % for each analysis, but this rarely happens. The analyzed sums are usually in the range of 92 to 102 %, with up to 113 % for apatite and down to 83 % for tourmaline. Low totals are due to some elements present in the minerals being left out in the analysis, like B in tourmaline, and high totals happen if some elements are present in much higher amount than the upper detection limits. The previously mentioned Si-problem might also affect the analyses. The EPMA also has a problem with Fe, because it can't distinguish between Fe^{2+} and Fe^{3+}, which can lead to erroneous interpretations. The thickness and structure of the carbon coating will also influence the results, in addition to acceleration voltage (kV). Higher kV will give higher spatial resolution and lower detection limits (Reed, 2000).

In some methods, it is particularly important to take precautions to avoid errors. Large degrees of porosity can give wrong density measurements, but by soaking the samples before measuring, this problem is minimized. In the NRM and demagnetization measurements, the samples were placed in the same direction for each measurement.

In all investigations, it is important to choose representative samples. Only one thin section from each location was made, assuming these are representative. Temperature dependent susceptibility was also performed on only one sample from each location, which could lead to non-representative results. In general, larger data sets give more secure results.

7. Petrology

In this chapter, rock and thin sections will be described one by one, before each mineral will be described texturally and chemically. XRF results are also presented.

7.1 Rock and thin section descriptions

Table 7.1: Summary of modal amounts of minerals in each thin section, estimated by optical microscopy. Black numbers are minerals confirmed present by EPMA, red numbers are minerals found only by optical microscopy.

Thin section	MOD35	MOD36	MOD37	MOD38	MOD39	MOD40	MOD41	HJ002	HJ003	MODHJK
Quartz	15	30	20	20	tr	38	68	20		80
Plagioclase	12	7	30	22	40	tr	tr	30		5
	An1	*An5/An30*	*An23*	*An25*	*An20*		*An15*	*An50*		
K-feldspar			tr		tr					5
Phlogopite	38	6	25	28	40	4	5	40		7
Talc	15	12	13	7	5	10				
Chlorite	tr	5				20	5			3
Mg-paragonite		tr					tr			
Unknown mineral			4	tr	tr					
Amphibole			3	10	5				67	
Pyroxene									27	
Kyanite		tr				10		tr		
Sillimanite	10	10								
Tourmaline	5	tr	tr	5	5	tr	5	5		
Zircon	tr			tr			tr			
Apatite	tr		tr	tr	tr	tr	tr		tr	tr
Hematite	5	20	5	8	5	18	17	5		tr
Ilmenite									3	
Rutile	tr								3	
Titanite			tr	tr	tr			tr		

Modal percentages were estimated by optical microscopy. Some of the samples are very coarse-grained and heterogeneous, and the modal compositions based on only one thin section may not be representative for whole outcrops. From table 7.1, MOD35-MOD40 can be divided into two groups based on the mineral assemblages. All these samples contain quartz, feldspar, phlogopite, talc, tourmaline, and hematite. In addition, MOD35, MOD36 and MOD40 contain chlorite and kyanite/sillimanite together with traces of paragonite, while MOD37, MOD38 and MOD39 contain amphibole, traces of K-feldspar, and an unknown mineral. MOD41 contains

quartz and hematite, in addition to minor amounts of albite, phlogopite, chlorite, and tourmaline. HJ002 is made up of quartz, feldspar, and phlogopite, and small amounts of hematite, tourmaline, kyanite and apatite. HJ003 is characterized by mainly mafic minerals; amphibole and pyroxene. MODHJK is composed of mostly quartz, with minor amounts of albite, K-feldspar, phlogopite, apatite, and hematite.

7.1.1 MOD35 - Phlogopite-talc schist with sillimanite-albite clusters

Hand specimen

Leucocratic, fine-grained grey groundmass with some white grains and some green mica. Oxide grains are visible. Clear foliation present.

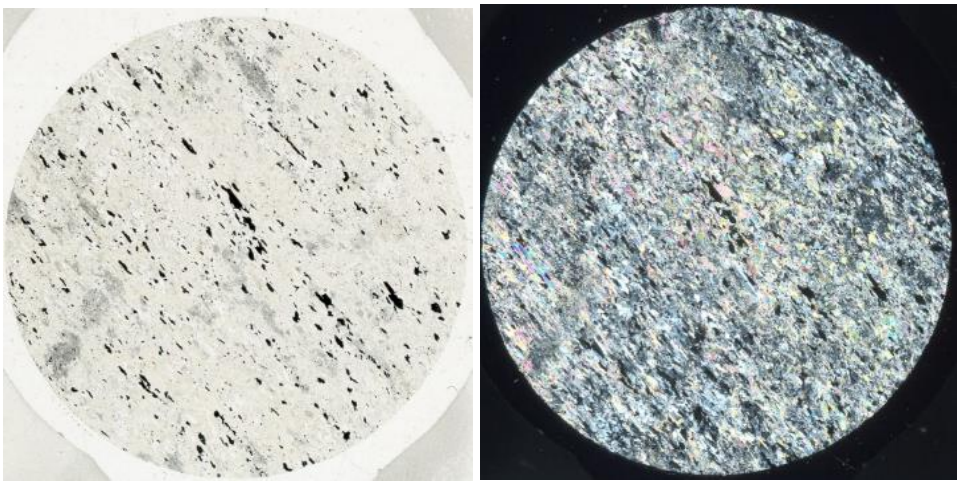

Petrographic description

The matrix is made up of mostly phlogopite and some quartz. Phlogopite is almost colorless with very weak green/brown pleochroism, and is difficult to distinguish from talc. Some grains are oriented down the c-axis, with first order grey interference colors and grain size up to 2 mm. Quartz shows undulose extinction and is commonly broken down to subgrains and surrounded by talc. Elongated talc and phlogopite is broken up and commonly overgrown by sillimanite, and makes up a weak foliation. Dusty areas are made up of sillimanite needles and feldspar. Feldspar is only present in association with sillimanite. Tourmaline is equigranular and euhedral, with pale brown pleochroism and second order interference colors. Tourmaline commonly occurs in clusters. Hematite is commonly crosscutting the silicates, with seriate distribution of grain sizes from 0.04 to 1.5 mm.

7.1.2 MOD36 – Sillimanite-hematite rock with talc and albite

Hand specimen

Phaneritic, inequigranular, areas with coarse-grained grains of quartz and areas with finer-grained oxides. The white layers define a clear stratification.

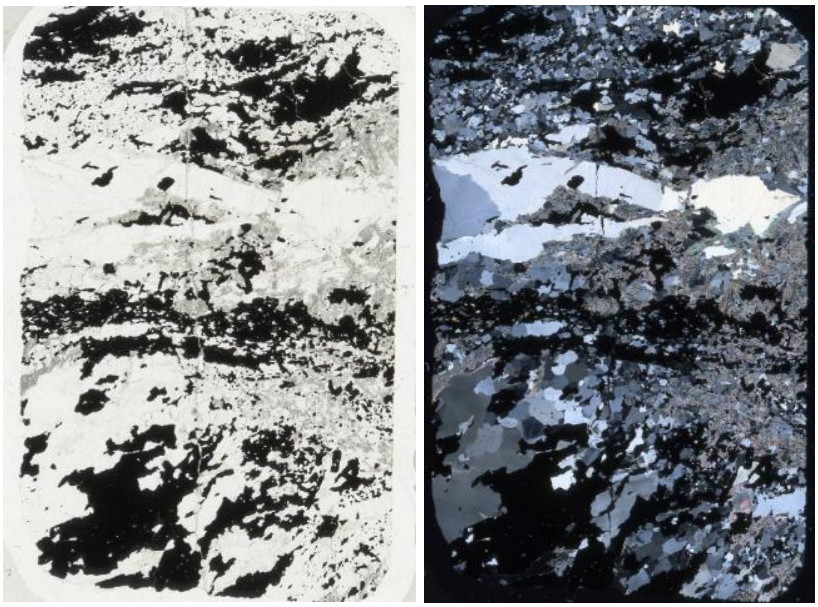

Petrographic description

Section is made up of coarse-grained, recrystallized quartz, coarse-grained hematite in clusters, and sillimanite. Quartz shows undulose extinction, and is partly broken into subgrains, with some pressure solution along grain boundaries. Sillimanite seems to be is growing in cracks in quartz. Relict kyanite grains are surrounded by fibrous and coarse-grained sillimanite, which is again surrounded by aggregates of paragonite, talc, phlogopite, and chlorite. Feldspar shows polysynthetic twinning, and some grains are heavily altered to sericite. Hematite encloses a few, thin mica grains and some feldspar, in addition to having inclusions of rutile. Tourmaline is pale green and fine-grained. Some mica grains are altered to chlorite and overgrown by secondary mica grains, and others are radial grains in fan-shaped clusters.

7.1.3 MOD37- Layered quartz-oligoclase-phlogopite rock with talc, amphibole and coarse-grained oligoclase lumps

Hand specimen

Phaneritic, leucocratic. Grey, fine-grained groundmass contains green and white mica grains. Surface shows cavities, probably as a result of mica that has been destroyed during preparation. Elongated mica grains define a foliation.

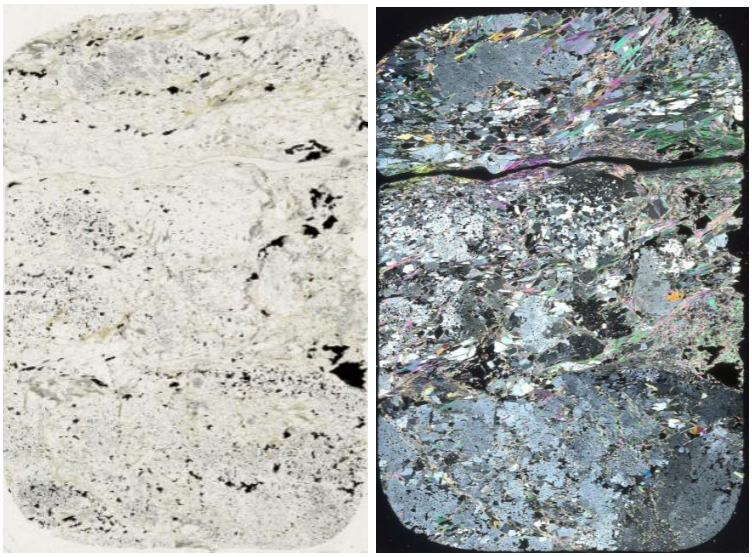

Petrographic description

The section shows stratification, with some areas with mostly quartz, and some areas made up of feldspar and elongated talc. Massive quartz is inequigranular with seriate grain size distribution and patchy extinction. Quartz shows recrystallization and bulging with straight grain boundaries with triple junctions. Platy talc is either long, thin grains with light pink and green interference color, or wider grains with clear green interference colors. The talc shows clear foliation. Platy phlogopite is weakly pleochroic, pale brown, displaying cleavage. Feldspar appears equigranular, show polysynthetic twinning. Feldspar is coarse-grained up to 2 mm, and has numerous inclusions of fine-grained quartz, talc, tourmaline, and hematite. Some grains have twins or dusty appearance, due to alteration to sericite. Amphibole is anhedral, and in clusters, some grains are zoned with higher interference color close to the middle of the grains. Anhedral apatite with grain size up to 05 mm. Hematite is bimodal, occurring as fine-grained inclusions in addition to coarse grains with lamellae of ilmenite. An unknown, yellow, almost isotropic, mineral is present, showing heavy alteration.

7.1.4 MOD38 - Layered quartz-oligoclase-phlogopite rock with talc, amphibole and coarse-grained oligoclase lumps

Hand specimen

Phaneritic, leucocratic. Grey, fine-grained groundmass with green and white mica grains enclosing quartz and feldspar. Surface shows cavities, probably as a result of mica that has been destroyed during preparation. Elongated mica and hematite grains define a foliation.

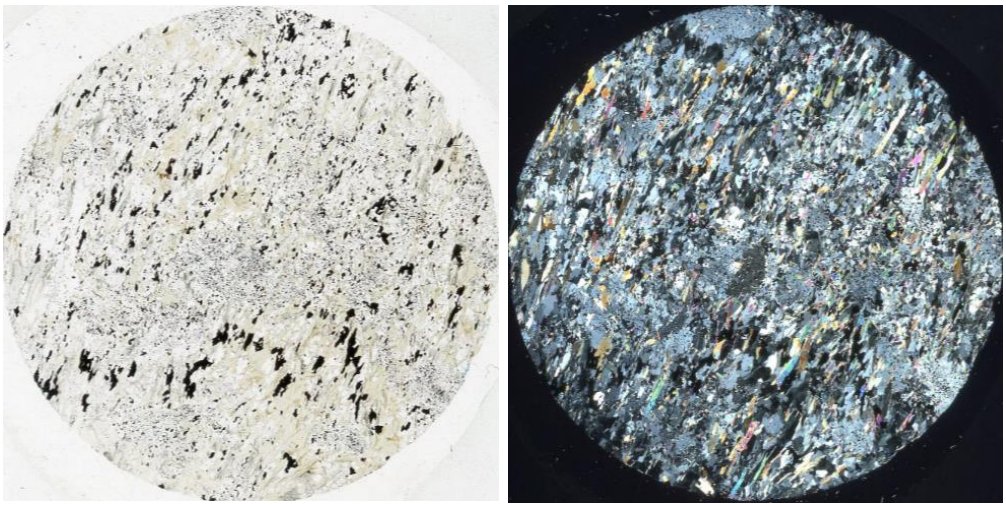

Petrographic description

Weak foliation due to elongated mica and hematite. Massive quartz is inequigranular with seriate grain size distribution and patchy extinction, and show some recrystallization with triple junctions. Recrystallized quartz grains are present in clusters. Coarse-grained feldspar appears equigranular, and has numerous inclusions of fine-grained quartz, phlogopite and hematite. Some grains have twins or dusty appearance, and feldspar is also present with smaller grain size. Talc and phlogopite appear platy and inequigranular, with bimodal grain size distribution, with one group around 0.2 mm and one group around 1-2 mm. Phlogopite grains are mostly displaying a weak yellow color, and is cut in a way that they display first order grey interference color. Some amphibole grains are visible, commonly cross-cutting foliation. Amphibole mainly shows one cleavage and commonly low second-order interference colors, and is in some places overgrown by talc. Pale brown tourmaline is fine-grained, and scattered around the section. Anhedral apatite with grain size up to 0.5 mm, occurs commonly as inclusions in phlogopite. Fine-grained inclusions of hematite can be found throughout the whole section, in addition to some clusters of coarse-grained hematite with ilmenite exsolutions lamellae. An unknown,

yellow, almost isotropic, mineral is growing in cracks and along grain boundaries, and shows heavy alteration.

7.1.5 MOD39 - Layered oligoclase-phlogopite rock with talc, amphibole, and coarse-grained oligoclase lumps. Graded beds in outcrop.

Hand specimen

Phaneritic, leucocratic. Grey feldspar and quartz are present in equal amounts as white and green mica grains. Elongated mica grains define a foliation.

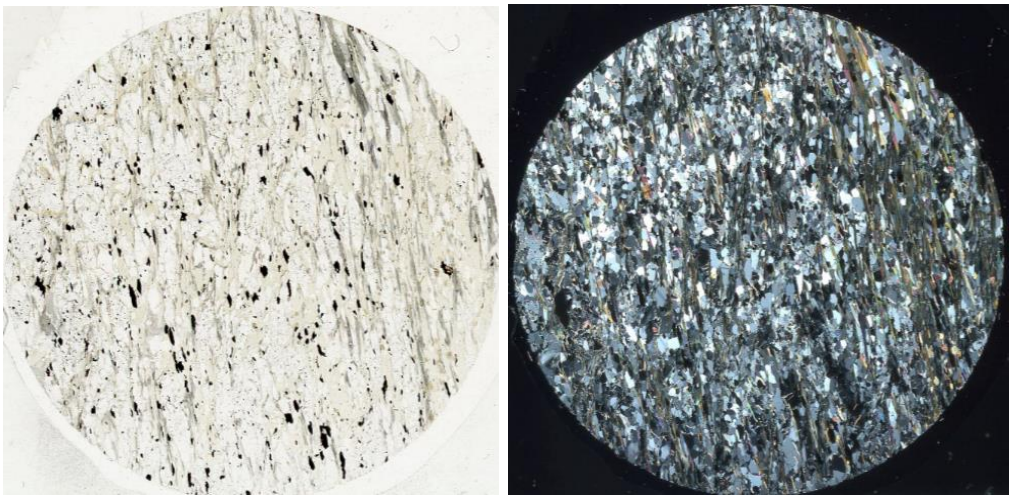

Petrographic description

Mostly subhedral grains, similar to MOD38, but with cleaner feldspar and phlogopite. Coarse-grained feldspar appears equigranular, and has numerous inclusions of fine-grained quartz, talc, and hematite. Feldspar shows mostly polysynthetic twinning and some perthite. Some feldspar appears very dusty. Coarse-grained phlogopite shows clear foliation. Phlogopite appears platy and inequigranular, with bimodal grain size distribution, with one group around 0.2 mm and one group around 1-2 mm. Phlogopite grains are sometimes oriented down c-axis, displaying a weak yellow color and first order grey interference color. Talc is fine-grained, narrow and elongated, sometimes adjoining phlogopite. Amphibole is found as a minor mineral, and is fine-grained, displaying first and second order interference colors. Pale brown tourmaline is euhedral, equigranular, locally zoned where core displays higher interference color. Apatite is coarse-grained and dusty, enclosing phlogopite, commonly in vicinity to hematite. Otherwise, hematite appears mostly coarse-grained, with some inclusions of rutile, and lamellae of ilmenite. The unknown, yellow, almost isotropic, mineral is growing in cracks and along grain boundaries, showing heavy alteration.

7.1.6 MOD40 – Chlorite-talc-kyanite-hematite schist with quartz and phlogopite

Hand specimen

Leucocratic, phaneritic. White groundmass of quartz contains visible, dark grains of oxides, up to 5 mm long. Clear foliation visible.

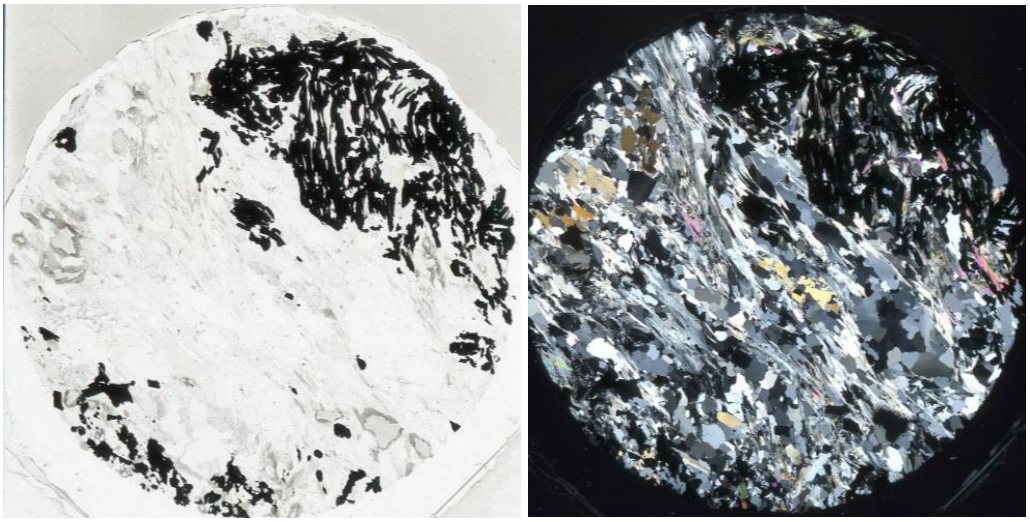

Petrographic description

Massive quartz is inequigranular with seriate grain size distribution and patchy extinction. Quartz shows undulose extinction, recrystallization and bulging with straight grain boundaries with triple junctions and development of subgrains. Radial talc grains are elongated with second order pink and green interference colors, and are mostly being replaced by chlorite. Chlorite is coarse-grained with first order grey interference colors. Chlorite is weakly green and doesn't show much pleochroism. Kinks in chlorite has led to cracks growing out in a "tree structure". Phlogopite is weakly pleochroic, and commonly altered to chlorite. Relict kyanite shows high relief, with wide cleavages filled with an unidentified, red mineral with no reflection in reflected light. The interference color of kyanite is first order grey, and some grains show twinning. Feldspar is found as an accessory mineral, show polysynthetic twinning, and some grains exhibit deformation lamellae. Apatite is coarse-grained, equigranular and very dusty. Tourmaline is present as inclusions in other minerals, commonly hematite. Hematite is coarse-grained and in clusters, with talc and chlorite growing into it, and with lamellae of rutile.

7.1.7 MOD41 - Quartz-hematite granulite

Hand specimen

Melanocratic, dark groundmass with evenly scattered mica and oxide grains. Some clusters of mica are visible, making up a weak foliation.

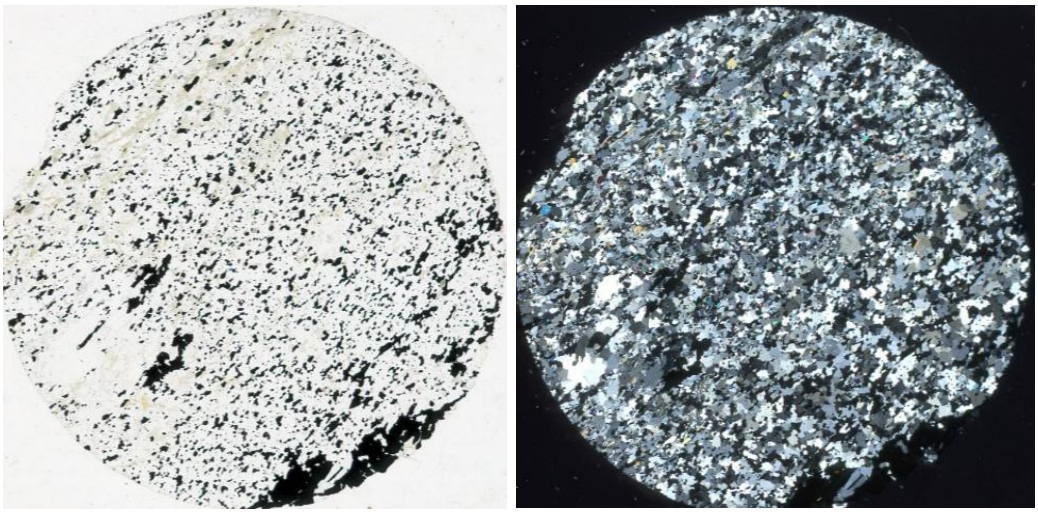

Petrographic description

Quartz has undulose extinction and show signs of extensive recrystallization. Most grains are relatively equigranular and show triple junctions. Most of the section is made up of quartz and coarse-grained hematite, along with some finer-grained tourmaline and phlogopite. Some feldspar grains show signs of alteration to sericite, and larger grains display subgrains. Phlogopite grains are mostly oriented down c-axis, displaying a weak yellow color and first order grey interference color. Some phlogopite grains are platy and partly altered to chlorite. Talc is absent. Tourmaline is pale green, euhedral, equigranular at 0.5 mm and shows zonation. Hematite is also present in more fine-grained fractions. The unknown, yellow, almost isotropic, mineral is present, showing heavy alteration. Some mica grains are completely altered to this yellow mineral.

7.1.8 HJ002 - Metasedimentary rock from near pyroxene-hornblendite

Hand specimen

Phaneritic, light and dark minerals are equigranular and evenly scattered around the surface. Green mica grains and oxides are visible. This section shows no foliation.

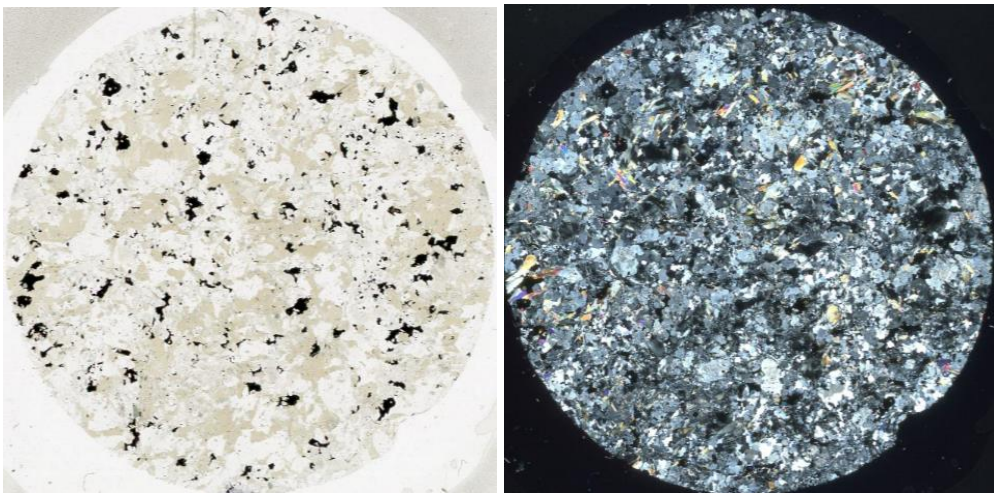

Petrographic description

Massive quartz is inequigranular with seriate grain size distribution and patchy extinction. Some recrystallized quartz occurs in clusters. Feldspar is inequigranular and anhedral, with polysynthetic twins, and some alteration to sericite. Phlogopite is green/yellow, weakly pleochroic with a large variation in interference colors, up to lower third order. Some phlogopite grains are oriented down c-axis, displaying first order grey interference colors. Tourmaline is pale green and fine-grained, evenly scattered around the section, also as inclusions in hematite. Tourmaline grains are equigranular, both trigonal and anhedral. A few kyanite grains are present in clusters. Oxides are made up of hematite with various degrees of rutile lamellae.

7.1.9 HJ003 - Pyroxene-hornblendite

Hand specimen

Melanocratic, phaneritic, equigranular. Dark amphibole and pyroxene make up the main minerals, some oxides present. No foliation is visible.

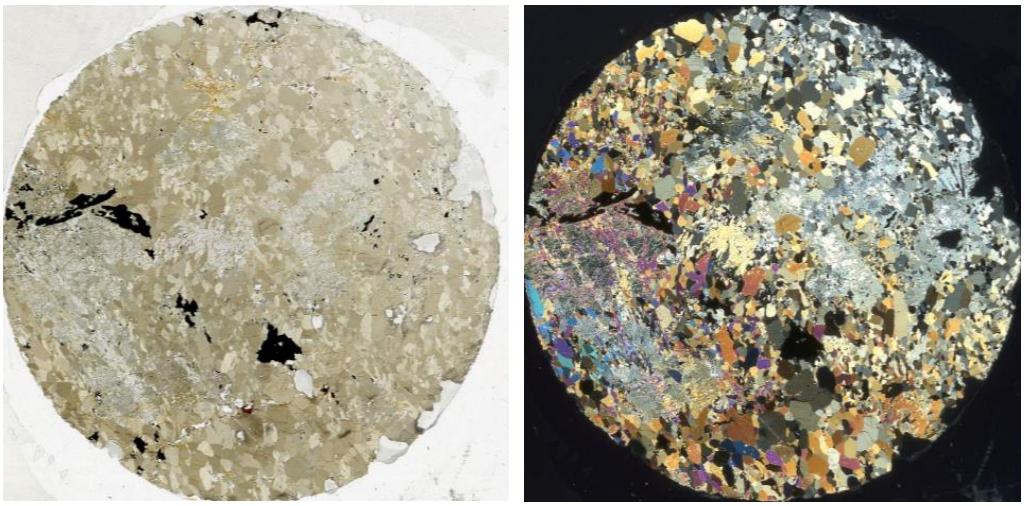

Petrographic description

Light green/yellow, pleochroic amphibole with granoblastic texture is equigranular with low second order interference colors. Also present is secondary green amphibole, with slightly higher interference colors and smaller, more elongated grains. Relict, coarse-grained orthopyroxene with first order interference colors is cracked and being replaced by amphibole. A yellow clay mineral is progressively growing in the cracks. Dark brown rutile is also growing in some holes and cracks. Apatite is found as an accessory mineral, and is heavily altered, displaying a brown, dusty color. A few, coarse-grained ilmenite grains are present.

7.1.10 MODHJK – Quartz-feldspar granulite

Hand specimen

Massive, holocrystalline, leucocratic, phaneritic, equigranular. Quartz-rich with dark minerals scattered evenly through rock. No foliation visible.

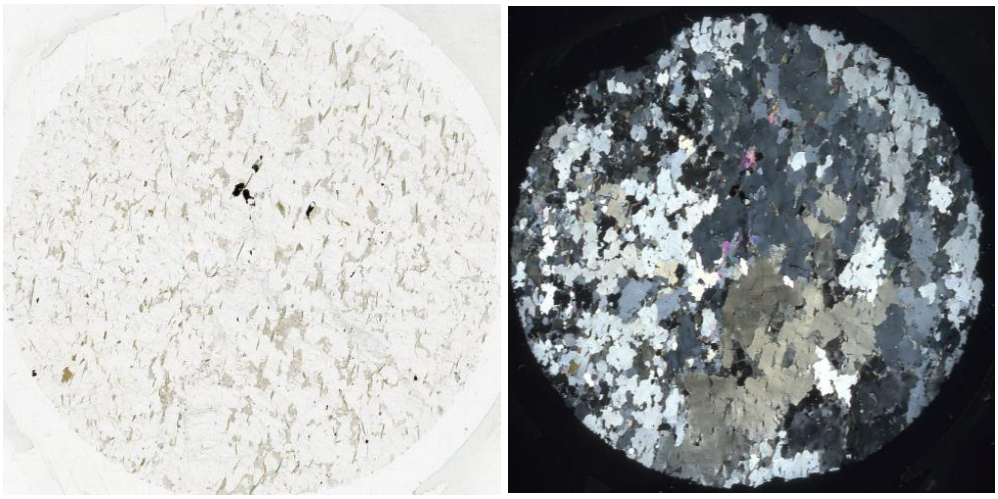

Petrographic description

Coarse-grained, anhedral quartz shows undulose extinction, subgrains and trails of fluid inclusions. Biotite is elongated, dark brown with clear pleochroism and is readily altered to chlorite. Chlorite is clear green with blue interference colors, indicating an Fe-rich variety. Feldspar is interstitial between coarser quartz, and is heavily altered to sericite. Both microcline with tartan twins, and plagioclase with perthite and polysynthetic twins are present. A few oxide grains are present, with three different phases.

7.2 Mineralogy

This section aims to describe the different minerals in the different rocks, both texturally and chemically.

7.2.1 Quartz

Quartz was identified by undulating extinction and low interference color. EPMA results show generally low totals in quartz. This can be due to wrong standards or missing elements in the analyses. However, the SiO_2-contents are very close to the totals. Some analyses show slight Fe-substitution, up to 0.13 wt.%. Quartz is present in all samples, except for HJ003. Microphotographs can be seen in figure 7.1.

In MOD35, quartz is part of the matrix, showing undulating extinction and is overgrown by talc. Quartz is bimodal in MOD36, with one group of coarse grains with straight boundaries to feldspar and one group with medium grains with anhedral grain boundaries. Quartz is xenomorph, weakly undulating, and present as interstitial grains between feldspar and display trails of fluid inclusions. In MOD37 and MOD38, quartz is present as fine-grained inclusions in feldspar, and recrystallized grains up to 0.5 mm. In MOD40, quartz is inequigranular, with grains ranging from 0.2 mm to 3.5 mm. MOD36, MOD37, MOD38, MOD39, MOD40 and HJ002 show signs of deformation with undulose extinction and grain boundary migration (GBM). Many grains have triple junctions and occur in recrystallized clusters.

MOD41 is mostly made up of anhedral, equigranular quartz grains with undulose extinction. Also in this section, quartz displays triple junctions. In HJ002, quartz is equigranular around 0.1-0.2 mm. MODHJK stands out, with very coarse quartz grains, up to 5 mm, enclosing feldspar in a poikilitic texture.

7.2.2. Feldspar

The feldspars in these samples include both plagioclase and K-feldspar. Plagioclase is abundant in most samples, while K-feldspar is a rare except, mostly present in MODHJK. Plagioclase is identified by its low interference colors and polysynthetic twinning. In ppl, the mineral is colorless and commonly shows signs of alteration, like sericitization, resulting in a dusty appearance in thin section. Microphotographs can be seen in figure 7.2.

Feldspar in MOD37, MOD38 and MOD39 are mostly alike, though those in MOD37 are slightly coarser grained than the others. Feldspars show bimodal distribution, the coarsest grains are up to 4 mm, and enclose smaller grains of quartz, tourmaline, phlogopite, and oxides. These

are porphyroblasts, commonly made up of multiple plagioclase crystals that have grown together in different directions. The medium-size group are without inclusions. Albite twins are common, and most grains show signs of sericitization.

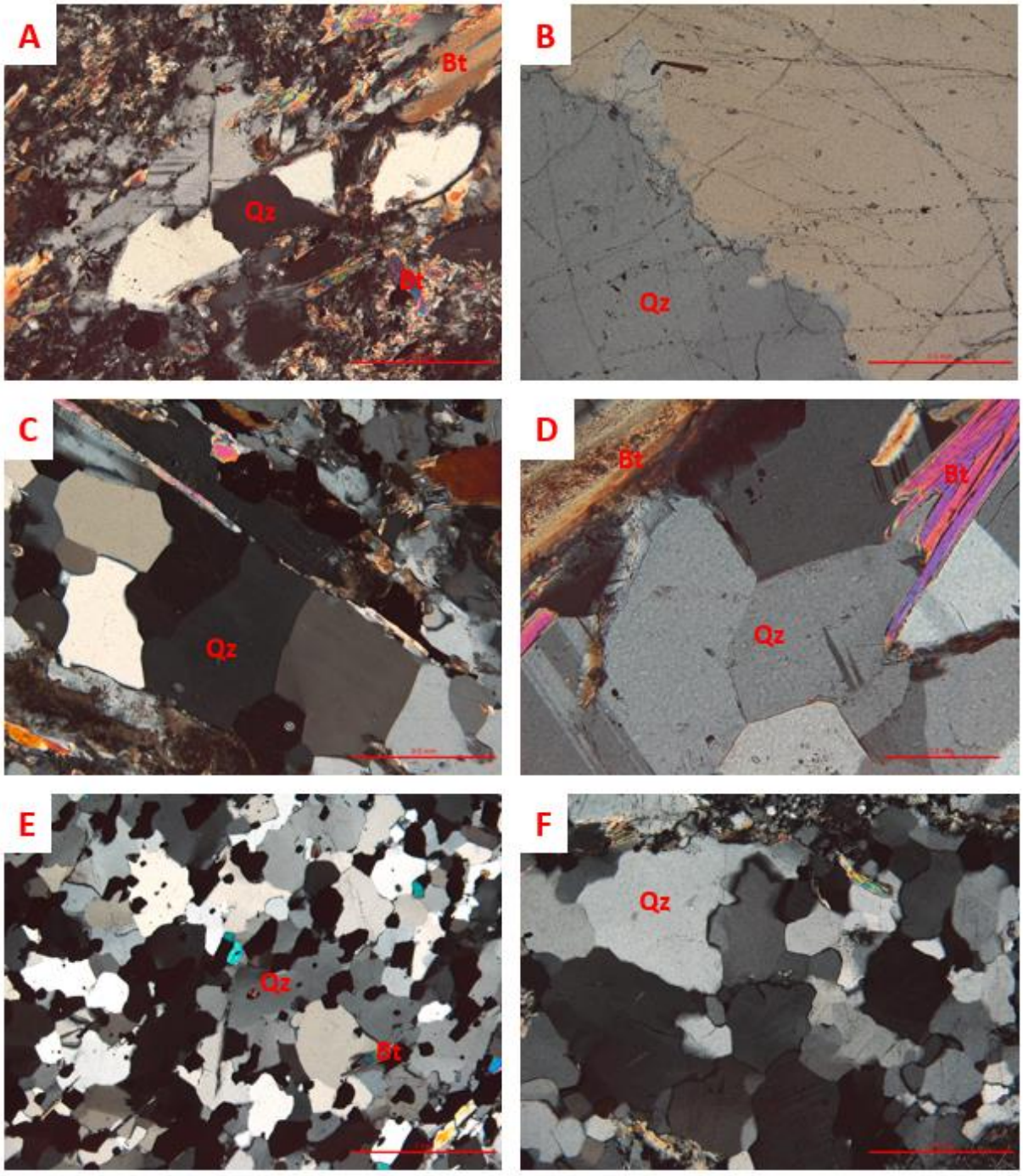

Figure 7.1: Photomicrographs of quartz. A: Quartz in MOD35. B: Quartz with trails of fluid inclusions in MOD36. C: Quartz in MOD38. D: Quartz with triple junction in MOD39. E: Matrix of quartz and hematite of MOD41. F: Recrystallized quartz in HJ002. A-C and F: Scalebar is 0.5 mm. D: Scalebar is 0.2 mm. E: Scalebar is 1 mm.

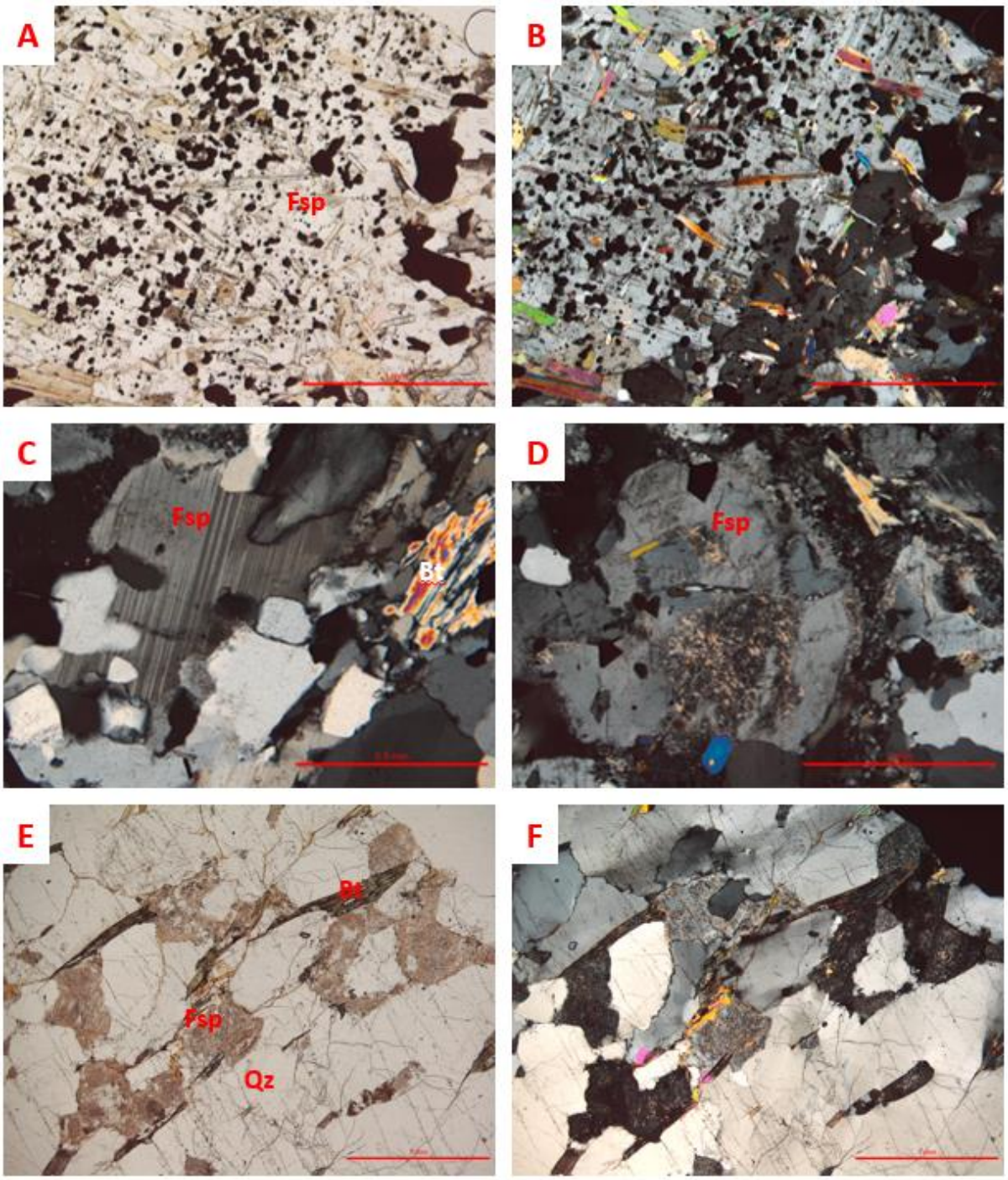

Figure 7.2: Photomicrographs of feldspar. A and B: Oligoclase porphyroblast in ppl and xpl, enclosing talc and hematite. From MOD38. C: Oligoclase in MOD41. D: Andesine with sericite core in HJ002. E and F: Feldspar altered to sericite in MODHJK. A-B, D-F: Scalebar is 1 mm. C: Scalebar is 0.5 mm.

In MOD35, feldspar is only associated with small areas together with sillimanite needles. These areas have a dusty appearance, and feldspar was only identified by EPMA. In MOD36, the feldspars are bimodal. The coarse grains are locally zoned, and extensively sericitized, while feldspar also occurs in the intergrowths together with sillimanite and talc. MOD40 and MOD41

have less feldspar, with only a few grains detected. The grains are equigranular with quartz, commonly lying interstitially in quartz and displaying albite twinning. HJ002 displays medium-grained feldspar with albite twins, but is heavily sericitized. In MODHJK, the feldspars are surrounded by quartz, and are also extensively sericitized. Here, some of the feldspar is microcline, displaying mostly tartan twinning, and some perthite.

The EPMA results indicate large variations in feldspar composition (fig. 7.3). MOD35 is pure albite. MOD38 is cluttered around An_{25}, MOD37 around An_{23}, MOD39 around An_{20} and MOD41 around An_{15}. MOD36 contains two groups, with area around An_{30-34} that is a part of the needle-shaped intergrowths with sillimanite and talc, and An_{4-10} as primary, coarse-grained feldspar. The K-content is generally low, except for one analysis of microcline from MOD37 of Or_{97}. HJ002 is the most Ca-rich feldspar, up to An_{50}, and is classified as andesine. Formulae are calculated based on 5 cations and 8 oxygen (table 7.2a-c). Due to the low content of feldspar in MOD40, no EPMA analyses are available from this section.

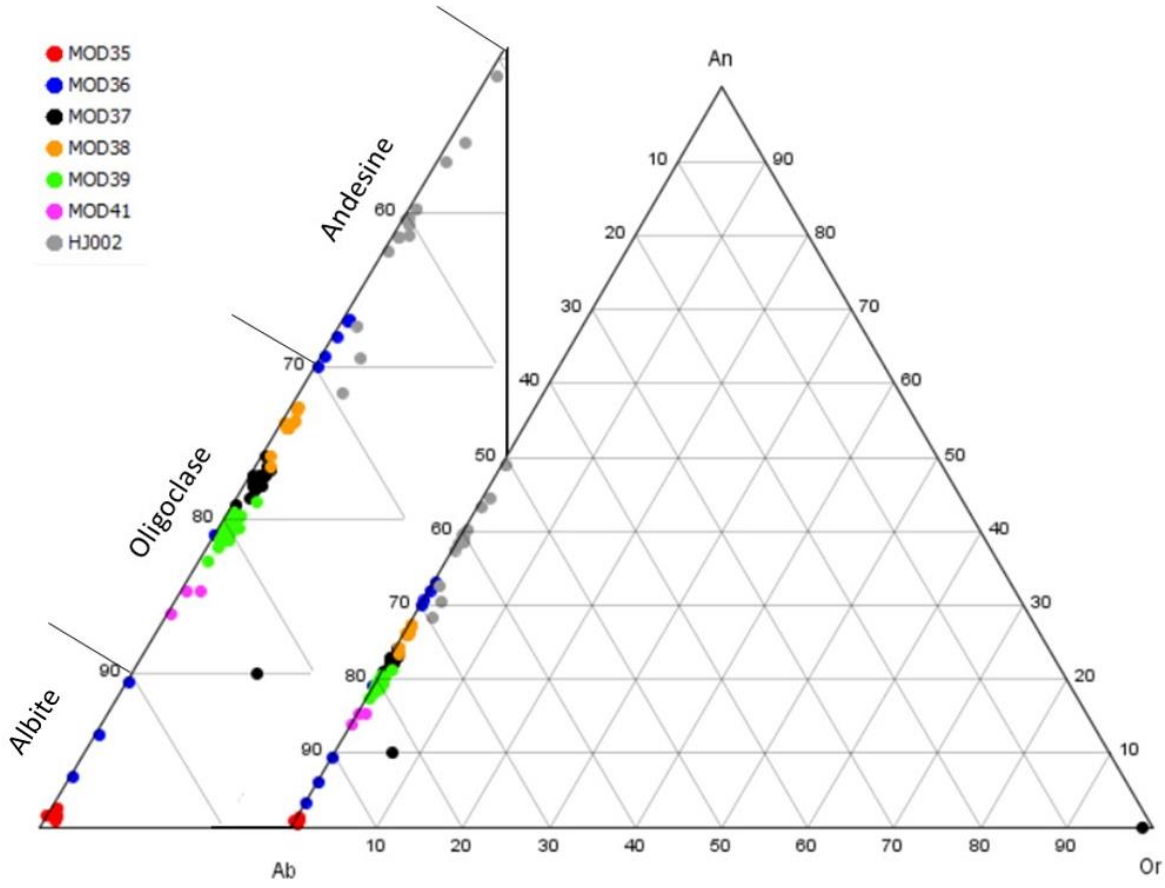

Figure 7.3: Ternary feldspar diagram of the compositional differences. Figure based on Deer et al. (1992).

Table 7.2a. Feldspar Analyses and Structural Formulae																			
		35-5.12	**35-6.6**	**35-7.1**	**35-7.8**	**35-8.10**	*35-1-8*	*35-1-14*	**36.2.4**	**36.2.7**	**36.3.1**	**36.3.7**	**36.3.8**	**36.4.1**	**36.4.5**	**36.4.7**	*36-3-2*	*36-4-1*	*36-4-9*
	SiO2	68.943	67.866	69.645	68.904	67.872	64.866	65.157	63.685	66.282	65.822	68.011	63.452	65.043	68.443	64.43	68.559	63.335	67.451
	TiO2	0.015	0.073	0.012	0	0.078	0	0.04	0	0	0.02	0.011	0	0.037	0	0	0	0.031	0
	Al2O3	19.471	19.137	20.717	19.727	19.402	20.446	20.782	22.288	20.658	22.334	19.018	22.248	22.559	19.495	22.492	20.25	23.529	21.004
	Cr2O3	0	0.009	0	0.031	0			0	0.013	0.034	0	0	0	0.007	0.012			
	Fe2O3	0.064	0.174	0.134	0.073	0.040	0.144	0.096	0.117	0.104	0.002	0.616	0.030	0.002	0.090	0.051	0.096	0.071	0.229
	FeO Total	0.058	0.157	0.121	0.066	0.036	0.13	0.086	0.105	0.094	0.002	0.554	0.027	0.002	0.081	0.046	0.086	0.064	0.206
	FeO	0.000	0.000	0.000	0.000	0.000	0.000	0.000	0.000	0.000	0.000	0.000	0.000	0.000	0.000	0.000	0.000	0.000	0.000
	MnO	0	0.058	0	0	0	0	0	0.031	0.023	0	0	0.019	0.001	0	0	0.04	0	0
	MgO	0.863	0.433	0.319	0.028	0.357	0.054	0.025	0	0.238	0.015	0.038	0	0	0.041	0.01	0.442	4.475	1.52
	CaO	0.086	0.149	0.047	0.086	0.097	0.1	0.126	4.095	2.359	4.037	0.391	4.317	4.405	0.725	4.486	0.128	0	0.147
	Na2O	11.175	11.552	10.728	11.154	11.045	11.924	12.085	9.247	10.016	9.399	11.395	9.169	8.948	11.292	9.054	11.853	9.392	11.529
	K2O	0.069	0.043	0.074	0	0.05	0.008	0.009	0.032	0	0.031	0.02	0.033	0.051	0.033	0.057	0.043	0.037	0.054
	BaO	0	0.041	0.014	0.014	0.043			0.041	0.124	0	0	0.06	0	0	0			
	Total	100.680	99.518	101.677	100.010	98.980	97.535	98.31	99.524	99.807	101.694	99.438	99.325	101.046	100.117	100.587	101.427	100.875	101.932
	Rev. Total	99.823	99.093	101.371	99.958	98.627	97.442	98.194	99.536	99.566	101.645	99.462	99.328	101.046	100.078	100.570	101.283	100.870	101.787
8 oxygen	**Si**	2.987	2.983	2.978	3.000	2.990	2.918	2.909	2.825	2.915	2.851	2.991	2.823	2.836	2.988	2.827	2.961	2.779	2.911
	Al	0.994	0.992	1.044	1.012	1.007	1.084	1.094	1.165	1.071	1.140	0.986	1.166	1.159	1.003	1.163	1.031	1.217	1.068
	Ti	0.000	0.002	0.000	0.000	0.003	0.000	0.001	0.000	0.000	0.001	0.000	0.000	0.001	0.000	0.000	0.000	0.001	0.000
	Cr	0.000	0.000	0.000	0.001	0.000	0.000	0.000	0.000	0.000	0.001	0.000	0.000	0.000	0.000	0.000	0.000	0.000	0.000
	Fe3+	0.002	0.006	0.004	0.002	0.001	0.005	0.003	0.004	0.003	0.000	0.020	0.001	0.000	0.003	0.002	0.003	0.002	0.007
4 cations	**Sum**	3.984	3.984	4.027	4.016	4.001	4.007	4.008	3.995	3.990	3.993	3.998	3.990	3.997	3.994	3.992	3.995	3.999	3.987
	Mg	0.056	0.028	0.020	0.002	0.023	0.007	0.008	0.000	0.016	0.001	0.002	0.000	0.000	0.003	0.001	0.008	0.000	0.009
	Fe2+																		
	Mn	0.000	0.002	0.000	0.000	0.000	0.000	0.000	0.001	0.001	0.000	0.000	0.001	0.000	0.000	0.000	0.001	0.000	0.000
	Ca	0.004	0.007	0.002	0.004	0.005	0.003	0.001	0.195	0.111	0.187	0.018	0.206	0.206	0.034	0.211	0.020	0.210	0.070
	Na	0.939	0.985	0.890	0.942	0.943	1.040	1.046	0.795	0.854	0.789	0.972	0.791	0.757	0.956	0.770	0.992	0.799	0.965
	K	0.004	0.002	0.004	0.000	0.003	0.000	0.001	0.002	0.000	0.002	0.001	0.002	0.003	0.002	0.003	0.002	0.002	0.003
	Ba	0.000	0.001	0.000	0.000	0.001	0.000	0.000	0.001	0.002	0.000	0.000	0.001	0.000	0.000	0.000	0.000	0.000	0.000
1 cation	**Sum**	1.002	1.025	0.916	0.948	0.975	1.050	1.056	0.994	0.984	0.979	0.994	1.000	0.965	0.994	0.985	1.025	1.012	1.048
5 cations	**Total**	4.986	5.009	4.944	4.963	4.976	5.057	5.064	4.989	4.974	4.973	4.992	4.990	4.962	4.988	4.977	5.020	5.011	5.035
	Ca/(Ca+Na)	0.004	0.007	0.002	0.004	0.005	0.002	0.001	0.197	0.115	0.192	0.019	0.206	0.214	0.034	0.215	0.020	0.208	0.068

Table 7.2b. Feldspar Analyses and Structural Formulae																			
		37.1.10	**37.1.11**	**37.2.12**	*37.1.11*	*37.2.14*	**37.3.2**	**37.3.10**	**37.6.10**	**37.6.11**	**37.7.5**	**37.8.7**	**37.9.9**	**38.1.2**	**38.2.1**	**38.3.2**	**38.3.4**	**38.3.8**	**38.5.4**	**38.7.9**
	SiO2	65.711	66.588	65.721	65.297	65.542	65.567	65.716	65.877	65.739	65.665	66.357	65.604	65.413	65.35	65.756	65.358	65.821	65.875	65.686
	TiO2	0.011	0	0	0	0.007	0.001	0.056	0	0.028	0.021	0	0.016	0.039	0.02	0	0	0	0.042	0.015
	Al2O3	21.199	20.973	21.124	22.285	22.089	21.106	21.417	20.869	20.98	21.151	20.941	21.149	21.511	21.725	21.45	21.35	21.472	21.877	21.677
	Cr2O3	0.028	0	0			0.021	0.016	0	0	0.028	0	0.028	0	0.004	0	0.008	0.013	0	0.006
	Fe2O3	0.056	0.018	0.078	0.061	0.251	0.069	0.053	0.106	0.172	0.072	0.030	0.082	0.050	0.060	0.050	0.101	0.036	0.078	0.043
	FeO Total	0.05	0.016	0.07	0.055	0.226	0.062	0.048	0.095	0.155	0.065	0.027	0.074	0.045	0.054	0.045	0.091	0.032	0.07	0.039
	FeO	0.000	0.000	0.000	0.000	0.000	0.000	0.000	0.000	0.000	0.000	0.000	0.000	0.000	0.000	0.000	0.000	0.000	0.000	0.000
	MnO	0	0	0	0.018	0.025	0	0.007	0.007	0	0	0.004	0	0.022	0	0.023	0	0.009	0.003	0.016
	MgO	0.043	0.018	0	3.027	2.898	0.004	0.017	0.024	0.015	0	0.041	0.021	0	0	0	0.001	0.003	0.01	0.012
	CaO	2.946	2.656	2.937	0.005	0	2.865	2.924	2.874	2.839	2.902	2.805	2.825	3.411	3.571	3.163	3.343	3.344	3.567	3.555
	Na2O	9.987	9.968	9.797	10.549	10.388	9.898	10.053	10.086	10.004	9.824	10.188	9.776	9.386	9.498	9.849	9.488	9.474	9.418	9.48
	K2O	0.04	0.032	0.073	0.042	0.061	0.128	0.092	0.096	0.103	0.07	0.102	0.103	0.089	0.061	0.064	0.065	0.082	0.058	0.064
	BaO	0	0	0			0.016	0	0.005	0	0	0	0	0	0	0	0.018	0	0	0.055
	Total	100.015	100.251	99.722	101.278	101.237	99.668	100.346	99.933	99.863	99.726	100.465	99.596	99.916	100.283	100.350	99.722	100.250	100.920	100.605
	Rev. Total	99.950	100.235	99.730	101.279	101.261	99.650	100.318	99.920	99.865	99.705	100.427	99.555	99.921	100.285	100.355	99.723	100.238	100.918	100.591
8 oxygen	**Si**	2.889	2.914	2.896	2.846	2.855	2.893	2.882	2.900	2.895	2.894	2.904	2.894	2.878	2.868	2.883	2.882	2.885	2.871	2.874
	Al	1.099	1.082	1.097	1.145	1.134	1.098	1.107	1.083	1.089	1.098	1.080	1.100	1.116	1.124	1.108	1.110	1.109	1.124	1.118
	Ti	0.000	0.000	0.000	0.000	0.000	0.000	0.002	0.000	0.001	0.001	0.000	0.001	0.001	0.001	0.000	0.000	0.000	0.001	0.000
	Cr	0.001	0.000	0.000	0.000	0.000	0.001	0.001	0.000	0.000	0.001	0.000	0.001	0.000	0.000	0.000	0.000	0.000	0.000	0.000
	Fe3+	0.002	0.001	0.003	0.002	0.008	0.002	0.002	0.003	0.006	0.002	0.001	0.003	0.002	0.002	0.002	0.003	0.001	0.003	0.001
4 cations	**Sum**	3.991	3.996	3.995	3.992	3.997	3.994	3.993	3.986	3.991	3.996	3.986	3.998	3.997	3.995	3.993	3.995	3.997	3.998	3.993
	Mg	0.003	0.001	0.000	0.000	0.000	0.000	0.001	0.002	0.001	0.000	0.003	0.001	0.000	0.000	0.000	0.000	0.000	0.001	0.001
	Fe2+																			
	Mn	0.000	0.000	0.000	0.001	0.001	0.000	0.000	0.000	0.000	0.000	0.000	0.000	0.001	0.000	0.001	0.000	0.000	0.000	0.001
	Ca	0.139	0.125	0.139	0.141	0.135	0.135	0.137	0.136	0.134	0.137	0.132	0.134	0.161	0.168	0.149	0.158	0.157	0.167	0.167
	Na	0.851	0.846	0.837	0.891	0.877	0.847	0.855	0.861	0.854	0.839	0.865	0.836	0.801	0.808	0.837	0.811	0.805	0.796	0.804
	K	0.002	0.002	0.004	0.002	0.003	0.007	0.005	0.005	0.006	0.004	0.006	0.006	0.005	0.003	0.004	0.004	0.005	0.003	0.004
	Ba	0.000	0.000	0.000	0.000	0.000	0.000	0.000	0.000	0.000	0.000	0.000	0.000	0.000	0.000	0.000	0.000	0.000	0.000	0.001
1 cation	**Sum**	0.995	0.973	0.980	1.036	1.017	0.990	0.999	1.004	0.995	0.980	1.005	0.977	0.967	0.980	0.990	0.973	0.967	0.966	0.977
5 cations	**Total**	4.986	4.969	4.975	5.028	5.014	4.984	4.992	4.990	4.986	4.976	4.990	4.975	4.965	4.974	4.983	4.969	4.964	4.964	4.970
	Ca/(Ca+Na)	0.140	0.128	0.142	0.137	0.134	0.138	0.138	0.136	0.136	0.140	0.132	0.138	0.167	0.172	0.151	0.163	0.163	0.173	0.172

Table 7.2c. Feldspar Analyses and Structural Formulae																		
		39.2.9	**39.3.1**	**39.4.6**	**39.4.11**	**39.5.1**	**39.5.3**	**39.6.9**	**39-3.3**	**39-3.5**	**39-3.7**	**39-3.8**	**41.2.8**	**41.3.2**	**002-3.5**	**002-4.6**	**002-5.5**	**002-5.10**	**002-3.5**
	SiO2	67.173	66.745	66.282	66.923	66.597	67.053	67.19	66.7	65.725	66.174	66.219	67.09	67.268	62.201	59.975	61.172	62.384	62.201
	TiO2	0.031	0	0	0	0.043	0.027	0	0.019	0.01	0	0	0.025	0.044	0.049	0.023	0.02	0	0.049
	Al2O3	20.497	20.747	20.533	20.596	20.799	20.609	20.385	21.85	21.637	21.672	22.295	20.475	20.769	24.025	25.548	24.392	24.384	24.025
	Cr2O3	0	0.002	0.011	0	0	0	0	0	0.017	0	0	0	0	0	0	0	0	0
	Fe2O3	0.093	0.067	0.091	0.042	0.017	0.073	0.068	0.036	0.081	0.050	0.067	0.000	0.026	0.028	0.004	0.107	0.037	0.028
	FeO Total	0.084	0.06	0.082	0.038	0.015	0.066	0.061	0.032	0.073	0.045	0.06	0	0.023	0.025	0.004	0.096	0.033	0.025
	FeO	0.000	0.000	0.000	0.000	0.000	0.000	0.000	0.000	0.000	0.000	0.000	0.000	0.000	0.000	0.000	0.000	0.000	0.000
	MnO	0	0	0	0.019	0.013	0	0.022	0.037	0.004	0.072	0.021	0	0.013	0	0.009	0.013	0.004	0
	MgO	0	0	0.189	0.003	0	0.005	0.011	0.023	0	0.088	0	0.003	0	0.036	0	0.044	0	0.036
	CaO	2.284	2.466	2.658	2.452	2.567	2.389	2.478	2.222	2.342	2.395	2.427	1.718	1.906	5.276	7.066	5.359	5.385	5.276
	Na2O	9.937	10.081	9.756	10.051	10.44	10.059	9.829	9.444	9.903	9.652	9.384	10.633	10.367	8.42	7.331	8.429	7.938	8.42
	K2O	0.086	0.144	0.155	0.101	0.088	0.077	0.072	0.059	0.087	0.102	0.041	0.03	0.132	0.056	0.075	0.124	0.062	0.056
	BaO	0	0	0.103	0	0	0	0	0.017	0	0	0	0.054	0.014	0.048	0	0.016	0.071	0.048
	Total	100.092	100.245	99.769	100.183	100.562	100.285	100.048	100.403	99.798	100.200	100.447	100.028	100.536	100.136	100.031	99.665	100.261	100.136
	Rev. Total	100.101	100.250	99.578	100.184	100.564	100.287	100.044	100.384	99.789	100.117	100.454	100.025	100.539	100.103	100.031	99.632	100.265	100.103
8 oxygen	**Si**	2.939	2.922	2.918	2.929	2.912	2.931	2.941	2.904	2.889	2.894	2.884	2.939	2.932	2.751	2.667	2.723	2.750	2.751
	Al	1.057	1.070	1.065	1.063	1.072	1.062	1.052	1.121	1.121	1.117	1.145	1.057	1.067	1.252	1.339	1.280	1.267	1.252
	Ti	0.001	0.000	0.000	0.000	0.001	0.001	0.000	0.001	0.000	0.000	0.000	0.001	0.001	0.002	0.001	0.001	0.000	0.002
	Cr	0.000	0.000	0.000	0.000	0.000	0.000	0.000	0.000	0.001	0.000	0.000	0.000	0.000	0.000	0.000	0.000	0.000	0.000
	Fe3+	0.003	0.002	0.003	0.001	0.001	0.002	0.002	0.001	0.003	0.002	0.002	0.000	0.001	0.001	0.000	0.004	0.001	0.001
4 cations	**Sum**	4.000	3.994	3.987	3.993	3.985	3.996	3.995	4.027	4.014	4.013	4.031	3.997	4.001	4.005	4.007	4.008	4.019	4.005
	Mg	0.000	0.000	0.012	0.000	0.000	0.000	0.001	0.001	0.000	0.006	0.000	0.000	0.000	0.002	0.000	0.003	0.000	0.002
	Fe2+																		
	Mn	0.000	0.000	0.000	0.001	0.000	0.000	0.001	0.001	0.000	0.003	0.001	0.000	0.000	0.000	0.000	0.000	0.000	0.000
	Ca	0.107	0.116	0.125	0.115	0.120	0.112	0.116	0.104	0.110	0.112	0.113	0.081	0.089	0.250	0.337	0.256	0.254	0.250
	Na	0.843	0.856	0.833	0.853	0.885	0.852	0.834	0.797	0.844	0.819	0.792	0.903	0.876	0.722	0.632	0.728	0.679	0.722
	K	0.005	0.008	0.009	0.006	0.005	0.004	0.004	0.003	0.005	0.006	0.002	0.002	0.007	0.003	0.004	0.007	0.003	0.003
	Ba	0.000	0.000	0.002	0.000	0.000	0.000	0.000	0.000	0.000	0.000	0.000	0.001	0.000	0.001	0.000	0.000	0.001	0.001
1 cation	**Sum**	0.955	0.979	0.981	0.975	1.011	0.969	0.956	0.907	0.959	0.945	0.909	0.987	0.973	0.978	0.973	0.994	0.938	0.978
5 cations	**Total**	4.954	4.974	4.968	4.968	4.996	4.965	4.951	4.934	4.973	4.958	4.940	4.984	4.974	4.984	4.981	5.002	4.956	4.984
	Ca/(Ca+Na)	0.113	0.119	0.131	0.119	0.120	0.116	0.122	0.115	0.116	0.121	0.125	0.082	0.092	0.257	0.348	0.260	0.273	0.257

7.2.3 Phlogopite/biotite

The phlogopite in MOD35-MOD41 is nearly colorless. Some grains show weak brown pleochroism. Most grains are platy and elongated, with good cleavage and second order interference colors. Phlogopite is more abundant in MOD35, MOD37, MOD38 and MOD39 than in the others. Phlogopite is commonly platy with second order interference colors. At times it occurs as anhedral grains with weak yellow color and grey, dull interference color, due to thin section being cut parallel to foliation. In MOD40 and MOD41, most of the phlogopite grains are partly altered to chlorite. In MOD37, the phlogopite is usually in clusters, and this is also the section showing the clearest foliation.

MODHJK differs from the other sections, displaying dark brown, pleochroic biotite. The grains are abundantly altered to green chlorite, and is present both as grains completely surrounded by quartz, and as platy grains along grain boundaries of feldspar.

The EPMA results show that the phlogopite grains are remarkable low in Fe and high in Mg. Formulae are calculated based on 7 tetrahedral and octahedral cations and variable oxygen (table 7.3a-c). MOD35 has the phlogopite with the highest Mg-content, with a ratio of Mg to $Mg+Fe_{tot}$ of up to 0.959. MOD36, MOD40 and MOD41 show a lower ratio, ranging up to 0.920, while HJ002 is the lowest at up to 0.89, even this being quite Mg-rich. The total Al ranges from 0.75 to 1.40. This is generally somewhat lower than typical biotite in mica schists, which have total Al ~ 1.33. The K-content is by far the lowest in MOD36, with a K/(Ka+Na) ratio of 0.84. In MOD 40 and MOD41, this ratio is 0.93-0.94, while the other sections display a ratio ranging from 0.95-0.98. From this, the biotite can be classified as phlogopite (fig. 7.5). General formulae are the following:

$$(K_{0,74\text{-}0,90}Na_{0,02\text{-}0,06})(Mg_{2,28\text{-}2,66}Fe^{2+}{}_{0\text{-}0,28}Fe^{3+}{}_{0,04\text{-}0,15}Al_{0,13\text{-}0,37}Ti_{0,03\text{-}0,13})Al_{0,98\text{-}1,21}(Si_{2,69\text{-}3,20}O_{10,96\text{-}11,12})(OH)_2$$

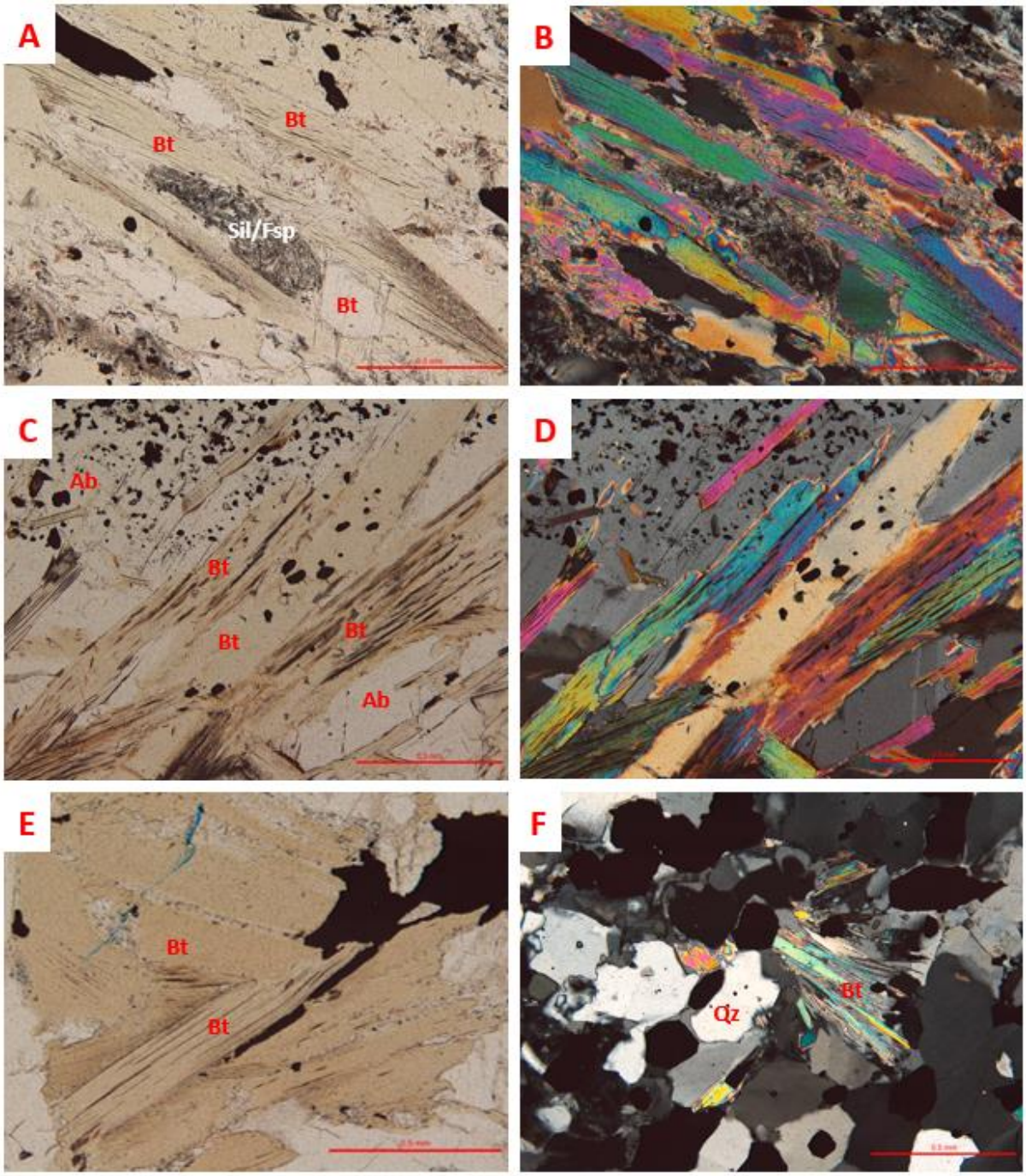

Figure 7.4: Photomicrographs of phlogopite. A and B: Phlogopite in MOD35 in ppl and xpl. C and D: Phlogopite ppl and xpl in MOD37. E: Biotite in ppl in HJ002. F: Phlogopite partially altered to chlorite in MOD41. Xpl. A-F: Scalebar is 0.5 mm.

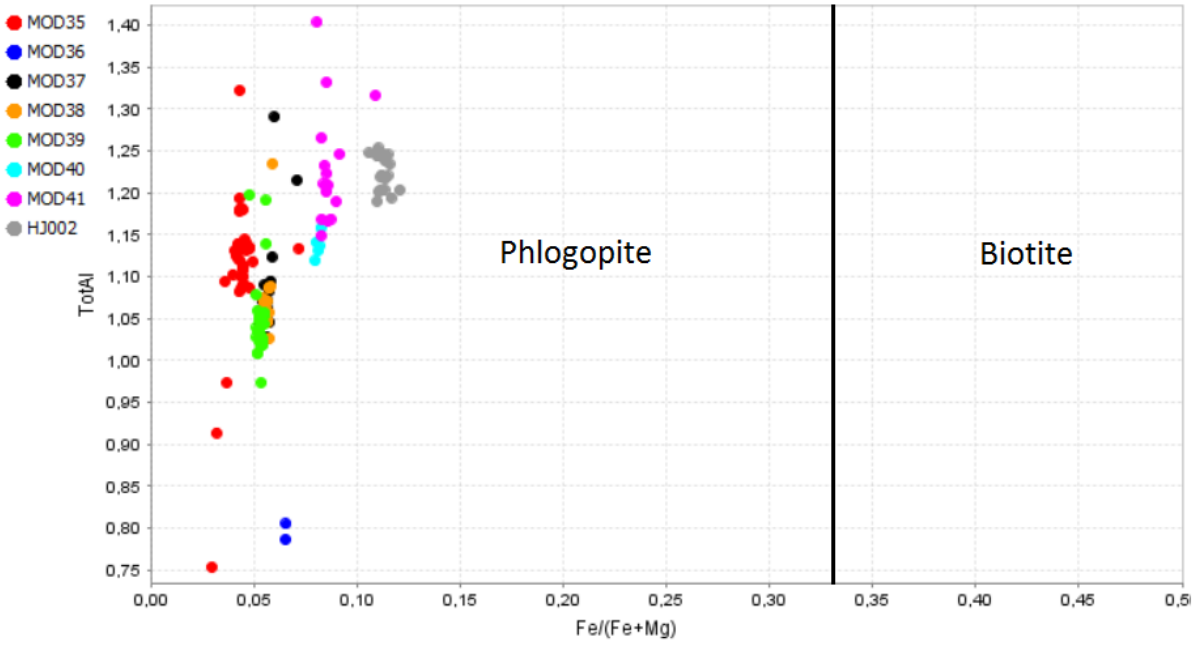

Figure 7.5: Fe/(Fe+Mg) plotted versus Total Al. Diagram for classification of biotite, where Al is based on content of Al in tetrahedral position from the general structural formula.

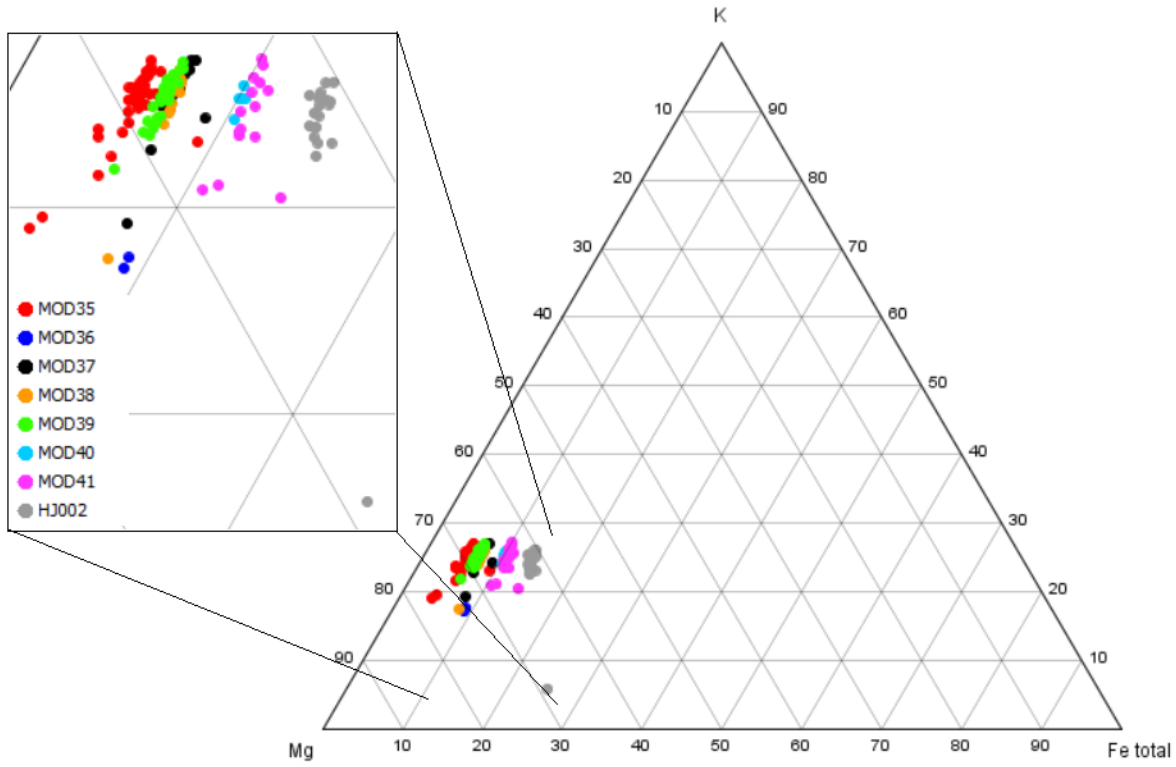

Figure 7.6: Ternary phlogopite diagram of the compositional differences in the various sections.

Table 7.3a. Biotite Analyses and Structural Formulae

		35-1a-1.3	35-1a-1.4	35-1a-1.7	35-1a-1.3	35-1a-2.2	35-1a-2.7	35-1a-4.5	35-1a-5.9	35-1a-7.6	35-1a-8.6	*35-1-3*	*35-1-7*	36.2.1	*36-4-3*	37.2.6	37.2.10	37.6.4	37.6.5	37.6.8	37.6.12	37.7.11
	Wt.% Oxides																					
	SiO2	42.47	42.216	42.133	42.534	42.341	41.288	42.679	42.531	42.368	42.079	43.908	44.451	47.298	47.898	41.722	42.365	42.818	42.664	41.345	42.204	42.645
	TiO2	0.937	0.978	0.911	0.758	0.617	0.721	0.679	0.844	0.95	0.829	0.904	0.766	0.253	0.324	0.859	0.803	0.866	0.889	0.792	0.893	0.93
	Al2O3	17.542	17.678	17.186	17.788	18.665	18.5	17.336	17.476	17.67	17.687	17.27	17.277	13.395	14.09	15.979	15.084	14.739	14.931	16.373	15.278	15.431
	Cr2O3	0.034	0.002	0	0	0.007	0.012	0.039	0.02	0.019	0.023			0.008		0.035	0.029	0.024	0.042	0	0.029	0
	Fe2O3	2.2107	1.8378	1.9720	0.8396	0.9820	1.0658	0.7865	1.1399	1.1988	1.6113	0.1287	0.3846	0.4163	0.0879	0.1788	0.2923	0.4934	0.1588	1.4075	1.0199	0.3853
	FeO Total	2.078	2.179	2.266	2.008	1.872	2.014	2.049	2.088	1.932	1.994	2.676	2.553	3.105	3.971	2.652	2.618	2.559	2.628	2.764	2.679	2.664
	FeO	0.089	0.525	0.492	1.253	0.988	1.055	1.341	1.062	0.853	0.544	2.5601	2.2070	2.730	3.8919	2.491	2.355	2.115	2.485	1.498	1.761	2.317
	MnO	0.071	0	0	0.082	0	0.011	0	0	0.012	0.067	0	0.012	0.033	0.026	0.03	0.006	0.018	0.031	0	0.002	0.026
	MgO	25.049	25.314	25.437	25.201	24.786	25.255	24.942	24.914	25.224	25.293	25.383	25.342	24.9	26.122	24.576	25.426	25.796	25.452	24.867	25.742	25.337
	CaO	0	0.086	0	0	0	0	0	0	0	0	0	0	0	0	0	0	0	0	0	0	0
	Na2O	0.244	0.31	0.262	0.212	0.158	0.17	0.215	0.334	0.349	0.271	0.275	0.275	0.705	0.636	0.194	0.153	0.162	0.228	0.135	0.196	0.154
	K2O	9.462	9.061	9.445	9.639	9.235	9.844	9.619	9.257	9.136	9.216	9.843	9.266	5.76	6.131	10.089	9.765	9.489	9.304	10.25	9.376	9.438
	Rev. Total	98.108	98.008	97.838	98.306	97.779	97.922	97.637	97.578	97.780	97.620	100.272	99.981	95.499	99.207	96.154	96.278	96.520	96.185	96.667	96.501	96.664
7 Cats IV+VI	**Si**	2.790	2.866	2.860	2.867	2.910	2.906	2.678	2.910	2.879	3.026	2.927	2.955	2.819	3.133	3.195	2.918	2.905	2.954	2.945	2.929	2.910
	Al	1.210	1.134	1.140	1.133	1.090	1.094	1.322	1.090	1.121	0.974	1.073	1.045	1.181	0.867	0.805	1.082	1.095	1.046	1.055	1.071	1.090
4 T sites	**Sum**	4.000	4.000	4.000	4.000	4.000	4.000	4.000	4.000	4.000	4.000	4.000	4.000	4.000	4.000	4.000	4.000	4.000	4.000	4.000	4.000	4.000
	Total Al	1.507	1.405	1.411	1.378	1.408	1.302	1.450	1.354	1.399	1.299	1.357	1.354	1.458	1.086	1.053	1.317	1.222	1.198	1.202	1.209	1.242
	Al	0.297	0.272	0.271	0.245	0.317	0.208	0.128	0.264	0.277	0.325	0.284	0.308	0.276	0.219	0.248	0.234	0.127	0.152	0.147	0.137	0.152
	Ti	0.130	0.044	0.050	0.047	0.040	0.033	0.045	0.046	0.044	0.030	0.045	0.038	0.033	0.016	0.014	0.045	0.046	0.045	0.043	0.048	0.046
3	**Cr**	0.034	0.000	0.000	0.000	0.000	0.000	0.001	0.003	0.001	0.001	0.000	0.000	0.000	0.000	0.000	0.002	0.002	0.001	0.000	0.001	0.002
Octahedral	**Fe3+**	0.113	0.094	0.101	0.043	0.050	0.055	0.040	0.058	0.061	0.082	0.006	0.019	0.021	0.004	0.009	0.015	0.026	0.008	0.074	0.053	0.020
sites	**Mg**	2.537	2.556	2.580	2.543	2.503	2.559	2.538	2.532	2.552	2.562	2.522	2.511	2.522	2.547	2.562	2.630	2.653	2.626	2.579	2.646	2.603
	Fe Total	0.118	0.123	0.129	0.114	0.106	0.114	0.117	0.119	0.110	0.113	0.149	0.142	0.176	0.217	0.155	0.152	0.148	0.152	0.161	0.154	0.154
	Fe2+	0.005	0.030	0.028	0.071	0.056	0.060	0.077	0.061	0.048	0.031	0.143	0.123	0.155	0.213	0.146	0.137	0.122	0.144	0.087	0.102	0.134
	Mn	0.004	0.000	0.000	0.005	0.000	0.001	0.000	0.000	0.001	0.004	0.000	0.001	0.002	0.001	0.002	0.000	0.001	0.002	0.000	0.000	0.002
	Sum	3.000	3.000	3.000	3.000	3.000	3.000	3.000	3.000	3.000	3.000	3.000	3.000	3.000	3.000	3.000	3.000	3.000	3.000	3.000	3.000	3.000
	Ca	0.000	0.006	0.000	0.000	0.000	0.000	0.000	0.000	0.000	0.000	0.000	0.000	0.000	0.000	0.000	0.000	0.000	0.000	0.000	0.000	0.000
Interlayer	**Na**	0.032	0.041	0.035	0.028	0.021	0.022	0.028	0.044	0.046	0.036	0.036	0.035	0.093	0.081	0.026	0.021	0.022	0.031	0.018	0.026	0.021
sites	**K**	0.820	0.783	0.820	0.833	0.798	0.854	0.838	0.805	0.791	0.799	0.837	0.786	0.499	0.512	0.900	0.865	0.835	0.822	0.910	0.825	0.830
	Sum	0.852	0.830	0.854	0.860	0.819	0.876	0.866	0.849	0.837	0.835	0.873	0.821	0.592	0.592	0.926	0.885	0.857	0.852	0.928	0.851	0.851
	Total	7.852	7.830	7.854	7.860	7.819	7.876	7.866	7.849	7.837	7.835	7.873	7.821	7.592	7.592	7.926	7.885	7.857	7.852	7.928	7.851	7.851
	Variable ox	11.12	11.08	11.08	11.08	11.08	11.05	11.10	11.10	11.08	11.07	11.090	11.090	11.07	10.990	11.09	11.05	11.04	11.04	11.09	11.03	11.05
	Mg/(MFeTot)	0.954	0.954	0.952	0.956	0.959	0.957	0.956	0.955	0.959	0.956	0.944	0.946	0.934	0.921	0.942	0.945	0.947	0.945	0.941	0.945	0.944
	Mg/(MFe2O)	0.996	0.988	0.989	0.971	0.978	0.977	0.971	0.977	0.981	0.987	0.946	0.953	0.941	0.922	0.946	0.950	0.956	0.947	0.967	0.963	0.951
	Al/(Al+Si)	0.351	0.329	0.330	0.325	0.326	0.309	0.351	0.318	0.327	0.300	0.317	0.314	0.341	0.257	0.248	0.311	0.296	0.289	0.290	0.292	0.299
	K/(K+Na)	0.962	0.951	0.960	0.968	0.975	0.974	0.967	0.948	0.945	0.957	0.959	0.957	0.843	0.864	0.972	0.977	0.975	0.964	0.980	0.969	0.976

Table 7.3b. Biotite Analyses and Structural Formulae

		37.7.12	*37.2.6*	38.1.9	38.2.2	38.4.8	38.5.1	38.6.2	38.6.5	38.6.11	38.7.5	39.1.9	39.3.3	39.3.8	39.4.2	39.4.7	39.4.10	39.5.7	39.5.9	39.6.6	39-1.11	39-3.4	39-3.11
	Wt.% Oxides																						
	SiO2	42.626	43.232	42.219	42.604	42.293	42.69	41.904	42.732	42.058	42.37	42.78	42.516	40.301	42.7	42.877	42.534	42.574	41.122	42.358	43.017	43.23	43.297
	TiO2	0.827	1	0.925	0.781	0.827	0.86	0.844	0.927	0.926	0.912	0.938	0.891	0.984	0.909	0.972	0.853	0.843	0.802	0.902	0.854	0.783	1.127
	Al2O3	15.215	16.866	15.284	15.07	15.436	15.2	15.358	14.804	15.52	15.428	14.894	14.775	16.441	14.46	14.657	14.469	15.181	15.915	14.848	15.992	15.745	15.499
	Cr2O3	0		0	0	0	0	0	0.014	0	0	0	0.01	0	0.019	0	0	0	0	0	0.041	0.032	0.035
	Fe2O3	0.5415	0.1590	1.029	0.532	0.780	0.846	0.850	0.888	0.634	0.872	0.537	0.553	1.135	0.582	1.231	0.345	0.585	0.879	2.002	0.343	0.188	0.7778
	FeO Total	2.716	2.697	2.615	2.72	2.562	2.709	2.597	2.734	2.73	2.595	2.466	2.548	2.665	2.444	2.557	2.526	2.474	2.688	2.657	2.542	2.634	2.519
	FeO	2.229	2.5539	1.689	2.242	1.860	1.948	1.833	1.935	2.160	1.811	1.982	2.050	1.644	1.920	1.449	2.215	1.948	1.897	0.855	2.233	2.464	1.819
	MnO	0	0	0	0.018	0.011	0	0.023	0.016	0.015	0	0	0.045	0.005	0	0.023	0	0.022	0	0.014	0.042	0	0.003
	MgO	25.553	25.26	25.319	25.318	25.081	25.265	25.091	25.101	25.313	25.046	25.414	25.419	25.341	25.115	25.523	25.182	25.085	25.429	25.477	24.929	25.315	26.282
	CaO	0	0	0	0	0	0	0	0	0	0	0	0	0	0	0	0	0	0	0	0	0	0
	Na2O	0.145	0.216	0.216	0.208	0.114	0.218	0.235	0.194	0.209	0.14	0.134	0.109	0.174	0.156	0.167	0.201	0.177	0.068	0.171	0.23	0.138	0.219
	K2O	9.476	10.326	9.597	9.329	10.017	9.864	9.626	9.112	9.846	9.348	9.82	9.455	10.174	9.562	9.48	9.699	9.527	9.864	9.429	8.821	9.012	9.51
	Rev. Total	96.612	99.613	96.278	96.101	96.419	96.891	95.763	95.723	96.681	95.926	96.500	95.823	96.199	95.423	96.379	95.499	95.942	95.976	96.057	96.502	96.908	98.569
7 Cats IV+VI	**Si**	2.940	2.916	2.926	2.930	2.952	2.942	2.929	2.765	2.973	2.932	2.948	2.967	2.992	2.809	2.991	2.977	2.945	2.963	2.981	2.947	2.940	2.802
	Al	1.060	1.084	1.074	1.070	1.048	1.058	1.071	1.235	1.027	1.068	1.052	1.033	1.008	1.191	1.009	1.023	1.055	1.037	1.019	1.053	1.060	1.198
4 T sites	**Sum**	4.000	4.000	4.000	4.000	4.000	4.000	4.000	4.000	4.000	4.000	4.000	4.000	4.000	4.000	4.000	4.000	4.000	4.000	4.000	4.000	4.000	4.000
	Total Al	1.254	1.341	1.278	1.250	1.246	1.265	1.244	1.243	1.214	1.257	1.198	1.258	1.176	1.351	1.194	1.192	1.277	1.245	1.182	1.241	1.291	1.292
	Al	0.193	0.257	0.203	0.181	0.198	0.207	0.173	0.008	0.187	0.189	0.147	0.224	0.168	0.160	0.185	0.169	0.221	0.208	0.163	0.188	0.231	0.095
	Ti	0.048	0.051	0.042	0.048	0.042	0.043	0.045	0.043	0.049	0.046	0.044	0.041	0.050	0.052	0.048	0.047	0.048	0.044	0.050	0.050	0.047	0.047
3	**Cr**	0.000	0.000	0.001	0.000	0.002	0.000	0.000	0.001	0.001	0.000	0.003	0.000	0.002	0.000	0.001	0.000	0.000	0.000	0.002	0.000	0.000	0.003
Octahedral	**Fe3+**	0.028	0.008	0.054	0.028	0.041	0.044	0.045	0.046	0.033	0.046	0.028	0.029	0.060	0.031	0.064	0.018	0.031	0.046	0.105	0.018	0.010	0.039
sites	**Mg**	2.626	2.540	2.619	2.616	2.600	2.605	2.612	2.603	2.613	2.594	2.626	2.635	2.633	2.623	2.634	2.631	2.602	2.636	2.639	2.554	2.581	2.644
	Fe Total	0.157	0.152	0.152	0.158	0.149	0.157	0.152	0.159	0.158	0.151	0.143	0.148	0.155	0.143	0.148	0.148	0.144	0.156	0.154	0.146	0.151	0.142
	Fe2+	0.128	0.144	0.098	0.130	0.108	0.113	0.107	0.113	0.125	0.105	0.115	0.119	0.096	0.113	0.084	0.130	0.113	0.110	0.050	0.128	0.141	0.103
	Mn	0.000	0.000	0.000	0.001	0.001	0.000	0.001	0.001	0.001	0.000	0.000	0.003	0.000	0.000	0.001	0.000	0.001	0.000	0.001	0.002	0.000	0.000
	Sum	3.000	3.000	3.000	3.000	3.000	3.000	3.000	3.000	3.000	3.000	3.000	3.000	3.000	3.000	3.000	3.000	3.000	3.000	3.000	3.000	3.000	3.000
	Ca	0.000	0.000	0.000	0.000	0.000	0.000	0.000	0.000	0.000	0.000	0.000	0.000	0.000	0.000	0.000	0.000	0.000	0.000	0.000	0.000	0.000	0.000
Interlayer	**Na**	0.019	0.028	0.029	0.028	0.015	0.029	0.032	0.026	0.028	0.019	0.018	0.015	0.024	0.021	0.022	0.027	0.024	0.009	0.023	0.031	0.018	0.029
sites	**K**	0.833	0.889	0.850	0.825	0.889	0.871	0.858	0.809	0.870	0.829	0.868	0.839	0.905	0.855	0.837	0.867	0.846	0.875	0.836	0.773	0.786	0.819
	Sum	0.853	0.917	0.879	0.853	0.904	0.900	0.889	0.835	0.898	0.847	0.886	0.853	0.928	0.876	0.860	0.894	0.870	0.884	0.859	0.804	0.805	0.847
	Total	7.853	7.917	7.879	7.853	7.904	7.900	7.889	7.835	7.898	7.847	7.886	7.853	7.928	7.876	7.860	7.894	7.870	7.884	7.859	7.804	7.805	7.847
	Variable ox	11.04	11.100	11.07	11.05	11.09	11.09	11.07	11.07	11.06	11.07	11.08	11.05	11.03	11.09	11.08	11.08	11.08	11.02	11.08	11.06	11.04	11.04
	Mg/(MFeTot)	0.944	0.943	0.945	0.943	0.946	0.943	0.945	0.942	0.943	0.945	0.948	0.946	0.944	0.948	0.946	0.947	0.947	0.944	0.944	0.945	0.945	0.949
	Mg/(MFe2O)	0.953	0.946	0.964	0.952	0.960	0.959	0.960	0.958	0.954	0.961	0.958	0.956	0.965	0.959	0.969	0.953	0.958	0.960	0.981	0.951	0.948	0.963
	Al/(Al+Si)	0.299	0.315	0.304	0.299	0.297	0.301	0.298	0.310	0.290	0.300	0.289	0.298	0.282	0.325	0.285	0.286	0.302	0.296	0.284	0.296	0.305	0.316
	K/(K+Na)	0.977	0.969	0.967	0.967	0.983	0.968	0.964	0.969	0.969	0.978	0.980	0.983	0.975	0.976	0.974	0.969	0.973	0.990	0.973	0.962	0.977	0.966

Table 7.3c. Biotite Analyses and Structural Formulae

		39-3.12	40.1.5	40.1.6	40.3.7	40.4.2	40.4.5	*40-3-7*	41.1.6	41.2.6	41.3.1	41.3.5	41.3.7	41.3.8	41.4.1	41.4.6	002-1.1	002-2.3	002-2.7	002-2.9	002-3.6	002-3.10	002-3.11
	Wt.% Oxides																						
	SiO2	43.998	41.054	41.148	40.021	40.67	41.083	40.883	39.862	38.728	40.428	40.022	40.459	38.419	39.966	38.998	39.8	40.03	39.653	39.687	40.546	39.614	39.797
	TiO2	0.997	0.694	0.685	0.76	0.673	0.629	0.864	0.483	0.387	0.409	0.572	0.427	0.301	0.55	0.43	1.037	0.943	1.135	1.072	1.208	1.114	1.021
	Al2O3	14.919	17.91	17.558	17.249	17.614	17.44	18.337	17.877	18.644	18.185	18.277	18.315	18.399	17.288	17.34	18.852	18.448	18.979	18.829	19.187	19.099	19.102
	Cr2O3	0	0	0	0.006	0.037	0.032		0.004	0.012	0	0	0.022	0.008	0	0	0	0.037	0.016	0.016	0	0.011	0.03
	Fe2O3	0.0988	1.4502	0.7508	1.4544	1.3065	1.3084	0.0170	2.2321	1.3937	1.4410	0.0673	0.0963	5.3909	2.3790	2.7513	2.0373	0.8119	2.1577	2.2664	0.0077	2.6229	1.8362
	FeO Total	2.531	3.625	3.588	3.707	3.66	3.711	4.786	3.968	3.713	3.863	3.666	3.65	5.193	3.969	3.934	5.165	4.971	4.968	5.241	4.85	4.988	5.092
	FeO	2.442	2.320	2.912	2.398	2.484	2.534	4.7707	1.959	2.459	2.566	3.605	3.563	0.342	1.828	1.458	3.332	4.240	3.026	3.202	4.843	2.628	3.440
	MnO	0	0.035	0.027	0.021	0.041	0.016	0	0.013	0.018	0	0	0	0.004	0	0	0.07	0.06	0.025	0	0.009	0	0
	MgO	25.037	23.338	23.209	23.163	23.046	23.481	23.998	23.731	22.709	23.129	22.74	22.754	23.838	23.311	23.67	22.61	22.404	22.571	22.661	22.06	22.625	22.615
	CaO	0	0	0	0	0.09	0	0	0.049	0	0	0	0	0	0	0	0	0	0	0	0	0	0
	Na2O	0.126	0.416	0.46	0.376	0.36	0.391	0.407	0.384	0.548	0.48	0.312	0.449	0.428	0.389	0.428	0.411	0.452	0.415	0.438	0.397	0.429	0.407
	K2O	9.717	9.099	9.345	9.063	8.521	9.185	9.286	8.469	9.684	9.466	9.825	9.401	7.46	9.028	8.59	9.318	9.604	9.297	9.27	9.205	8.673	8.938
	Rev. Total	97.335	96.316	96.095	94.512	94.843	96.099	98.563	95.064	94.583	96.104	95.421	95.487	94.590	94.739	93.666	97.467	97.030	97.275	97.441	97.463	96.816	97.186
7 Cats IV+VI	**Si**	2.922	2.974	2.859	2.881	2.842	2.864	2.781	2.799	2.810	2.754	2.834	2.831	2.851	2.684	2.790	2.668	2.781	2.799	2.756	2.747	2.810	2.749
	Al	1.078	1.026	1.141	1.119	1.158	1.136	1.219	1.201	1.190	1.246	1.166	1.169	1.149	1.316	1.210	1.332	1.219	1.201	1.244	1.253	1.190	1.251
4 T sites	**Sum**	4.000	4.000	4.000	4.000	4.000	4.000	4.000	4.000	4.000	4.000	4.000	4.000	4.000	4.000	4.000	4.000	4.000	4.000	4.000	4.000	4.000	4.000
	Total Al	1.233	1.258	1.470	1.449	1.444	1.462	1.470	1.471	1.469	1.457	1.502	1.524	1.521	1.515	1.503	1.494	1.540	1.520	1.555	1.520	1.567	1.562
	Al	0.155	0.232	0.328	0.330	0.286	0.326	0.251	0.270	0.279	0.210	0.336	0.355	0.372	0.198	0.293	0.162	0.321	0.319	0.311	0.267	0.377	0.311
	Ti	0.057	0.049	0.036	0.036	0.041	0.036	0.044	0.026	0.029	0.022	0.022	0.030	0.023	0.016	0.029	0.022	0.049	0.050	0.059	0.062	0.063	0.058
3	**Cr**	0.002	0.001	0.000	0.000	0.000	0.002	0.000	0.000	0.000	0.002	0.000	0.000	0.001	0.000	0.000	0.001	0.000	0.002	0.001	0.000	0.000	0.001
Octahedral	**Fe3+**	0.005	0.076	0.040	0.078	0.069	0.069	0.001	0.118	0.075	0.076	0.004	0.005	0.283	0.127	0.147	0.106	0.043	0.113	0.118	0.000	0.137	0.096
sites	**Mg**	2.567	2.422	2.422	2.452	2.419	2.444	2.433	2.476	2.418	2.416	2.398	2.390	2.482	2.461	2.512	2.339	2.335	2.338	2.344	2.279	2.340	2.335
	Fe Total	0.146	0.211	0.210	0.220	0.216	0.217	0.272	0.232	0.222	0.226	0.217	0.215	0.303	0.235	0.234	0.300	0.291	0.289	0.304	0.281	0.289	0.295
	Fe2+	0.140	0.135	0.171	0.142	0.146	0.148	0.271	0.115	0.147	0.150	0.213	0.210	0.020	0.108	0.087	0.193	0.248	0.176	0.186	0.281	0.153	0.199
	Mn	0.000	0.002	0.002	0.001	0.002	0.001	0.000	0.001	0.001	0.000	0.000	0.000	0.000	0.000	0.000	0.004	0.004	0.001	0.000	0.001	0.000	0.000
	Sum	3.000	3.000	3.000	3.000	3.000	3.000	3.000	3.000	3.000	3.000	3.000	3.000	3.000	3.000	3.000	3.000	3.000	3.000	3.000	3.000	3.000	3.000
	Ca	0.000	0.000	0.000	0.000	0.007	0.000	0.000	0.004	0.000	0.000	0.000	0.000	0.000	0.000	0.000	0.000	0.000	0.000	0.000	0.000	0.000	0.000
Interlayer	**Na**	0.017	0.056	0.062	0.052	0.049	0.053	0.054	0.052	0.076	0.065	0.043	0.061	0.058	0.053	0.059	0.055	0.061	0.056	0.059	0.053	0.058	0.055
sites	**K**	0.853	0.808	0.835	0.821	0.765	0.818	0.806	0.756	0.883	0.846	0.887	0.845	0.665	0.816	0.780	0.825	0.857	0.824	0.821	0.814	0.768	0.790
	Sum	0.869	0.864	0.897	0.873	0.821	0.871	0.859	0.812	0.959	0.912	0.929	0.906	0.723	0.869	0.839	0.880	0.918	0.880	0.880	0.867	0.826	0.844
	Total	7.869	7.864	7.897	7.873	7.821	7.871	7.859	7.812	7.959	7.912	7.929	7.906	7.723	7.869	7.839	7.880	7.918	7.880	7.880	7.867	7.826	7.844
	Variable ox	11.12	11.10	11.11	11.08	11.08	11.09	10.990	11.02	11.09	11.10	11.09	11.09	10.96	11.08	11.02	11.08	11.09	11.09	11.08	11.09	11.07	11.06
	Mg/(MFeTot)	0.946	0.919	0.920	0.917	0.917	0.918	0.899	0.914	0.916	0.914	0.917	0.917	0.891	0.913	0.915	0.885	0.888	0.890	0.885	0.890	0.890	0.888
	Mg/(MFe2O)	0.948	0.946	0.934	0.945	0.942	0.943	0.900	0.955	0.942	0.941	0.918	0.919	0.992	0.958	0.967	0.922	0.903	0.929	0.927	0.890	0.939	0.921
	Al/(Al+Si)	0.297	0.297	0.340	0.335	0.337	0.338	0.346	0.345	0.343	0.346	0.346	0.350	0.348	0.361	0.350	0.359	0.356	0.352	0.361	0.356	0.358	0.362
	K/(K+Na)	0.981	0.935	0.930	0.941	0.940	0.939	0.938	0.936	0.921	0.928	0.954	0.932	0.920	0.939	0.930	0.937	0.933	0.936	0.933	0.938	0.930	0.935

7.2.4 Talc

Talc is a Mg-rich, tri-octahedral sheet silicate, in which the layers typically are held together only by Van der Waals bonding, making it the softest of minerals. Possible parageneses are low-grade metamorphism and hydrothermal alteration of ultrabasic rocks, or contact and regional metamorphism of siliceous dolomite (Deer et al., 1992). It is also found in whiteschists, as described by Schreyer (1973, 1977). Talc was determined by the platy grain shape and bright interference colors, with thin section properties similar to muscovite. When abundant, it can be distinguished from muscovite by slippery behavior in hand specimen. Microphotographs can be seen in figure 7.7.

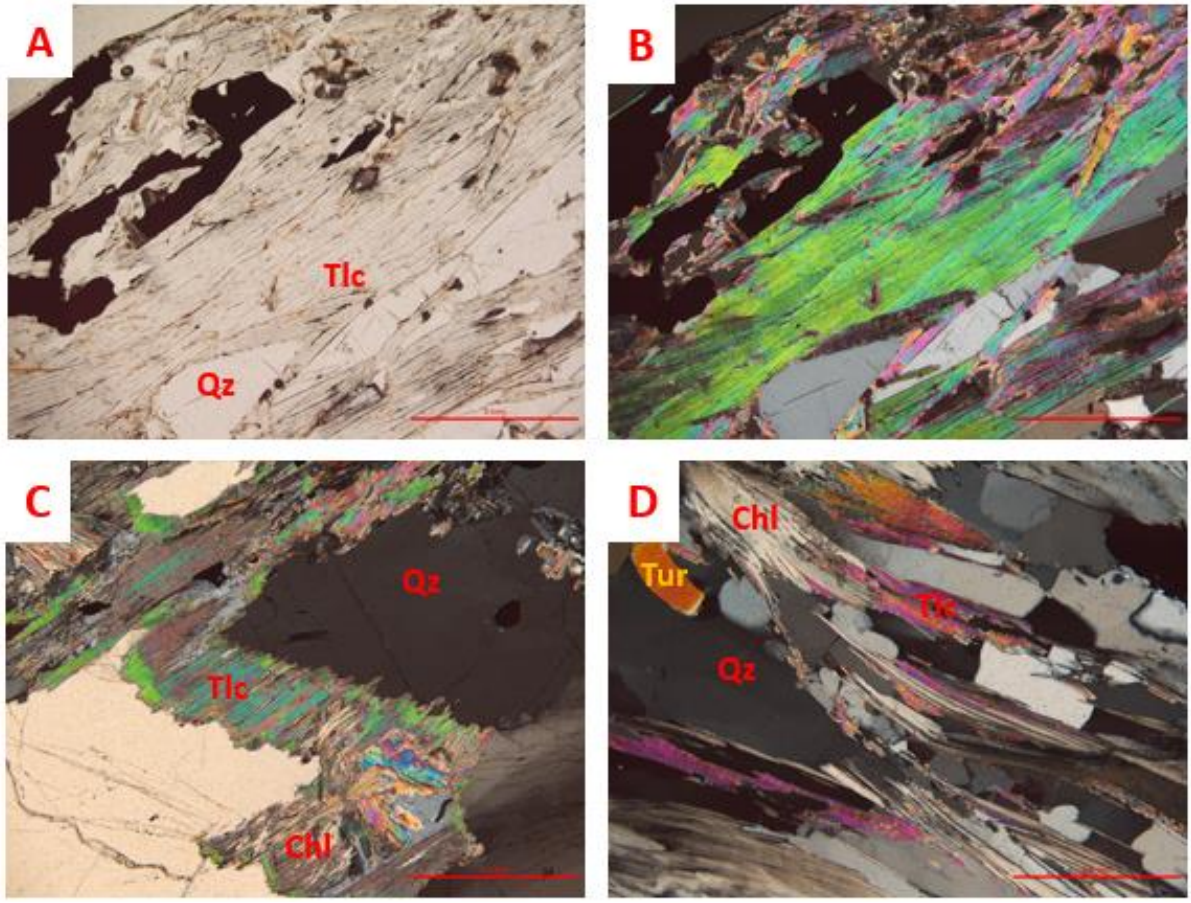

Figure 7.7: Photomicrographs of talc. A and B: Talc-phlogopite aggregate in MOD37 in ppl and xpl. Scalebar is 1 mm. C: Talc growing against quartz in MOD36. D: Talc partially altered to chlorite in MOD40. C and D: Scalebar is 0.5 mm.

Talc in MOD35 is fine-grained, commonly enclosing phlogopite, and overgrowing other minerals. The grains are colorless, elongated and radial, and showing bright green and pink interference colors. In MOD36, the talc is relict, having been replaced by chlorite in retrograde reaction with kyanite. In MOD37, MOD38 and MOD39, the talc is elongated and platy. In

MOD37, it occurs in clusters, making up the foliation together with phlogopite, while in MOD38, the talc is more fine-grained and commonly oriented at an angle to the foliation. In MOD39, talc is bimodal, present both as thin grains adjoining phlogopite, and as wider, partially altered grains. In MOD40, talc is almost impossible to separate from phlogopite, with radial texture and second order interference colors, but in this rock, talc has gone to chlorite in major proportion.

The formulation of talc (table 7.4a and 7.4b) show that there is a problem with Al. Formulae are calculated based on 7 cations and variable oxygen. Some analyses show negative Al formulations. This can be due to instrumental error, or errors in formulation of iron. The amounts of Fe^{2+} and Fe^{3+} influences the amount of Al that can fit in the different sites, and errors in these estimations can cause errors in estimations of how much Al there is in tetrahedral positions.

The EPMA-results show that the talc in MOD35, MOD36 and MOD40 is more aluminous than the talc in the other sections. The Al-content in MOD35 and MOD36 varies from 2 to 6 wt.%, in MOD 40 the content is around 3 wt.%, while MOD37, MOD38 and MOD39 contain only 0.5-1.9 wt.% Al. The FeO-content in MOD35, MOD37, MOD38 and MOD39 is generally low, X_{Mg}=0.99-1.00, while in MOD36 and MOD40 is slightly higher, up to 2 wt.%. No talc was found in MOD41.

According to Deer et al. (1963), talc usually doesn't display much variation in chemistry. Sometimes small amounts of Al or Ti can substitute for Si, and small amounts of Mn/Al and Fe^{2+}/Fe^{3+} can substitute for Mg. The talc usually shows a correlation between high Na and high Al-content (fig. 7.9). From figure 7.9 and 7.10, two groups of talc can be recognized, which can imply that the talc is derived from two different sources. MOD35, MOD36 and MOD40 show variable Al, and a correlation between elevated content of Na and Al. The NaAl-substitution in MOD35, MOD36 and MOD40, visible from the figures, are not a common thing, and can be tied to the different mineral assemblages in the rocks.

Table 7.4a. Talc Analyses and Structural Formulae

		35-1.2	35-1.11	35-2.6	35-3.7	35-4.6	35-5.3	35-5.4	35-6.9	*35-1-5*	36.1.2	36.1.8	36.2.3	36.2.6	36.2.8	36.3.6	36.4.3	36.4.6	*36-3-10*	*36-4-4*	37.2.5	37.3.4	37.3.8	37.3.9
	Wt.% Oxides																							
	SiO2	62.774	61.295	58.200	62.323	61.156	58.674	58.290	58.351	65.402	60.771	57.281	61.011	58.290	59.623	59.087	58.514	58.345	60.013	60.063	62.316	61.925	62.147	62.080
	TiO2	0.077	0.090	0.246	0.138	0.125	0.188	0.336	0.000	0.028	0.073	0.210	0.053	0.191	0.106	0.012	0.071	0.016	0.101	0	0.065	0.058	0.074	0.068
	Al2O3	2.175	4.322	6.916	3.001	3.156	4.994	5.911	4.292	3.078	3.557	5.538	2.937	4.729	3.187	4.417	3.796	6.195	5.757	4.361	1.240	1.227	1.064	1.138
	Cr2O3	0.035	0.073	0.005	0.000	0.021	0.000	0.017	0.000		0.000	0.002	0.054	0.000	0.000	0.005	0.000	0.000			0.004	0.000	0.000	0.000
	Fe2O3	0.307	0.665	0.549	0.052	0.394	0.258	0.354	0.360	0.151	1.564	1.716	0.148	1.814	0.764	1.392	1.691	0.279	0.352	2.263	0.210	0.565	0.313	0.043
	FeO Total	0.544	0.636	0.967	0.551	0.599	0.858	0.829	0.558	0.781	1.757	1.934	1.627	1.901	1.626	1.839	1.716	1.997	2.027	2.253	0.479	0.557	0.504	0.530
	FeO	0.268	0.037	0.473	0.504	0.245	0.626	0.510	0.234	0.645	0.350	0.390	1.494	0.269	0.939	0.586	0.195	1.746	1.710	0.217	0.290	0.049	0.223	0.492
	MnO	0.000	0.000	0.000	0.031	0.000	0.004	0.000	0.000	0	0.000	0.057	0.000	0.015	0.016	0.052	0.000	0.010	0	0.024	0.031	0.013	0.000	0.000
	MgO	32.348	29.438	30.390	31.875	32.059	30.746	30.316	30.209	31.685	30.922	29.353	31.223	30.013	30.490	30.410	30.173	26.484	28.547	30.687	31.969	31.755	32.616	32.623
	CaO	0.000	0.017	0.000	0.000	0.000	0.003	0.016	0.003	0.027	0.000	0.039	0.031	0.033	0.021	0.048	0.023	0.048	0	0.019	0.037	0.083	0.017	0.034
	Na2O	0.204	0.429	0.290	0.220	0.254	0.955	1.158	0.163	0.138	0.594	0.717	0.381	0.918	0.476	0.601	0.448	0.083	0.235	0.811	0.259	0.286	0.165	0.162
	K2O	0.162	0.047	2.729	0.320	0.635	0.237	0.204	0.188	0.046	0.029	0.315	0.054	0.008	0.053	0.089	0.028	0.975	0.703	0.05	0.000	0.099	0.049	0.018
	Total	98.319	96.347	99.743	98.459	98.005	96.659	97.077	93.764	101.19	97.703	95.446	97.371	96.098	95.598	96.560	94.769	94.153	97.383	98.268	96.400	96.003	96.636	96.653
	Rev. Total	98.350	96.414	99.798	98.464	98.044	96.685	97.112	93.800	101.20	97.860	95.618	97.386	96.280	95.675	96.699	94.938	94.181	97.418	98.495	96.421	96.060	96.667	96.657
7 Cats IV+VI	Si	3.851	3.868	3.617	3.828	3.779	3.692	3.663	3.751	3.915	3.779	3.666	3.798	3.698	3.785	3.719	3.742	3.824	3.781	3.726	3.898	3.897	3.867	3.861
	Al	0.149	0.132	0.383	0.172	0.221	0.308	0.337	0.249	0.085	0.221	0.334	0.202	0.302	0.215	0.281	0.258	0.176	0.219	0.274	0.102	0.103	0.133	0.139
4 T sites	Sum	4.000	4.000	4.000	4.000	4.000	4.000	4.000	4.000	4.000	4.000	4.000	4.000	4.000	4.000	4.000	4.000	4.000	4.000	4.000	4.000	4.000	4.000	4.000
	Total Al	0.157	0.321	0.507	0.217	0.230	0.370	0.438	0.325	0.217	0.261	0.418	0.215	0.354	0.238	0.328	0.286	0.479	0.427	0.319	0.091	0.091	0.078	0.083
	Al	0.009	0.190	0.123	0.045	0.009	0.062	0.100	0.076	0.132	0.039	0.083	0.013	0.051	0.023	0.047	0.028	0.302	0.208	0.045	-0.011	-0.012	-0.055	-0.055
	Ti	0.004	0.004	0.011	0.006	0.006	0.009	0.016	0.000	0.001	0.003	0.010	0.002	0.009	0.005	0.001	0.003	0.001	0.005	0.000	0.003	0.003	0.003	0.003
3	Cr	0.002	0.004	0.000	0.000	0.001	0.000	0.001	0.000	0.000	0.000	0.000	0.003	0.000	0.000	0.000	0.000	0.000	0.000	0.000	0.000	0.000	0.000	0.000
Octahedral	Fe3+	0.014	0.032	0.026	0.002	0.018	0.012	0.017	0.017	0.007	0.073	0.083	0.007	0.087	0.036	0.066	0.081	0.014	0.017	0.106	0.010	0.027	0.015	0.002
sites	Mg	2.958	2.769	2.815	2.918	2.953	2.884	2.839	2.894	2.827	2.866	2.800	2.897	2.838	2.885	2.853	2.876	2.587	2.680	2.837	2.981	2.979	3.025	3.024
	Fe Total	0.028	0.034	0.050	0.028	0.031	0.045	0.044	0.030	0.039	0.091	0.104	0.085	0.101	0.086	0.097	0.092	0.109	0.107	0.117	0.025	0.029	0.026	0.028
	Fe2+	0.014	0.002	0.025	0.026	0.013	0.033	0.027	0.013	0.032	0.018	0.021	0.078	0.014	0.050	0.031	0.010	0.096	0.090	0.011	0.015	0.003	0.012	0.026
	Mn	0.000	0.000	0.000	0.002	0.000	0.000	0.000	0.000	0.000	0.000	0.003	0.000	0.001	0.001	0.003	0.000	0.001	0.000	0.001	0.002	0.001	0.000	0.000
	Sum	3.000	3.000	3.000	3.000	3.000	3.000	3.000	3.000	3.000	3.000	3.000	3.000	3.000	3.000	3.000	3.000	3.000	3.000	3.000	3.000	3.000	3.000	3.000
	Ca	0.000	0.001	0.000	0.000	0.000	0.000	0.001	0.000	0.002	0.000	0.003	0.002	0.002	0.001	0.003	0.002	0.003	0.000	0.001	0.002	0.006	0.001	0.002
Interlayer	Na	0.024	0.052	0.035	0.026	0.030	0.117	0.141	0.020	0.016	0.072	0.089	0.046	0.113	0.059	0.073	0.056	0.011	0.029	0.098	0.031	0.035	0.020	0.020
sites	K	0.013	0.004	0.216	0.025	0.050	0.019	0.016	0.015	0.004	0.002	0.026	0.004	0.001	0.004	0.007	0.002	0.082	0.056	0.004	0.000	0.008	0.004	0.001
	Sum	0.037	0.057	0.251	0.051	0.080	0.136	0.159	0.036	0.021	0.074	0.117	0.052	0.116	0.064	0.084	0.059	0.095	0.085	0.103	0.034	0.048	0.025	0.023
	Total	7.037	7.057	7.251	7.051	7.080	7.136	7.159	7.036	7.021	7.074	7.117	7.052	7.116	7.064	7.084	7.059	7.095	7.085	7.103	7.034	7.048	7.025	7.023
	Variable ox	10.96	11.08	11.02	10.97	10.95	10.96	10.986	10.94	11.04	10.986	10.986	10.94	10.986	10.96	10.96	10.96	11.12	11.05	10.99	10.97	10.986	10.93	10.92
	Mg/(MFeTot)	0.991	0.988	0.982	0.990	0.990	0.985	0.985	0.990	0.986	0.969	0.963	0.972	0.965	0.971	0.966	0.969	0.959	0.962	0.960	0.991	0.990	0.991	0.991
	Al/(Al+Si)	0.039	0.077	0.123	0.054	0.057	0.091	0.107	0.080	0.053	0.065	0.102	0.054	0.087	0.059	0.081	0.071	0.111	0.102	0.079	0.023	0.023	0.020	0.021
	Na+K	0.037	0.056	0.251	0.051	0.080	0.136	0.157	0.036	0.020	0.074	0.115	0.050	0.114	0.063	0.080	0.058	0.092	0.085	0.101	0.031	0.043	0.024	0.021

Table 7.4b. Talc Analyses and Structural Formulae

		37.3.11	37.4.10	37.7.3	37.9.3	37.9.4	37.9.6	*37.2.5*	38.1.7	38.2.6	39.1.7	39.4.3	39.4.4	39.5.8	39-1.5	39-1.7	39-1.8	39-3.6	39-2.4	40.3.8	40.4.1	40.4.3	*40-3-9*
	Wt.% Oxides																						
	SiO2	58.049	57.546	62.959	61.717	62.152	62.438	65.587	61.835	59.677	61.986	62.887	62.347	59.610	61.994	63.223	59.971	58.338	61.753	60.190	60.367	60.008	60.312
	TiO2	0.011	0.048	0.083	0.074	0.052	0.014	0.095	0.000	0.021	0.074	0.093	0.074	0.101	0.034	0.037	0.000	0.073	0.110	0.060	0.067	0.018	0.103
	Al2O3	1.005	1.236	1.195	1.191	0.639	0.513	1.4	1.127	1.309	1.205	0.981	1.235	1.339	1.309	1.367	1.284	1.159	1.115	3.149	2.796	2.862	2.468
	Cr2O3	0.000	0.016	0.000	0.000	0.002	0.005		0.011	0.011	0.002	0.000	0.000	0.011	0.058	0.056	0.000	0.004	0.000	0.000	0.000	0.000	
	Fe2O3	0.766	0.206	0.556	0.587	0.275	0.020	0.329	0.348	0.115	0.067	0.168	0.341	0.541	0.271	0.314	0.388	0.447	0.390	1.517	1.480	1.341	1.360
	FeO Total	0.692	0.490	0.669	0.568	0.554	0.568	0.523	0.514	0.626	0.836	0.498	0.473	0.505	0.474	0.405	0.496	0.431	0.516	1.381	1.342	1.304	1.596
	FeO	0.002	0.305	0.169	0.040	0.306	0.550	0.227	0.201	0.522	0.776	0.347	0.166	0.018	0.230	0.122	0.147	0.029	0.165	0.016	0.010	0.097	0.372
	MnO	0.025	0.000	0.012	0.000	0.000	0.000	0.027	0.000	0.005	0.020	0.020	0.000	0.000	0.024	0.004	0.000	0.015	0.000	0.007	0.000	0.000	0
	MgO	29.199	29.369	32.653	32.291	32.653	32.386	32.934	32.113	31.390	32.099	32.358	32.227	29.424	30.256	30.951	29.137	29.683	31.115	30.863	30.729	30.487	31.928
	CaO	0.209	0.145	0.006	0.027	0.002	0.022	0.044	0.077	0.085	0.054	0.019	0.028	0.245	0.046	0.116	0.234	0.131	0.044	0.037	0.017	0.000	0.025
	Na2O	0.140	0.229	0.184	0.199	0.089	0.136	0.292	0.115	0.172	0.187	0.166	0.242	0.217	0.336	0.289	0.238	0.224	0.131	0.555	0.371	0.377	0.426
	K2O	0.098	0.022	0.035	0.000	0.006	0.022	0.008	0.111	0.037	0.057	0.031	0.000	0.101	0.000	0.000	0.057	0.065	0.031	0.046	0.000	0.027	0.077
	Total	89.428	89.101	97.796	96.067	96.149	96.104	100.91	95.903	93.333	96.520	97.053	96.626	91.553	94.531	96.448	91.417	90.123	94.815	96.288	95.689	95.083	96.935
	Rev. Total	89.505	89.122	97.852	96.126	96.177	96.106	100.943	95.938	93.345	96.527	97.070	96.660	91.607	94.558	96.479	91.456	90.168	94.854	96.440	95.837	95.217	97.071
7 Cats IV+VI	Si	3.931	3.902	3.877	3.865	3.882	3.909	3.929	3.883	3.848	3.873	3.903	3.887	3.953	3.977	3.973	3.986	3.912	3.931	3.792	3.819	3.821	3.762
	Al	0.069	0.098	0.123	0.135	0.118	0.091	0.071	0.117	0.152	0.127	0.097	0.113	0.047	0.023	0.027	0.014	0.088	0.069	0.208	0.181	0.179	0.238
4 T sites	Sum	4.000	4.000	4.000	4.000	4.000	4.000	4.000	4.000	4.000	4.000	4.000	4.000	4.000	4.000	4.000	4.000	4.000	4.000	4.000	4.000	4.000	4.000
	Total Al	0.080	0.099	0.087	0.088	0.047	0.038	0.099	0.083	0.099	0.089	0.072	0.091	0.105	0.099	0.101	0.101	0.092	0.084	0.234	0.208	0.215	0.181
	Al	0.011	0.001	-0.036	-0.047	-0.071	-0.053	0.028	-0.033	-0.052	-0.038	-0.025	-0.023	0.058	0.076	0.075	0.086	0.004	0.015	0.026	0.028	0.036	-0.057
	Ti	0.001	0.002	0.004	0.003	0.002	0.001	0.004	0.000	0.001	0.003	0.004	0.003	0.005	0.002	0.002	0.000	0.004	0.005	0.003	0.003	0.001	0.005
3	Cr	0.000	0.001	0.000	0.000	0.000	0.000	0.000	0.001	0.001	0.000	0.000	0.000	0.001	0.003	0.003	0.000	0.000	0.000	0.000	0.000	0.000	0.000
Octahedral	Fe3+	0.039	0.011	0.026	0.028	0.013	0.001	0.015	0.016	0.006	0.003	0.008	0.016	0.027	0.013	0.015	0.019	0.023	0.019	0.072	0.070	0.064	0.064
sites	Mg	2.947	2.968	2.997	3.014	3.040	3.022	2.941	3.006	3.017	2.990	2.994	2.994	2.909	2.893	2.899	2.886	2.967	2.952	2.898	2.898	2.894	2.968
	Fe Total	0.039	0.028	0.034	0.030	0.029	0.030	0.026	0.027	0.034	0.044	0.026	0.025	0.028	0.025	0.021	0.028	0.024	0.027	0.073	0.071	0.069	0.083
	Fe2+	0.000	0.017	0.009	0.002	0.016	0.029	0.011	0.011	0.028	0.041	0.018	0.009	0.001	0.012	0.006	0.008	0.002	0.009	0.001	0.001	0.005	0.019
	Mn	0.001	0.000	0.001	0.000	0.000	0.000	0.001	0.000	0.000	0.001	0.001	0.000	0.000	0.001	0.000	0.000	0.001	0.000	0.000	0.000	0.000	0.000
	Sum	3.000	3.000	3.000	3.000	3.000	3.000	3.000	3.000	3.000	3.000	3.000	3.000	3.000	3.000	3.000	3.000	3.000	3.000	3.000	3.000	3.000	3.000
	Ca	0.015	0.011	0.000	0.002	0.000	0.001	0.003	0.005	0.006	0.004	0.001	0.002	0.017	0.003	0.008	0.017	0.009	0.003	0.002	0.001	0.000	0.002
Interlayer	Na	0.018	0.030	0.022	0.024	0.011	0.017	0.034	0.014	0.022	0.023	0.020	0.029	0.028	0.042	0.035	0.031	0.029	0.016	0.068	0.046	0.047	0.052
sites	K	0.008	0.002	0.003	0.000	0.000	0.002	0.001	0.009	0.003	0.005	0.002	0.000	0.009	0.000	0.000	0.005	0.006	0.003	0.004	0.000	0.002	0.006
	Sum	0.042	0.043	0.025	0.026	0.011	0.020	0.037	0.028	0.030	0.031	0.024	0.031	0.054	0.045	0.043	0.052	0.044	0.022	0.074	0.047	0.049	0.059
	Total	7.042	7.043	7.025	7.026	7.011	7.020	7.037	7.028	7.030	7.031	7.024	7.031	7.054	7.045	7.043	7.052	7.044	7.022	7.074	7.047	7.049	7.059
	Variable ox	11.02	10.986	10.95	10.94	10.92	10.94	11.01	10.95	10.92	10.94	10.96	10.96	11.06	11.06	11.06	11.08	11	11	10.986	10.986	10.986	10.92
	Mg/(MFeTot)	0.986	0.991	0.988	0.990	0.991	0.990	0.991	0.991	0.989	0.985	0.991	0.992	0.990	0.991	0.993	0.991	0.992	0.991	0.975	0.976	0.977	0.973
	Al/(Al+Si)	0.020	0.025	0.022	0.022	0.012	0.010	0.025	0.021	0.025	0.022	0.018	0.023	0.026	0.024	0.025	0.025	0.023	0.021	0.058	0.052	0.053	0.046
	Na+K	0.027	0.032	0.025	0.024	0.011	0.018	0.035	0.023	0.025	0.027	0.022	0.029	0.036	0.042	0.035	0.035	0.035	0.019	0.071	0.046	0.049	0.058

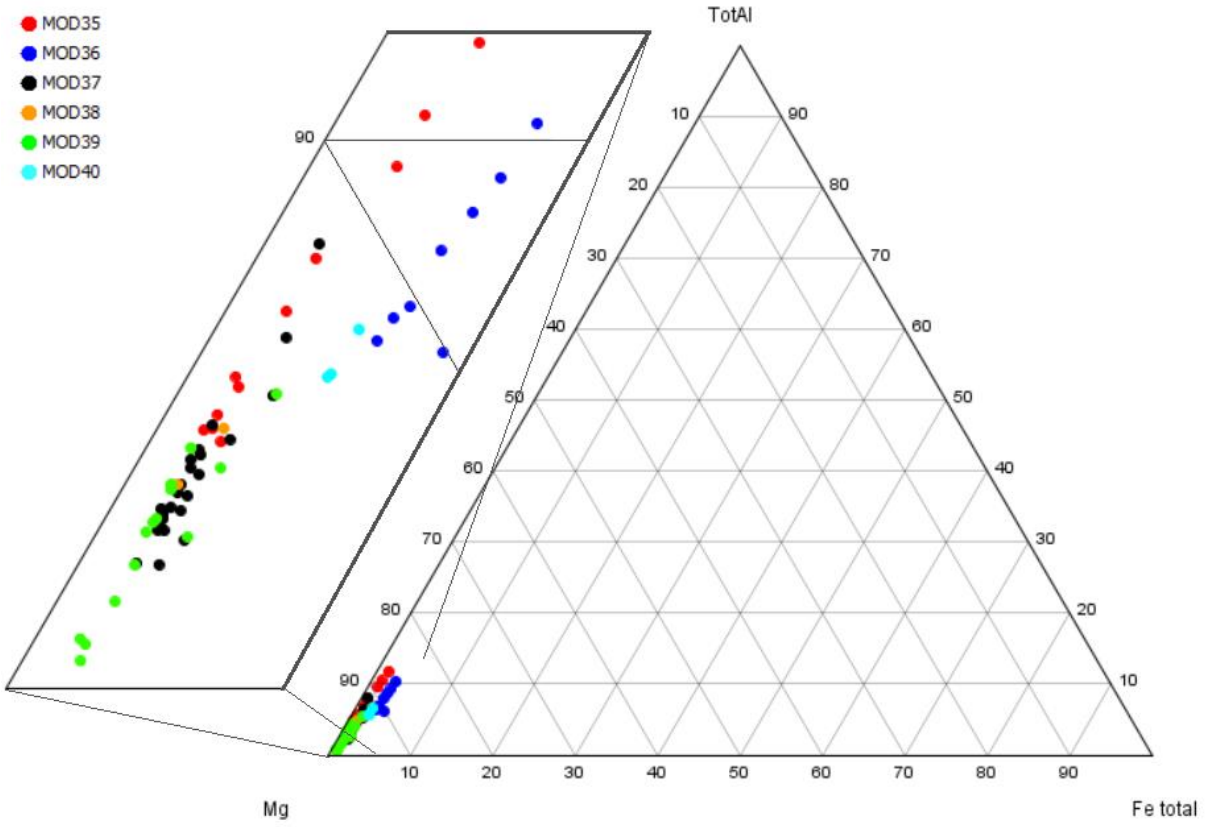

Figure 7.8: Ternary talc diagram of the compositional differences in the various sections.

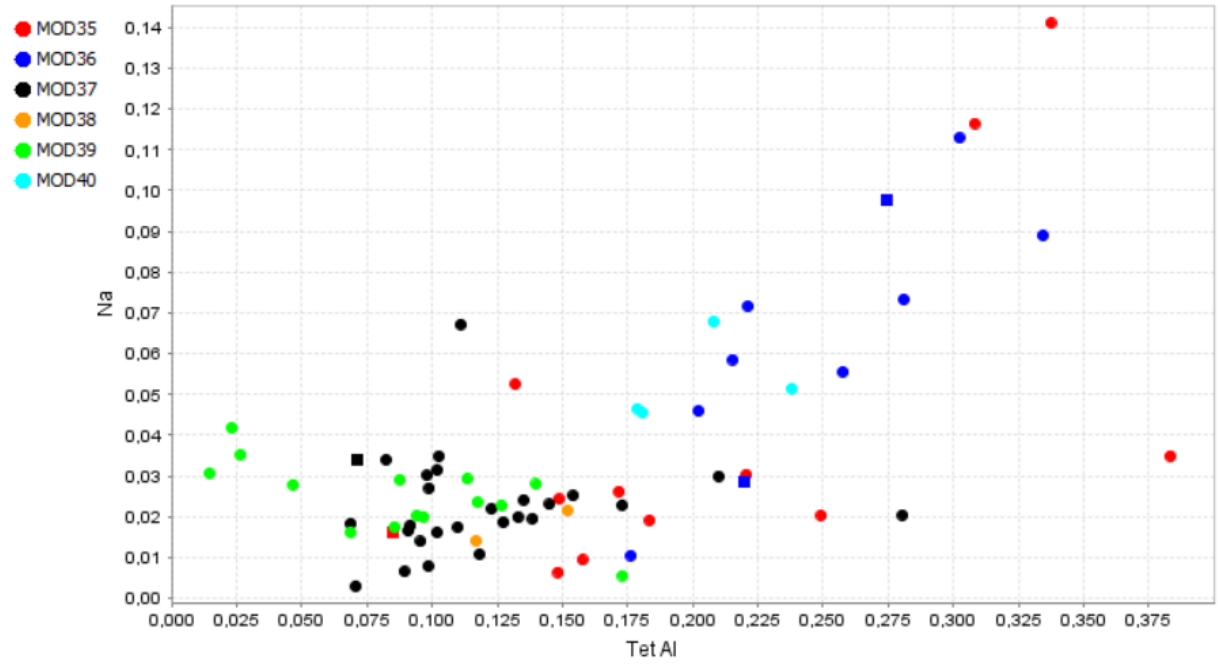

Figure 7.9: Plot of Na in A site versus Al for talc. Na and Al are based on content of Na in A site and Al in tetrahedral position from the general structural formulae.

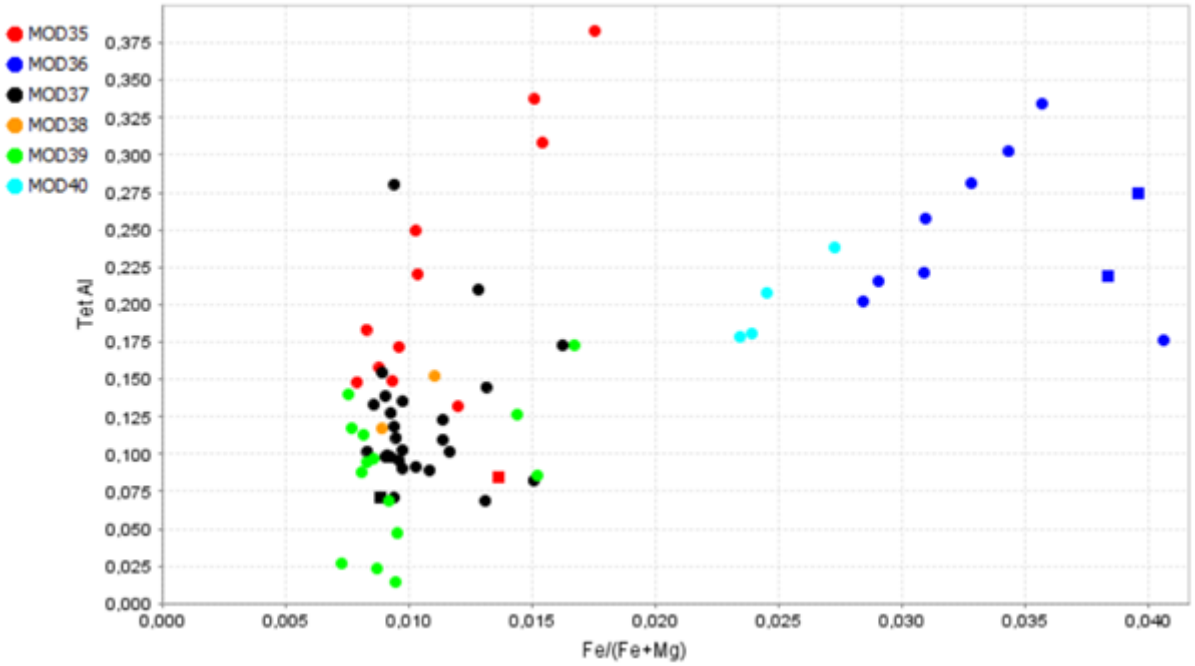

Figure 7.10: Fe/(Fe+Mg) plotted versus Al for talc. Al is based on content of Al in tetrahedral position from the general structural formula.

7.2.5 Amphibole

Normal hornblende is usually identified by its strong, green or brownish green pleochroism. However, like phlogopite, here the amphiboles are almost colorless. It was therefore identified by interference colors and cleavages. Some grains were difficult to tell apart from phlogopite. Microphotographs can be seen in figure 7.11.

Amphibole in MOD37 is colorless, showing second order interference colors and is equigranular. Grains showing two cleavages are rounded, while the rest are elongated. Amphibole grains are usually present in clusters of 2-5 grains. Amphibole in MOD38 is coarser, elongated and shows lower interference colors and most abundant in this section. It is more scarce in MOD39, and the grains are finer grained. Here, the grains are more subhedral and display no cleavage. In great contrast, HJ003 contains 65% amphibole which is green and pleochroic and shows low second order interference colors.

The EPMA on MOD37, MOD38 and MOD39 show large variation in total Al, from 0.46 to 1.03, with the highest values in MOD38. Formulae are calculated based on 16 cations and 23 oxygen (table 7.5a-b). The Ca in M4-site varies in all these sections, from 1.59 to 1.89. The Mg-content is high, ranging from 4.24 to 4.77. HJ003 contains more NaO, FeO and Al_2O_3, up to 2.13 total Fe in the formula and 2.70 total Al. In addition, this amphibole contains up to 1.1

wt.% Cl. The Mg-content is lower in HJ003 than in MOD37-MOD39, and even though HJ003 also contain calcic amphibole, the Ca in M4-site is below 1.63.

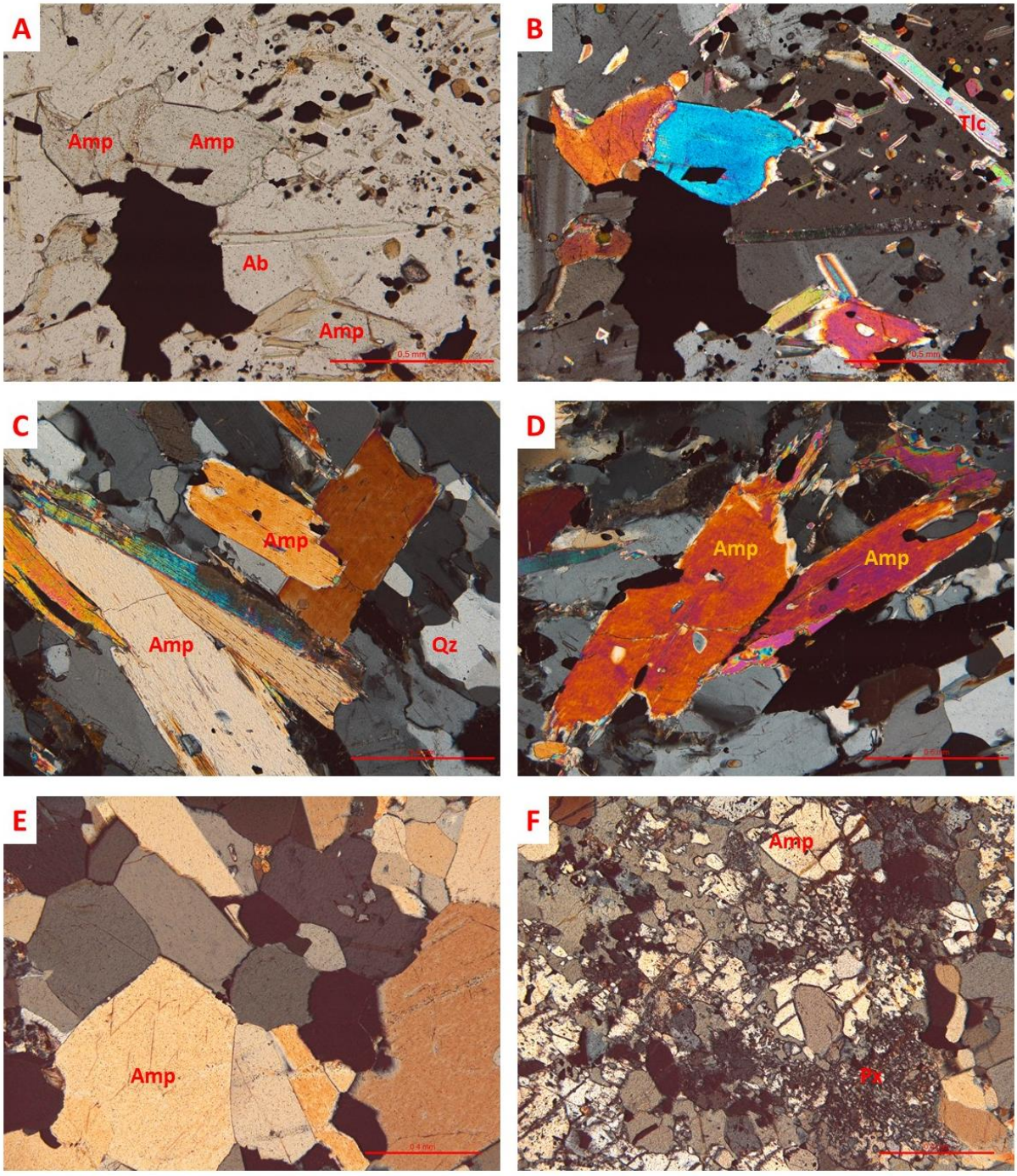

Figure 7.11: Photomicrographs of amphibole. A and B: Amphibole in ppl and xpl in MOD37. C and D: Amphibole in xpl in MOD38. E and F: Amphibole with granoblastic texture and replacing pyroxene in HJ003. A-D: Scalebar is 0.5 mm. E-F: Scalebar is 0.4 mm.

For MOD37-MOD39, the general formula is

$$Na_{0.16\text{-}0.25}(Na_{0.08\text{-}0.29}Ca_{1.58\text{-}1.74}Mg_{0.01\text{-}0.16}Fe^{2+}{}_{0\text{-}0.12})(Mg_{4.27\text{-}4.62}Fe^{3+}{}_{0.22\text{-}0.48}Al_{0.13\text{-}0.29})$$
$$(Si_{7.27\text{-}7.57}Al_{0.43\text{-}0.73}O_{22})(OH)_2$$

showing that this is a Mg-rich calcic amphibole close to tremolite (fig. 7.12), but with NaAl-substitution, bringing many analyses a short distance into the field described as magnesiohornblende. A similar plot for HJ003, with higher content of Na and K, would plot HJ003 in the field of pargasite. Figure 7.13-7.14 shows that the amphibole in HJ003 comes from a different source, plotting much closer to ideal hornblende (Robinson et al., 1969).

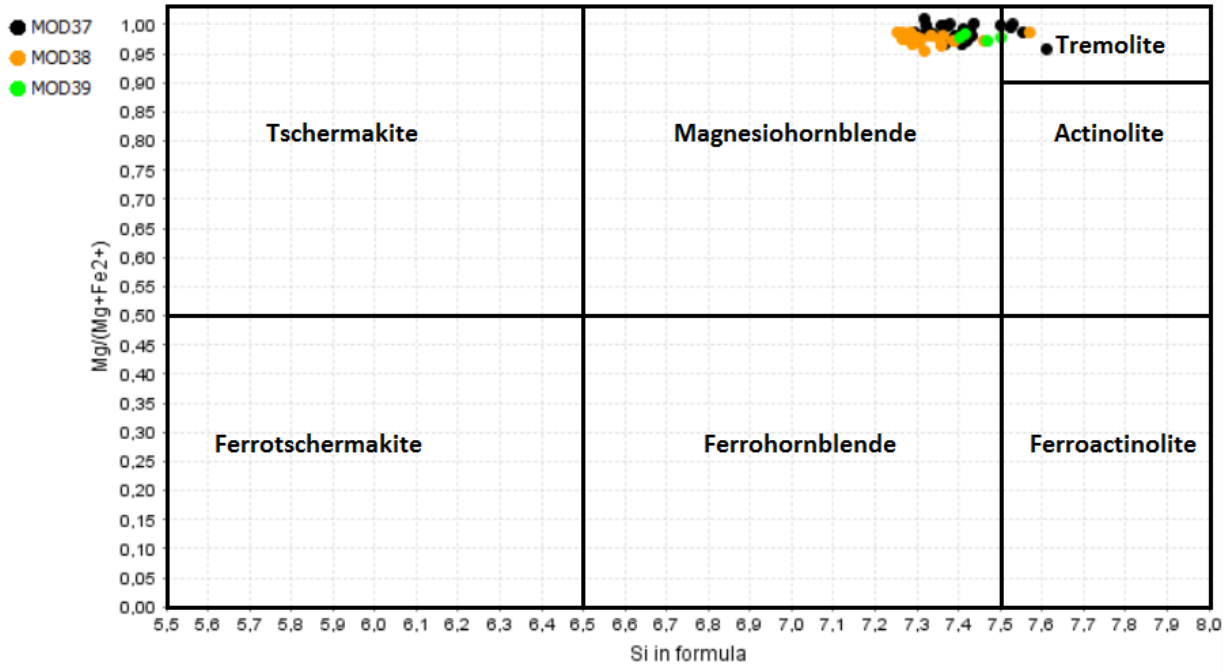

Figure 7.12: Classification diagram for amphibole based on Leake et al (1978). The diagram parameters are Ca_B > 1.50; $(Na+K)_A$ < 0.50. This does not fit for HJ003, where $(Na+K)_A$ > 0.50.

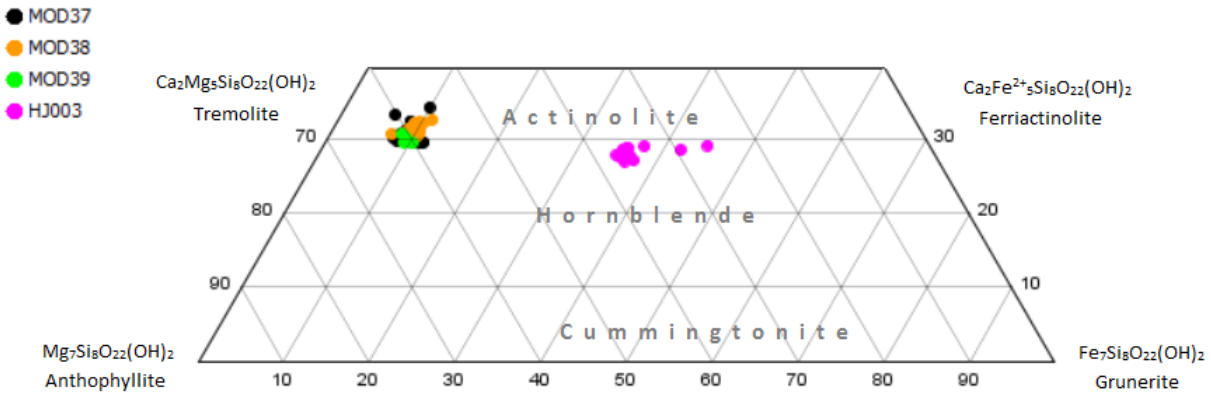

Figure 7.13: Amphibole quadrilateral showing the compositional differences compared to standard amphiboles. Figure based on quadrilateral from Putnis (1992).

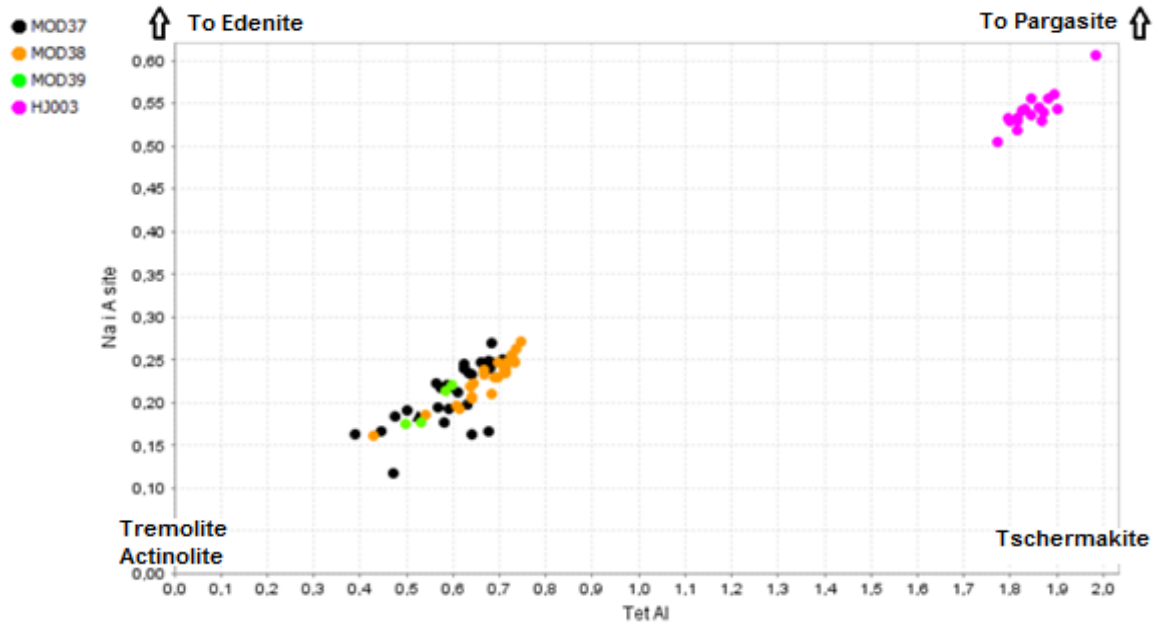

Figure 7.14: Tetrahedral Al plotted versus Na in A site for amphiboles.

Table 7.5a. Amphibole Analyses and Structural Formulae

		37.1.1	37.1.6	37.1.8	37.2.1	37.2.3	37.2.4	37.2.7	37.3.1	37.7.6
	SiO2	55.445	53.799	54.292	53.142	55.37	54.194	53.046	52.832	54.302
	TiO2	0.221	0.236	0.265	0.234	0.175	0.188	0.207	0.195	0.229
	Al2O3	4.005	5.344	5.008	5.397	3.674	4.915	5.46	5.574	4.439
	Cr2O3	0	0	0	0.013	0	0.013	0.017	0.039	0
	Fe2O3	3.410	4.643	3.120	3.457	2.553	2.217	3.358	3.564	3.110
	FeO Total	3.075	4.241	3.744	3.748	2.848	3.432	3.697	3.683	3.182
	FeO	0.006	0.063	0.937	0.638	0.551	1.437	0.675	0.476	0.383
	MnO	0.003	0.012	0.009	0.012	0.031	0.029	0.001	0.01	0
	MgO	22.864	21.546	22.109	21.956	23.098	22.394	22.035	21.845	22.903
	CaO	11.026	10.84	10.831	11.255	11.187	11.86	10.948	11.269	11.147
	Na2O	1.303	1.693	1.739	1.61	1.3	1.045	1.601	1.627	1.445
	K2O	0.084	0.107	0.067	0.116	0.08	0.091	0.127	0.148	0.065
	Total	98.026	97.818	98.064	97.483	97.763	98.161	97.139	97.222	97.712
	Rev. Total	98.368	98.283	98.377	97.829	98.019	98.383	97.475	97.579	98.024
Varied cation sum formula	Si	7.529	7.359	7.414	7.316	7.554	7.408	7.322	7.294	7.428
	Al	0.471	0.641	0.586	0.684	0.446	0.592	0.678	0.706	0.572
	Sum	8.000	8.000	8.000	8.000	8.000	8.000	8.000	8.000	8.000
	Total Al	0.641	0.862	0.806	0.876	0.591	0.792	0.888	0.907	0.716
M1-2-3 sites	Al	0.170	0.221	0.220	0.192	0.145	0.200	0.210	0.201	0.143
	Ti	0.023	0.024	0.027	0.024	0.018	0.019	0.021	0.020	0.024
	Cr	0.000	0.000	0.000	0.001	0.000	0.001	0.002	0.004	0.000
	Fe3+	0.349	0.478	0.321	0.358	0.262	0.228	0.349	0.370	0.320
	Mg	4.459	4.277	4.433	4.424	4.575	4.551	4.418	4.404	4.513
	Sum	5.000	5.000	5.000	5.000	5.000	5.000	5.000	5.000	5.000
	(MgTotal)	4.628	4.393	4.500	4.506	4.697	4.563	4.533	4.495	4.669
	(Fe Total)	0.349	0.485	0.428	0.432	0.325	0.392	0.427	0.425	0.364
M4 site	Mg	0.169	0.116	0.067	0.082	0.121	0.011	0.115	0.091	0.156
	Fe2+	0.001	0.007	0.107	0.073	0.063	0.164	0.078	0.055	0.044
	Mn	0.000	0.001	0.001	0.001	0.004	0.003	0.000	0.001	0.000
	Ca	1.604	1.589	1.585	1.660	1.635	1.737	1.619	1.667	1.634
	Na	0.225	0.287	0.240	0.183	0.177	0.084	0.188	0.186	0.166
	Sum	2.000	2.000	2.000	2.000	2.000	2.000	2.000	2.000	2.000
	NaTotal	0.343	0.449	0.460	0.430	0.344	0.277	0.428	0.436	0.383
A site	Na	0.118	0.162	0.220	0.246	0.167	0.193	0.241	0.250	0.217
	K Total	0.015	0.019	0.012	0.020	0.014	0.016	0.022	0.026	0.011
	Sum	0.132	0.181	0.232	0.267	0.181	0.209	0.263	0.276	0.228
	Total cat	15.132	15.181	15.232	15.267	15.181	15.209	15.263	15.276	15.229
	Mg/(Mg+Fetot	0.930	0.901	0.913	0.913	0.935	0.921	0.914	0.914	0.928
	Mg/(Mg+Fe2O	1.000	0.998	0.977	0.984	0.987	0.965	0.983	0.988	0.991
	Ca/(Ca+Na+K)	0.818	0.773	0.770	0.787	0.820	0.856	0.782	0.783	0.805

Table 7.5b. Amphibole Analyses and Structural Formulae																				
		37.7.8	**37.8.2**	***37.1.9***	**38.2.3**	**38.2.5**	**38.4.1**	**38.4.2**	**38.4.3**	**38.4.4**	**38.4.10**	**38.5.2**	**38.5.3**	**38.5.5**	**38.7.6**	**39.2.1**	**39.2.6**	**39.5.2**	**39.6.5**	**003-1.1**
	SiO2	53.185	54.345	56.758	53.593	54.034	53.099	54.439	53.998	53.737	53.381	54.393	55.68	52.804	53.138	53.279	53.761	54.622	54.574	42.395
	TiO2	0.268	0.24	0.227	0.192	0.13	0.19	0.156	0.158	0.19	0.153	0.194	0.07	0.102	0.187	0.202	0.199	0.166	0.21	1.238
	Al2O3	5.276	4.757	4.996	5.58	5.306	5.743	4.763	5.567	5.689	6.33	5.351	3.474	5.92	6.177	4.943	4.642	4.329	4.781	14.137
	Cr2O3	0	0.016		0	0	0	0	0.03	0.011	0.024	0	0.007	0.01	0	0.005	0.012	0	0.033	0.03
	Fe2O3	3.382	3.103	2.616	3.307	2.449	3.092	2.351	2.452	3.065	3.279	2.496	2.355	3.091	3.230	3.148	2.385	2.434	3.123	5.059
	FeO Total	3.504	3.116	3.376	3.719	3.292	3.341	3.211	3.574	3.56	3.65	3.382	2.728	3.815	3.84	3.727	3.29	3.108	3.449	12.464
	FeO	0.460	0.324	1.022	0.743	1.088	0.559	1.095	1.368	0.802	0.700	1.136	0.609	1.033	0.934	0.894	1.144	0.918	0.639	7.912
	MnO	0	0.031	0.017	0.035	0.016	0	0.023	0	0.039	0	0.038	0.007	0.04	0.005	0.03	0.027	0	0.03	0.262
	MgO	22.349	22.8	22.865	21.854	22.141	22.379	22.279	22.329	22.029	21.818	22.478	23.43	21.661	21.664	21.842	21.945	22.38	22.724	13.27
	CaO	11.01	11.105	11.592	11.26	11.67	11.47	11.367	11.325	11.323	11.277	11.372	11.539	12.016	11.381	10.655	10.933	11.258	11.007	9.924
	Na2O	1.584	1.521	1.619	1.677	1.257	1.386	1.316	1.269	1.579	1.71	1.282	1.085	1.317	1.655	1.641	1.363	1.344	1.545	2.758
	K2O	0.082	0.089	0.095	0.11	0.127	0.095	0.076	0.115	0.108	0.129	0.165	0.055	0.124	0.088	0.097	0.123	0.092	0.102	0.416
	Total	97.258	98.02	101.545	98.02	97.973	97.703	97.63	98.365	98.265	98.472	98.655	98.075	97.809	98.135	96.421	96.295	97.299	98.455	96.894
	Rev. Total	97.597	98.331	101.807	98.351	98.218	98.013	97.866	98.611	98.572	98.801	98.905	98.311	98.119	98.459	96.736	96.534	97.543	98.768	97.401
Varied	**Si**	7.325	7.410	7.475	7.335	7.391	7.285	7.460	7.360	7.332	7.272	7.386	7.571	7.266	7.273	7.402	7.470	7.503	7.416	6.188
cation sum	**Al**	0.675	0.590	0.525	0.665	0.609	0.715	0.540	0.640	0.668	0.728	0.614	0.429	0.734	0.727	0.598	0.530	0.497	0.584	1.812
formula	**Sum**	8.000	8.000	8.000	8.000	8.000	8.000	8.000	8.000	8.000	8.000	8.000	8.000	8.000	8.000	8.000	8.000	8.000	8.000	8.000
	Total Al	0.856	0.764	0.775	0.900	0.855	0.929	0.769	0.894	0.915	1.016	0.856	0.557	0.960	0.996	0.809	0.760	0.701	0.766	
M1-2-3 sites	**Al**	0.181	0.174	0.250	0.235	0.247	0.214	0.230	0.254	0.247	0.288	0.243	0.127	0.226	0.269	0.211	0.230	0.204	0.181	0.619
	Ti	0.028	0.025	0.022	0.020	0.013	0.020	0.016	0.016	0.019	0.016	0.020	0.007	0.011	0.019	0.021	0.021	0.017	0.021	0.136
	Cr	0.000	0.002	0.000	0.000	0.000	0.000	0.000	0.003	0.001	0.003	0.000	0.001	0.001	0.000	0.001	0.001	0.000	0.004	0.004
	Fe3+	0.351	0.318	0.259	0.341	0.252	0.319	0.242	0.251	0.315	0.336	0.255	0.241	0.320	0.333	0.329	0.249	0.252	0.319	0.566
	Mg	4.440	4.481	4.468	4.405	4.488	4.448	4.512	4.475	4.417	4.358	4.482	4.624	4.442	4.379	4.438	4.499	4.528	4.474	2.887
	Sum	5.000	5.000	5.000	5.000	5.000	5.000	5.000	5.000	5.000	5.000	5.000	5.000	5.000	5.000	5.000	5.000	5.000	5.000	5.000
	(MgTotal)	4.588	4.633	4.488	4.458	4.514	4.576	4.551	4.536	4.480	4.430	4.550	4.748	4.443	4.419	4.523	4.545	4.582	4.602	
	(Fe Total)	0.404	0.355	0.372	0.426	0.377	0.383	0.368	0.407	0.406	0.416	0.384	0.310	0.439	0.440	0.433	0.382	0.357	0.392	1.540
M4 site	**Mg**	0.147	0.152	0.020	0.053	0.027	0.129	0.039	0.062	0.063	0.072	0.067	0.124	0.001	0.040	0.085	0.046	0.054	0.128	
	Fe2+	0.053	0.037	0.113	0.085	0.124	0.064	0.126	0.156	0.091	0.080	0.129	0.069	0.119	0.107	0.104	0.133	0.105	0.073	0.164
	Mn	0.000	0.004	0.002	0.004	0.002	0.000	0.003	0.000	0.005	0.000	0.004	0.001	0.005	0.001	0.004	0.003	0.000	0.003	0.032
	Ca	1.625	1.622	1.636	1.651	1.710	1.686	1.669	1.654	1.655	1.646	1.655	1.681	1.772	1.669	1.586	1.628	1.657	1.602	1.552
	Na	0.175	0.185	0.229	0.207	0.136	0.121	0.164	0.128	0.186	0.202	0.145	0.125	0.104	0.184	0.222	0.190	0.183	0.194	0.252
	Sum	2.000	2.000	2.000	2.000	2.000	2.000	2.000	2.000	2.000	2.000	2.000	2.000	2.000	2.000	2.000	2.000	2.000	2.000	2.000
	NaTotal	0.423	0.402	0.413	0.445	0.333	0.369	0.350	0.335	0.418	0.452	0.338	0.286	0.351	0.439	0.442	0.367	0.358	0.407	
A site	**Na**	0.248	0.217	0.184	0.238	0.197	0.248	0.186	0.207	0.232	0.250	0.193	0.161	0.247	0.256	0.220	0.177	0.175	0.213	0.529
	K Total	0.014	0.015	0.016	0.019	0.022	0.017	0.013	0.020	0.019	0.022	0.029	0.010	0.022	0.015	0.017	0.022	0.016	0.018	0.077
	Sum	0.263	0.232	0.200	0.257	0.219	0.264	0.199	0.227	0.251	0.272	0.221	0.171	0.269	0.271	0.237	0.199	0.191	0.231	0.606
	Total cat	15.263	15.232	15.200	15.258	15.252	15.264	15.199	15.227	15.251	15.272	15.221	15.171	15.269	15.271	15.237	15.199	15.191	15.231	15.606
	Mg/(Mg+Fet)	0.919	0.929	0.923	0.913	0.923	0.923	0.925	0.918	0.917	0.914	0.922	0.939	0.910	0.910	0.913	0.922	0.928	0.922	0.652
	Mg/(Mg+Fe2O	0.989	0.992	0.976	0.981	0.973	0.986	0.973	0.967	0.980	0.982	0.972	0.986	0.974	0.976	0.978	0.972	0.977	0.984	0.946
	Ca/(Ca+Na+K)	0.788	0.795	0.792	0.781	0.828	0.814	0.821	0.823	0.791	0.776	0.819	0.850	0.826	0.786	0.775	0.807	0.816	0.790	0.719

7.2.6 Chlorite

Chlorite was identified by low interference color and grain shape, or as an alteration texture in phlogopite (fig. 7.15). No pure chlorite was found in MOD37, MOD38 and MOD39. In MOD36 and MOD41, chlorite is only found as an apparent alteration of phlogopite. The chlorite in MOD36 occurs in clusters together with sillimanite, talc, and feldspar. In MOD35, chlorite was identified as part of the clusters with feldspar and sillimanite. MOD40 contains pure, bladed, coarse-grained chlorite, enclosing relicts of talc. The grains display a weak green color and first order grey interference colors. The chlorite makes up a foliation and is commonly in cracks, bending around kyanite, or filling interstitial spaces.

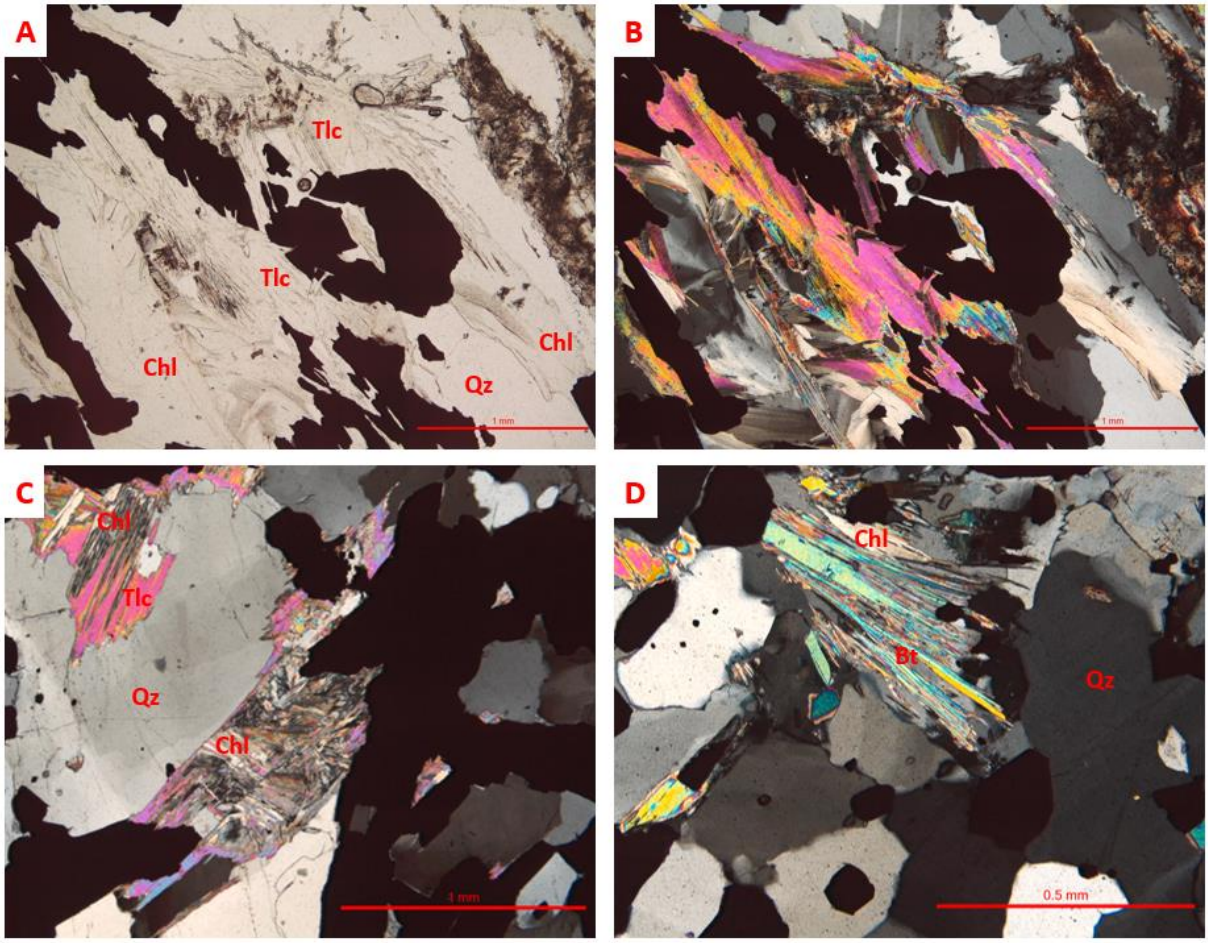

Figure 7.15: Photomicrographs of chlorite. A and B: Talc with radial texture is altered to chlorite in ppl and xpl in MOD40. C: Aggregates of talc and chlorite in MOD36. D: Chlorite as an apparent alteration product from phlogopite in MOD41. A-C: Scalebar is 1 mm. D: Scalebar is 0.5 mm.

The EPMA results show that the chemical composition of chlorite is approximately the same between the sections, though MOD35 shows the lowest Fe/(Fe+Mg)-ratio, and MOD41 has the highest Al/(Al+Si)-ratio. Formulae are calculated based on 10 cations and 14 oxygen. The general chlorite formulae are the following:

$$(Mg_{4,41\text{-}4,50}Fe^{2+}_{0,16\text{-}0,30}Fe^{3+}_{0\text{-}0,13}Al_{1,20\text{-}1.28})(Si_{2,65\text{-}2,88}Al_{1,12\text{-}1,35})O_{10}(OH)_8$$

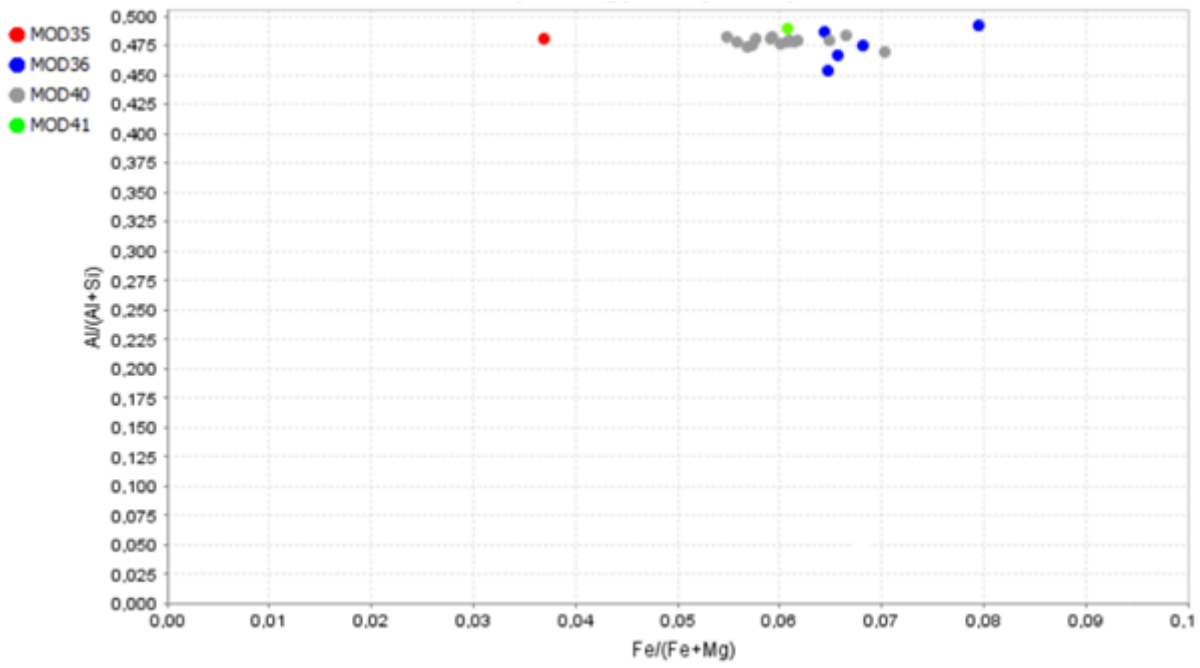

Figure 7.16: Chlorite diagram showing the compositional differences, where Fe/(Fe+Mg) is plotted versus Al/(Al+Si). Fe is plotted as Fe_{tot}.

Table 7.6. Chlorite Analyses and Structural Formulae

		35-1.9	36.1.7	36.2.2	36.2.9	*36-3-3*	40.1.1	40.1.2	40.1.9	40.2.1	40.2.7	40.3.1	40.3.3	40.3.5	40.4.6	40.4.7	40.4.8	*40-3-3*	41.1.5
	Wt.% Oxides																		
	SiO2	31.369	29.208	30.649	28.66	28.34	29.006	29.049	29.162	28.316	28.262	28.622	29.104	28.521	28.608	28.531	28.827	29.138	27.705
	TiO2	0.046	0.081	0.059	0.019	0.049	0.026	0	0.03	0.077	0.042	0.027	0.043	0.08	0	0.013	0.064	0.061	0
	Al2O3	24.624	21.748	21.565	21.963	23.265	22.527	22.694	23.07	22.416	22.215	22.469	22.466	22.191	22.017	22.279	22.44	23.663	22.576
	Cr2O3	0.047	0.006	0.024	0		0.02	0	0.004	0.018	0	0.007	0	0.006	0.018	0.029	0		0.025
	Fe2O3	0.184	0.179	0.497	0.068	2.062	0.532	0.080	0.160	1.100	0.799	0.314	0.133	0.481	0.362	0.136	0.230	2.084	1.799
	FeO Total	2.076	3.976	3.9	4.041	4.898	3.381	3.918	3.33	3.556	3.516	3.445	3.641	3.663	3.415	3.613	3.641	4.287	3.639
	FeO	1.911	3.815	3.453	3.979	3.042	2.903	3.846	3.186	2.566	2.797	3.163	3.521	3.230	3.089	3.490	3.434	2.412	2.020
	MnO	0.024	0.011	0.032	0.018	0.019	0.03	0.04	0.075	0.027	0.048	0.063	0.059	0.007	0.056	0.041	0.027	0	0.019
	MgO	30.417	31.732	31.591	31.008	31.842	32.109	31.719	32.24	31.702	31.415	31.555	31.982	31.437	31.515	31.209	31.585	33.024	31.529
	CaO	0.023	0.048	0	0.01	0.001	0.012	0.049	0.066	0.006	0.016	0.017	0.105	0.015	0.02	0.024	0	0.012	0
	Na2O	0.102	0	0	0.016	0.077	0	0	0	0	0	0.01	0.01	0	0.014	0	0.002	0.014	0.035
	K2O	0.025	0.014	0.108	0	0.015	0	0.076	0	0.018	0.016	0.011	0.006	0.014	0.029	0	0	0.021	0.039
	V2O3	0.000	0.01	0.003	0		0	0.021	0.009	0.031	0.008	0	0.01	0.02	0.014	0.021	0		0
	Total	88.441	86.834	87.931	85.735	88.506	87.111	87.566	87.986	86.167	85.538	86.226	87.426	85.954	85.706	85.76	86.586	90.22	85.567
	Rev. Total	88.442	86.842	87.978	85.742	88.713	87.164	87.553	87.993	86.246	85.610	86.257	87.429	85.982	85.728	85.753	86.609	90.429	85.747
10 Cats IV+VI	**Si**	2.917	2.768	2.878	2.751	2.639	2.729	2.731	2.718	2.695	2.710	2.723	2.736	2.725	2.739	2.733	2.733	2.652	2.654
	Al	1.083	1.232	1.122	1.249	1.361	1.271	1.269	1.282	1.305	1.290	1.277	1.264	1.275	1.261	1.267	1.267	1.348	1.346
4 T sites	**Sum**	4.000	4.000	4.000	4.000	4.000	4.000	4.000	4.000	4.000	4.000	4.000	4.000	4.000	4.000	4.000	4.000	4.000	4.000
	Total Al	2.698	2.429	2.386	2.485	2.554	2.498	2.514	2.534	2.515	2.511	2.520	2.489	2.499	2.484	2.515	2.508	2.538	2.549
	Al	1.615	1.196	1.264	1.236	1.193	1.226	1.245	1.253	1.210	1.221	1.243	1.225	1.224	1.223	1.248	1.241	1.190	1.203
	Ti	0.003	0.006	0.004	0.001	0.003	0.002	0.000	0.002	0.006	0.003	0.002	0.003	0.006	0.000	0.001	0.005	0.004	0.000
6	**Cr**	0.003	0.000	0.002	0.000	0.000	0.001	0.000	0.000	0.001	0.000	0.001	0.000	0.000	0.001	0.002	0.000	0.000	0.002
Octahedral	**Fe3+**	0.013	0.013	0.035	0.005	0.145	0.038	0.006	0.011	0.079	0.058	0.022	0.009	0.035	0.026	0.010	0.016	0.143	0.130
sites	**Mg**	4.215	4.482	4.421	4.437	4.420	4.502	4.444	4.479	4.498	4.490	4.475	4.481	4.477	4.497	4.456	4.464	4.480	4.502
	Fe Total	0.161	0.315	0.306	0.324	0.382	0.266	0.308	0.260	0.283	0.282	0.274	0.286	0.293	0.273	0.289	0.289	0.326	0.292
	Fe2+	0.149	0.302	0.271	0.319	0.237	0.228	0.302	0.248	0.204	0.224	0.252	0.277	0.258	0.247	0.280	0.272	0.184	0.162
	Mn	0.002	0.001	0.003	0.001	0.001	0.002	0.003	0.006	0.002	0.004	0.005	0.005	0.001	0.005	0.003	0.002	0.000	0.002
	Sum	6.000	6.000	6.000	6.000	6.000	6.000	6.000	6.000	6.000	6.000	6.000	6.000	6.000	6.000	6.000	6.000	6.000	6.000
Interlayer	**Ca**	0.002	0.005	0.000	0.001	0.000	0.001	0.005	0.007	0.001	0.002	0.002	0.011	0.002	0.002	0.002	0.000	0.001	0.000
sites	**Na**	0.018	0.000	0.000	0.003	0.014	0.000	0.000	0.000	0.000	0.000	0.002	0.002	0.000	0.003	0.000	0.000	0.002	0.007
	K	0.003	0.002	0.013	0.000	0.002	0.000	0.009	0.000	0.002	0.002	0.001	0.001	0.002	0.004	0.000	0.000	0.002	0.005
	Sum	0.024	0.007	0.013	0.004	0.016	0.001	0.014	0.007	0.003	0.004	0.005	0.013	0.003	0.008	0.002	0.000	0.006	0.011
	Total	10.024	10.007	10.013	10.004	10.016	10.001	10.014	10.007	10.003	10.004	10.005	10.013	10.003	10.008	10.002	10.000	10.006	10.011
	Mg/(MFeTot)	0.963	0.934	0.935	0.932	0.920	0.944	0.935	0.944	0.940	0.940	0.941	0.939	0.939	0.942	0.938	0.939	0.932	0.939
	Mg/(MFeO2)	0.966	0.937	0.942	0.933	0.949	0.951	0.936	0.946	0.956	0.952	0.946	0.941	0.945	0.947	0.940	0.942	0.961	0.965
	Al/(Al+Si)	0.481	0.467	0.453	0.475	0.492	0.478	0.479	0.483	0.483	0.481	0.481	0.476	0.478	0.476	0.479	0.478	0.489	0.490

7.2.7 Tourmaline

Euhedral to subhedral tourmaline in MOD35, MOD36, MOD38, MOD39 and MOD40 is quite equigranular, ranging from 0.1-0.4 mm. In MOD36, tourmaline is only found as inclusions in hematite, and in MOD37, as tiny inclusions in feldspar. In MOD41, the tourmaline is slightly

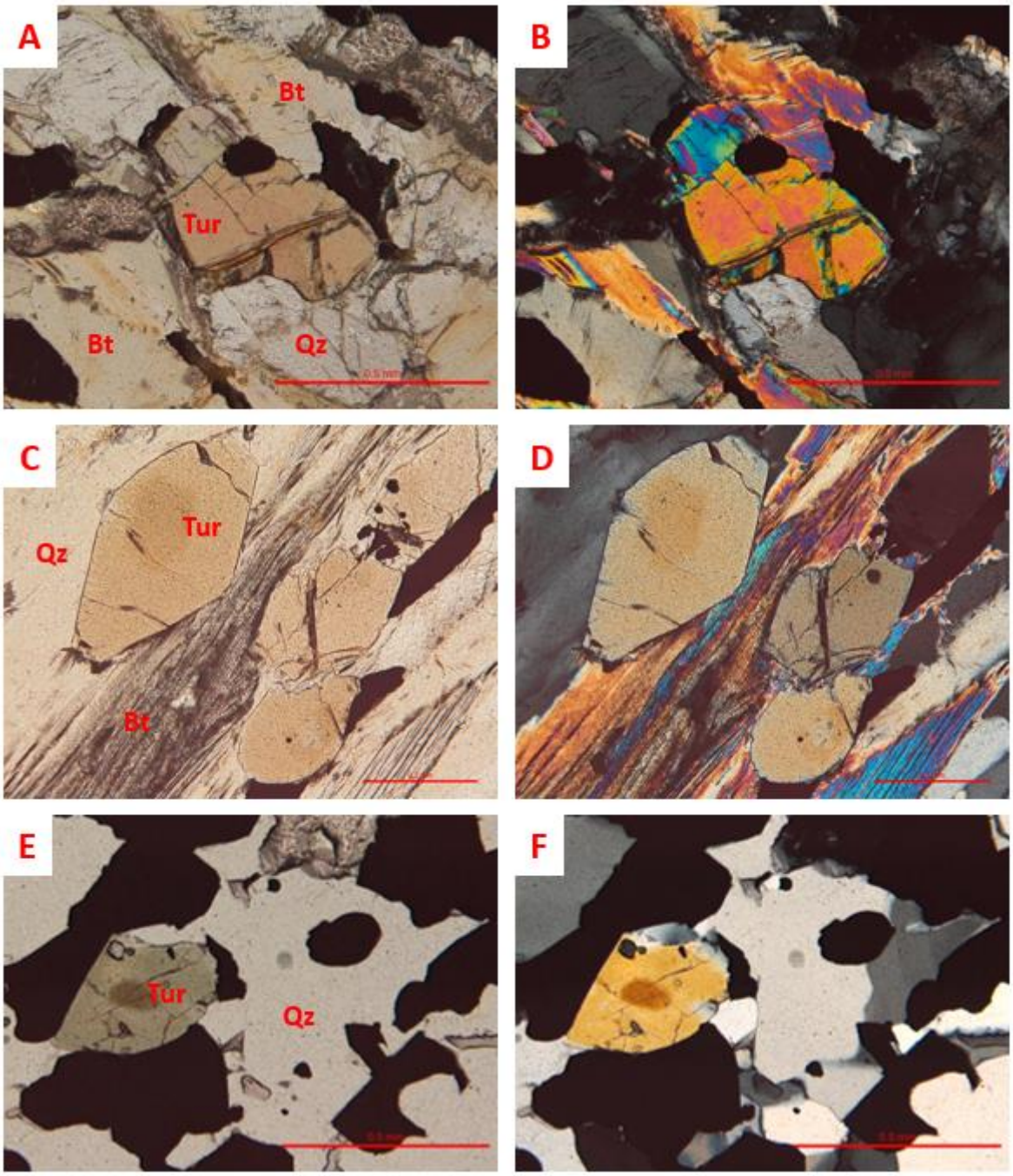

Figure 7.17: Photomicrographs of tourmaline. A and B: Cracked tourmaline in MOD38 in ppl and xpl. C and D: Tourmaline in 39, ppl and xpl. Tourmaline is displaying a brown color, zoning, and euhedral shape. E and F: Green, zoned tourmaline in MOD41, ppl and xpl. A-B, E-F: Scalebar is 0.5 mm. C-D: Scalebar is 0.2 mm.

coarser, up to 0.6 mm, and in MOD40, the tourmaline occurs in clusters together with oxides. The grains in MOD38 and MOD39 are extensively cracked. All tourmaline is pleochroic, though MOD35-MOD40 are mostly pale brown, MOD41 is pale green to brown and HJ002 is clear pale green (fig. 7.17).

The EPMA results show that the Fe-content of tourmaline is ~4 wt.% in MOD41 and 5-6 wt.% in MOD38 and MOD39, and the Mg-content is ~9 wt.% in MOD41 and ~11 wt.% in MOD38 and MOD39. This generally gives a Fe/Mg-ratio of 1:2 in MOD38, MOD39 and MOD41. In MOD36 the ratio is 1:7. MOD38 and MOD39 show approximately the same content of CaO and Na_2O, while MOD35 and MOD41 have slightly higher Na_2O and lower CaO-content (fig. 7.18). MOD41 is also more aluminous. Furthermore, MOD36 has lower Na_2O-content, Fe-content of only 1.4 wt.%, and a much higher Al_2O_3 and SiO_2-content. This also gives a much higher analytical sum than the other sections.

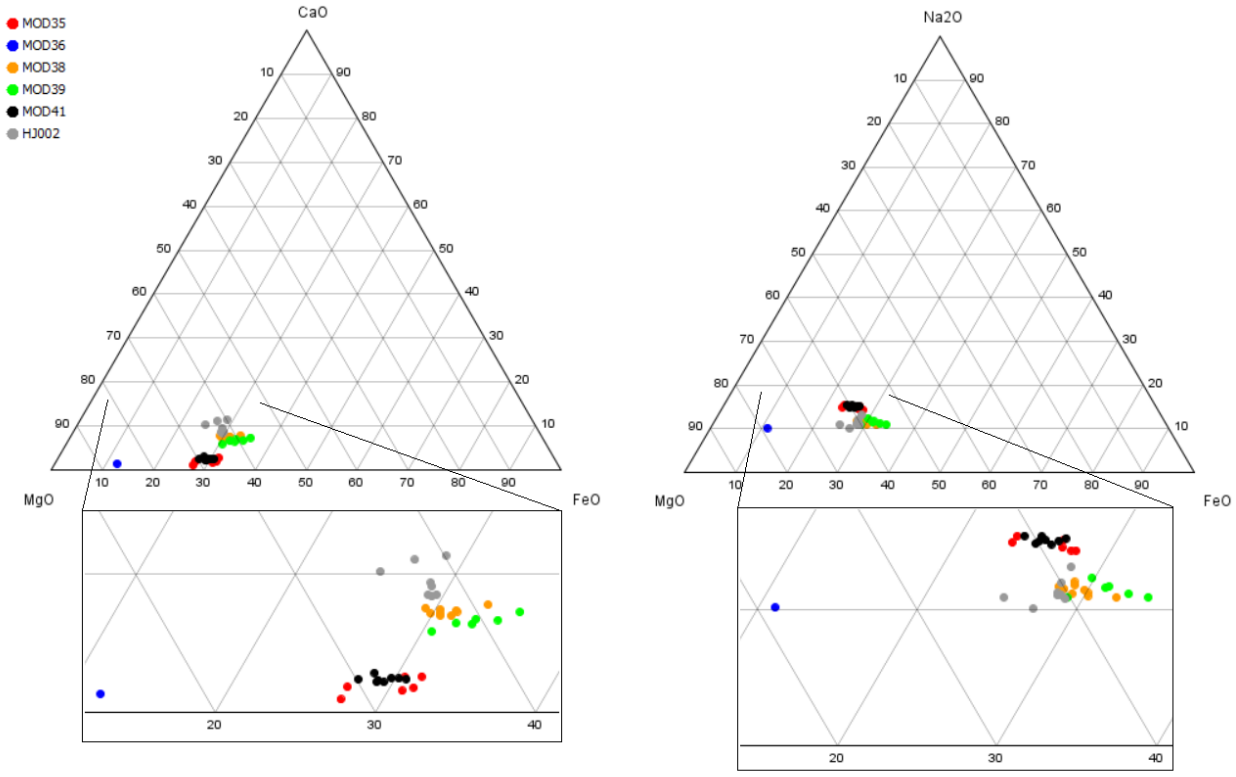

Figure 7.18: Ternary tourmaline diagram showing compositional differences. The rocks with amphibole contain more Ca-rich tourmaline, while the tourmaline in the Al-silicate rocks are more Na-rich.

7.2.8 Kyanite/Sillimanite

Kyanite was identified by the high relief and yellow interference colors, and sillimanite by its high relief, and fibrous or needle-like texture. Photomicrographs can be seen in figure 7.19.

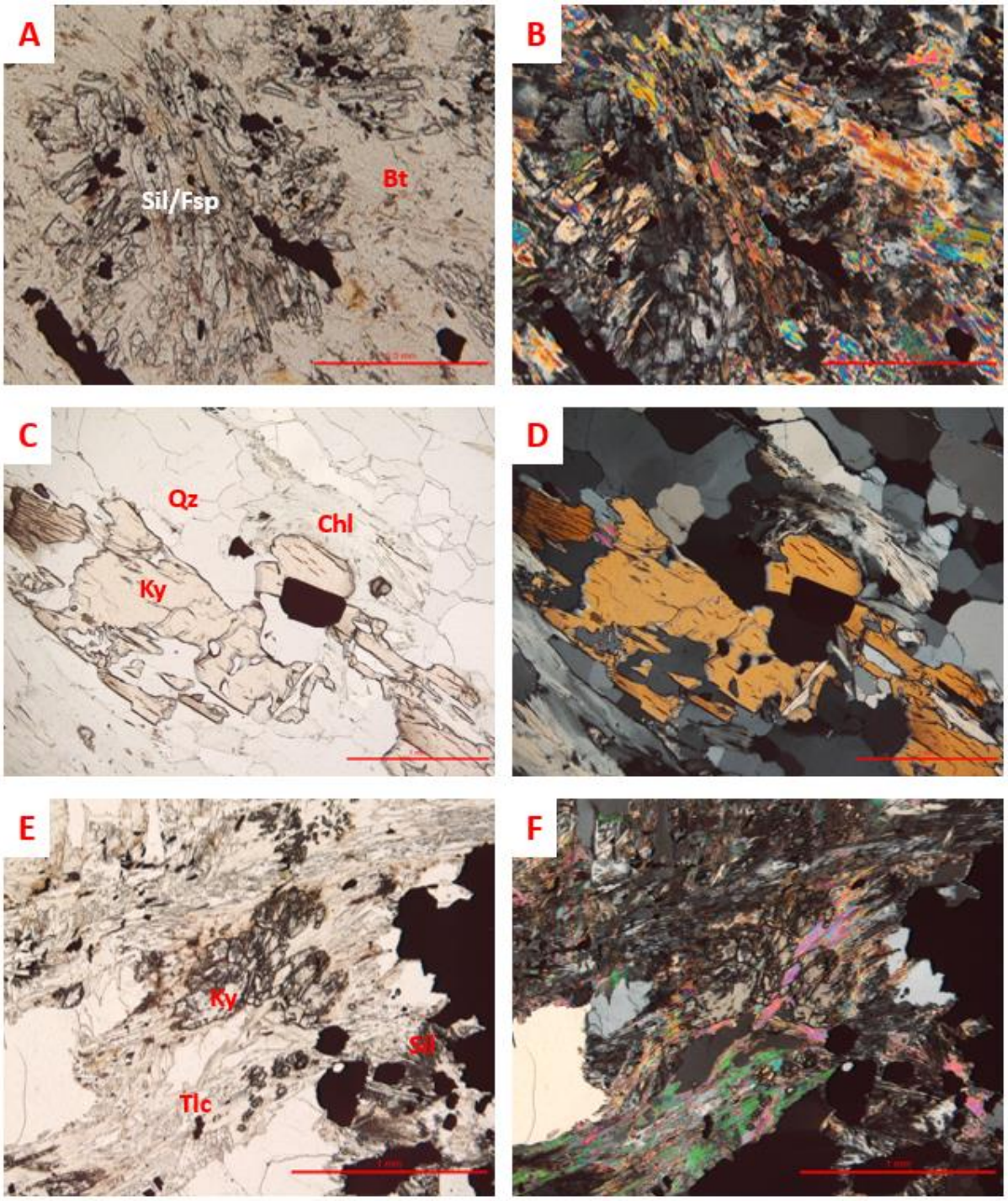

Figure 7.19: Photomicrographs of kyanite and sillimanite. A and B: Clusters of sillimanite and feldspar in MOD35, ppl and xpl. Scalebar is 0.5 mm. C and D: Kyanite in MOD40, ppl and xpl. E and F: Relict kyanite surrounded by talc, paragonite, plagioclase (~An_{30}) and sillimanite in MOD36, ppl and xpl. C-F: Scalebar is 1 mm.

In MOD35 sillimanite is fine-grained and needle-shaped, occurring together with feldspar in clusters. MOD36 displays relict kyanite in fibrous/needle-shaped intergrowths with sillimanite, together with talc, paragonite and plagioclase (~An_{30}). Kyanite is colorless with yellow interference colors, while sillimanite gets a brown color due to the fibrous texture. In MOD40, the kyanite is coarse-grained and colorless, occurring as porphyroblasts up to 2.5 mm in size, commonly surrounded by a rim of quartz. The grains have brown lamellae of an unidentified mineral, and are displaying 60-degree cleavage. HJ002 contains a few small kyanite grains with high relief and first order interference color.

EPMA results show a variation in Al_2O_3-content between 54 and 60 wt.% and a SiO_2-content between 37 and 40 wt.% for all sections. The results show slight FeO substitution, with up to 1.2 wt.%. MOD35 has generally a lower FeO-content. The only difference in chemical composition for sillimanite and kyanite is that kyanite tends to have a slightly higher FeO-content. The formulations are not included, due to analyses showing low totals.

7.2.9 Apatite

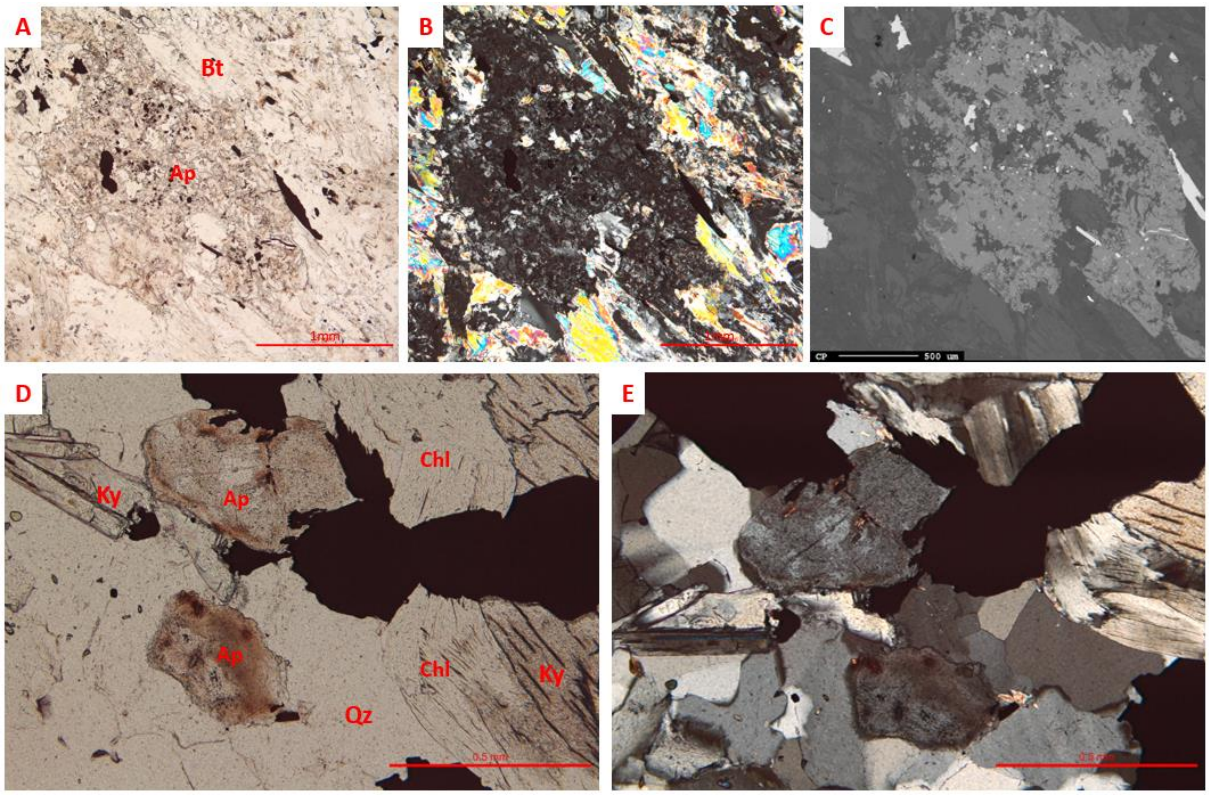

Figure 7.20: Photomicrographs of apatite. A-C: Apatite in MOD35, ppl, xpl and EPMA. D and E: Dusty apatite in MOD40. A-B: Scalebar is 1 mm. C-E: Scalebar is 0.5 mm.

Apatite was identified by its intermediate relief and low interference colors. Microphotographs can be seen in figure 7.20. In all sections where apatite is present, apatite is coarse-grained at around 0.5-1mm. MOD37, MOD38 and MOD39 show progressive alteration in apatite, from unaltered in MOD37 to heavily altered in MOD39. MOD40 is also unaltered, while MOD35 and MOD40 show heavy alteration, giving the grains a dusty, brown appearance. In MOD40 and MOD41, apatite occurs in the vicinity to oxides.

EPMA results show fluorine-content around 3 wt.% for MOD37, MOD38, MOD39 and MOD40, while MOD41 has a higher fluorine-content, around 4 wt.%. The chlorine-content varies a lot. Formulae are based on 8 cations and 12.5 oxygen. Mechanical errors gave too high totals for most analyses, leading to overestimation of P_2O_5-contents, giving up to 4.016 for P in formulae.

Table 7.7. Apatite Analyses and Structural Formulae

	35-1a-2.1	37.4.9	37.4.11	37.5.5	37.5.11	38.4.6	38.7.1	38.7.3	39.1.2	39.1.3
CaO	51.376	55.608	55.804	54.739	55.789	54.293	55.257	55.388	54.171	54.165
Na_2O	1.2	0	0	0	0	0.034	0	0	0	0
MnO	0	0.004	0	0	0.001	0	0	0.005	0.008	0.007
FeO	0.162	0.01	0.002	0.059	0	0.047	0.041	0.384	0.023	0.02
P_2O_5	40.625	54.815	54.788	53.248	55.539	53.596	56.131	52.946	53.842	52.713
SiO_2	0.354	0	0	0	0	0	0	0	0	0
Cl	1.042	1.835	0.366	2.233	1.934	2.929	2.853	3.256	1.161	1
F	3.36	3.771	3.813	3.669	3.756	3.514	3.725	3.637	3.851	3.743
Total	97.044	114.097	113.209	111.948	115.119	112.797	115.804	113.374	111.173	109.846
Ca	4.652	5.035	5.053	4.957	5.052	4.916	5.004	5.015	4.905	4.905
Na	0.197	0.000	0.000	0.000	0.000	0.006	0.000	0.000	0.000	0.000
Mn	0.000	0.000	0.000	0.000	0.000	0.000	0.000	0.000	0.001	0.001
Fe	0.011	0.001	0.000	0.004	0.000	0.003	0.003	0.027	0.002	0.001
P	2.907	3.922	3.920	3.810	3.974	3.835	4.016	3.788	3.853	3.772
Si	0.030	0.000	0.000	0.000	0.000	0.000	0.000	0.000	0.000	0.000
Cl	0.263	0.052	0.320	0.277	0.420	0.409	0.466	0.166	0.143	0.137
F	0.898	1.008	1.019	0.981	1.004	0.939	0.996	0.972	1.029	1.000
Total	8.297	9.458	9.473	9.271	9.526	9.260	9.523	9.331	9.260	9.178
	39.1.4	40.2.3	40.2.10	41.2.1	41.2.7	003-3.1	003-3.2	003-3.5	003-3.7	003-5.4
CaO	55.804	55.597	54.402	53.177	54.359	54.416	50.781	54.095	52.593	51.142
Na_2O	0	0	0	0	0	0	0	0	0.006	0
MnO	0.02	0.118	0.019	0.017	0.026	0.023	0.062	0.001	0	0.032
FeO	0	0.045	0.02	0.108	0.069	0.29	0.132	0.108	1.126	0.225
P_2O_5	52.73	54.614	54.35	52.34	54.506	41.272	42.116	40.528	40.921	41.884
SiO_2	0	0	0	0	0	1.445	0	0	0	0
Cl	0.959	0.952	1.486	1.997	2.093	0.951	1.044	1.204	0.922	1.145
F	3.724	3.872	3.805	3.819	3.779	3.628	3.68	3.531	3.637	3.581
Total	111.546	113.362	112.215	109.497	112.874	100.529	96.142	97.855	97.692	96.511
Ca	5.053	5.034	4.926	4.815	4.922	4.927	4.598	4.898	4.762	4.631
Na	0.000	0.000	0.000	0.000	0.000	0.000	0.000	0.000	0.001	0.000
Mn	0.001	0.008	0.001	0.001	0.002	0.002	0.004	0.000	0.000	0.002
Fe	0.000	0.003	0.001	0.008	0.005	0.020	0.009	0.008	0.080	0.016
P	3.773	3.908	3.889	3.745	3.900	2.953	3.014	2.900	2.928	2.997
Si	0.000	0.000	0.000	0.000	0.000	0.122	0.000	0.000	0.000	0.000
Cl	0.136	0.459	0.286	0.368	0.136	0.150	0.172	0.132	0.164	0.000
F	0.995	1.035	1.017	1.021	1.010	0.970	0.984	0.944	0.972	0.957
Total	9.327	9.454	9.318	9.069	9.329	8.525	8.126	8.306	8.271	8.146

7.2.10 Unknown mineral

This mineral was identified by its yellow color, texture like a sheet silicate, and nearly isotropic optics. Microphotographs can be seen in figure 7.21. The mineral has been found in MOD37, MOD38, MOD39 and MOD41, mostly filling in cracks. MOD37 contains more of this mineral than the other sections, and both here and in MOD41 it is also found as a pseudomorph after mica. In MOD38 and MOD39, the mineral has only been found in cracks.

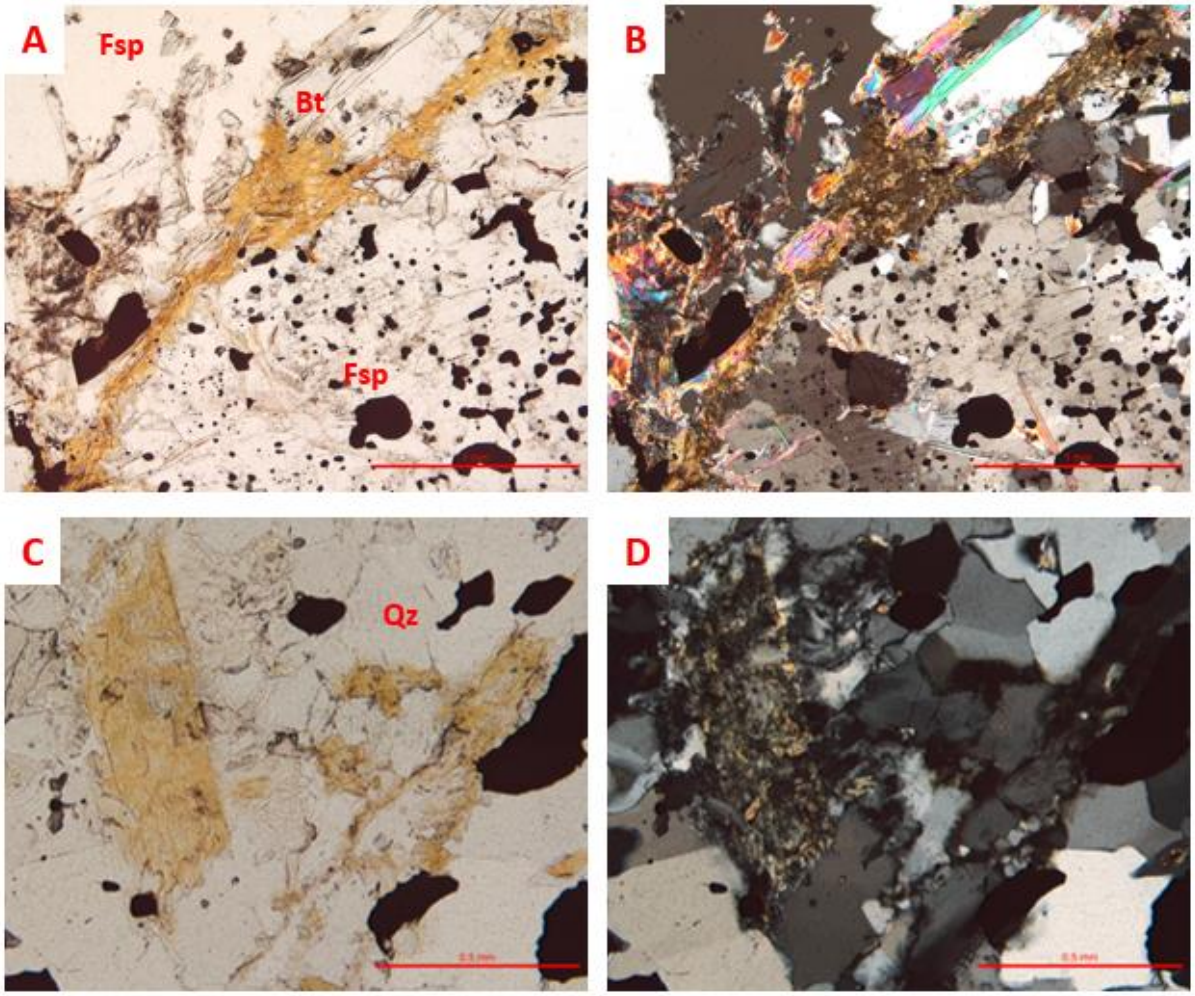

Figure 7.21: Photomicrographs of the unknown mineral. A and B: Mystery mineral in MOD37. Scalebar is 1 mm. C and D: Unknown mineral as possible pseudomorph of mica in MOD41. Scalebar is 0,5 mm.

Two possible theories have been explored for the origin of the unknown mineral. In 1982, Schreyer et al. published a paper on a new metamorphic phyllosilicate mineral called kulkeite. This was found to be a mixed-layer mineral with a composition like a 1:1 mixture of chlorite and talc. Kulkeite occurs as platy, colorless, porhyroblastic, single crystals up to 2 mm in size

in low-grade dolomite rocks associated with metamorphosed Triassic evaporite. It is associated with sodian aluminian talc, chlorite polytypes and K and Na-phlogopite. From table 7.9, it is obvious that our analyses to some extent fit well with the composition of kulkeite, except for FeO, CaO and Na_2O. The high Na in the kulkeite analyses may relate to origin in an evaporite.

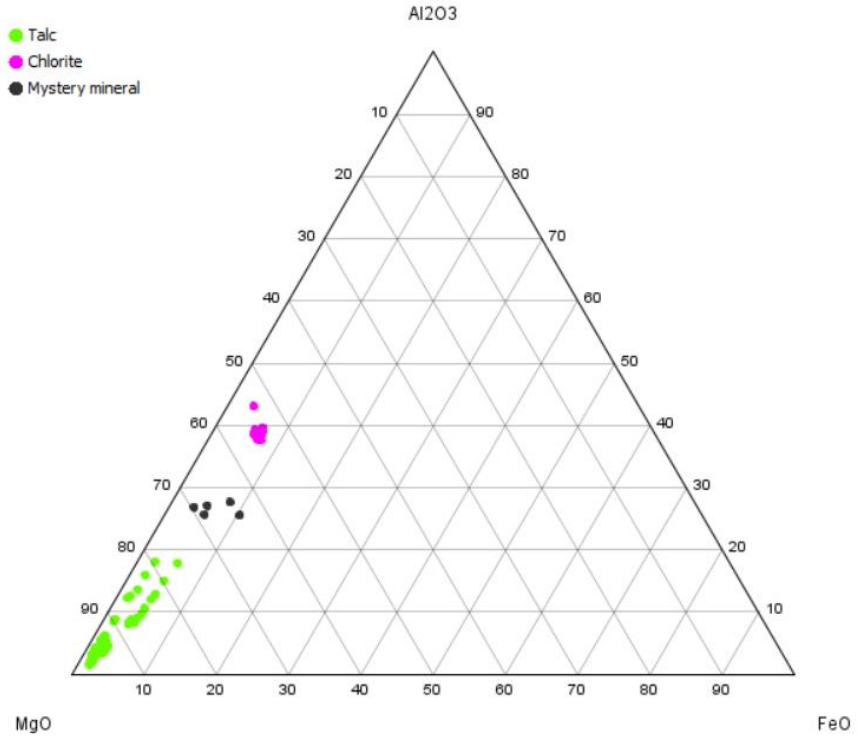

Figure 7.22: Ternary diagram showing composition of mystery mineral compared to chlorite and talc.

Table 7.8: Comparison of the mystery mineral with kulkeite.

Sample	MOD37	MOD37	MOD37	MOD37	Kulkeite	Kulkeite	Kulkeite
Mineral	37.1.4	37.1.5	37.2.9	37.7.9			
SiO2	36.768	38.154	35.862	36.608	41.44	40.53	42.07
Al2O3	13.589	12.578	12.398	13.117	12.42	12.64	12.98
FeO	2.625	2.716	5.049	1.737			
MgO	34.02	33.757	30.993	34.028	33.05	33.19	34.2
CaO	0.499	0.562	0.703	0.433	0.07	0.06	
Na2O	0	0	0.046	0.009	0.94	1.2	1.15
K2O	0.002	0.019	0	0.019	0.2	0.07	
MnO	0.022	0	0.055	0.005			
TiO2	0	0.002	0.002	0			
Cr2O3	0.007	0	0	0			
P2O5	0	0.087	0	0.053			
BaO	0.07	0.019	0.021	0.05			
V2O3	0.001	0.009	0	0			
F	0.033	0	0.001	0.032			
Cl	0.019	0.012	0.009	0.01			
Total	100.46	100.79	97.52	98.73			

With the aid of John Schumacher, the unknown mineral has also been compared to AK6, a mineral found in kimberlites. This mineral is thought to be an ordered structural layering at the submicroscopic scale of various sheet silicates. This would be about a 1:1 mixture of chlorite and serpentine with a small amount of the dioctahedral analog of serpentine (kaolinite). In table 7.10, it is clear that the unknown mineral also fits this composition very well. The unknown mineral can be placed intermediately between AK6 and kulkeite, which is rich in Na.

Table 7.9: Comparison of the unknown mineral with AK6, mineral found in kimberlites.

Sample	**MOD37**	**MOD37**	**MOD37**	**MOD37**	**AK6**	**AK6**	**AK6**					
Mineral												
SiO2	36.768	38.154	35.862	36.608	36.49	36.89	36.78					
Al2O3	13.589	12.578	12.398	13.117	10.3	11.46	10.55					
FeO	2.625	2.716	5.049	1.737	18.14	15.86	13.76					
MgO	34.02	33.757	30.993	34.028	22.37	22.78	23.43					
CaO	0.499	0.562	0.703	0.433	1.26	1.18	1.05					
Na2O	0	0	0.046	0.009	0.15	0.15	0.14					
K2O	0.002	0.019	0	0.019	0.05	0.06	0.03					
MnO	0.022	0	0.055	0.005	0.16	0.19	0.16					
TiO2	0	0.002	0.002	0								
Cr2O3	0.007	0	0	0								
P2O5	0	0.087	0	0.053								
BaO	0.07	0.019	0.021	0.05								
V2O3	0.001	0.009	0	0								
F	0.033	0	0.001	0.032								
Cl	0.019	0.012	0.009	0.01								
H2O	12.94	13	12.41	12.77	12.11	12.24	12.00					
Total	100.46	100.79	97.52	98.73	101.04	100.83	97.91			**Experiment:**		
		7 ox			**7 ox**				**Mixture**	**0.4 Serpentine**	**0.1 Kaolinite**	**0.5 Chlinochlore**
Si	1.704	1.760	1.732	1.719	1.807	1.807	1.838	**Si**	**1.750**	2	2	1.5
Al	0.296	0.240	0.268	0.281	0.193	0.193	0.162	**Al**	**0.25**	0	0	0.5
Sum	2.000	2.000	2.000	2.000	2.000	2.000	2.000					
Al	0.446	0.444	0.438	0.445	0.408	0.469	0.459	**Al**	**0.45**	0	2	0.5
Ti	0.000	0.000	0.000	0.000	0.000	0.001	0.000					
Mg	2.351	2.321	2.232	2.382	1.651	1.663	1.745					
Fe	0.102	0.105	0.204	0.068	0.751	0.650	0.575					
Mn	0.001	0.000	0.002	0.000	0.007	0.008	0.007					
Ca	0.025	0.028	0.036	0.022	0.067	0.062	0.056					
Na	0.000	0.000	0.004	0.001	0.014	0.014	0.014					
K	0.000	0.001	0.000	0.001	0.003	0.004	0.002					
Sum	**2.924**	**2.899**	**2.917**	**2.919**	**2.902**	**2.871**	**2.858**					
Sum (R2+ + R1+)	**2.478**	**2.455**	**2.479**	**2.474**	**2.493**	**2.401**	**2.399**	**Mg**	**2.45**			
Total	4.925	4.899	4.917	4.919	4.901	4.870	4.859					

7.2.11 Accessory minerals

Several accessory minerals were found.

Rutile is locally found as discrete, small grains, and is commonly found as lamellae in hematite. Titanite is found in MOD37, MOD38, MOD39 and HJ002, commonly as inclusions in hematite. Zircon is found as discrete grains in some sections, usually small grains with a size less than 0.1 mm, and commonly as inclusions in feldspar porphyroblasts.

7.2.11.1 Paragonite

In MOD36 and MOD41, a dioctahedral mica resembling paragonite was found. The EPMA results however, show that the mineral is too Mg-rich to be pure paragonite, but it could be a part of a three-way solid solution between paragonite, talc and Na- phlogopite. It is found in clusters with phlogopite and talc, implying that it is a part of a metamorphic process. The general formula can be written as

$$(Na_{0.58\text{-}0.87}Ca_{0.01\text{-}0.03}K_{0.01\text{-}0.07})(Al_{1.76\text{-}1.91}Mg_{0.04\text{-}0.21})Al_{0.85\text{-}1.02}Si_{2.97\text{-}3.15}O_{10}$$

Table 7.10: EPMA results and structural formulae of the dioctahedral mica/Mg-paragonite.

	36.4.9	41.4.3	41.1.4			36.4.9	41.4.3	41.1.4
Wt.% Oxides								
SiO2	53.07	44.782	46.374		**Total Al**	2.610	2.931	2.809
TiO2	0	0.006	0.139		**Al**	1.761	1.906	1.799
Al2O3	37.302	37.427	36.957		**Ti**	0.000	0.000	0.007
Cr2O3	0	0.001	0.053		**Cr**	0.000	0.000	0.003
Fe2O3	0.2600	0.2250	0.4036		**Fe3+**	0.012	0.011	0.020
FeO Total	0.542	1.043	1.064		**Mg**	0.212	0.036	0.134
FeO	0.3080	0.8405	0.7009		**Fe Total**	0.027	0.058	0.057
MnO	0.011	0	0		**Fe2+**	0.015	0.047	0.038
MgO	2.39	0.364	1.394		**Mn**	0.001	0.000	0.000
CaO	0.55	0.183	0.161		**Sum**	2.000	2.000	2.000
Na2O	5.036	6.764	5.96					
K2O	0.09	0.59	0.817		**Ca**	0.035	0.013	0.011
Total	98.991	91.16	92.919		**Na**	0.580	0.871	0.745
Rev. Total	99.017	91.183	92.959		**K**	0.007	0.050	0.067
					Sum	0.622	0.934	0.823
Si	3.151	2.975	2.990					
Al	0.849	1.025	1.010		**Total**	6.622	6.934	6.823
Sum	4.000	4.000	4.000		**Variable ox**	10.79	10.92	10.83

7.2.12 Oxides

Titanohematite was identified by its light grey color and strong anisotropy in reflected light, while ilmenite and rutile were determined by their darker grey color. Reflected-light micrographs can be seen in figure 7.23.

Titanohematite is present in MOD35-MOD41. In MOD35, titanohematite is coarse-grained and contains both rutile-lamellae and larger areas of rutile. It is also present as fine grains in the clusters of sillimanite and feldspar. MOD36 has aggregates of coarse-grained titanohematite with fine lamellae of rutile, and it also includes twins of an unknown lighter phase, possibly

hematite. In MOD37, MOD38 and MOD39, titanohematite is present as fine inclusions in the coarse-grained feldspar, and as coarse-grained aggregates. MOD37 and MOD38 have long lamellae of rutile, while in MOD39, the lamellae are finer. Like MOD35, MOD39 also encloses larger areas of rutile. In MOD40, titanohematite is coarse-grained, occurring in areas with tourmaline and kyanite, and containing inclusions of tourmaline. The titanohematite displays randomly scattered lamellae of rutile as the previous described sections. Robinson et al. (2014) found that titanohematite from Modum contained lamellae of spinel and rutile, and even though no EPMA-analyses of spinel are available in this thesis, it is assumed to be present.

MOD41 separates from the others, where the titanohematite has unknown, white anisotropic lamellae. In MOD37, MOD41 and MODHJK, titanohematite commonly display darker areas around the grains. MODHJK has a very low oxide content, only displaying a few grains. In HJ002, the titanohematite is evenly scattered and contains lamellae of a darker phase than the other sections. HJ003 stand out from the others, with oxides with only one phase with a cream white/light yellow color, proven to be ilmenite from EPMA. Here the ilmenite is present as plentiful fine-grained inclusions in relict pyroxene.

EPMA results from MOD35, MOD36, MOD37, MOD39, MOD40 and HJ003 show that multiple phases are present in the oxides. MOD35, MOD36, MOD37, MOD39 and MOD40 shows titanohematite with rutile. HJ003 contains ilmenite without lamellae. Due to mechanical errors, all analyses showed low totals. Therefore, FeO was multiplied with a correction factor of 0.89.

In the first round of investigation, MOD35 and MOD39 were examined, but these results had to be discarded due to mechanical errors. In the second round, line scans were performed for one grain each in MOD35, MOD36, MOD37 and MOD40. Some compositional differences were detected along the lines. In terms of end-member composition, the results showed up to 0.829% $MgTiO_3$ and 0.623% Al_2O_3, pointing to small degrees of Mg- and Al-substitution, or possibly overlap. The Ti-contents were calculated, and two groups were recognized. The titanohematite in MOD35 and MOD37 is located at Ilmenite 00.03-0.05, while in MOD36 and MOD40, the titanohematite is located at Ilmenite 0.06-0.08.

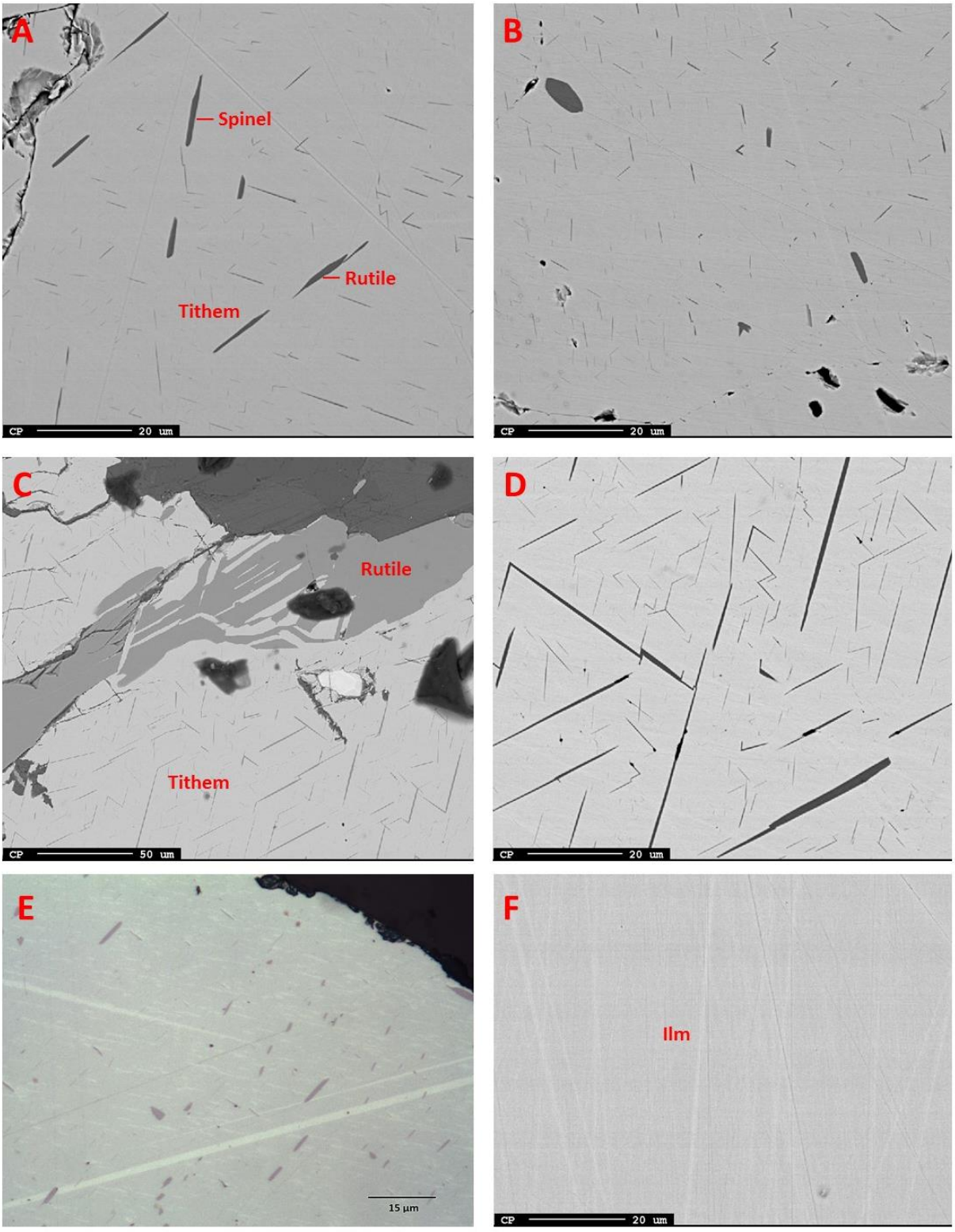

Figure 7.23: A: MOD35 and B: MOD39, showing two darker phases; rutile as the coarser phase and another phase as thin lamellae. C-D: HJ002, showing two darker phases as lamellae and larger area with rutile lamellae. E: Microphotograph from MOD38, showing titanohematite with inclusions of rutile and fine, lighter lamellae of possibly hematite twins. F: HJ003, showing only one phase of ilmenite. Light streaks are due to polishing.

Table 7.11a. Titanohematite analyses, cation formulae and end-members														
		35-3-1a	**35-3-2**	**35.3.9a**	**35.3.9d**	**35.3.9e**	**35.3.9f**	**35.3.9h**	**35.3.9j**	**35.3.9k**	**36-4-11**	**36-4-11**	**36-4-11**	**36-4-11**
Wt% oxides	**SiO2**	0.013	0.000	0.128	0.000	0.000	0.000	0.033	0.000	0.015	0.000	0.000	0.000	0.000
	TiO2	2.841	1.645	1.631	2.315	1.658	1.726	1.744	1.884	3.547	3.387	3.599	3.780	3.631
	Al2O3	0.348	0.269	0.275	0.311	0.341	0.308	0.367	0.305	0.298	0.380	0.403	0.353	0.364
	Cr2O3													
	Fe2O3	95.312	96.640	96.594	95.225	96.450	96.206	96.651	96.440	92.844	93.642	93.418	92.942	93.052
	Fe Total	88.249	88.292	88.178	87.580	88.097	88.026	88.332	88.295	86.535	87.207	87.200	86.957	86.891
	FeO	2.486	1.335	1.261	1.896	1.310	1.459	1.364	1.518	2.993	2.947	3.142	3.327	3.162
	MnO	0.023	0.046	0.000	0.002	0.006	0.000	0.022	0.000	0.008	0.001	0.000	0.001	0.000
	MgO	0.034	0.055	0.201	0.103	0.098	0.052	0.124	0.099	0.116	0.055	0.053	0.040	0.058
	CaO	0.000	0.000	0.000	0.000	0.000	0.000	0.000	0.000	0.000	0.000	0.000	0.000	0.000
	Total	102.567	101.243	101.328	101.155	101.144	100.994	101.548	101.538	101.262	101.860	102.071	101.878	101.686
	Corr.Total	101.057	99.990	100.090	99.852	99.863	99.751	100.305	100.245	99.821	100.412	100.615	100.442	100.266
Cats	**Si**	0.000	0.000	0.003	0.000	0.000	0.000	0.001	0.000	0.000	0.000	0.000	0.000	0.000
	Ti	0.056	0.033	0.032	0.046	0.033	0.034	0.035	0.037	0.071	0.067	0.071	0.075	0.072
	Al	0.011	0.008	0.009	0.010	0.011	0.010	0.011	0.009	0.009	0.012	0.012	0.011	0.011
	Fe3+	1.877	1.926	1.920	1.898	1.923	1.921	1.918	1.916	1.849	1.854	1.845	1.840	1.845
	Mg	0.001	0.002	0.008	0.004	0.004	0.002	0.005	0.004	0.005	0.002	0.002	0.002	0.002
	Fe Total	1.931	1.956	1.948	1.940	1.952	1.954	1.948	1.949	1.915	1.919	1.914	1.913	1.914
	Fe2+	0.054	0.030	0.028	0.042	0.029	0.032	0.030	0.034	0.066	0.065	0.069	0.073	0.070
	Mn	0.001	0.001	0.000	0.000	0.000	0.000	0.000	0.000	0.000	0.000	0.000	0.000	0.000
	Ca	0.000	0.000	0.000	0.000	0.000	0.000	0.000	0.000	0.000	0.000	0.000	0.000	0.000
% of end-members	**MgTiO3**	0.133	0.217	0.791	0.407	0.387	0.206	0.487	0.390	0.458	0.216	0.207	0.157	0.228
	FeTiO3	5.407	2.956	2.448	4.200	2.903	3.239	2.922	3.350	6.583	6.484	6.898	7.318	6.966
	MnTiO3	0.051	0.103	0.000	0.004	0.013	0.000	0.049	0.000	0.018	0.002	0.000	0.002	0.000
	Sum	5.591	3.276	3.240	4.611	3.304	3.445	3.458	3.740	7.058	6.702	7.105	7.477	7.194
	Fe2O3	93.839	96.304	95.994	94.903	96.164	96.073	95.885	95.786	92.437	92.709	92.272	91.976	92.241
	Al2O3	0.537	0.420	0.428	0.485	0.532	0.482	0.570	0.474	0.465	0.589	0.623	0.547	0.565
	Total	99.966	100.000	99.662	100.000	100.000	100.000	99.913	100.000	99.960	100.000	100.000	100.000	100.000

		Table 7.11b. Titanohematite analyses, cation formulae and end-members										*Table 7.12. Ilmenite analyses, cation for*		
		37.2.15d	**37.2.15e**	**37.2.15g**	**37.2.15i**	**37.2.15j**	**37.2.15l**	**40-3-10**	**40-3-10**	**40-3-10**	**40-3-10**	**003-aA-5.1**	**003-aA-5.**	**003-aA-5.3**
Wt% oxides	**SiO2**	0.064	0.000	0.019	0.000	0.000	0.000	0.000	0.000	0.000	0.096	0	0	0
	TiO2	2.289	2.229	2.401	2.399	2.287	2.294	3.934	4.042	4.096	3.522	52.795	52.188	53.018
	Al2O3	0.252	0.273	0.222	0.251	0.252	0.259	0.358	0.372	0.362	0.321	0.04	0	0
	Cr2O3											0.028	0	0.058
	Fe2O3	95.022	95.633	95.541	95.157	95.326	95.690	93.050	92.646	92.475	93.641	0.899	0.405	0.002
	Fe Total	87.533	87.799	87.894	87.384	87.595	87.952	87.057	86.922	86.671	87.383	45.013	44.680	44.899
	FeO	2.031	1.747	1.925	1.761	1.819	1.849	3.330	3.558	3.461	3.123	44.204	44.316	44.898
	MnO	0.000	0.006	0.000	0.022	0.009	0.000	0.010	0.000	0.017	0.000	0.643	0.614	0.575
	MgO	0.058	0.141	0.144	0.210	0.128	0.120	0.111	0.043	0.115	0.089	1.453	1.114	1.219
	CaO	0.000	0.000	0.000	0.000	0.000	0.000	0.000	0.000	0.000	0.000	0.023	0.004	0.017
	Total	101.041	101.314	101.613	101.093	101.105	101.496	102.230	102.137	101.973	102.212	97.391	96.116	97.276
	Corr.Total	99.716	100.029	100.252	99.799	99.821	100.212	100.793	100.661	100.526	100.793	101.348	99.365	100.289
Cats	**Si**	0.002	0.000	0.001	0.000	0.000	0.000	0.000	0.000	0.000	0.003	0.000	0.000	0.000
	Ti	0.046	0.044	0.048	0.048	0.046	0.046	0.077	0.080	0.081	0.069	0.986	0.992	0.994
	Al	0.008	0.009	0.007	0.008	0.008	0.008	0.011	0.012	0.011	0.010	0.001	0.000	0.000
	Fe3+	1.897	1.903	1.897	1.897	1.901	1.901	1.834	1.829	1.827	1.846	0.017	0.008	0.000
	Mg	0.002	0.006	0.006	0.008	0.005	0.005	0.004	0.002	0.005	0.003	0.054	0.042	0.045
	Fe Total	1.942	1.941	1.939	1.936	1.941	1.942	1.907	1.907	1.903	1.915	0.935	0.945	0.937
	Fe2+	0.045	0.039	0.042	0.039	0.040	0.041	0.073	0.078	0.076	0.068	0.918	0.937	0.936
	Mn	0.000	0.000	0.000	0.000	0.000	0.000	0.000	0.000	0.000	0.000	0.014	0.013	0.012
	Ca	0.000	0.000	0.000	0.000	0.000	0.000	0.000	0.000	0.000	0.000	0.001	0.000	0.000
% of end-	**MgTiO3**	0.229	0.556	0.566	0.829	0.506	0.472	0.433	0.168	0.450	0.348	5.3797	4.1991	4.5316
members	**FeTiO3**	4.338	3.863	4.197	3.900	4.032	4.082	7.293	7.806	7.599	6.592	91.8278	93.7240	93.6487
	MnTiO3	0.000	0.013	0.000	0.049	0.020	0.000	0.022	0.000	0.038	0.000	1.3529	1.3152	1.2147
	Sum	4.568	4.432	4.764	4.778	4.558	4.554	7.749	7.974	8.087	6.940	98.560	99.238	99.395
	Fe2O3	94.869	95.142	94.841	94.830	95.049	95.043	91.699	91.450	91.353	92.313	0.8403	0.3849	0.0014
	Al2O3	0.394	0.425	0.345	0.392	0.394	0.403	0.553	0.575	0.560	0.496	0.0586	0.0000	0.0000
	Total	99.830	100.000	99.950	100.000	100.000	100.000	100.000	100.000	100.000	99.748	99.459	99.623	99.396

7.3 XRF results

XRF was performed on one sample from each location, in addition to one scapolite rock from nearby in the Modum area. Both main and trace elements were run (table 7.13-7.14). Loss of ignition in these samples ranges from 0.55 to 4.41 %, reflecting loss of CO_2, H_2O and lightweight elements like B and Li. All samples but MOD36 show relatively poor totals, which can be due to an instrumental error, or missing elements like Cl, which is an element proven present by EPMA in various minerals. Some elements are below the detection limits from table 6.2. The contents of Cu and Cs are below the detection limits in several samples, while the Th-contents are all below. In addition, the Fe_2O_3-content is higher than the maximum detection limits in MOD36 and MOD41, which decreases the accuracy. All samples are remarkably low in MnO.

Table 7.13: XRF results, main elements.

Pr.mrk.	**MOD 35**	**MOD 36**	**MOD 37**	**MOD 38**	**MOD 39**	**MOD 40**	**MOD 41**	**MOD HJK**	**HJ 002**	**HJ 003**	**MOD 7 scapolite**
SiO_2 (%)	50.13	46.38	61.01	52.69	53.80	53.07	57.23	89.22	63.88	40.95	48.25
TiO_2 (%)	0.94	1.26	0.90	0.78	1.00	1.23	1.18	0.12	1.09	1.62	1.59
Al_2O_3 (%)	13.43	7.25	8.58	11.34	11.88	9.15	4.67	4.09	10.66	11.80	16.62
Fe_2O_3 (%)	9.80	36.67	13.18	15.41	13.74	23.38	29.82	0.93	7.32	17.88	6.15
MgO (%)	15.00	4.56	6.80	7.87	7.67	6.70	2.63	0.38	6.29	12.12	6.90
MnO (%)		0.01	0.01	0.01	0.01	0.02	0.01	0.01	0.01	0.22	0.01
CaO (%)	0.11	0.46	1.70	2.56	1.44	0.62	0.37	0.08	0.88	9.19	5.61
Na_2O (%)	1.33	1.44	3.30	3.86	4.36	1.00	0.99	0.10	1.54	2.12	4.99
K_2O (%)	2.49	0.25	0.88	1.53	1.79	0.05	0.57	1.96	2.63	0.35	3.40
P_2O_5 (%)	0.18	0.12	0.14	0.13	0.13	0.30	0.28	0.05	0.23	0.05	0.16
LOI (%) 1000°C	4.41	1.48	1.35	1.73	1.63	2.86	1.03	0.55	2.73	0.76	3.53
Sum (%)	97.83	99.87	97.86	97.92	97.45	98.38	98.77	97.48	97.26	97.05	97.21

Table 7.14: XRF results, trace elements.

Pr.mrk.	**MOD 35**	**MOD 36**	**MOD 37**	**MOD 38**	**MOD 39**	**MOD 40**	**MOD 41**	**MOD HJK**	**HJ 002**	**HJ 003**	**MOD 7 scapolite**
Sc (PPM)	24	18	20	19	14	15	7	4	16	29	22
V (PPM)	83	138	61	60	65	175	126	13	103	222	218
Cr (PPM)	45	38	45	62	62	58	40	1	32	298	102
Co (PPM)	10	60	35	48	32	39	83	136	49	139	41
Ni (PPM)	68	96	57	66	66	77	68	6	53	414	124
Cu (PPM)	4	7	3	5	3	4	8	5	2	80	2
Zn (PPM)	4	3	7	9	11	15	6	7	5	62	4
Ga (PPM)	21	23	16	18	20	21	16	7	17	20	23
As (PPM)	6	26	24	21	23	19	24	30	17	5	8
Rb (PPM)	76	17	42	73	91	7	24	30	72	8	147
Sr (PPM)	26	13	42	69	46	16	11	25	20	155	130
Y (PPM)	28	9	22	24	17	19	16	11	24	33	14
Zr (PPM)	193	552	263	192	208	235	356	147	207	100	90
Nb (PPM)	12	10	15	7	16	8	12	5	12	4	7
Sb (PPM)	5	2	7	1	5			5	4		2
Cs (PPM)			13							1	9
Ba (PPM)	20	12	21	22	12	11	28	133	71	64	51
La (PPM)	23	15	7	20	9	15	12		11	21	10
Ce (PPM)	70	16	38	48	46	35	22	42	74	30	38
Pb (PPM)											
Th (PPM)	5	4	5	4	5	8	3	4	4	1	3
U (PPM)		3				1	1		1		1

All samples are rich in SiO_2, reflecting large amounts of quartz and feldspar. MODHJK contains extremely large amounts of SiO_2, because this rock is made up of basically only quartz and feldspar. HJ003, the only metamorphosed mafic igneous rock without quartz and feldspar, has the lowest amounts of SiO_2. MOD41 contains mostly quartz and hematite, giving this rock a chemical composition of mostly SiO_2 and Fe_2O_3. Fe_2O_3 is the highest in MOD36, because this

rock contains large clusters of hematite. This rock also contains low amounts of MgO. MgO is by far the highest in MOD35, reflecting a high content of phlogopite.

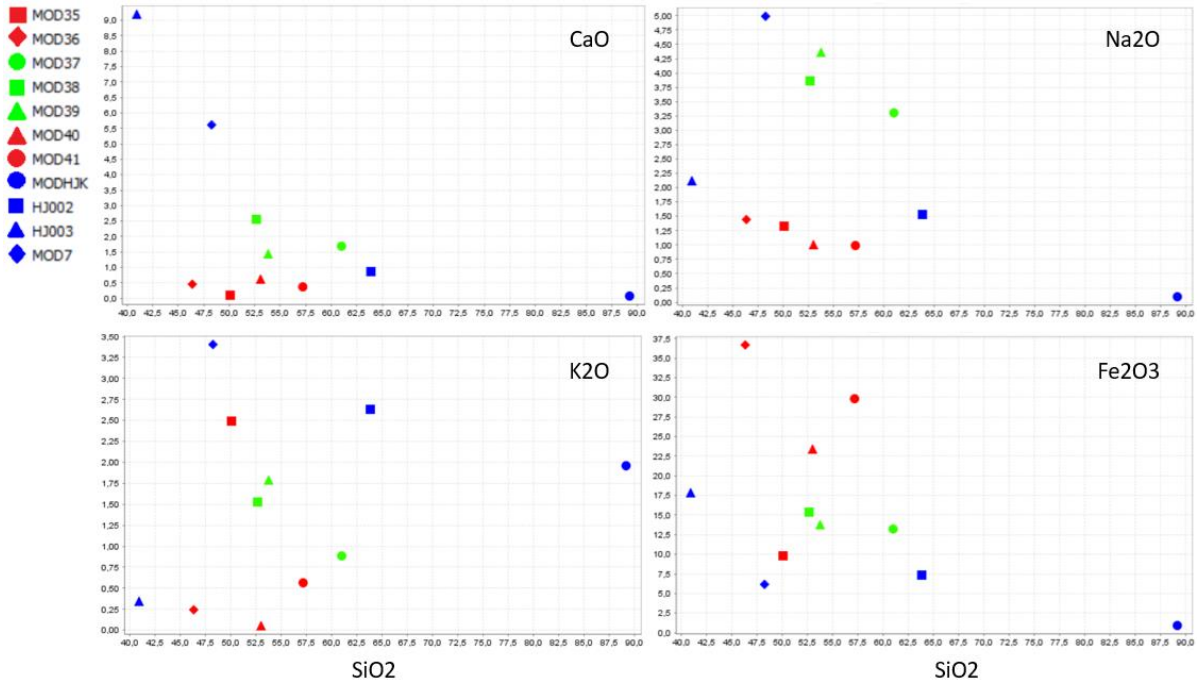

Figure 7.24: Harker diagrams showing the whole rock chemistry, wt.% of SiO_2 plotted against the other main elements in the samples.

CaO is elevated in MOD37, MOD38 and MOD39, consistent with the fact that these rocks contain calcic amphibole. HJ003 and MOD7, the hornblendite and scapolite rock, also contain Ca-amphibole, similarly showing high Ca-content. Na_2O amounts are relatively low compared to other albite-rich rocks, suggesting that plagioclase may be concentrated in big crystals. This can be seen in MOD37, MOD38 and MOD39. These rocks have the highest content of Na_2O, and display large oligoclase crystals. K_2O is highest in MOD7, together with MOD35 and HJ002 which contain much phlogopite. These tendencies can be seen in the Harker diagrams in figure 7.24, where SiO_2 is plotted against various other elements.

The hornblendite (HJ003) and the scapolite rock (MOD7) display the highest V-content, usually related to liquid in mafic magmas. HJ003 also shows the highest content or Cr, Co, Ni, Cu, and Zn, implying that is was derived from basalt. The Zr-content is quite high in all the rocks, and is related to zircon content. Ba stands out with a high content only in MODHJK. Pb, Th and U contents are very low, reflecting an oxidized environment, in contrast to a reduced black shale.

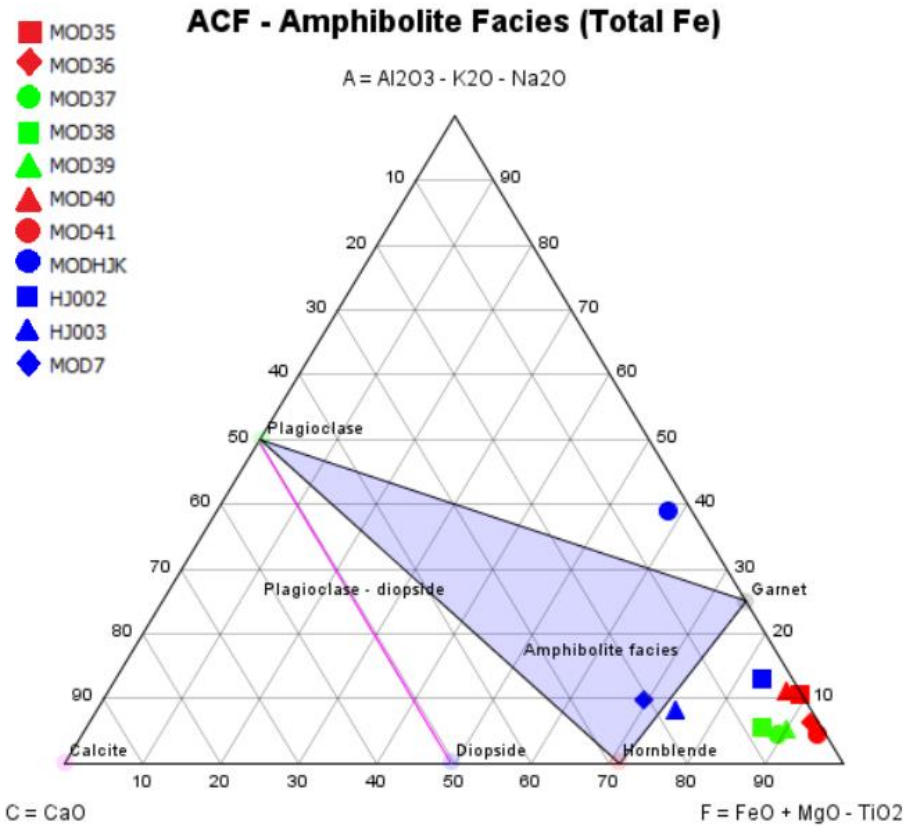

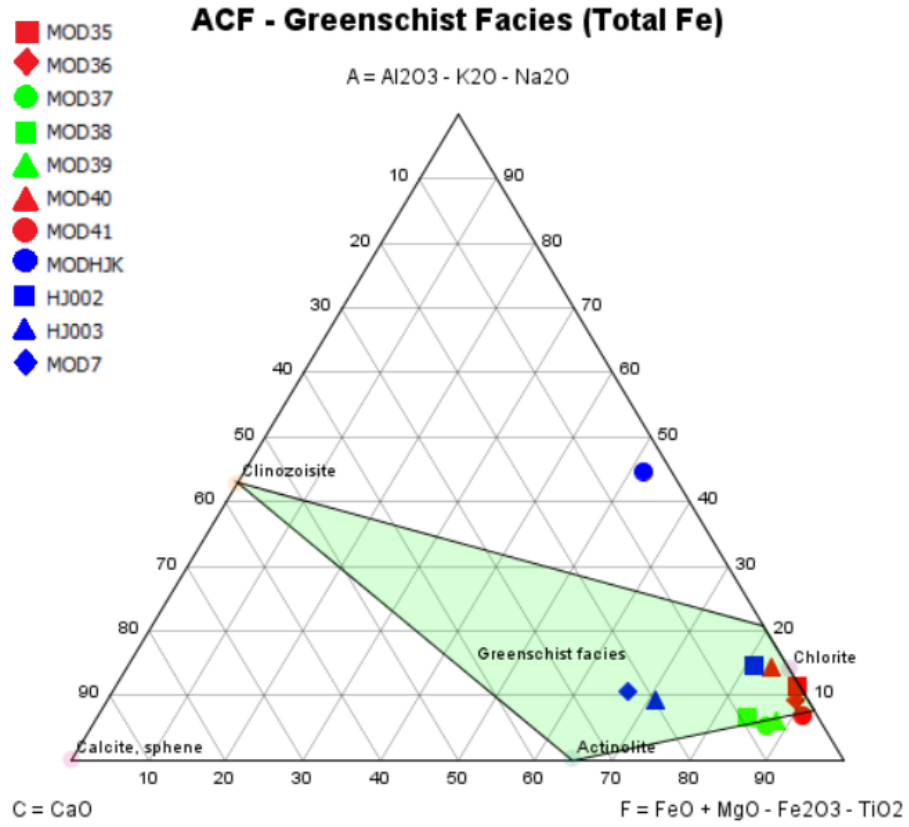

Figure 7.25: ACF diagrams with XRF main element chemistry for amphibolite facies and greenschist facies.

The geochemical results from XRF-main elements are plotted in two different ACF-diagrams to investigate which diagram fits the best. The tie-lines connect the mineral assemblages in amphibolite facies and greenschist facies (fig. 7.25). The two diagrams in figure 7.25 are based on index minerals for the specific facies. As mentioned in chapter 4.2.1, mafic rocks in amphibole facies are based on the presence of hornblende and plagioclase (Winter, 2010), and in metasedimentary rocks, the presence of quartz, albite, muscovite, chlorite, rutile and commonly biotite and tourmaline (Graham et al., 1983). Greenschist facies in mafic rocks are based on chlorite, albite, epidote, actinolite and quartz, and is of slightly lower metamorphic grade than amphibolite facies (Winter, 2010). All samples plot within the greenschist facies field, but some lack chlorite. These contain amphibole, implying that the rocks went through a higher metamorphic grade. Only some fall into the amphibolite facies field, which can be due to too many components or a particularly high amount of one component in the rocks, like the high Mg-contents here. The rocks clearly fit best into the greenschist facies area, but kyanite and sillimanite never belong to greenschist facies, pointing to these rocks being very atypical.

For sedimentary rocks, it is not so easy to find a simple relationship between the mineralogy and chemical composition as it is for igneous rocks (Rollinson, 1993). It is therefore common to differentiate between mature and immature sediments. In addition, a low SiO_2/Al_2O_3 ratio implies a high content of clay and feldspar. The figures below are not too useful for naming purposes, but show some relationships between elemental composition, mineralogy and rock type. However, Na and K can be mobilized during diagenesis and metamorphism, meaning the diagrams must be used with caution.

From figures 7.27-7.29, most samples are classified as clay-rich, sedimentary rocks. MOD41 and HJ002 are richer in quartz and feldspar than MOD35-MOD40, and are therefore classified as more sandy. MODHJK is the coarsest rock containing mostly quartz and feldspar, hence this sample plots as arkose.

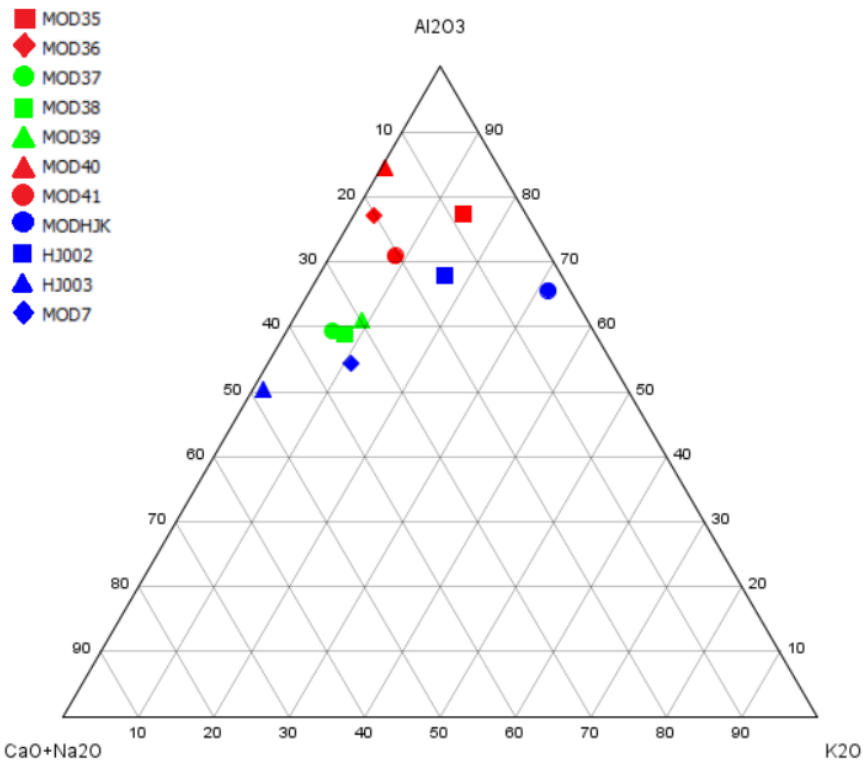

Figure 7.26: Showing weathering trends, closer to Al_2O_3 means more advanced weathering. After Rollinson (1993).

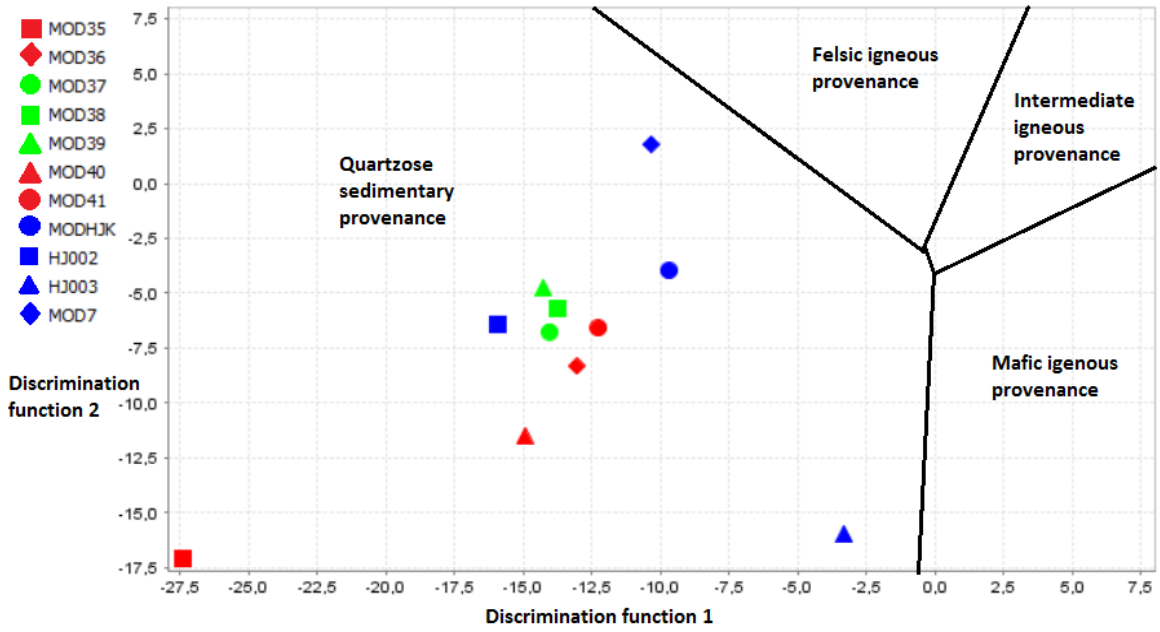

Figure 7.27: Discriminant function diagram for the provenance signatures of sandstone-mudstone suites using major elements. Discriminant function 1 = - 1.773TiO_2 + 0.607Al_2O_3 + 0.76Fe_2O_3(total) - l.5MgO + 0.616CaO + 0.509Na_2O - 1.224K_2O - 9.09. Discriminant function 2 = 0.445TiO_2 + 0.07 Al_2O_3 - 0.25Fe_2O_3(total) - 1.142MgO + 0.438CaO + 1.475Na_2O + 1.426K_2O - 6.861. Note that all Fe_2O_3 is assumed to be in hematite and therefore omitted, except for in HJ003. After Rollinson (1993).

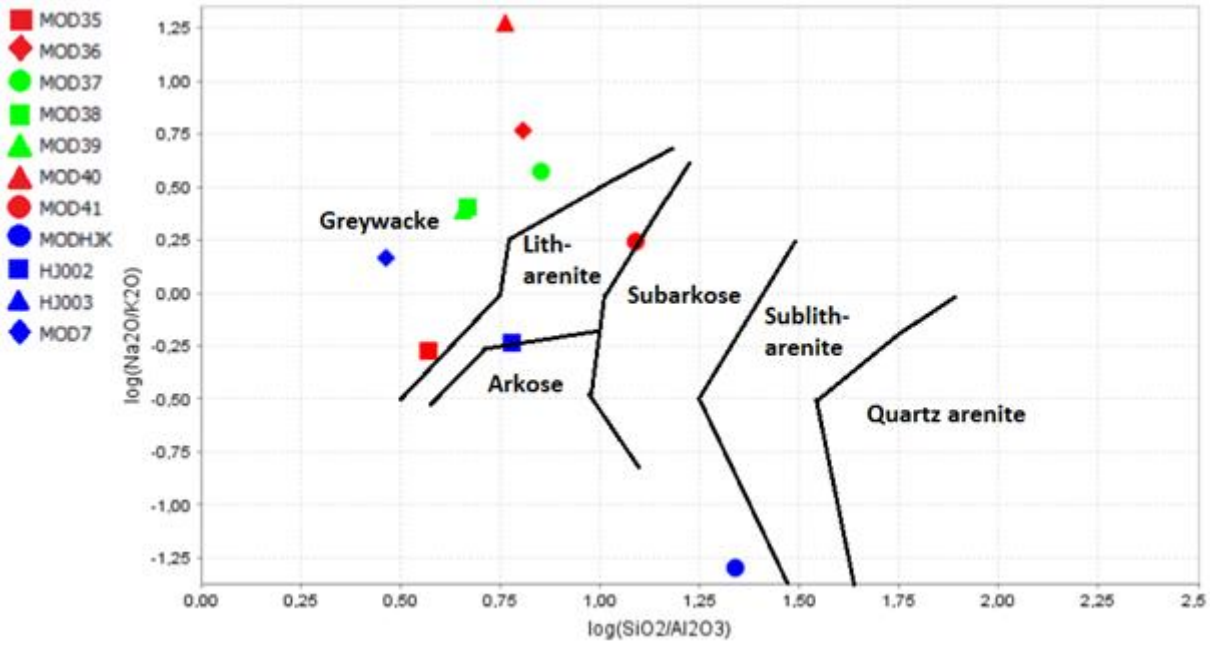

Figure 7.28: The classification of terrigenous sandstones using log(Na_2O/K_2O) vs log(SiO_2/Al_2O_3). After Rollinson (1993).

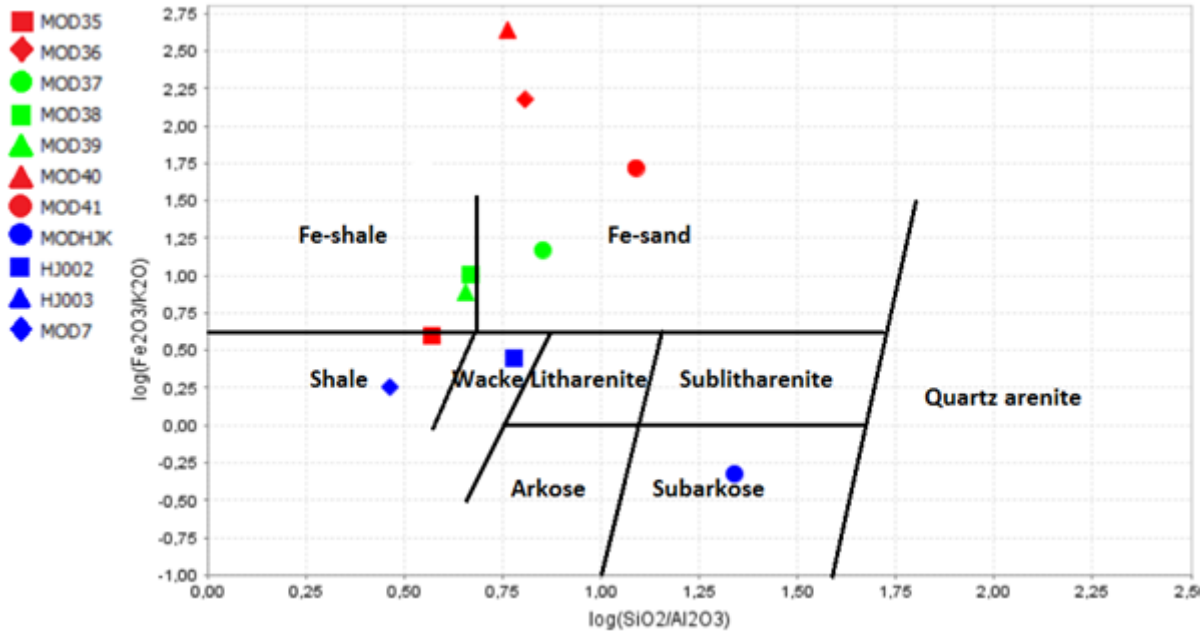

Figure 7.29: Classification of terrigenous sandstones and shales using log(Fe_2O_3/K_2O) vs log(SiO_2/Al_2O_3). After Rollinson (1993).

8. Petrophysical properties

Measurements on density, susceptibility and NRM were measured on 72 samples. Samples from MOD36 were un-oriented blocks, while the rest of the samples were oriented cores. The samples are all highly oxidized with titanohematite as the main magnetic mineral.

Table 8.1: Summary of magnetic properties. Original data can be found in Appendix A.

	Estimated	Density				NRM			
	oxide amount	Max	Min	Average	StDev	Max	Min	Average	StDev
MOD35	5 %	2.88	2.77	2.84	0.038	1.44	0.80	1.15	0.247
MOD36	20 %	3.15	2.91	3.00	0.104	14.05	4.34	9.35	3.752
MOD37	5 %	2.82	2.79	2.80	0.016	2.80	2.09	2.50	0.373
MOD38	8 %	2.90	2.80	2.85	0.040	4.80	2.78	3.77	0.750
MOD39	5 %	2.90	2.76	2.83	0.045	2.41	1.39	1.91	0.337
MOD40	18 %	3.54	2.93	3.12	0.216	65.32	4.38	20.24	20.973
MOD41	17 %	3.83	2.78	3.15	0.298	24.41	1.59	9.82	6.533
HJ002	5 %	2.77	2.71	2.74	0.048	3.50	1.89	3.00	0.003
HJ003	3 %	3.28	3.21	3.25	0.024	0.22	0.02	0.12	0.564
MODHJK	Tr	2.63	2.52	2.60	0.049	0.01	0.00	0.00	0.139
	Estimated	**Susceptibility**				**Q-value**			
	oxide amount	**Max**	**Min**	**Average**	**StDev**	**Max**	**Min**	**Average**	**StDev**
MOD35	5 %	2.7E-04	2.5E-04	2.6E-04	1.0E-05	142.99	70.89	108.48	25.130
MOD36	20 %	8.6E-03	2.7E-03	4.8E-03	2.0E-03	64.70	38.78	49.58	10.701
MOD37	5 %	5.8E-04	5.4E-04	5.6E-04	1.7E-05	127.28	90.97	110.04	18.223
MOD38	8 %	6.4E-04	3.2E-04	5.3E-04	1.1E-04	211.93	111.66	179.71	31.587
MOD39	5 %	7.2E-04	4.7E-04	6.1E-04	9.0E-05	98.62	58.30	77.14	12.719
MOD40	18 %	5.6E-03	1.6E-03	3.0E-03	2.0E-03	287.87	68.24	130.90	76.030
MOD41	17 %	9.4E-04	2.4E-03	4.9E-03	3.0E-03	162.62	22.93	56.11	42.508
HJ002	5 %	5.2E-04	3.6E-04	4.6E-04	1.1E-05	179.96	129.54	159.01	1.605
HJ003	3 %	5.5E-03	1.7E-03	3.6E-03	5.5E-05	0.97	0.03	0.64	15.535
MODHJK	Tr	6.6E-05	3.9E-05	4.7E-05	2.7E-03	3.92	0.00	1.59	0.465

8.1 Densities

Measured densities display a large range. For MOD35-MOD41, the densities are ranging from 2.76 to 3.54 g/cm^3. Of these, MOD36, MOD40 and MOD41 show the highest density, due to higher contents of oxides. These cores also show a large variation between the different samples, which implies that the oxide content varies in the cores. HJ002 is in the lower range, with a mean of 2.74 g/cm^3, while MODHJK is standing out with the lowest mean density of 2.59 g/cm^3, reflecting a content of >90% felsic minerals. HJ003 is in the upper range with a mean of 3.25 g/cm^3, reflecting a high content of mafic minerals rather than oxides.

8.2 Susceptibility values

The susceptibility values in the measured samples are generally very low, with a total mean of $1.92*10^{-3}$ SI. This is comparable with the values reported by Fabian et al. (2008), which found rocks from Modum to have an average susceptibility of $7*10^{-3}$ SI.

Three groups of susceptibility distributions are visible (fig. 8.1). MODHJK has the absolutely lowest susceptibility values, with a mean of $4.72*10^{-5}$ SI. MOD35, MOD37-MOD39 and HJ002 are in the middle group, ranging from $3.24*10^{-4}$ to SI to $7.21*10^{-4}$ SI, while MOD36, MOD40, MOD41 and HJ003 are in the group with the highest susceptibility, ranging from $9.44*10^{-4}$ to $8.65*10^{-3}$ SI.

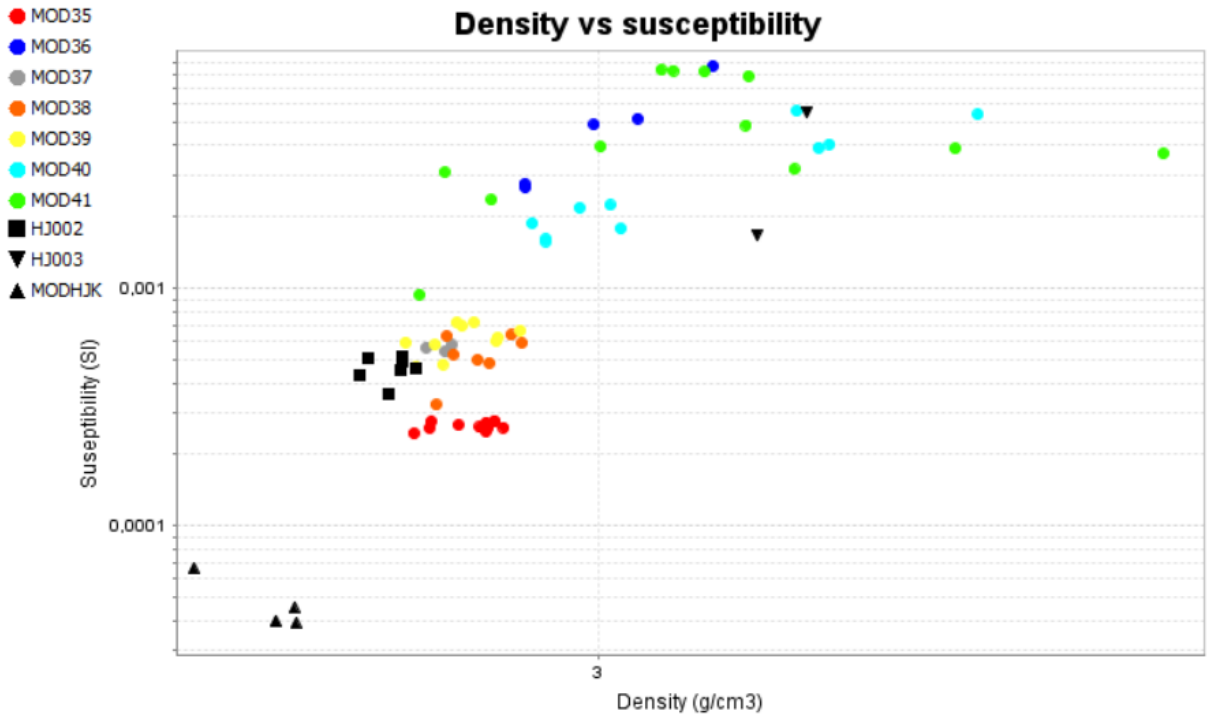

Figure 8.1: Density values (g/cm^3) plotted versus susceptibility values (SI).

8.3 NRM intensities

The NRM intensities are generally high, with a total mean of 6.30 A/m, reflecting oxide amounts and micro-structures. Fabian et al. (2008) reported average NRM values in rocks from Modum to be 1.8 A/m, which is quite a lot lower, but this was in sillimanite gneiss with extremely low oxide amounts. The NRM intensities plotted versus density can be seen in figure 8.2. MOD35, MOD37-MOD39 and HJ002 can be recognized as one group, with intensities

ranging from 0.80 to 4.46 A/m. MOD36, MOD40 and MOD41 show higher NRM intensities, and a substantially larger range. These are ranging from 4.35 to 65.32 A/m. MOD40 is the core with the absolutely highest values, but this can also be divided into two groups of an average NRM intensity of 7.11 and 41.71 A/m.

MODHJK and HJ003 stands out with much lower intensities, with a mean NRM intensity of resp. 0.003 and 0.12 A/m, indicating lower amounts of oxides for MODHJK and other types of oxides for HJ003, which contains ilmenite in contrast to the others containing titanohematite. In addition, the NRM vs density plot shows low NRM for density <2.7 g/cm^3 and much higher density above 2.7 g/cm^3. Density is primarily controlled by rock type; however, a higher oxide content will increase density of the sample from the same rock type.

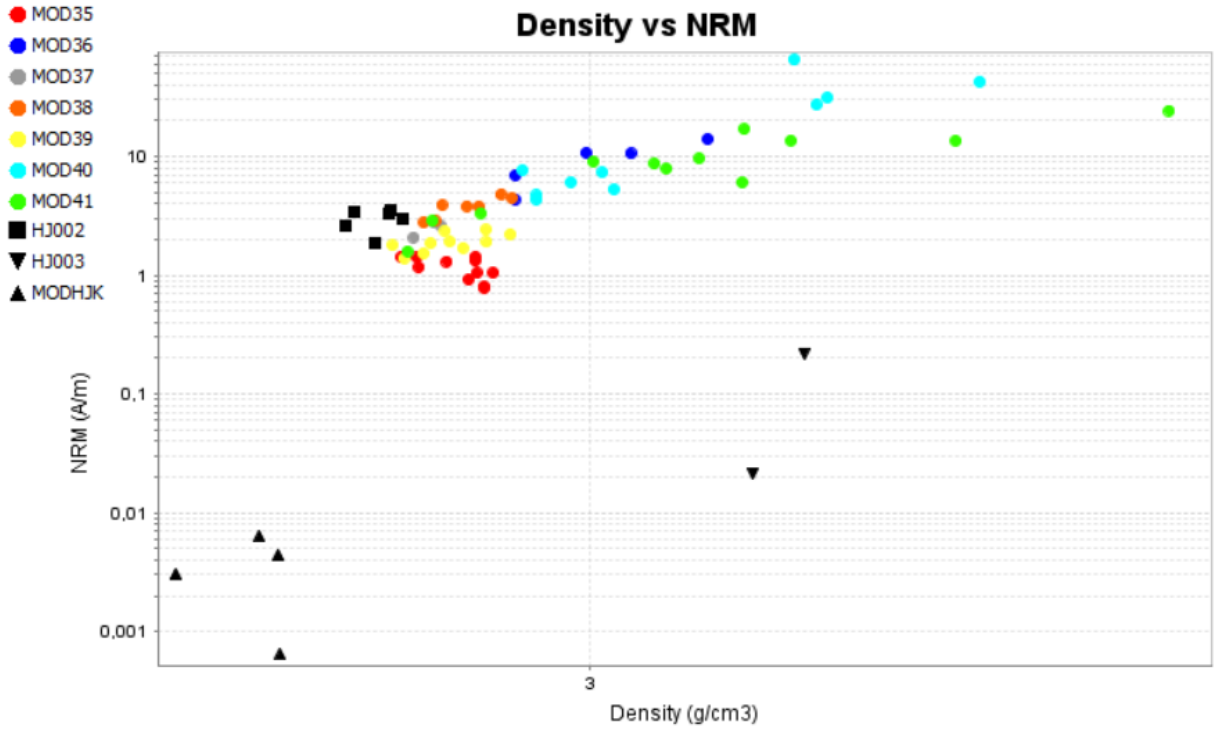

Figure 8.2: Density values (g/cm^3) plotted versus NRM values (A/m).

Figure 8.3 shows the directions of the NRM intensity vectors. It is obvious that the rocks have a reversed paleomagnetic vector with a mean declination of 293.6° and inclination of -42.3°. Robinson et al. (2014) found that rocks from Modum had a declination of 276° and inclination of -67°, which is comparable to this. This is at a large angle to the present Earth field vector which have a declination of 2° and inclination of +72.5°.

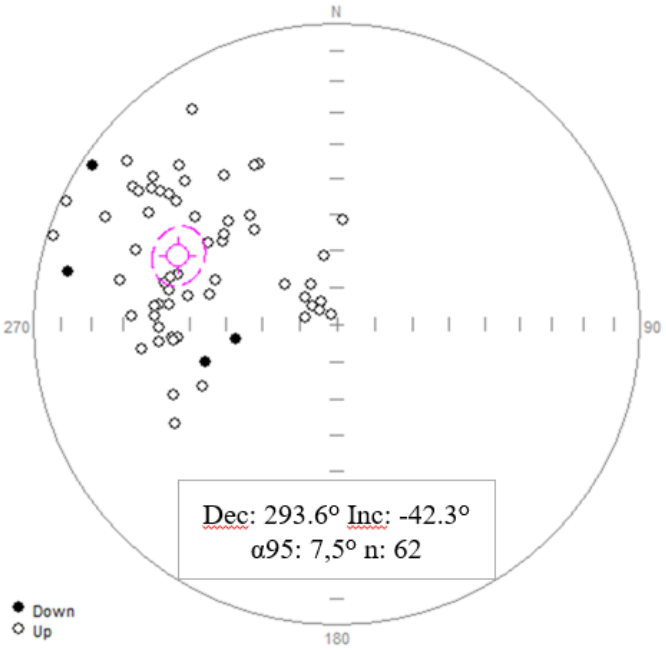

Figure 8.3: Plot of directions of the NRM intensities.

8.4 Köenigsberg ratio (Q-value)

Q-value was calculated using a local field of 40.6 A/m, using the formula

Q = NRM / (susceptibility * local field)

Calculation of Q-value revealed high values and a large variation. Fabian et al. (2008) states that the average Q-value from a large study on Modum rocks were found to be 92, with nearly 70% of the samples having Q-values above 10. Mean Q-value found in this study is 96, with most values above 10. The only samples with Q-value below 10, are from MODHJK and HJ003. MODHJK and HJ003 show a mean Q-value of 1.3, while MOD35-MOD41 and HJ002 together display a mean of 106. These are ranging from 23 to 288.

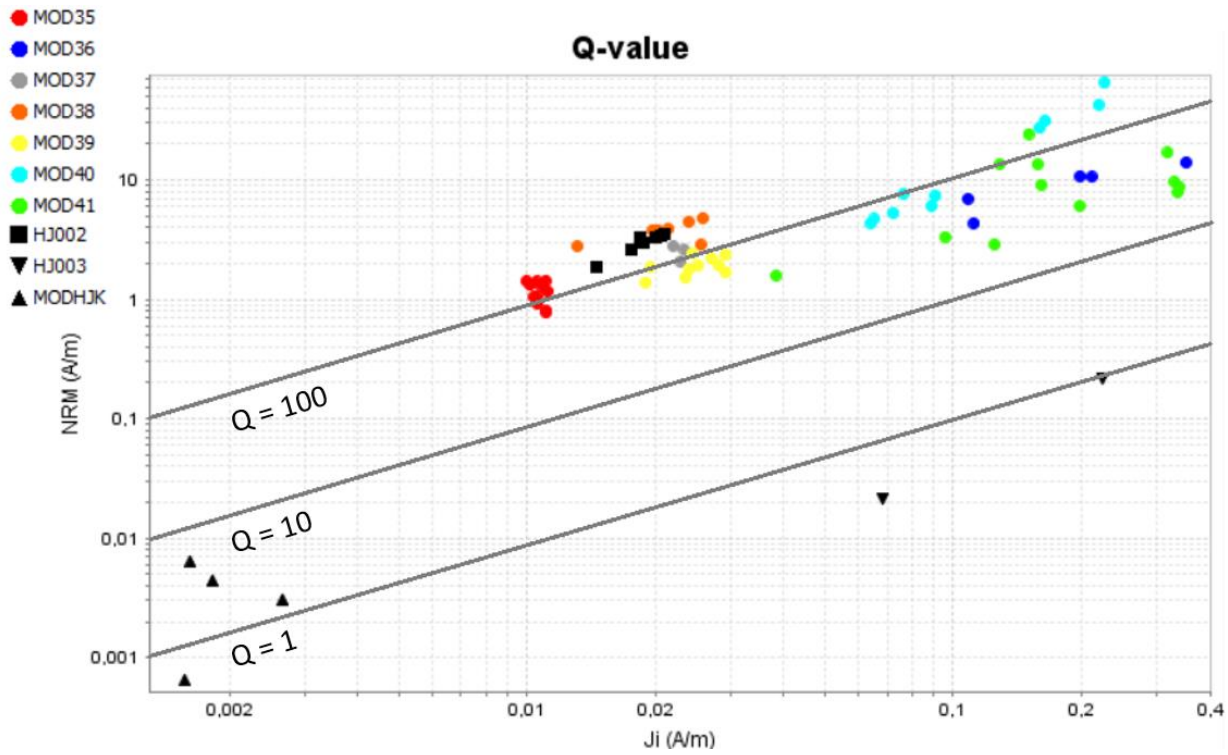

Figure 8.4: Log-log plot of NRM (A/m) vs induced magnetization J_i (A/m). Q-value diagonals indicate the distribution of Q-values for each specimen.

8.5 AF demagnetization

AF demagnetization curves were selected for 10 samples, and all curves are included in appendix B. In figure 8.5, one curve from each location can be seen. Most samples showed a small increase in magnetization at low fields. MOD35, MOD37, MOD38, MOD39 and HJ002 had a M_{max} at ~40 mT, while MOD40 and MOD41 display this peak at lower fields, around 20 mT. MODHJK shows the same behaviour, but with M_{max} at ~60 mT.

MOD35, MOD37, MOD38, MOD39, MOD40 and MOD41 displayed an initial increase in NRM by up to 20%, while HJ002 increased with 30%. MOD36 and HJ003 did not show an initial increase. After M_{max}, MOD35-MOD41 showed a rapid decrease in remanent magnetization. At fields with magnitudes of 100 mT, these samples had less than 10% of the magnetization left. The median destructive field (MDF) for MOD36, MOD40 and MOD41 is around 30 mT, while for MOD35, MOD37, MOD38 and MOD39, these values are around 70 mT. The curve for HJ002 follows the same pattern, but loses its magnetization slower, with MDF of 50 mT. MODHJK also follows this pattern, but has a higher MDF, around 100 mT. Both HJ002 and MODHJK has less than 10% of the magnetization remaining at 150 mT. HJ003

stands out, showing a steady decrease, reaching M(90%) at only 43 mT. This is very low compared to the rest. MDF is plotted versus NRM in figure 8.7, showing a clear correlation between the two and the already recognized grouping.

Figure 8.6 shows one Zijderveld diagram for each sample. These plots show information about the direction and intensity of the remanent magnetization, and how this changes during AF demagnetization. The Zijderveld plots can give information about whether the samples are composed by one or more components. If the lines are straight, this implies only one component, and a curved or bent line indicates more than one component. Abrupt changes of direction imply non-overlapping demagnetization spectres.

As seen from the figure, basically all samples have bent lines, indicating more than one component. Note that *b. MOD36* and *j. MODHJK* are not oriented. MOD36, MOD37 and HJ002 show sudden changes, while MOD35, MOD38, MOD39, MOD40 and MOD41 have more smooth curves, indicating overlap in demagnetization spectres. The straightest lines are found at HJ003 and MODHJK, though these ones also show signs of more phases.

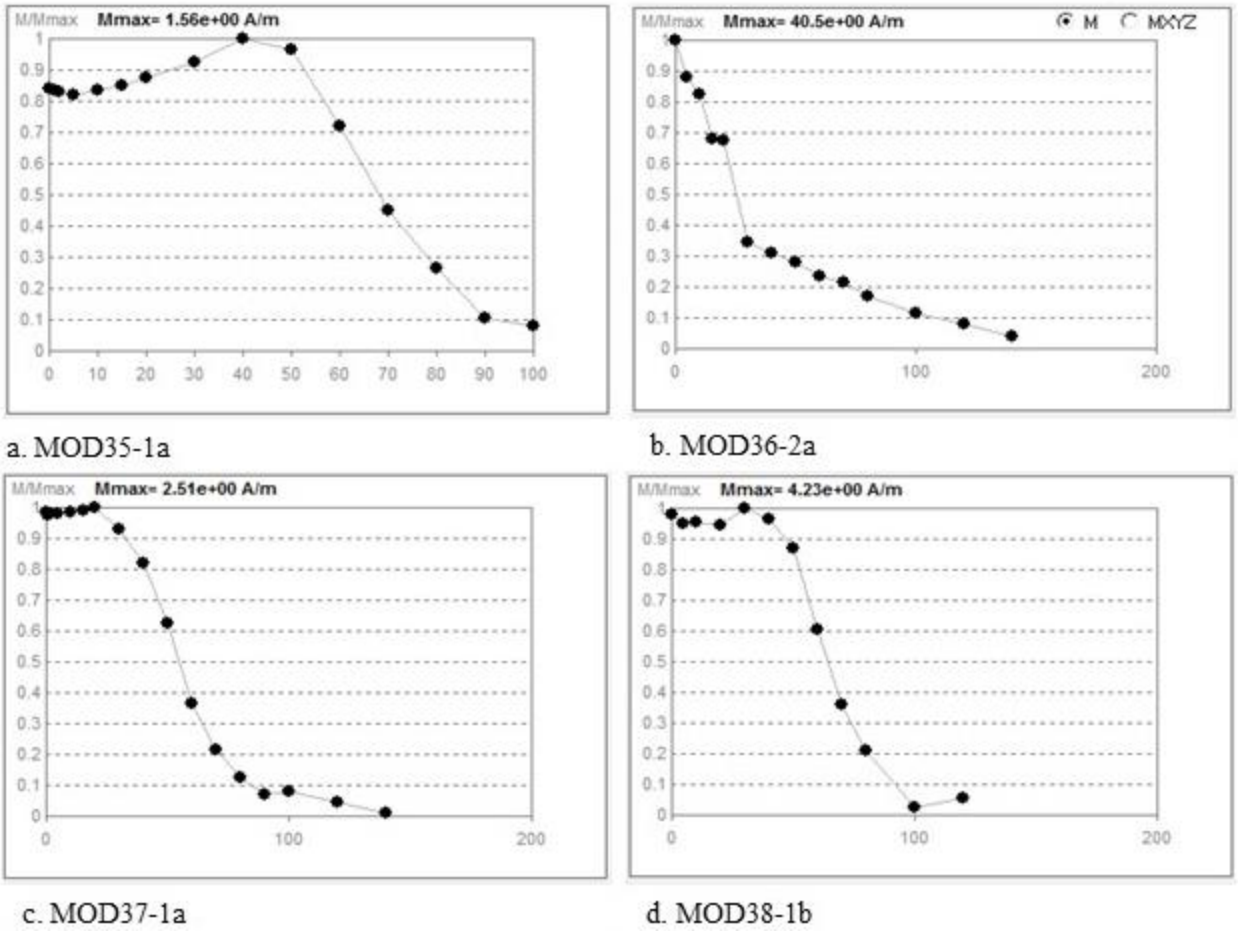

a. MOD35-1a

b. MOD36-2a

c. MOD37-1a

d. MOD38-1b

Figure 8.5: AF demagnetization curves for selected samples.

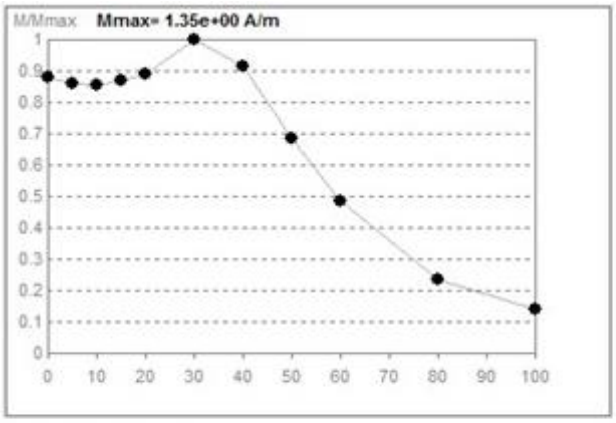

e. MOD39-4t

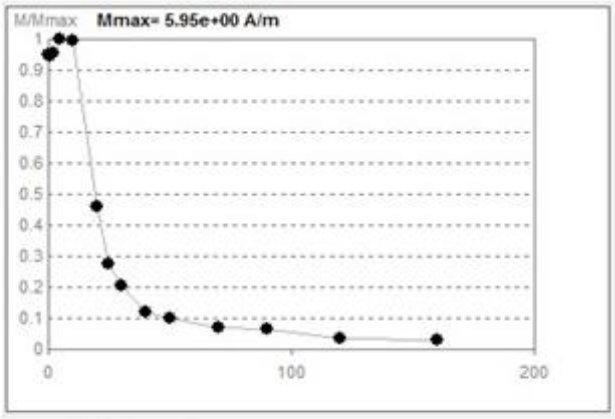

f. MOD40-1b

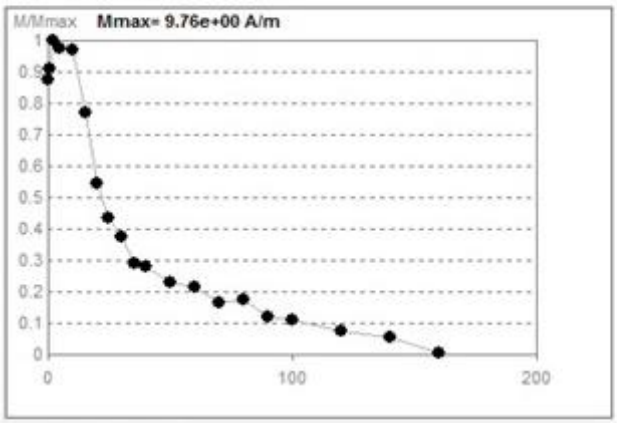

g. MOD41-4b

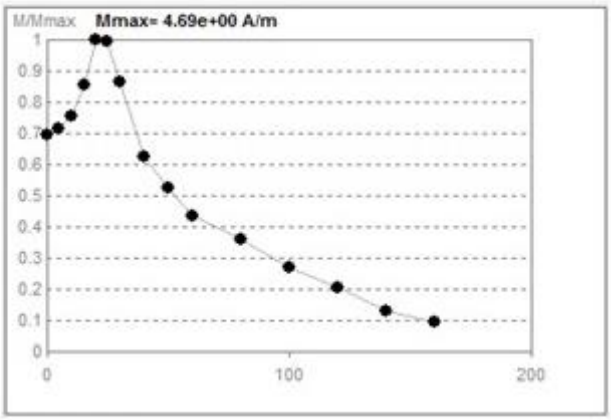

h. HJ002-aa

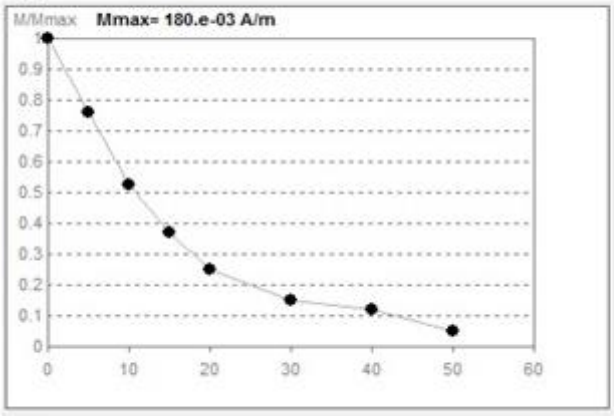

i. HJ003-aa

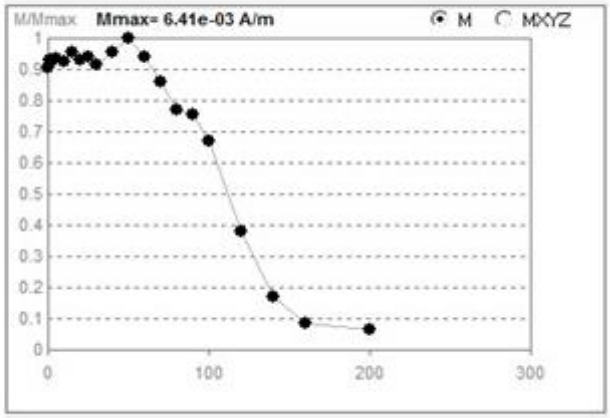

j. MODHJK-1a

Figure 8.5 (cont.): AF demagnetization curves for selected samples.

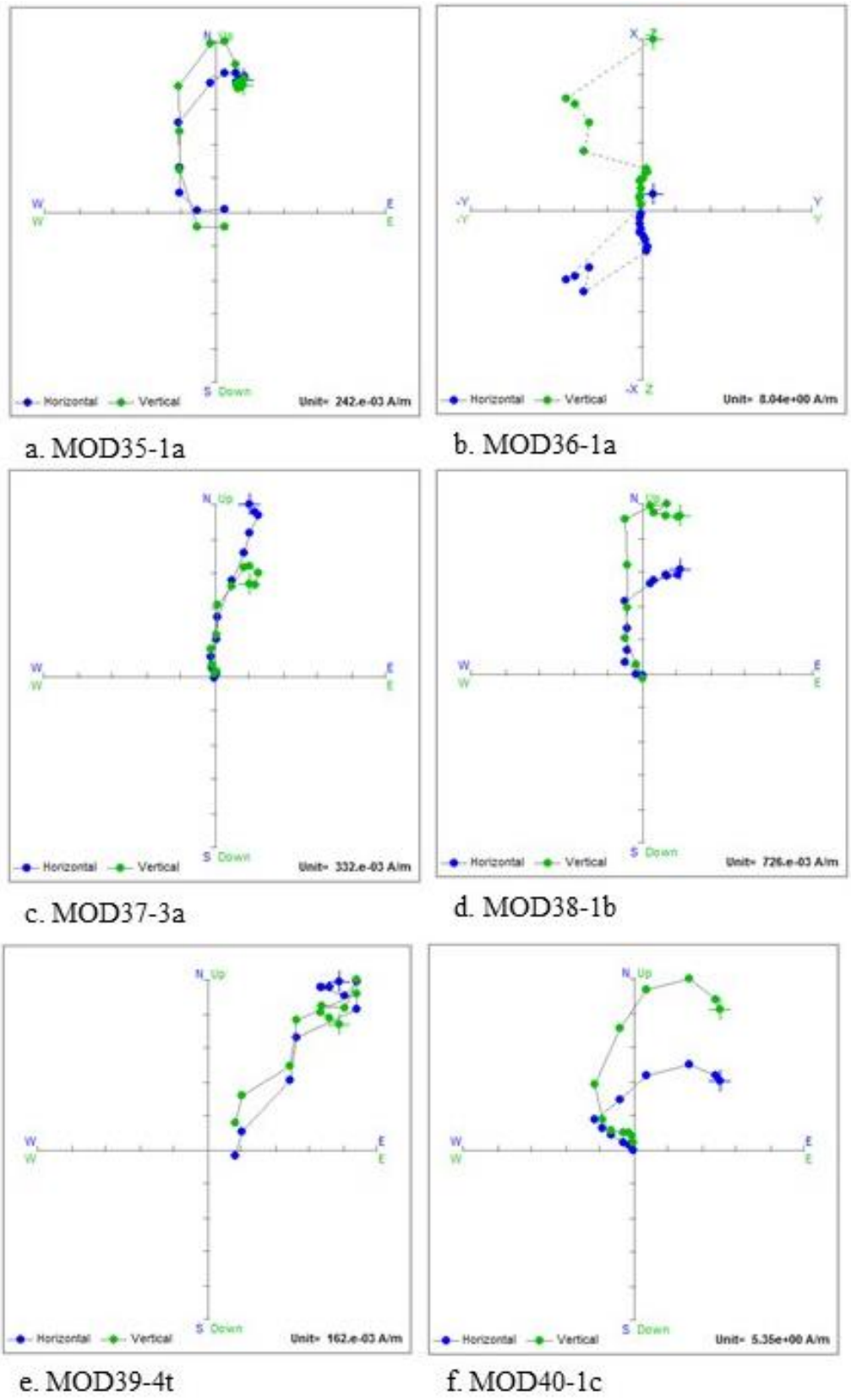

Figure 8.6: Zijderveld diagrams from AF demagnetization for selected samples. Note that b. MOD36-1a and j. MODHJK-1a are not oriented!

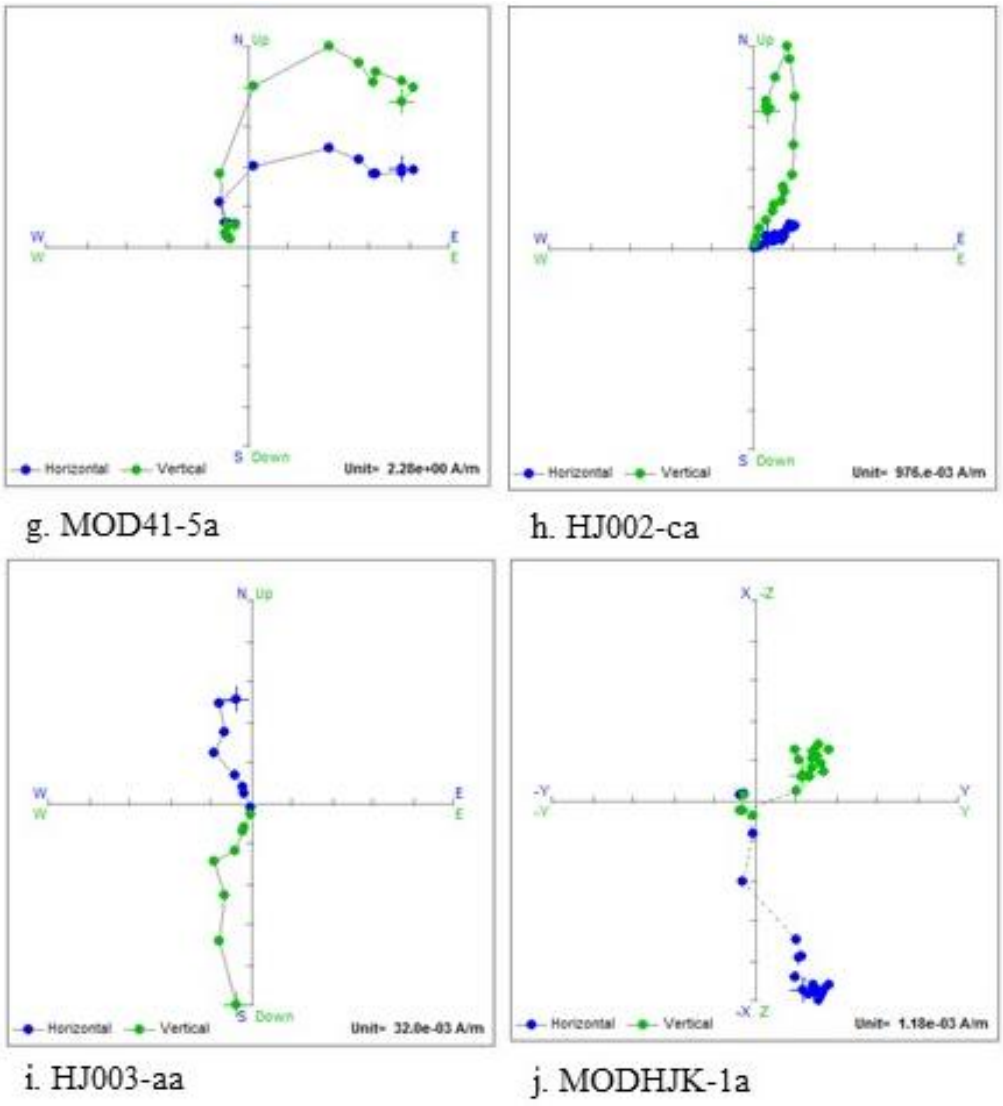

g. MOD41-5a

h. HJ002-ca

i. HJ003-aa

j. MODHJK-1a

Figure 8.6 (cont.): Zijderveld diagrams from AF demagnetization for selected samples. Note that b. MOD36-1a and j. MODHJK-1a are not oriented!

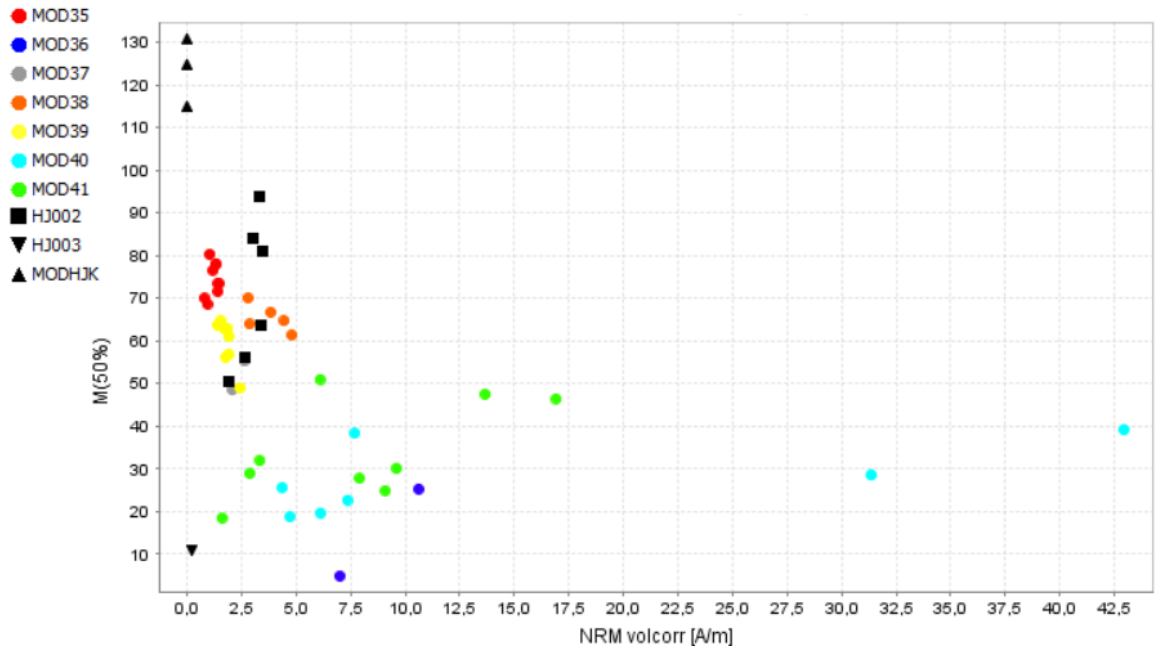

Figure 8.7: NRM plotted versus M(50%); field intensity where 50% of the magnetization is lost.

8.6 Temperature dependent susceptibility

The curves displaying temperature versus susceptibility were measured at a magnetic field of 200 A/m, which is about four times stronger than the Earth's field. All samples were measured in air, and measured at low temperatures both before and after heating to 700°C. Figure 8.5 shows all measured curves. The green curve is after heating. Some curves show a deviation between end point on low temperature curves and starting point at high temperature curves, which can be due to mechanical discrepancies or errors in calibration.

Sample MOD35-MOD41 all showed a peak in susceptibility between 600 and 630°C, referred to as Hopkinson's peak, followed by a steep decrease. The mean value of inflection for these curves were 626°C, ranging between 612 and 641°C. All measured curves can be seen in figure 8.8. The recorded Neel temperatures imply presence of titanium in the hematite, and by using the software IgorPro, the titanium content was calculated. An overview over the results are included in table 8.2.

Two groups of similar curves can be recognized. MOD36, MOD40 and MOD41 display no Verwey transition at low temperatures, and no other phases during heating. These curves show a sharp drop with a mean Neel temperature of 614°C and a slightly lower Hopkinson's peak and susceptibility during cooling. The curves display good reversibility, but some alteration. In addition, the curves show a distinct peak around 100°C.

MOD37, MOD38, MOD39 show a clear Verwey transition at low temperatures, and a minor increase in susceptibility around 300°C. The curves then decrease slightly around 550°C. The Neel temperatures are somewhat higher, with an average of 634°C. These curves show a significantly higher Hopkinson's peak during cooling, together with a clear Verwey transition also during the second cold run. However, this peak is lower than during the first measurement.

The MOD35-curve show mostly the same tendency as MOD37-MOD39, except for the absence of Verwey transitions. This curve show a decrease in susceptibility until 200°C, and a decrease around 540°C. The Neel temperature is similar to MOD37-MOD39 and the curve display the same high Hopkinson's peak.

Table 8.2: Results from thermoremanent susceptibility measurements. All temperatures are in Celsius. T_V1: Verwey transition temperature in the first cold measurement. T_V2: Verwey transition temperature in the second cold measurement, done after heating up to 700°C. T_N1: Neel temperature of hematite, measured during heating. T_N2: Neel temperature of hematite, measured during cooling, after heating up to 700°C. T_C: Curie temperature of magnetite, measured during heating. %Ti is estimated from Neel temperatures using IgorPro.

Sample	**T_V1**	**T_V2**	**T_N(hem)**	**T_N (hem)**	**T_C (magn)**	**%Ti**
MOD35			635	638		7
MOD36			613	612		10
MOD37	-108	-96	635	638	554	7
MOD38	-122	-104	627	631		8
MOD39	-120	-106	641	644	552	7
MOD40			616	612		10
MOD41			612	610		10
HJ002		-142	619	618	574	10
HJ003					559	
MODHJK					563	

HJ002, HJ003 and MODHJK separates from the others. None of these curves display Verwey transitions during the first measurements. HJ002 shows a minor increase at 450-500°C, followed by a slight decrease around 580°C, and a sharp drop with a Neel temperature of 619°C. Like MOD37-MOD39, the Hopkinson's peak increased significantly during cooling, and the curve has the same peak at around 100°C as MOD36, MOD40 and MOD41. In HJ003, the susceptibility decreases steadily until the drop at 559°C, and almost perfect reversibility.

MODHJK show a distinct increase around 450°C with a peak at 500°C and a Curie temperature of 563°C. This curve display an extreme increase during cooling with a peak at 350°C, followed by a steady decrease until room temperature.

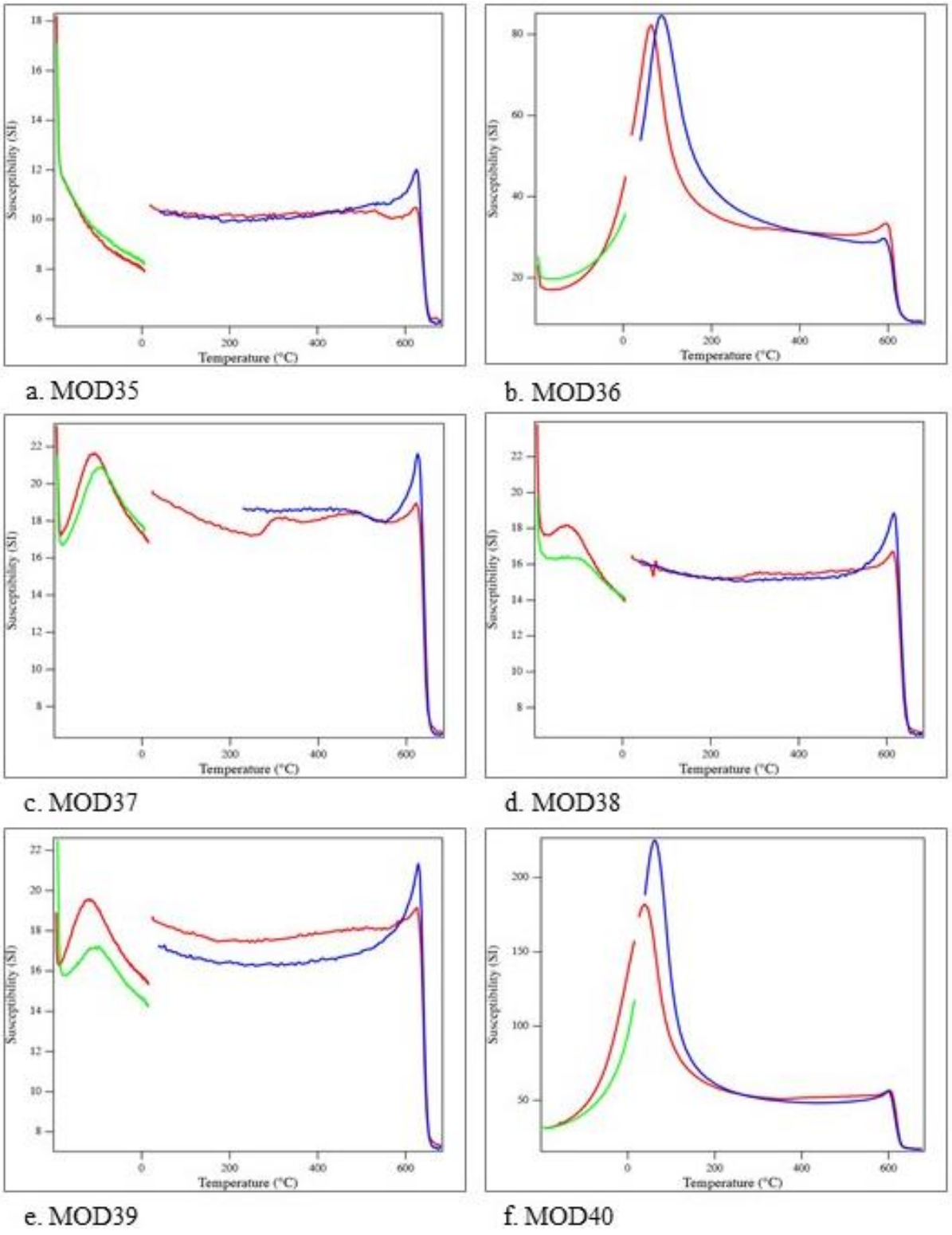

Figure 8.8: Temperature dependent susceptibility curves from all samples. The heating curves are red, while the cooling curves are blue. The post-heating cooling curves are green.

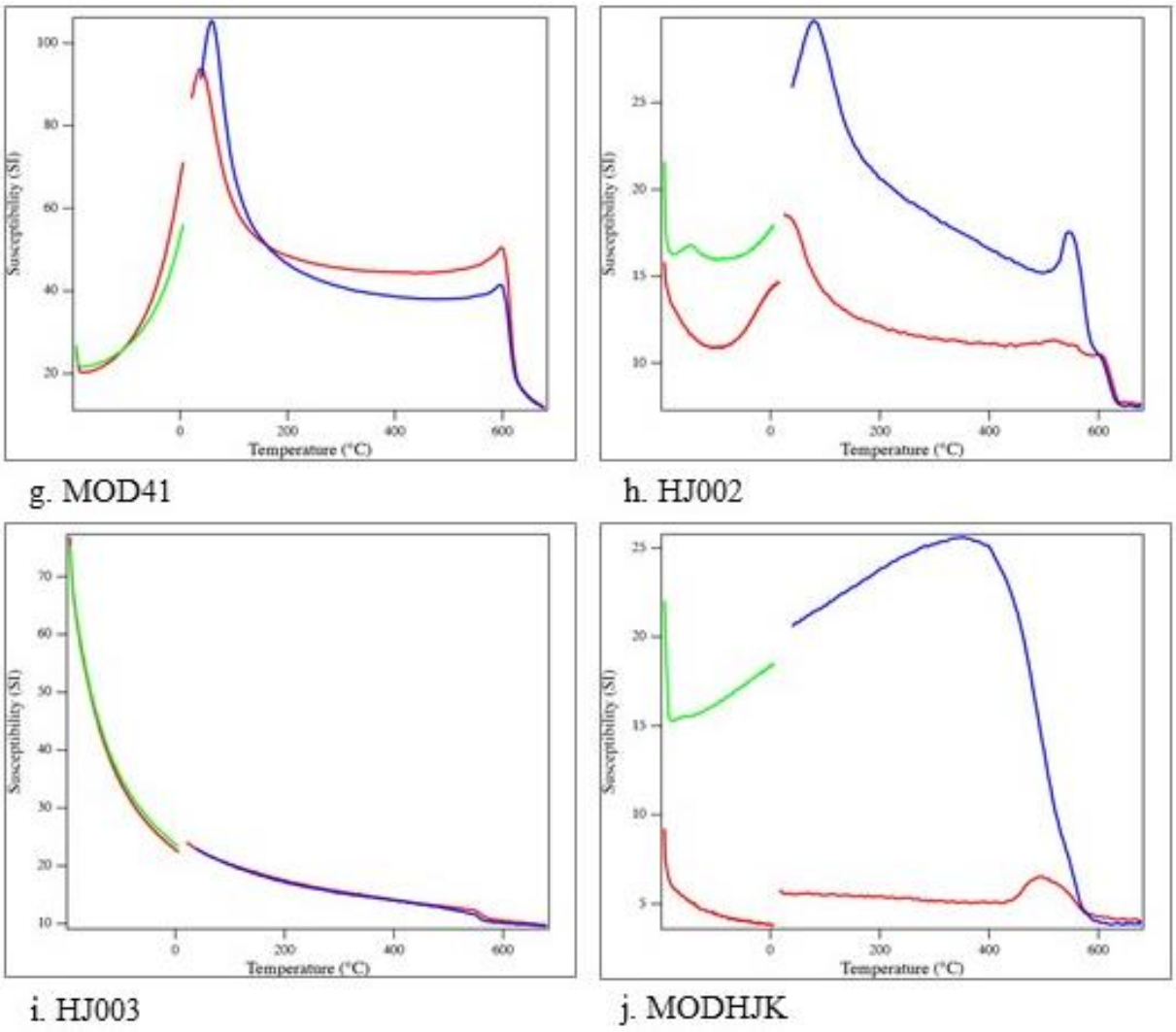

Figure 8.8 (cont.): Temperature dependent susceptibility curves from all samples. The heating curves are red, while the cooling curves are blue. The post-heating cooling curves are green.

9. Discussion

In an attempt to deduce what the protoliths were and why the rocks are so oxidized, the related mineral assemblages and phase relations will be discussed, with focus on samples MOD35-MOD41. To investigate the chemical spaces of these rocks, a chemography based on MgO-CaO-Na_2O-Al_2O_3 is presented, and the XRF-results are compared to published chemical compositions of sedimentary rocks. In addition, possible environments are discussed to find the reason why the rocks are so oxidized. The petrophysical properties are then discussed to find the primary remanence carrier, and to decide whether titanohematite is the only oxide phase present.

9.1 Related assemblages and phase relations

Samples MOD35-MOD40 can be divided into two groups based on the mineral assemblages (table 7.1). They all contain quartz, feldspar, talc and phlogopite. In addition, MOD35, MOD36 and MOD40 contain chlorite, and an Al_2SiO_5-polymorph. MOD37, MOD38 and MOD39 represent compositions where kyanite and chlorite were not stable, but were appropriate for the formation of amphibole. These differences, in addition to that the samples studied occur within a very restricted area, indicate that the two groups originate from different protoliths, metamorphosed from unusual sedimentary rocks.

9.1.1 Rocks with kyanite/sillimanite

In MOD35, the primary mineral assemblage is made up of quartz and phlogopite. Phlogopite is altered to talc which also overgrows quartz. Na-feldspar and sillimanite are formed during prograde metamorphism and found in clusters together with minor amounts of hematite and chlorite. These feldspar-sillimanite clusters are overgrowing phlogopite, and is possibly an alteration product from prograde breakdown of former dioctahedral mica, like the Mg-paragonite found in MOD36 and MOD41. Winter (2010) states that chlorite is not stable in the sillimanite zone, implying that this must be a retrograde reaction, but for Mg-rich rocks like these, chlorite is stable in the sillimanite-orthoclase zone far above muscovite breakdown. The lack of K and high content of Mg in these rocks may have prevented retrograde muscovite from replacing the sillimanite, because phlogopite formed instead of muscovite.

In MOD36, quartz, feldspar, and phlogopite are primary, and kyanite is formed at prograde metamorphism, and later partially altered to sillimanite. Chloritized phlogopite is broken down to talc (fig. 7.7c).

In MOD40, the primary assemblage is made up of quartz and feldspar. Chlorite bends around the kyanite, implying that chlorite is post-dating kyanite (fig. 7.19c-d). Munz (1990) suggested that gedrite was present as a part of the primary assemblage, leading to gedrite and quartz breaking down to kyanite and talc, which later broke down to quartz and chlorite by retrogression. No gedrite has been found here, so it is more likely that quartz and chlorite broke down to kyanite and talc during prograde metamorphism, before returning along the same path by retrogression. This reaction can be seen in figure 7.7d and 9.1, and marks the transition from a previous greenschist to whiteschist (Winter, 2010).

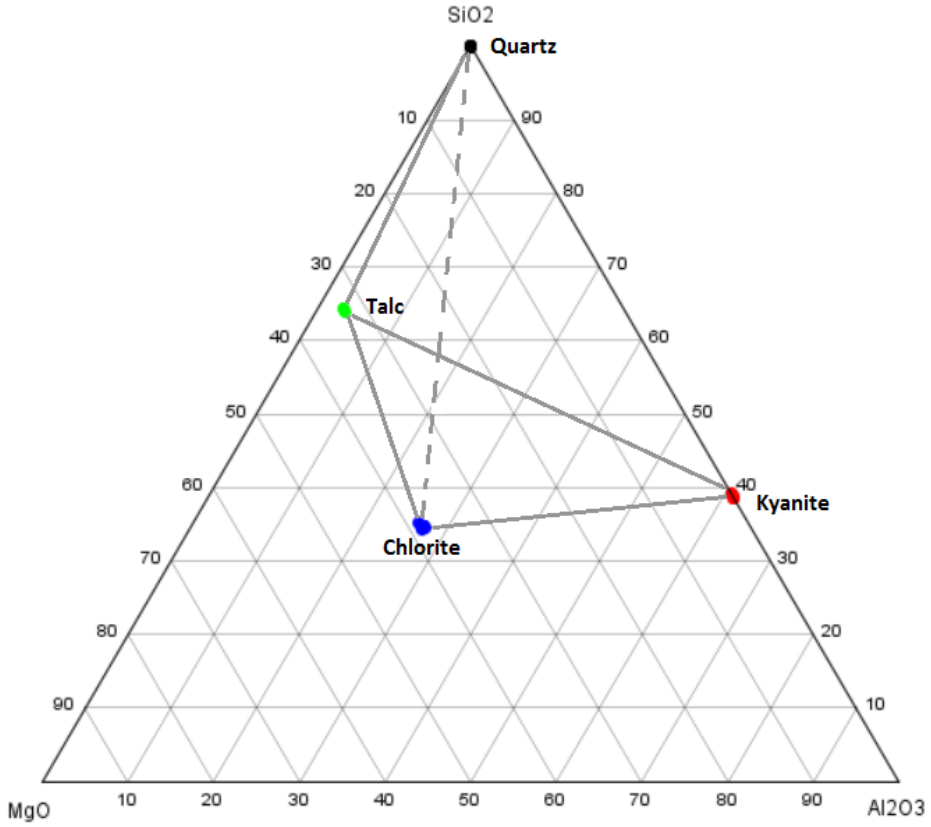

Figure 9.1: Ternary diagram showing that talc-kyanite breaks down to chlorite-quartz in MOD40. Based on figure from Kulke and Schreyer (1973).

Talc and kyanite do not occur together commonly. This is because they have such different mineral chemistry, which can be seen in triangular plots, where they plot is completely different corners. In MOD36, muscovite was initially believed to be present, but for the same reason,

muscovite and talc are unlikely to occur together. EPMA results displayed no muscovite, so it has been concluded that no muscovite is present. Al-silicates rarely occur with pure Mg-silicates, and if such assemblages do occur, they are a clear indication of high pressure metamorphism (Kulke and Schreyer, 1973). Talc only forms in very Mg-rich and Fe-poor rocks, implying that talc must have formed because most Fe in the rock is in hematite. As mentioned, the assemblage of talc and kyanite has previously been called whiteschist. Schreyer (1977) stated that whiteschists can be described mainly by MgO, Al_2O_3, SiO_2 and H_2O, with the presence of talc and kyanite, and often some quartz and chlorite. This fit well with the observations from MOD35, MOD36 and MOD40, except for significant Na_2O owing to albite, and K_2O owing to a high content of phlogopite in MOD35.

Cordierite has been found in other studies from the area (Robinson, pers. comm., 2017), and it has been proposed that talc and kyanite can be a product of cordierite breakdown. However, no evidence of cordierite has been found here. The talc in MOD35, MOD36 and MOD40 is more aluminous and also more sodic than the talc in MOD37-MOD39, implying that this talc is either derived from another source, or that a special coupled NaAl-substitution was operating (Friend et al., 1993). This was also reported by Munz (1990), and has in this study been interpreted to be substitution, where Na goes into the interlayer A site and is compensated by Al replacing Si, following

$$Mg_3Si_4O_{10}(OH)_2 \rightarrow Na_{0.5}Mg_3Al_{0.5}Si_{3.5}O_{10}(OH)_2$$

though the talc studied here doesn't get this far (table 7.4). Mg-paragonite, found in MOD36 and MOD41, can be formed by a retrograde reaction where kyanite/sillimanite, albite and a small amount of talc break down to mica, or it could be involved in a prograde reaction producing albite and sillimanite. This follows the same principle as when muscovite and quartz breaks down to K-feldspar, sillimanite and H_2O, but instead, follows the equation

Mg-paragonite + quartz = sillimanite + albite + NaAl-talc

As mentioned in chapter 7.2.1, there are two groups of albites in MOD36, reflecting the primary albite and the albite that is possibly formed from Mg-paragonite. The phlogopite has a Na+K content less than 1, suggesting it can be involved in solid solution a short way towards talc with intermediate wonesite. The phlogopite is Na-rich, implying it can be influenced by the same Na-Al substitution as talc. Wonesite is a trioctahedral sheet silicate plotting between biotite and talc in figure 9.2, and is a mineral showing optical and chemical similarities with phlogopite.

Spear et al. (1981) reported wonesite as intergrowths with phlogopite, and found that wonesite has alkali deficiency compared to an ideal Na-analog of biotite.

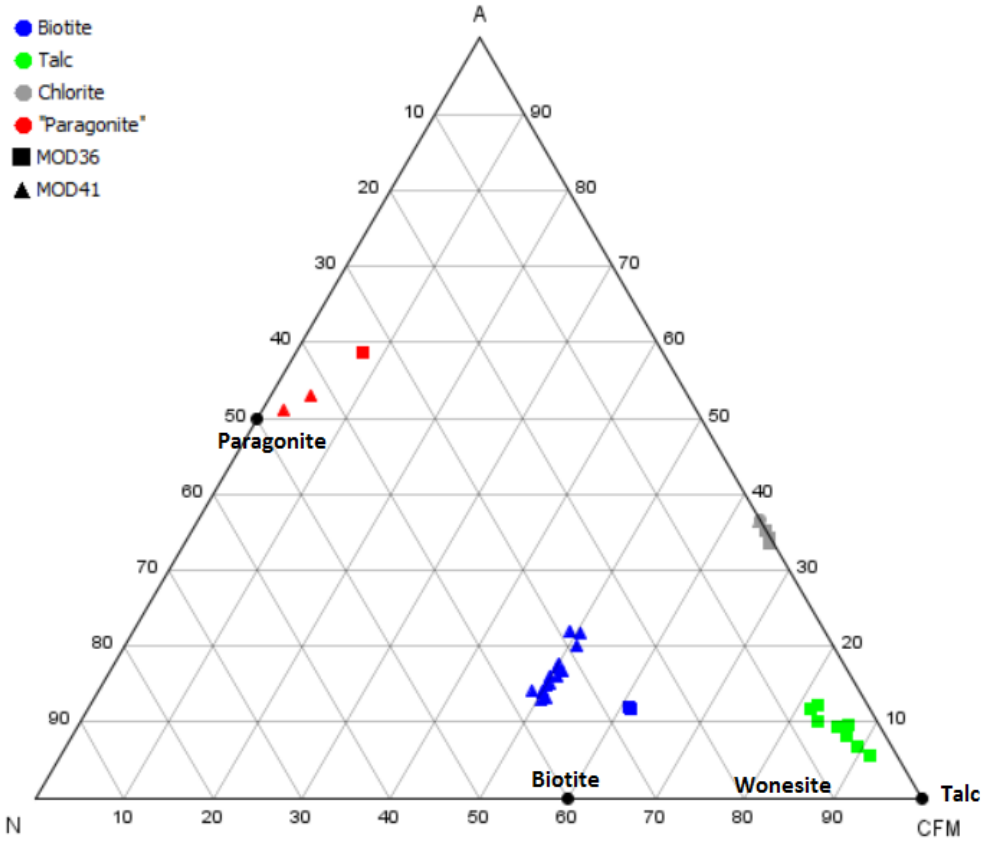

Figure 9.2: Showing biotite, talc and chlorite found in MOD36 and MOD41 plotted together with Mg-paragonite. Parameters are A = Al + Fe^{3+} + Cr + 2Ti – Na – K. N = 2Na + 2K. CFM = Ca + Fe^{2+} + Mg + Mn – Ti.

Lo Pò and Braga (2014) stated that the formation of primary hematite prevents the formation of biotite at increasing temperatures, which can explain why the studied rocks contain phlogopite and not biotite. Hematite can also act as a sink for ferric iron so that none goes into the formation of biotite. Phlogopite is believed to be formed early on in this study. If the protolith was oxidized from the beginning, all iron would be present as Fe^{3+}, and silicates tend to have mostly Fe^{2+} incorporated in its lattices (Boger et al., 2012). Therefore, all Fe^{3+} goes into formation of hematite, while phlogopite and talc are formed from the significant amounts of Mg during early stages of metamorphism.

9.1.2 Rocks with amphibole

In MOD37, MOD38 and MOD39, quartz and feldspar are primary sedimentary minerals. Traces of alkali feldspar have been found in these rocks, which could imply that the primary assemblage has been transformed to albite and possibly biotite early on, but it is most likely that the plagioclase sediments contained rare K-feldspar grains together with albite. Feldspar is sericitized (fig. 7.2d), with invasion of fluids during low temperature conditions at late stages of alteration. This can be described through the following reaction (Pirajno, 2009):

$$3NaAlSi_3O_8 + 2H^+ + K^+ = KAl_3Si_3O_{10}(OH)_2 + 6SiO_2 + 3Na^+$$

Phlogopite is the main K-bearing phase, and is being replaced by talc, which can be seen in figure 9.3. This could imply removal of K. Feldspar has grown into porphyroblasts with inclusions of talc, tourmaline, and hematite during prograde alteration. Coarse-grained talc is bending around these porphyroblasts and coarse-grained hematite.

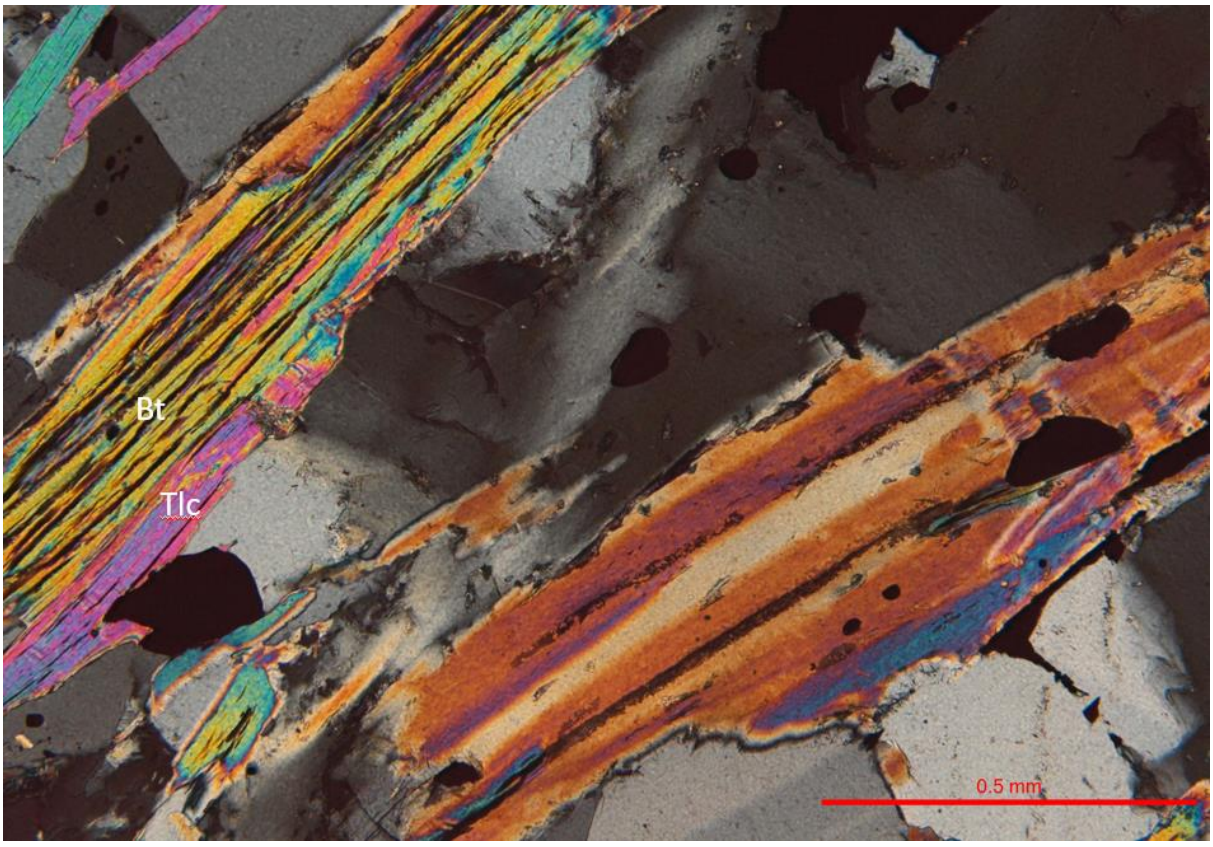

Figure 9.3: Microphotograph from MOD39, showing talc replacing biotite.

MOD37-MOD39 contain higher amounts of Ca than the talc-kyanite rocks, so that amphibole was stable instead of kyanite. The amphibole is a Ca-rich amphibole containing moderate

amounts of Na_2O, interpreted to be modestly NaAl-substituted tremolite. Other authors have described secondary formed tremolite with substitution of sodium as relatively common, similar to the much rarer sodium substitution described in talc from MOD36 and MOD40. In the amphibole-bearing rocks, the feldspars are mainly oligoclase. Some of the amphibole in HJ003 and apatite is relatively Cl-rich. Amphibole has also been described as an alteration product of pyroxene (Munz and Morvik, 1991, Jøsang, 1966), however, in this study, pyroxene has only been found in the mafic pyroxene-hornblendite, HJ003.

Also present are small amounts of the mystery mineral, apatite, tourmaline and titanite. Some of the tourmalines are zoned, possibly marking a discontinuity between detrital tourmaline and metamorphic overgrowths (Henry and Guidotti, 1985). In this study, tourmaline is found in higher concentrations in mica-rich layers and usually as an inclusion phase, representing a relict detrital and/or early-formed metamorphic mineral.

9.1.3 Quartz-hematite rock

MOD41 is made up primarily of quartz and hematite, with minor amounts of phlogopite and feldspar. Phlogopite is partially altered to chlorite and Mg-paragonite. Chlorite and paragonite are possibly formed through alteration of phlogopite and albite.

HJ002 is made up of quartz, feldspar, and phlogopite, with minor amounts of hematite and tourmaline. Kyanite and apatite are also present. HJ003 is characterized by mainly mafic minerals, and is in large degree made up of amphibole and pyroxene, partially altered to amphibole, in addition to rutile, apatite and ilmenite. HJ002 and HJ003 show no planar fabric, contrasting the other rocks. Most of the magmatic texture in HJ003 is preserved, implying that the alteration could be a result from pyroxene reacting with fluids, or changed P-T conditions. MODHJK is composed of mostly quartz, with minor amounts of albite, K-feldspar, biotite, apatite, and hematite. Some of the biotite is altered to chlorite.

9.2 Chemography

The rare chemical composition of these rocks has not been explored to great extent before. Most of the previous studies from the area point to metasomatism as the main reason for the chemical differences. In this study, several findings, which are summarized here, support the grouping of a Ca-rich composition and a composition displaying NaAl-substitution. Therefore, a new theory was suggested, contrasting previous studies. As a main argument for the new theory, the

tourmaline results are important. Tourmaline is an extremely stable mineral, and is even more resistant to retrograde reactions than garnet (Goldschmidt and Muir, 1954). The tourmaline analyses are bimodal, with MOD35 and MOD41 in a Na-rich group, and MOD38, MOD39 and HJ002 in a Ca-rich group (fig. 7.18). Once tourmaline is formed, usually during metamorphism of marine clay, it is incredibly resistant to alteration, suggesting that the chemical differences between the two rock groups were present from before tourmaline crystallized early in the metamorphism. Plagioclases are separated into two groups, Ca-richer in MOD37, MOD38 and MOD39 (An_{18-28}), and Na-richer in MOD35, MOD36 and MOD41 (An_{1-15}). In addition, MOD36 is an exception, where analyses in the clusters with talc-sillimanite are much more Ca-rich (An_{30-34}), possibly as breakdown products of Ca-bearing paragonite. Although K/(K+Na) ratios in phlogopite are very high, they are slightly higher in the Ca-rich group than in the AlNa-rich group. Talc is slightly more Ca-rich in the amphibole-rocks, and there is a greater NaAl-substitution in talc in the rocks with kyanite/sillimanite. These features provide many arguments indicating that the chemical grouping of the rocks reflects minor differences in the original iron-rich sediments.

To display these differences, chemographic diagrams were produced for each key mineral assemblage. This make it possible to see the chemical spaces and identify what divides them. All samples contain tourmaline and titanohematite, and probably rutile, so neither Fe nor Ti are crucial to display the assemblages. Phlogopite is also present in all samples as the main K-bearing phase, together with quartz. Therefore, K_2O and SiO_2 are treated as excess and not determining chemical inert components. Many of the minerals are hydrous silicates, so according to convention, H_2O is treated as a perfectly mobile component. Al_2O_3, MgO, CaO and Na_2O are thus plotted in a tetrahedron (fig. 9.6). They define two four-phase spaces that have between them one or several versions of the same three-phase plane.

The rocks that are richer in AlNa (fig. 9.4), contain plagioclase, chlorite, sillimanite/kyanite, talc and may also involve paragonite. In this rock group, the talc has substantial substitution of Al and coupled Na. This brings the composition to a position where it is not on the same chemical line as kyanite-chlorite, but if the plagioclase is pure albite, this means that an assemblage albite-kyanite-talc-chlorite could possibly all lie on a single plane.

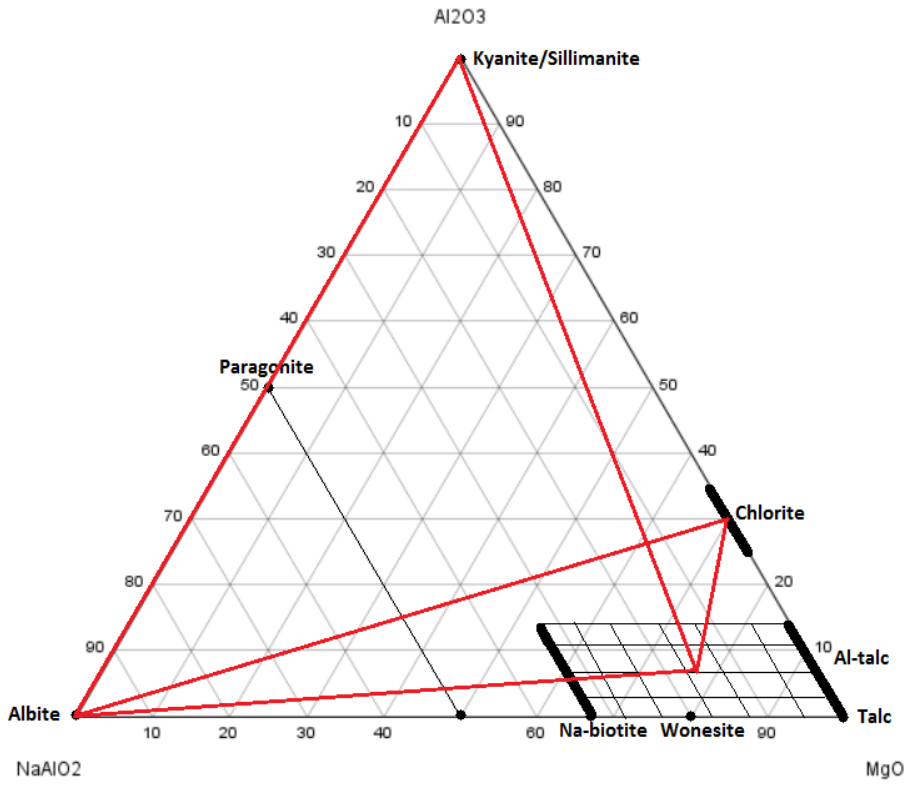

Figure 9.4: The Na-rich volume.

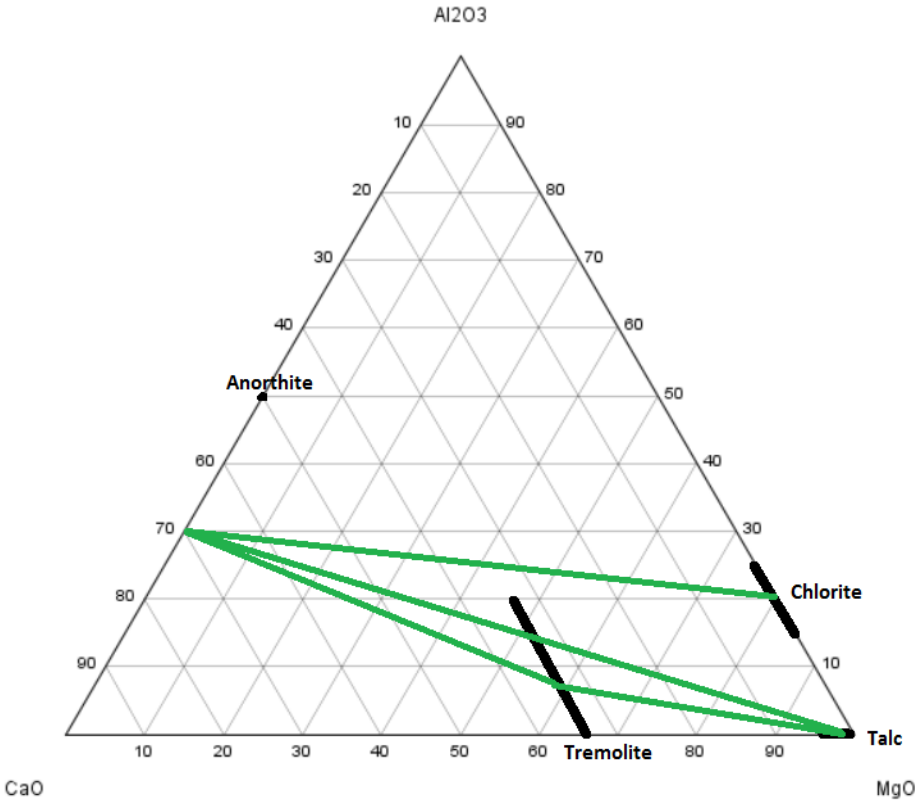

Figure 9.5: Ca-rich volume. Chlorite is assumed to be present, even though no evidence was found.

The Ca-rich rocks contain plagioclase, talc, and amphibole, so that the suggested diving three-phase assemblage would be plagioclase, chlorite, and talc. No chlorite was found in the amphibole-rocks, but for these rocks to coexist in a chemical space, amphibole-rocks with chlorite must be present for an intermediate composition that may or may not occur in the area. The CaO content is mainly controlled by the presence of amphibole and titanite. Since no amphibole is present in the rocks with kyanite or sillimanite, the CaO content of these samples most likely accounts for the trace amounts of apatite. From figure 9.6, the two rock compositions show slight differences, but that they share a hypothetical feldspar-talc-chlorite plane.

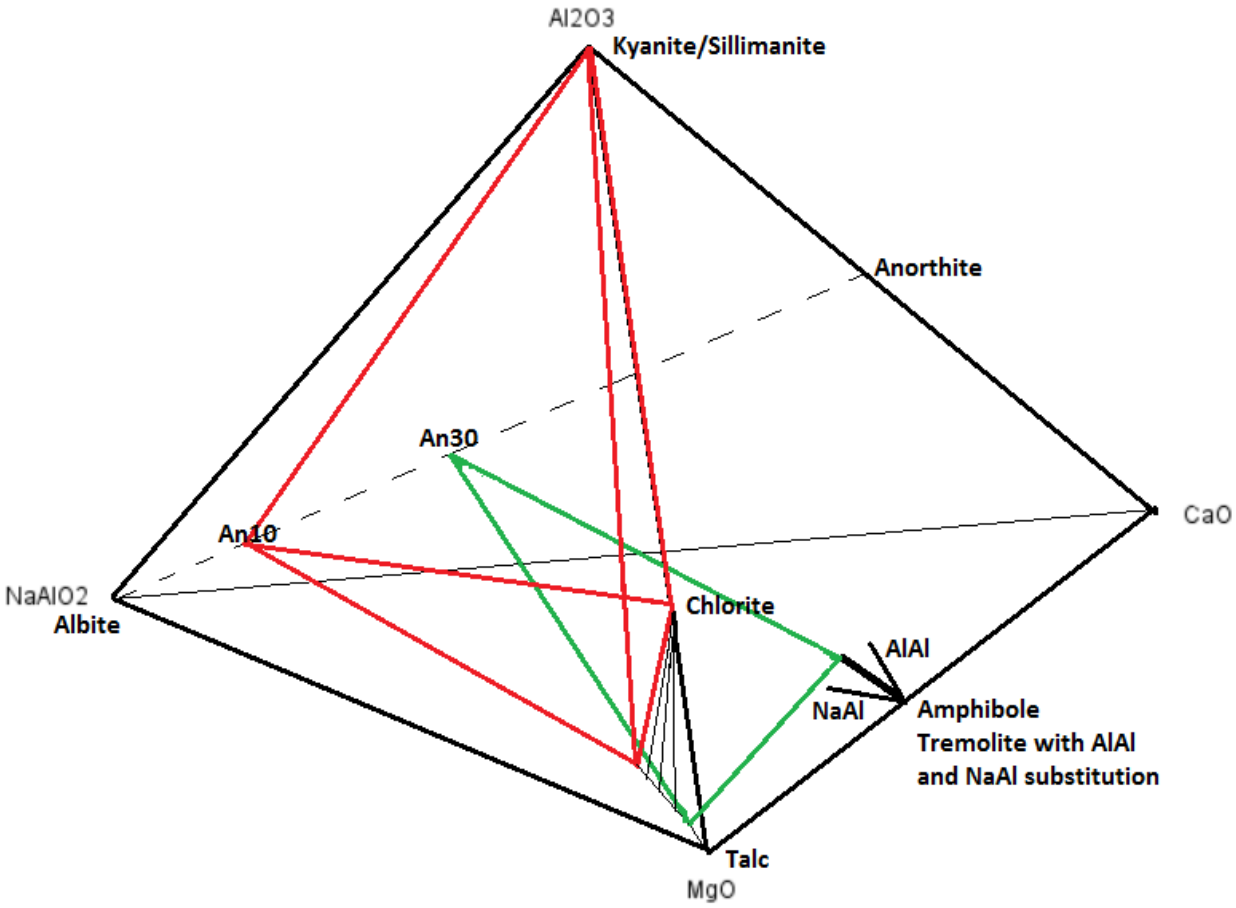

Figure 9.6: Tetrahedron showing the chemical spaces

9.3 Possible protoliths

In NGU's database (NGU, 2017a), these rocks are classified as metasandstone; mica schist and quartzite, in places with elements of biotite-hornblende gneiss and amphibolite. MOD35-MOD41, HJ002 and MODHJK are samples rich in quartz and mica, and varying amounts of

amphibole. This implies a sedimentary origin. In addition, rocks with Al-rich minerals like kyanite are typical for sedimentary origins. From figure 7.27, all that these rocks plot as sedimentary rocks. Because all Fe_2O_3 is omitted in this figure, HJ003 also appears as sedimentary. This sample plots closest to the mafic igneous field, and is likely a metamorphosed mafic volcanic or intrusive. To try to deduce what the possible protoliths were, several different lithologies will be discussed and compared with the studied samples.

Tourmaline is a common mineral in marine clay. Boron is abundant in sea water and in marine sediments compared to igneous rocks (Goldschmidt and Muir, 1954). Tourmaline is more commonly found in muddy layers over sandy layers, and marine oxidized sediments have been found to contain considerable amounts of boron. Boron can also be concentrated in evaporite sediments, like marine deposited salt or as borates in evaporitic lakes. Tourmaline is present in all samples from MOD35-MOD41, suggesting marine origin. In other studies, the mineral has been found where evaporate sediments have undergone regional metamorphism.

Table 9.1: Typical chemical composition for various rocks (Bucher and Grapes, 2011, Goldschmidt and Muir, 1954).

	SiO_2	**Al_2O_3**	**FeO (total)**	**MgO**	**CaO**	**Na_2O**	**K_2O**	**CO_2**	**Sum of CO_2+C+ H_2O**
Igneous rocks	59.12	15.34	6.57	3.49	5.08	3.84	3.13	0.10	1.25
78 shales	58.38	15.40	6.07	2.45	3.12	1.31	3.25	2.64	7.66
52 terri-genous muds	57.05	17.22	6.86	2.17	2.04	1.05	2.25		8.66
18 phyllites	57.29	20.00	6.79	1.76	0.37	1.40	4.30	0.05	4.91
11 phyllites	63.09	16.70	6.16	2.43	0.40	1.32	4.59	Tr	4.05
12 phyllites	65.10	14.92	5.84	2.23	1.11	0.98	4.82	0.65	3.74
30 mica schists	67.34	13.78	6.37	3.05	1.38	1.31	3.34	0.10	2.08
11 mica schists	61.25	17.26	7.62	4.83	1.05	1.35	3.22	0.30	2.46
Sandstones, greywackes	70.0	8.2	2.0	0.9	4.3	0.58	2.1	3.9	7.16
Shales (platforms)	50.7	15.1	6.5	3.3	7.2	0.8	3.5	5.0	11.77
Pelites	54.9	16.6	9.7	3.4	0.72	1.3	2.7		9.2

Table 9.1 shows a compilation of chemical analyses of different lithologies. In comparison, the studied rocks are generally similar, but showing a large range in SiO_2. They contain less Al_2O_3 and more iron than typical shales. CaO-contents are low and varied like shales, and K_2O are

generally much lower than in shales. The LOI are lower than shales and schists, implying lower abundance of hydrous minerals. Argillaceous sediments commonly absorb Mg from the sea water in preference to sodium, which can be a reason why the rocks are so Mg-rich, but this is not true with respect to iron. The rocks are relatively sparse in potassium, which may be concentrated in shales (Goldschmidt and Muir, 1954). Paragonite is usually found in detrital and authigenic sediments, in addition to in phyllites, schists and gneisses (Deer et al., 1992). Wackes are generally rich in Al_2O_3, Fe_2O_3, MgO and Na_2O, like the studied rocks. Chemically precipitated cement may form mudstones, which can also form from alteration of volcanic ash to clay.

Marine sediments generally do not form whiteschists because this type of sediments generally have too high Fe-content (Franz et al., 2013), but here the iron was incorporated into hematite early on, so that the remaining minerals were quite iron-poor. Iron is most abundant in fine-grained sedimentary rocks, and is commonly associated with clays (Dentith and Mudge, 2014). In marine evaporite sediments of Mg-salt, ferrous iron (Fe^{2+}) is commonly originally present in considerable amounts. Later, the iron is oxidized to ferric iron and precipitates as oriented hematite crystals, which fit with the studied rocks. Evaporites are usually sparse in Ti. The normal amounts in shales are 0.5-1.5% TiO_2, which corresponds well with the measured values in these rocks. Garnet is absent because of too low amounts of Fe^{2+} and Mn^{2+}, and does not commonly form in Mg-rich sandy pelites, quartzites and marble. Hornfels, formed from sediments exposed to contact metamorphism, commonly contains biotite, quartz, feldspar, tourmaline, iron oxides and locally Al_2SiO_5-silicates, which, in addition to the talc, is identical to the mineral assemblage in the studied rocks with kyanite/sillimanite.

Pelites have been considered as a possible protolith for the studied rocks. Pelites are mica-schist and are the metamorphic equivalent of clay rich rocks. Metamorphosed normal pelites always contain muscovite or K-feldspar (Bucher and Grapes, 2011), both absent in the rocks studied here. However, extremely Mg-rich rocks like whiteschist might be an exception. Pelites contain around 16.6 wt.% Al_2O_3, 10 wt.% iron, and moderate amounts of MgO and alkalis, in addition to extremely low amounts of CaO (<0.7 wt.%). If iron is assumed to be present only in hematite and therefore omitted from the XRF-results, the Al_2O_3-contents will increase, but they will still be too low to be normal pelites according to Bucher and Grapes' definition. MOD35-MOD41 are generally lower on aluminum and higher in iron, magnesium, and calcium. However, pelites with higher silt contents can display a lower content of Al_2O_3. MOD35, MOD36 and MOD40 contain relatively low amounts of Al_2O_3, but they contain kyanite or sillimanite, implying that

they are nevertheless Al-saturated. Part of the explanation is showed in fig. 9.4; when chlorite breaks down to kyanite and talc, a rock low in Al might have Al-silicates.

The higher level of CaO in MOD37-MOD39 implies that a carbonate source might be a feature in the sediments. Phlogopite is common in metamorphosed limestones, as are tourmaline and amphibole. Talc and tremolite are common hydrous minerals in many marbles (Bucher and Grapes, 2011). Carbonate rocks are furthermore associated with albitic rocks (Engvik et al., 2011), and Schreyer (1977) and Franz et al. (2013) stated that whiteschists can be derived from mudstones associated with evaporites, with low concentrations of alkalis and calcium. In addition, talc is a common mineral in saline lakes and evaporites. If so, talc is not of detrital origin, but precipitated from Mg and Si in oceans and saline lakes. Talc has also been found to be stable in marine muds, or it can form by contact and regional metamorphism of siliceous dolomite. Schreyer et al. (1982) noted that kulkeite occurred in low-grade dolomite rocks associated with a metamorphosed evaporite.

There are mostly volcanic rocks surrounding the studied sediments, so the amphiboles could have a source from eroded volcanic rocks. Franz et al. (2013) stated that few protoliths are suitable for formation of whiteschist, and that they most likely are derived from continental sedimentary rocks or hydrothermally altered felsic to mafic rocks. High Mg-contents, like in the studied rocks, are commonly found in oceanic sediments with high sedimentation rates and in both marine and non-marine evaporites. Formation of talc requires a Mg-rich and Ca-poor environment, which is generally formed by hydrothermal alteration of low grade metamorphic rocks derived from ultrabasic to basic igneous rocks (Deer et al., 1992, Nelson, 2011). Talc is a common prograde product of serpentine and siliceous dolomite. The MgO-content of sand, clay, marine muds and shales rarely exceeds 3%, but the addition of tuffs and clastic material derived from basic igneous rocks may result in considerable amounts of non-carbonate MgO being concentrated in sediments derived from chemical weathering of primary rocks (Goldschmidt and Muir, 1954). The rocks studied here contain much higher amounts of MgO, up to 15%, implying that sand and normal clay can't be the sole responsible source. Bentonites are formed from weathering of volcanic ash, and commonly contain low amounts of Na^+ and K^+, and high amounts of Mg^{2+} and Fe. In chemically weathered sediments, talc forms from decomposition of Mg-minerals from the ash, and clastic amphibole is also commonly found. In addition, more than 2% CaO is a strong indicator of a mixture with volcanic ash, and MOD37-MOD39 show CaO-content close to these levels.

In the stratigraphy, MOD41 is located underneath the other rocks in the syncline. This rock is likely to have originated from a sandier protolith/layer, and from figure 7.29, it is classified as Fe-sand. Mature sandstones tend to be iron-poor and unable to produce significant amounts of magnetic minerals (Dentith and Mudge, 2014), implying that only argillaceous rocks are likely to be magnetic, though black magnetite sands are not unusual in quartzites. MOD41 however, is both arenaceous and magnetic, because of the unusual high iron-content creating titanohematite with lamellar magnetism (see chapter 9.5.2). Waque (1996) reported that quartzo-feldspathic rocks are the most common lithology among the sedimentary rocks in the Modum district, and these were overlain by more aluminous sediments forming protoliths for the more clay-rich rocks, which fits well with the rocks studied here. The bedding visible in MOD39 (fig. 1.1) might suggest that the rocks are composed of sandy, silty, and muddy layers. This layering could be a result of tidal or turbidity currents.

9.4 Oxidized protolith

Silicates in high-grade pelitic rocks tend to have mostly ferrous iron incorporated in its lattices (Boger et al., 2012), and with an oxidized protolith, all iron would be ferric. The iron was therefore incorporated in hematite, which was probably already in the original sediments, but coarsened during metamorphism. Phlogopite formed from the large amounts of magnesium present, and the silicates in oxidized rocks will thus appear more magnesian the more oxidized they get. The amount of boron also points to a marine oxidized sediments, considering fresh-water beds rarely contain notable amounts of boron (Goldschmidt and Muir, 1954). The focus of this sub-chapter is therefore to try to figure out why the protoliths were so oxidized.

Hematite indicates oxidizing conditions and high oxygen fugacity above the magnetite-hematite equilibria (fig. 4.2, 4.3) (Dentith and Mudge, 2014, Franz et al., 2013). Low amounts of free O_2-gas inhibits silicates crystallizing with Fe^{2+} and Mg to form mafic minerals, so that mainly felsic and magnesium-rich minerals will form (Bucher and Grapes, 2011, Winter, 2010), which is what happened in the studied rocks. The same goes for high partial pressure of oxygen, leading to iron being oxidized and forming Fe-(Ti-)minerals like hematite.

The rocks were most likely deposited as an oxidized (red-bed) assemblage, or were rapidly oxidized during burial and diagenesis. Oxidation occurs in terrestrial weathering or in shallow marine waters, where access of sunlight leads to production of oxygen by organisms living in the photic zone (Robb, 2005). Oxidizing and alkaline (high pH) conditions promotes

precipitation of iron, and ironstones tend to form in shallow marine environments. Several arguments indicate tropical weathering, like the presence of apatite, which most common in alkaline, warm-water conditions. The low amounts of MnO in the rocks imply that the rocks can't be deep marine sediments, but could be deposited offshore in an area with tropical weathering (Robinson, pers. comm., 2017). In addition, the noticeable amounts of Zr reflects presence of zircon, which could be fine detritus that would survive weathering.

Oxidizing waters are commonly formed from being in contact with the atmosphere, which leads to minerals with ferrous iron being oxidized to minerals containing ferric iron, like hematite (Dentith and Mudge, 2014). The fluids that circulated through the studied rocks could have interacted with evaporites, commonly creating neutral (pH 5-9), oxidized and moderately saline fluids (Robb, 2005). Sedimentary ferric iron ores generally form by oxidation of ferrous solutions. This is common on shallow lacustrine, brackish, or marine waters with easy access to air. Here, plants help to consume carbonic acid and produce oxygen (Goldschmidt and Muir, 1954), contributing to oxidation of the rocks.

Tourmaline is frequently found in sedimentary basins (Henry and Guidotti, 1985). Munz et al. (1995) found from fluid inclusion studies that the rocks in Modum were influenced by a brine comparable to modern seawater, indicating that the fluids originated from sedimentary basins. Continental, sedimentary rocks similar to the studied rocks are typically formed in closed evaporitic basins, under dry climatic conditions (Franz et al., 2013). In the absence of organic carbon, clay-rich rocks stay oxidized. When buried, the rocks may convert all Fe^{3+} hydroxide to hematite. Hematite can also form by precipitation from iron-rich fluids in the pore spaces of clastic sediments, forming red-beds (Dunlop, 1990). Whiteschists have been interpreted to be derived from a crustal source, pushed down into the deep during metamorphism, exposing the sediments to high pressure, commonly associated with subduction.

9.5 Discussion of petrophysical properties

To interpret the magnetic behaviour of the Modum samples, it is important to investigate the minerals, and to correlate magnetic properties with mineral variations. Especially the amounts of the different oxides can be used to interpret magnetic behaviour.

9.5.1 Oxide content and petrophysical properties

As explained in section 7.2.10, titanohematite was found as the main magnetic oxide, ranging in amounts from <1 to 30 %. HJ003 stands out, as the only sample containing ilmenite without lamellae. The titanohematite content was determined based on optical microscopy, and there is therefore a possibility that the contents aren't representative for all core samples.

The titanium contents in the titanohematite were measured from electron microprobe analyses and temperature dependent susceptibility measurements, together with the IgorPro software. Two groups of Ti-content were recognized, where MOD35, MOD37, MOD38 and MOD39 showed slightly lower values than MOD36, MOD40 and HJ002. The values obtained from IgorPro were generally somewhat higher than the values obtained through EPMA-calculations. IgorPro showed 7-8 % Ti for the first group and 10 % Ti for the second group, while calculations from EPMA results gave respectively 3-5 % Ti and 6-8 % Ti for the two groups. The values from EPMA are usually higher than the values obtained from the IgorPro, because the EPMA tend to do overlap analyses with ilmenite. However, this is not the case here, which is probably due to substitution of other elements in the titanohematite. The titanohematite formulae calculations (table 7.11) display up to 0.62 wt.% Al_2O_3-substitution, and even though it is not enough to explain the gap between the IgorPro and the EPMA-values, this might be one of the reasons for the difference.

Density shows a clear correlation with hematite content, where MOD36, MOD40 and MOD41 show highest density and highest content of hematite. MOD37-MOD39 are in the mid-range of both density and oxide content, while MODHJK shows the lowest density and only trace amounts of oxides. HJ003 has the highest density, but this is mostly due to high content of mafic minerals, and not so much oxide content. As shown in fig. 8.2, NRM vs density display two distinct groups; low NRM for density below 2.7 g/cm^3, and much higher NRM for densities above 2.7 g/cm^3. Susceptibility shows the same correlation, again displaying highest values for MOD36, MOD40 and MOD41.

The rocks show very low susceptibility values, which could be a result of the high oxidation state of the rocks. This, combined with moderate to high NRM values in most samples, result in the extremely high Q-values. Based on these Q-values, the samples from MOD35-MOD41 and HJ002 showed that remanence is controlling the total field vector. The NRM component is negative, meaning that this is the main reason for the negative anomalies seen in the units

studied here. MODHJK and HJ003 are the only samples with low Q-values, indicating that induced magnetization is the primary contributor to magnetization.

MOD36, MOD40 and MOD41 display higher densities, NRM values, susceptibility values and oxide content than MOD35, MOD37, MOD38 and MOD39, making it possible to conclude that there is a clear correlation between oxide contents and petrophysical values. This grouping resembles the grouping found in the petrographic investigations, where MOD35, MOD36, and MOD40 are recognized as having a different chemical composition than MOD37, MOD38 and MOD39. Though MOD35 belong to the same chemical group as MOD36 and MOD40 but contains the same amount of titanohematite as MOD37-MOD39, these findings can imply that the differences in chemical composition also influenced the amounts of oxides created.

9.5.2 Amount, size, and types of exsolutions

The amount, size and types of exsolutions in the titanohematite in the Modum area has been a topic of discussion for a long time. The oxides have in previous studies been found to be titanohematite with ilmenite exsolution lamellae (Fabian et al., 2008; McEnroe et al., 2009a, 2016). Robinson et al. (2014) found that ilmenite exsolutions were too small to see in most samples, and that the darker phases seen in reflected light were rutile and spinel (fig. 7.23a).

Temperature-dependent susceptibility and AF demagnetization measurements indicates at least two phases in the titanohematite studied here. As previously mentioned, remanent magnetism has been found to be the primary factor controlling magnetism in this study. Pure hematite is antiferromagnetic, and can't carry a strong remanence, meaning that there must be multiple phases in the titanohematite, like ilmenite exsolutions. Robinson et al. (2014) proposed that lamellar magnetism of nanoscale ilmenite exsolution in titanohematite is responsible for the remanent magnetism in the Modum area. Lamellar magnetism is created at the temperature of chemical exsolution, where there are contact layers in the hematite adjacent to ilmenite lamellae. They contain a mixture of Fe^{2+} and Fe^{3+} cations, with a net magnetization that is in the opposite direction from that of the hematite layers, but with greater intensity (Robinson et al. 2002, 2004).

From AF demagnetization measurements, samples generally fall into two distinct groups; samples with high coercivity and high thermal stability, and samples with soft components and low coercivity, which lose their magnetization rapidly (McEnroe et al., 2009b). Most demagnetization curves (fig. 8.5) in this study show an initial increase of magnetization, implying an overprint of softer magnetization in the opposite direction to that of the harder

magnetization (Fabian et al., 2008). When demagnetizing, the soft component, possibly owing to magnetite, is removed first, leading to higher magnetization. This behaviour correlates with the Zijderweld diagrams (fig. 8.6), showing two components. The average mean fields of demagnetization are variable from 20 mT to above mT, and may depend on the amount and size of exsolution in the titanohematite. MDF can be plotted against NRM to see if there is a correlation. HJ003 show M(90%) at only 43 mT, which is must lower than the rest. This implies multi-domain behaviour owing to small amounts of ilmenite (Dunlop and Argyle, 1991), which correlates to their low NRM values compared to the others.

Incorporation of titanium in hematite, lowers its Curie temperature. From the temperature dependent susceptibility measurements, the mean value of inflection for MOD35-MOD41 was found to be 625°C. The Curie temperature for pure hematite is 680°C (Dentith and Mudge, 2014), implying some Ti must be present. The difference in temperatures between the samples can be due to impurities in the lattice or differences in degree of oxidation, or compositional differences, which is the most likely answer here. Curves from MOD37-MOD39 show lower susceptibility during cooling, meaning some magnetic material was destroyed during heating. These curves also display a peak during measurements at low temperatures, called Verwey transition, implying some magnetite was initially present. Wide Verwey transition peaks means that the magnetite was not pure. HJ002 does not display an initial Verwey transition, but the curve shows that some magnetite was created around 450-500°C. This is also visible from the higher Hopkinson's peak during cooling, and from the Verwey transition that is visible in the second cold run. Four curves, MOD36, MOD40, MOD41 and HJ002, also display a peak at around 100°C. This peak is believed to be a Curie temperature implying a Cr- or Ti-rich component, or an unblocking temperature, but this was not investigated further. It is however clear that the peak is located at similar temperatures for all four samples, thus it is likely that the same reaction was operating in all samples.

9.6 Suggestions for further work

- Analysis of the fluid inclusions in quartz grains. Fluid inclusion studies, with hydrogen and oxygen isotope studies, can be used to estimate temperatures and salinities. This can say something about the origin of the fluids affecting the metasedimentary rocks.
- Boron isotope studies can be used to infer the source of the boron, but this is very expensive and probably not very informative.

- Geothermometric and geobarometric investigations to provide better details of P and T of metamorphism.
- Detailed mapping and more extensive sampling through fieldwork, especially of stratified rocks.
- VSM measurements to investigate domain state of the titanohematite and to possibly find unblocking temperature to identify the mysterious peak in temperature dependent susceptibility measurements.

10. Conclusions

To answer the aims of this study, varied laboratory work has been completed. The main conclusions are summarized here.

How do these rocks plot geochemically?

The samples are generally rich in SiO_2, MgO and Fe_2O_3, display variable amounts of Al_2O_3 and extremely low contents of MnO. The chemical compositions of the rocks are bimodal, where one group are richer in CaO and lower in Fe_2O_3 than the other, which display a coupled NaAl-substitution. These differences led to the development of two different mineral assemblages in the rocks. The rocks with elevated CaO-contents contain amphibole, while the others contain chlorite and kyanite or sillimanite. In common, they all consist of quartz, plagioclase, phlogopite, talc, tourmaline and titanohematite. The bimodality in chemical composition are interpreted to have been present in the original iron-rich sediments from before metamorphism.

Is it possible to decide what the sedimentary protoliths were, and why the rocks are so oxidized?

From comparing the XRF-results with various literature, a hematite-rich, Al-poor, silty pelite could be a suitable protolith for MOD35-MOD40. Components of volcanic ash and/or evaporite chemistry could be possible, where MOD37-MOD39 show the greatest influence by evaporites, but what connection is most logical is hard to know for sure. MOD41 might stem from a Fe-rich sand. The rocks have been exposed to regional metamorphism, and fluids have caused retrograde chlorite and sericite at a late stage.

The hematite was most likely present in the original sediments, implying that the protoliths were oxidized from the beginning. They were probably formed in shallow marine waters, possibly in a sedimentary basin. The combination of little organic carbon present and burial into the deep, kept the clay-rich rocks oxidized and preserved the hematite.

What is causing the negative anomalies?

Titanohematite is identified as the main magnetic carrier, displaying negative NRM-values, causing the negative anomalies. The amounts of Ti in the titanohematite are bimodal, where the amphibole-bearing rocks contain slightly lower amounts of Ti than the kyanite/sillimanite-bearing rocks. This grouping is also followed in the petrophysical properties, giving the

amphibole-bearing rocks somewhat lower NRM and susceptibility, also reflecting lower amounts of oxides which again reflects the lower density.

Lamellar magnetism has in previous studies been proposed as the reason for the remanent magnetism in the titanohematite. This study has not been able to conclude whether this lamellar magnetism is present in the studied rocks, but temperature dependent susceptibility and AF demagnetization measurements imply that two phases are present. AF demagnetization curves display a softer overprint in negative direction, while temperature dependent susceptibility curves show that some magnetite was initially present in the amphibole-bearing rocks. The kyanite-bearing rocks display a peak around 100°C, but the reason for this is still unknown.

11. References

ANDERSEN, T. & GRORUD, H.-F. 1998. Age and lead isotope systematics of uranium-enriched cobalt mineralization in the Modum complex, South Norway: Implications for Precambrian crustal evolution in the SW part of the Baltic Shield. *Precambrian Research,* 91**,** 419-432.

ANDERSEN, T. & MUNZ, I. A. 1995. Radiogenic whole-rock lead in Precambrian metasedimentary gneisses from South Norway ; evidence of Sveconorwegian LILE mobility. *Norsk geologisk tidsskrift,* 75**,** 156-168.

BACH, W., JÖNS, N. & KLEIN, F. 2013. *Metasomatism Within the Ocean Crust,* Springer.

BASAVAIAH, N. 2011. *Geomagnetism: Solid Earth and Upper Atmosphere Perspective,* The United States of America, Springer.

BEBOUT, G. E. 2013. *Metasomatism in Subduction Zones of Subducted Oceanic Slabs, Mantle Wedges, and the Slab-Mantle Interfac,* Springer.

BEST, M. G. 2003. *Igneous and metamorphic petrology,* Malden, MA, Blackwell.

BINGEN, B., NORDGULEN, O. & VIOLA, G. 2008. A four-phase model for the Sveconorwegian orogeny, SW Scandinavia. *Norw. J. Geol.*

BOGER, S. D., WHITE, R. W. & SCHULTE, B. 2012. The importance of iron speciation (Fe+2/Fe+3) in determining mineral assemblages: an example from the high-grade aluminous metapelites of southeastern Madagascar. *J. Metamorph. Geol.,* 30**,** 997-1018.

BUCHER, K. & GRAPES, R. 2011. *Petrogenesis of Metamorphic Rocks,* Berlin, Heidelberg, Springer Berlin Heidelberg: Berlin, Heidelberg.

BUTLER, R. F. 2004. *PALEOMAGNETISM: Magnetic Domains to Geologic Terranes (Electronic Edition),* Oregon, University of Portland.

COUTINHO, J., KRÄUTNER, H., SASSI, F., SCHMID, R. & SEN, S. 2007. A systematic nomenclature for metamorphic rocks: 8. Amphibolite and Granulite *Recommendations by the IUGS Subcommission on the Systematics of Metamorphic Rock*.

DEER, W. A., HOWIE, R. A. & ZUSSMAN, J. 1992. *An Introduction to the Rock-Forming Minerals,* Essex, Person Education Limited.

DENTITH, M. & MUDGE, S. T. 2014. *Geophysics for the Mineral Exploration Geoscientist,* United Kingdom, Cambridge University Press.

DUNLOP, D. J. 1990. Developments in rock magnetism.

DUNLOP, D. J. & ARGYLE, K. S. 1991. Separating multidomain and single-domain-like remanences in pseudo-single-domain magnetites (215–540 nm) by low-temperature demagnetization. *Journal of Geophysical Research,* 96**,** 2007.

DUNLOP, D. J. & ÖZDEMIR, Ö. 1997. *Rock Magnetism: Fundamentals and frontiers,* United Kingdom, Cambridg University Press.

ENGVIK, A. K., MEZGER, K., WORTELKAMP, S., BAST, R., CORFU, F., KORNELIUSSEN, A., IHLEN, P., BINGEN, B. & AUSTRHEIM, H. 2011. Metasomatism of gabbro; mineral replacement and element mobilization during the Sveconorwegian metamorphic event. *Journal of Metamorphic Geology,* 29**,** 399-423.

ESKOLA, P. 1920. The mineral facies of rocks. . *Norsk. Geol. Tidsskr.,* 6**,** 143-194.

FABIAN, K., MCENROE, S. A., ROBINSON, P. & SHCHERBAKOV, V. P. 2008. Exchange bias identifies lamellar magnetism as the origin of the natural remanent magnetization in titanohematite with ilmenite exsolution from Modum, Norway. *Earth and Planetary Science Letters,* 268**,** 339-353.

FRANZ, L., ROMER, R. L. & DE CAPITANI, C. 2013. Protoliths and phase petrology of whiteschists. *Contributions to Mineralogy and Petrology,* 166**,** 255-274.

FRIEND, C. R. L., JANARDHAN, A. S. & SHADAKSHARA SWAMY, N. 1993. A retrogressive sapphirine-cordierite-talc paragenesis in a spinel-orthopyroxenite from southern Karnataka, India. *Mineralogical Magazine,* 57**,** 273-288.

GOLDSCHMIDT, V. M. & MUIR, A. 1954. *Geochemistry,* Oxford, Clarendon Press.

GRAHAM, C., GREIG, K., SHEPPARD, S. & TURI, B. 1983. Genesis and mobility of the H2O-CO2 fluid phase during regional greenschist and epidote amphibolite facies metamorphism: a petrological and stable isotope study in the Scottish Dalradian. *Journal of the Geological Society,* 140**,** 577-599.

GRORUD, H.-F. 1997. Textural and compositional characteristics of cobalt ores from the Skuterud mines of Modum, Norway. *Norsk geologisk tidsskrift,* 77**,** 31-38.

GUO, J., KOOPMAN, M., FANG, Z. Z., WANG, X., FAN, P. & ROWE, M. C. 2013. FE-EPMA measurements of compositional gradients in cemented tungsten carbides. *International Journal of Refractory Metals and Hard Materials,* 36**,** 265-270.

HARRISON, R. J. & FEINBERG, J. M. 2009. Mineral magnetism; providing new insights into geoscience processes. *Elements***,** 209-215.

HENRY, D. J. & GUIDOTTI, C. V. 1985. Tourmaline as a petrogenetic indicator mineral: an example from the staurolite-grade metapelites of NW Maine. *American Mineralogist,* 70**,** 1-15.

JACOBSEN, S. B. & HEIER, K. S. 1978. *Rb-Sr isotope systematics in metamorphic rocks, Kongsberg sector, south Norway / Stein B. Jacobsen & Knut S. Heier,* S.l., s.n.

JØSANG, O. 1966. *Geologiske og petrografiske undersøkelser i Modumfeltet,* Oslo, Universitetsforlaget.

KULKE, H. & SCHREYER, W. 1973. Kyanite-talc schist from Sar e Sang, Afghanistan. *Earth and Planetary Science Letters,* 18**,** 324-328.

LEAKE, B. E. 1978. Nomenclature of amphiboles. *American Mineralogist,* 63**,** 1023-1052.

LO PÒ, D. & BRAGA, R. 2014. Influence of ferric iron on phase equilibria in greenschist facies assemblages: the hematite-rich metasedimentary rocks from the Monti Pisani (Northern Apennines. *Journal of Metamorphic Geology,* 32**,** 371-387.

MCENROE, S. A. & BROWN, L. L. 2000. A closer look at remanence-dominated aeromagnetic anomalies; rock magnetic properties and magnetic mineralogy of the Russell Belt microcline-sillimanite gneiss, Northwest Adirondack Mountains, New York. *Journal of Geophysical Research,* 105**,** 16,437-16,456.

MCENROE, S. A., BROWN, L. L. & ROBINSON, P. 2009b. Remanent and induced magnetic anomalies over a layered intrusion: Effects from crystal fractionation and magma recharge. *Tectonophysics,* 478**,** 119-134.

MCENROE, S. A., FABIAN, K., ROBINSON, P., GAINA, C. & BROWN, L. L. 2009a. Crustal magnetism, lamellar magnetism and rocks that remember. *Elements***,** 241-246.

MCENROE, S. A., HARRISON, R. J., ROBINSON, P., GOLLA, U. & JERCINOVIC, M. J. 2001. Effect of fine-scale microstructures in titanohematite on the acquisition and stability of natural remanent magnetization in granulite facies metamorphic rocks, Southwest Sweden; implications for crustal magnetism. *Journal of Geophysical Research,* 106**,** 30,523-30,546.

MCENROE, S. A., HARRISON, R. J., ROBINSON, P. & LANGENHORST, F. 2002. Nanoscale haematite–ilmenite lamellae in massive ilmenite rock: an example of 'lamellar magnetism' with implications for planetary magnetic anomalies. *Geophysical Journal International,* 151**,** 890-912.

MCENROE, S. A., LANGENHORST, F., ROBINSON, P., BROMILEY, G. D. & SHAW, C. S. J. 2004b. What is magnetic in the lower crust? *Earth and Planetary Science Letters,* 226**,** 175-192.

MCENROE, S. A., ROBINSON, P., MIYAJIMA, N., FABIAN, K., DYAR, D. & SKLUTE, E. 2016. Lamellar magnetism and exchange bias in billion-year-old titanohematite with nanoscale ilmenite exsolution lamellae: I. Mineral and magnetic characterization. *Geophysical Journal International,* 206**,** 470-486.
MOSKOWITZ, B. M. n.d. *Hitchhiker's Guide to Magnetism.*
MUNZ, I., WAYNE, D. & AUSTRHEIM, H. 1994. Retrograde fluid infiltration in the high-grade Modum Complex South Norway: evidence for age, source and REE mobility. *Contributions to Mineralogy and Petrology,* 116**,** 32-46.
MUNZ, I. A. 1990. Whiteschists and orthoamphibole-cordierite rocks and the P- T- t path of the Modum Complex, south Norway. *LITHOS,* 24**,** 181-199.
MUNZ, I. A. & MORVIK, R. 1991. Metagabbros in the Modum Complex, southern Norway: an important heat source for Sveconorwegian metamorphism. *Precambrian Research,* 52**,** 97-113.
MUNZ, I. A., YARDLEY, B. W. D., BANKS, D. A. & WAYNE, D. 1995. Deep penetration of sedimentary fluids in basement rocks from southern Norway: Evidence from hydrocarbon and brine inclusions in quartz veins. *Geochimica et Cosmochimica Acta,* 59**,** 239-254.
MUSSET, A. E. & KHAN, M. A. 2000. *Looking Into the Earth: An Introduction to Geological Geophysics,* The United States of America, Cambridge University Press.
NELSON, S. A. 2011. Triangular Plots in Metamorphic Petrology. Available: http://www.tulane.edu/~sanelson/eens212/triangular_plots_metamophic_petrology.htm.
NGU. 2017a. *Berggrunnskart 250 med lineamenter* [Online]. Available: http://geo.ngu.no/kart/berggrunn/ [Accessed 05.08.16].
PETRUK, W. 2000. *Applied mineralogy in the mining industry,* Amsterdam, Elsevier.
PILPOTTS, A. A. 2003. *Petrography of Igneous and Metamorphic Rocks,* The United States of America, Waveland Press Inc.
PIRAJNO, F. 2009. *Hydrothermal Processes and Mineral Systems,* Dordrecht, Springer Netherlands: Dordrecht.
PIRAJNO, F., HARLOV, D. E. & AUSTRHEIM, H. 2013. *Effects of metasomatism on mineral systems and their host rocks; alkali metasomatism, skarns, greisens, tourmalinites, rodingites, black-wall alteration and listvenites,* Berlin, Berlin, Germany: Springer.
PUTNIS, A. 1992. *Introduction to mineral sciences,* Cambridge, Cambridge University Press.
REED, S. J. B. 2000. Quantitative Trace Analysis by Wavelength-Dispersive EPMA. *Micro and Trance Analysis,* 132**,** 145-151.
REYNOLDS, J. M. 2011. *An Introduction to Applied and Environmental Geophysics,* Oxford, Wiley-Blackwell.
ROBB, L. 2005. *Introduction to Ore-Forming Processes,* Blackwell Publishing.
ROBINSON, P., FABIAN, K., BALLARAN, T. B., LANGENHORST, F. & MCENROE, F. 2014. Ferroan geikielite and coupled spinel-rutile exsolution from titanohematite: Interface characterization and magnetic properties. *American Mineralogist,* 99**,** 1694-1712.
ROBINSON, P., HARRISON, R. J. & MCENROE, S. A. 2006. Fe 2+ /Fe 3+ charge ordering in contact layers of lamellar magnetism: Bond valence arguments. *American Mineralogist,* 91**,** 67-72.
ROBINSON, P., HARRISON, R. J., MCENROE, S. A. & HARGRAVES, R. B. 2004. Nature and origin of lamellar magnetism in the hematite-ilmenite series. *American Mineralogist,* 89**,** 725-747.
ROBINSON, P., JAFFE, H., KLEIN, C. & ROSS, M. 1969. Equilibrium coexistence of three amphiboles. *Contributions to Mineralogy and Petrology,* 22**,** 248-258.

ROLLINSON, H. R. 2013. Using geochemical data : evaluation, presentation, interpretation. Milton Park, Abingdon, Oxon: Routledge.
SCHEIBER, T., VIOLA, G., BINGEN, B., PETERS, M. & SOLLI, A. 2015. Multiple reactivation and strain localization along a Proterozoic orogen-scale deformation zone: The Kongsberg-Telemark boundary in southern Norway revisited. *Precambrian Research,* 265**,** 78.
SCHREYER, W. 1973. Whiteschist: A High-Pressure Rock and its Geologic Significance. *The Journal of Geology,* 81**,** 735-739.
SCHREYER, W. 1977. Whiteschists: Their compositions and pressure-temperature regimes based on experimental, field, and petrographic evidence. *Tectonophysics,* 43**,** 127-144.
SCHREYER, W., ABRAHAM, K. & KULKE, H. 1980. Natural sodium phlogopite coexisting with potassium phlogopite and sodian aluminian talc in a metamorphic evaporite sequence from Derrag, Tell Atlas, Algeria. *Contributions to Mineralogy and Petrology,* 74**,** 223-233.
SCHREYER, W., MEDENBACH, O., ABRAHAM, K., GEBERT, W. & MÜLLER, W. F. 1982. Kulkeite, a new metamorphic phyllosilicate mineral: Ordered 1∶1 chlorite/talc mixed-layer. *Contributions to Mineralogy and Petrology,* 80**,** 103-109.
SMULIKOWSKI, W., DESMONS, J., FETTES, D. J., HARTE, B., SASSI, F. P. & SCHMID, R. 2003. Types, grade and facies of metamorphism. *Recommendations by the IUGS Subcommision on the Systematics of Metamorphic Rocks*.
SPEAR, F. S., HAZEN, R. M. & RUMBLE, D., III 1981. Wonesite; a new rock-forming silicate from the Post Pond Volcanics, Vermont. *American Mineralogist,* 66**,** 100-105.
STARMER, I. C. 1980. A Proterozoic mylonite zone in the Kongsberg Series north of Hokksund, South-central Norway. *Norsk Geologisk Tidsskrift,* 60**,** 189-193.
TOURET, J. L. R. & NIJLAND, T. G. 2013. *Prograde, Peak and Retrograde Metamorphic Fluids and Associated Metasomatism in Upper Amphibolite to Granulite Facies Transition Zone,* Springer.
WAQUÉ, P. A. M. 1996. Element mobility during Sveconorwegian metamorphism in the Modum complex, South Norway. National Library of Canada = Bibliothèque nationale du Canada.
WINTER, J. D. 2010. *Principles of Igneous and Metamorphic Petrology,* United States of America, Pearson University Inc.
YARDLEY, B. W. D., HARLOV, D. E. & AUSTRHEIM, H. 2013. *The chemical composition of metasomatic fluids in the crust,* Berlin, Berlin, Germany: Springer.
ZHARIKOV, V. A., PERTSEV, N. N., RUSINOV, V. L., CALLEGARI, E. & FETTES, D. J. 2006. Metasomatism and metasomatic rocks. *Recommendations by the IUGS Subcommision on the Systematics of Metamorphic Rocks*.

Appendix

Appendix A – Magnetic properties

Appendix B – AF demagnetization

Appendix C – Castle Meeting conference poster

Appendix A – Magnetic properties

	Density [g/cm3]	NRM volcorr [A/m]	Sus volcorr [SI]	Q-value
MOD35-1A	2.789	1.412	2.591E-04	134.252
MOD35-1T	2.868	0.798	2.739E-04	71.724
MOD35-2A	2.791	1.175	2.750E-04	105.204
MOD35-2B	2.824	1.307	2.657E-04	121.132
MOD35-2T	2.869	0.788	2.738E-04	70.886
MOD35-3A	2.860	1.045	2.559E-04	100.545
MOD35-3B	2.770	1.423	2.452E-04	142.988
MOD35-4A	2.858	1.436	2.719E-04	130.057
MOD35-4T	2.850	0.921	2.602E-04	87.236
MOD35-5A	2.858	1.317	2.497E-04	129.927
MOD35-5T	2.880	1.047	2.597E-04	99.338
MOD36-1A	2.906	4.345	2.759E-03	38.784
MOD36-1B	2.907	6.996	2.663E-03	64.697
MOD36-1C	2.995	10.777	4.900E-03	54.168
MOD36-2A	3.052	10.606	5.202E-03	50.217
MOD36-2B	3.153	14.051	8.650E-03	40.012
MOD37-1A	2.816	2.620	5.767E-04	111.881
MOD37-2A	2.808	2.803	5.425E-04	127.280
MOD37-3A	2.785	2.085	5.646E-04	90.973
MOD38-1A	2.810	2.852	6.291E-04	111.662
MOD38-1B	2.903	4.456	5.888E-04	186.400
MOD38-2A	2.862	3.798	4.864E-04	192.352
MOD38-2B	2.889	4.803	6.363E-04	185.897
MOD38-3A	2.797	2.784	3.235E-04	211.933
MOD38-3B	2.848	3.825	5.008E-04	188.133
MOD38-4B	2.818	3.902	5.291E-04	181.610
MOD39-1A	2.872	1.907	6.220E-04	75.503
MOD39-1B	2.901	2.215	6.656E-04	81.964
MOD39-1T	2.871	2.406	6.008E-04	98.615
MOD39-2A	2.843	1.707	7.211E-04	58.297
MOD39-2B	2.805	1.859	4.791E-04	95.595
MOD39-3A	2.828	1.923	6.955E-04	68.104
MOD39-3B	2.822	2.363	7.166E-04	81.212
MOD39-3BB	2.760	1.778	5.927E-04	73.893
MOD39-4A	2.796	1.526	5.791E-04	64.894
MOD39-4T	2.773	1.394	4.680E-04	73.355
MOD40-1A	2.933	4.709	1.611E-03	71.997
MOD40-1B	2.976	6.112	2.189E-03	68.761
MOD40-1C	3.317	31.357	4.048E-03	190.807
MOD40-2A	2.933	4.378	1.580E-03	68.240
MOD40-2B	3.270	65.318	5.589E-03	287.869
MOD40-2bb	2.916	7.700	1.882E-03	100.790
MOD40-2T	3.030	5.303	1.782E-03	73.300

MOD40-3A	3.016	7.340	2.240E-03	80.708
MOD40-3B	3.301	27.235	3.927E-03	170.824
MOD40-3C	3.537	42.938	5.403E-03	195.728
MOD41-1A	2.865	3.350	2.357E-03	34.997
MOD41-1B	3.099	7.922	8.281E-03	23.562
MOD41-1C	3.502	13.571	3.879E-03	86.178
MOD41-2A	3.083	8.728	8.334E-03	25.793
MOD41-2B	2.807	2.871	3.084E-03	22.933
MOD41-2C	3.199	6.091	4.874E-03	30.781
MOD41-3A	3.832	24.413	3.698E-03	162.615
MOD41-4A	3.202	16.925	7.854E-03	53.076
MOD41-4B	3.004	9.102	3.956E-03	56.670
MOD41-5A	3.266	13.681	3.174E-03	106.162
MOD41-5B	3.142	9.611	8.158E-03	29.016
MOD41-T	2.777	1.590	9.440E-04	41.493
MODHJK-1A	2.609	0.006	3.999E-05	3.923
MODHJK-1B	2.619	0.000	4.649E-05	0.000
MODHJK-1C	2.518	0.003	6.588E-05	1.155
MODHJK-1aa	2.630	0.004	4.495E-05	2.455
MODHJK-1bb	2.632	0.001	3.877E-05	0.408
HJ-002AA	2.755	3.325	4.550E-04	179.963
HJ-002BA	2.772	3.002	4.608E-04	160.452
HJ-002CA	2.715	3.365	5.090E-04	162.816
HJ-002CC	2.740	1.890	3.594E-04	129.543
HJ-002DA	2.757	3.500	5.195E-04	165.926
HJ-002EA	2.756	3.257	4.919E-04	163.078
HJ-002EB	2.705	2.651	4.316E-04	151.276
HJ-003AA	3.284	0.218	5.532E-03	0.969
HJ-003BA	3.214	0.021	1.683E-03	0.311

Appendix B – AF demagnetization

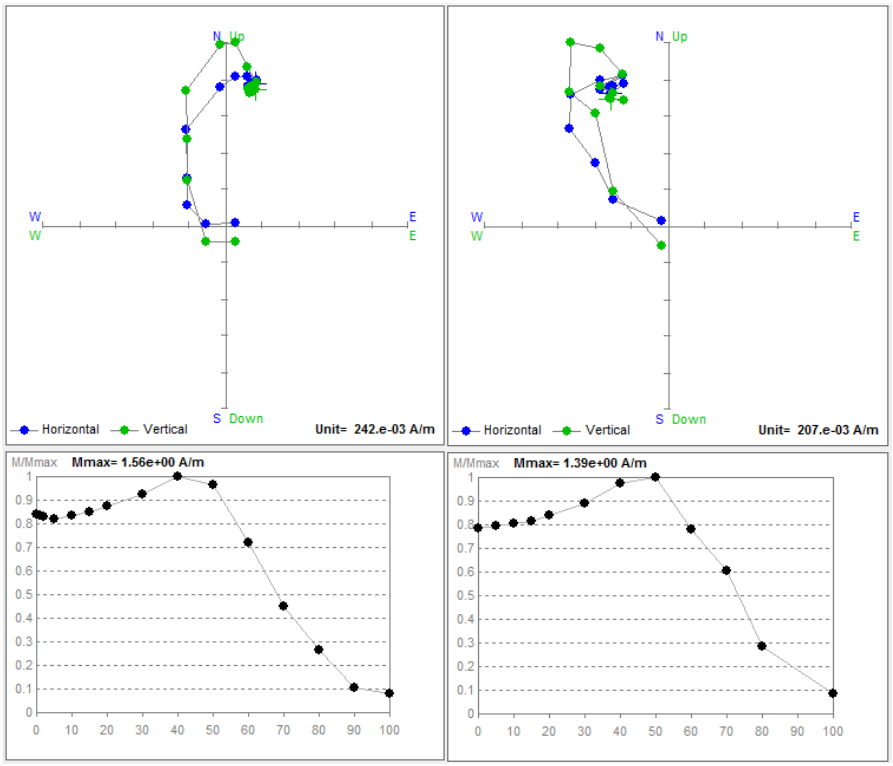

MOD35-1a MOD35-2a

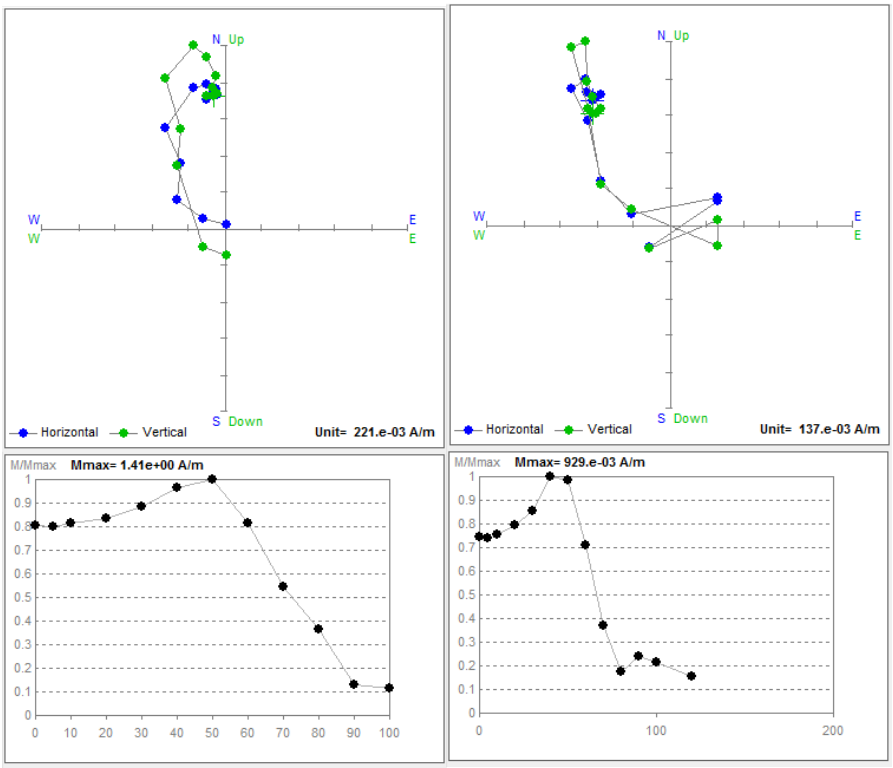

MOD35-2b MOD35-2t

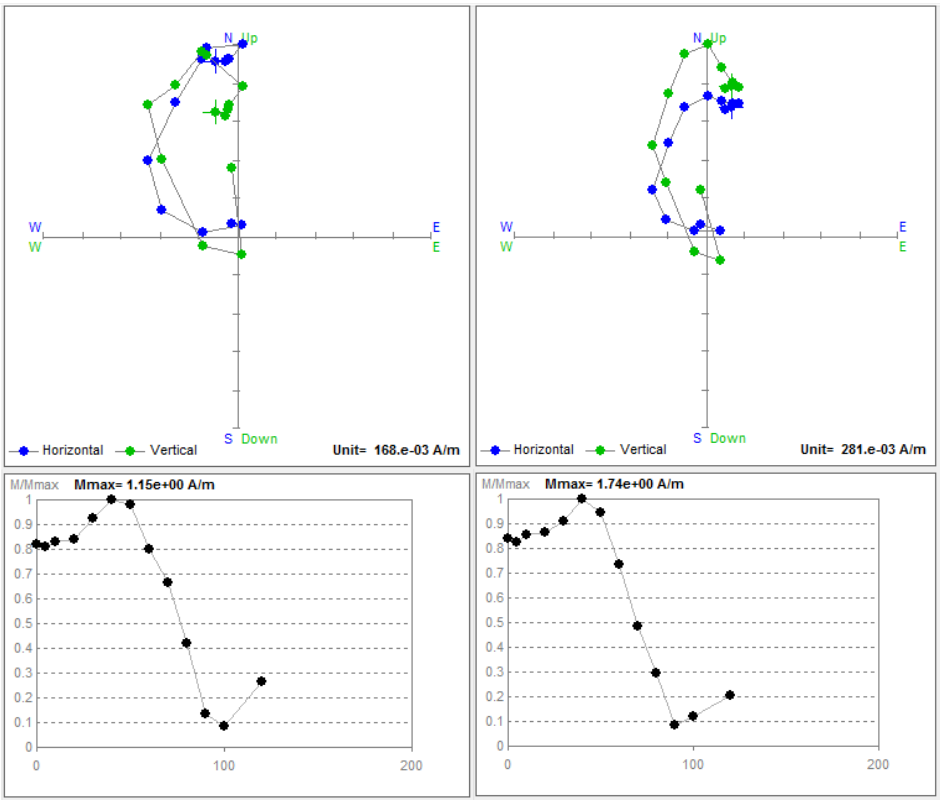

MOD35-3a MOD35-3b

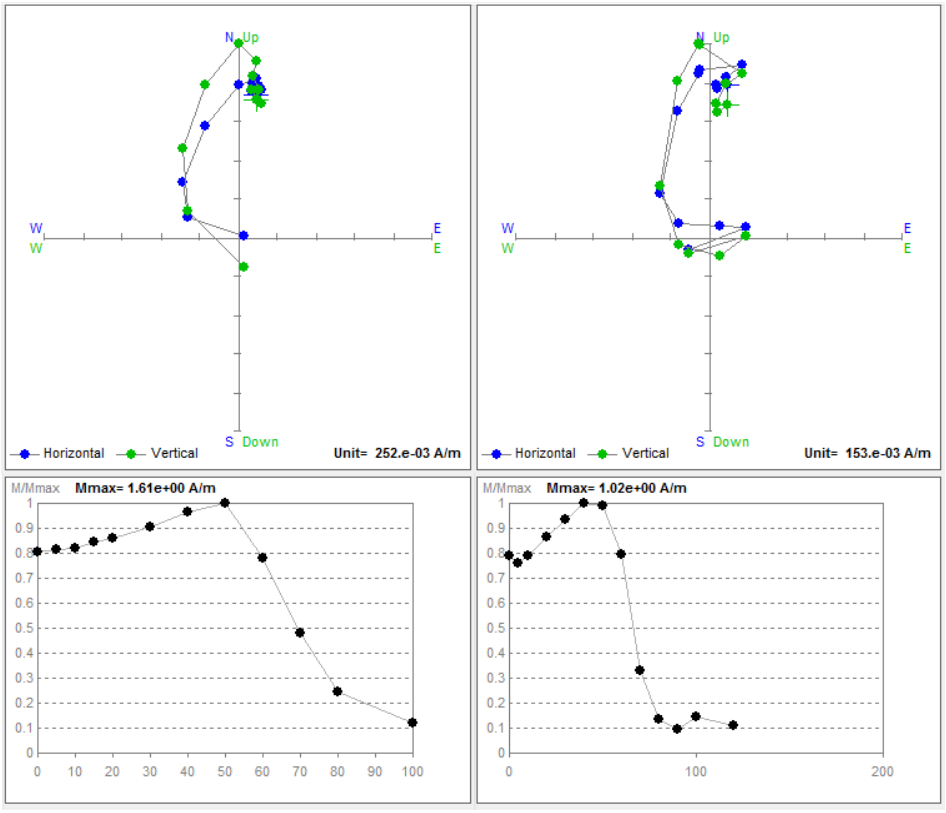

MOD35-4a MOD35-4t

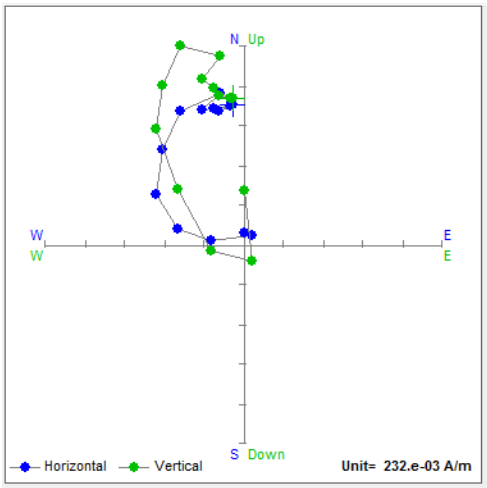

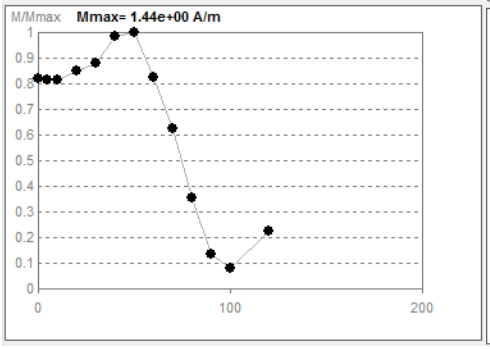

MOD35-5a

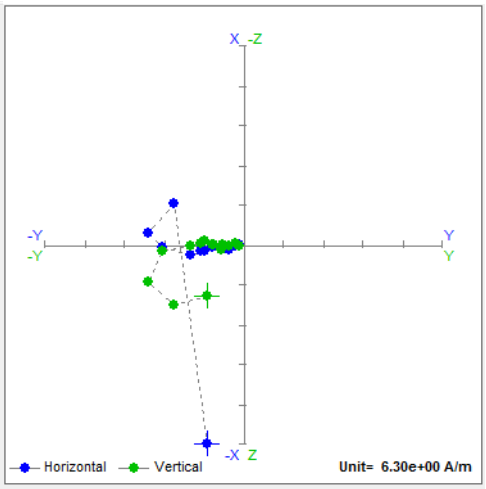

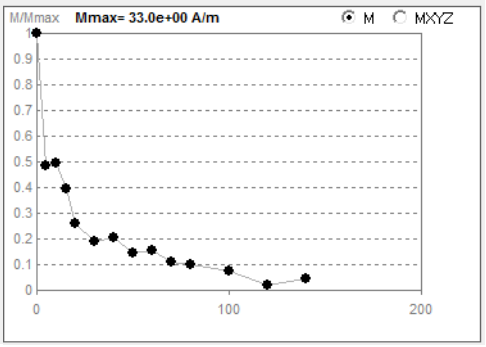

MOD36-1b

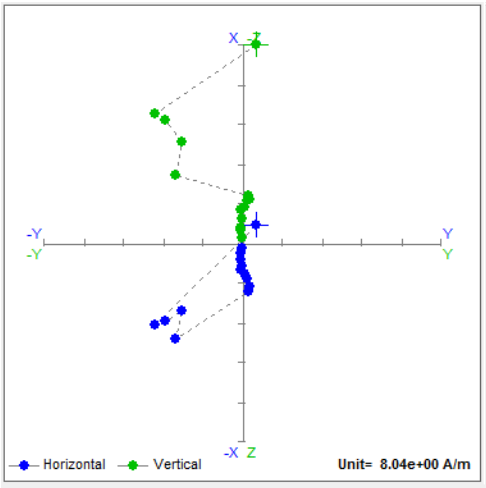

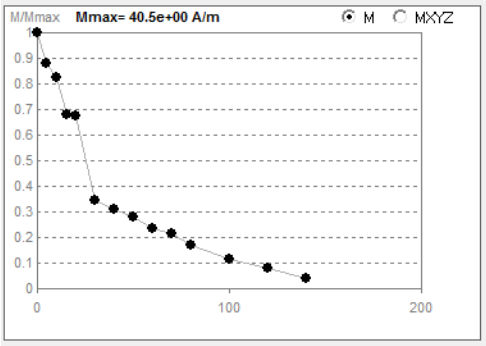

MOD36-2a

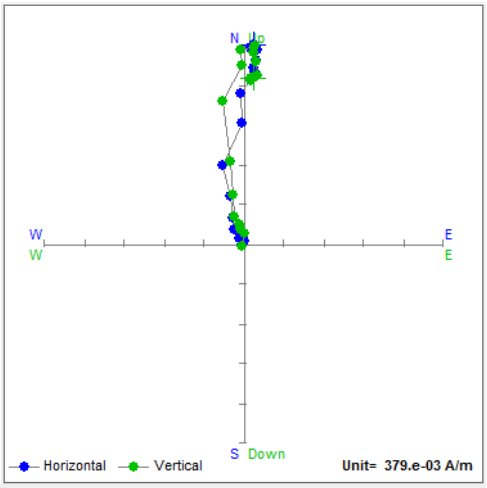

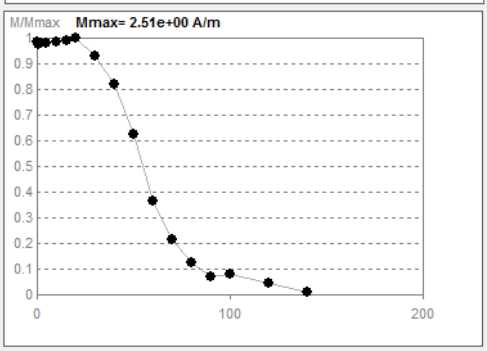

MOD37-1a

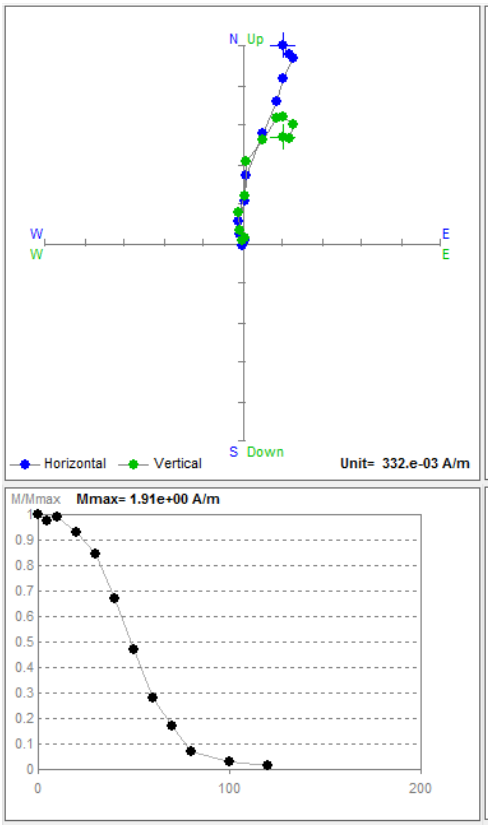

MOD37-3a

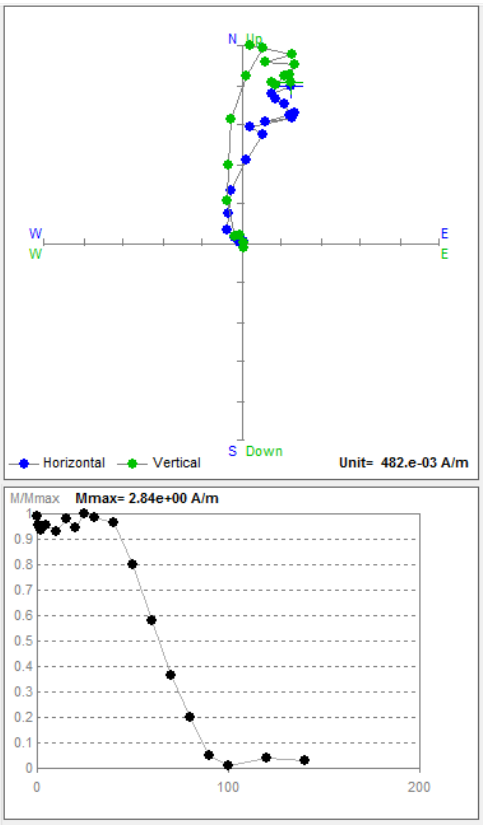

MOD38-1a

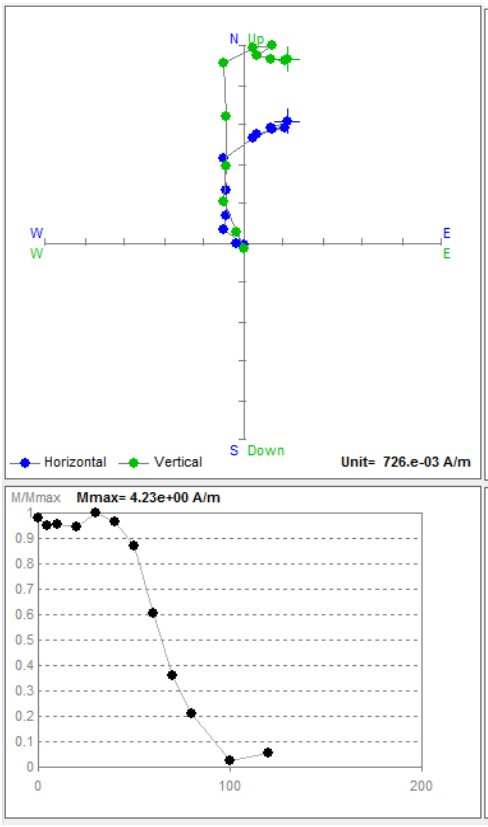

MOD38-1b

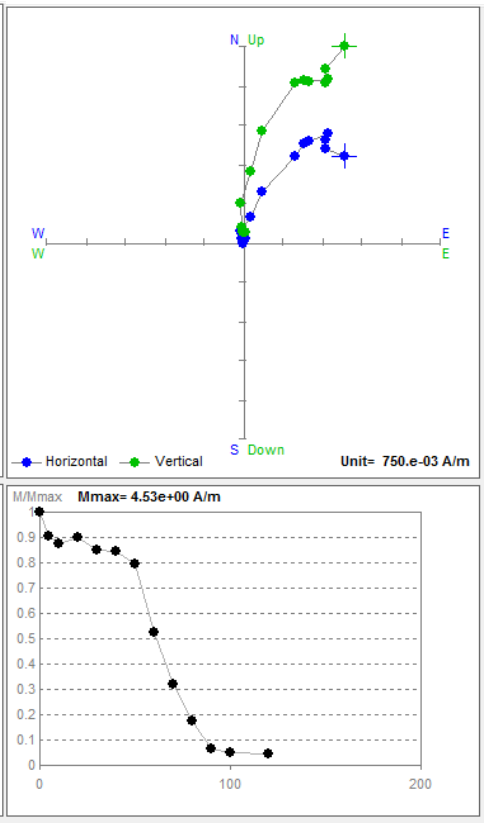

MOD38-2b

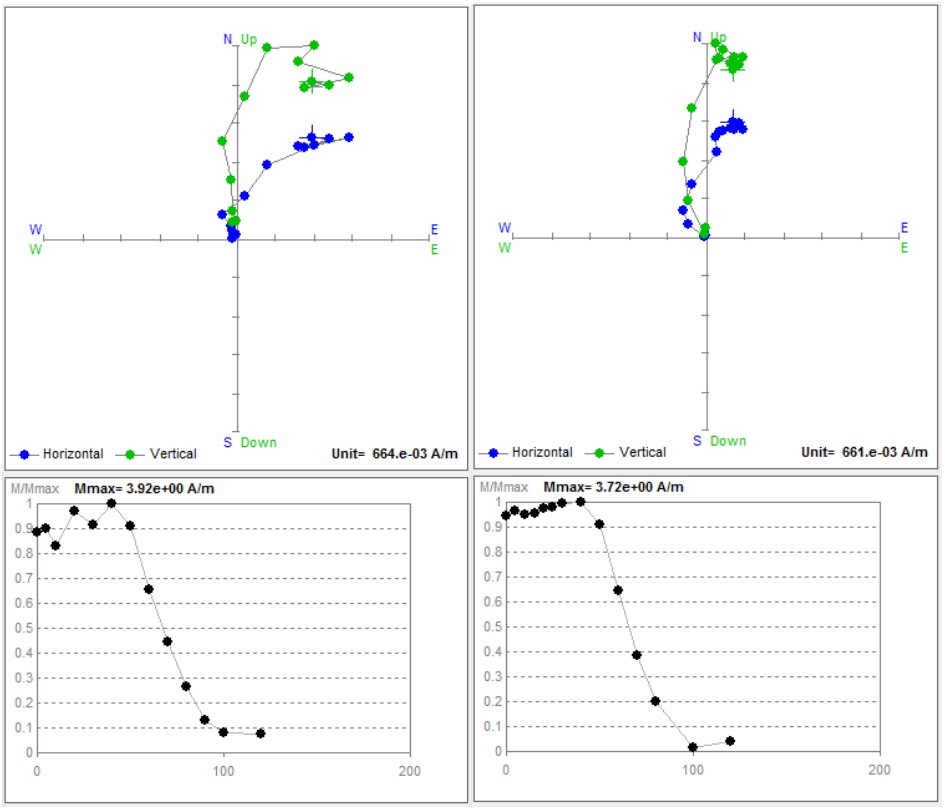

MOD38-3a MOD38-3b

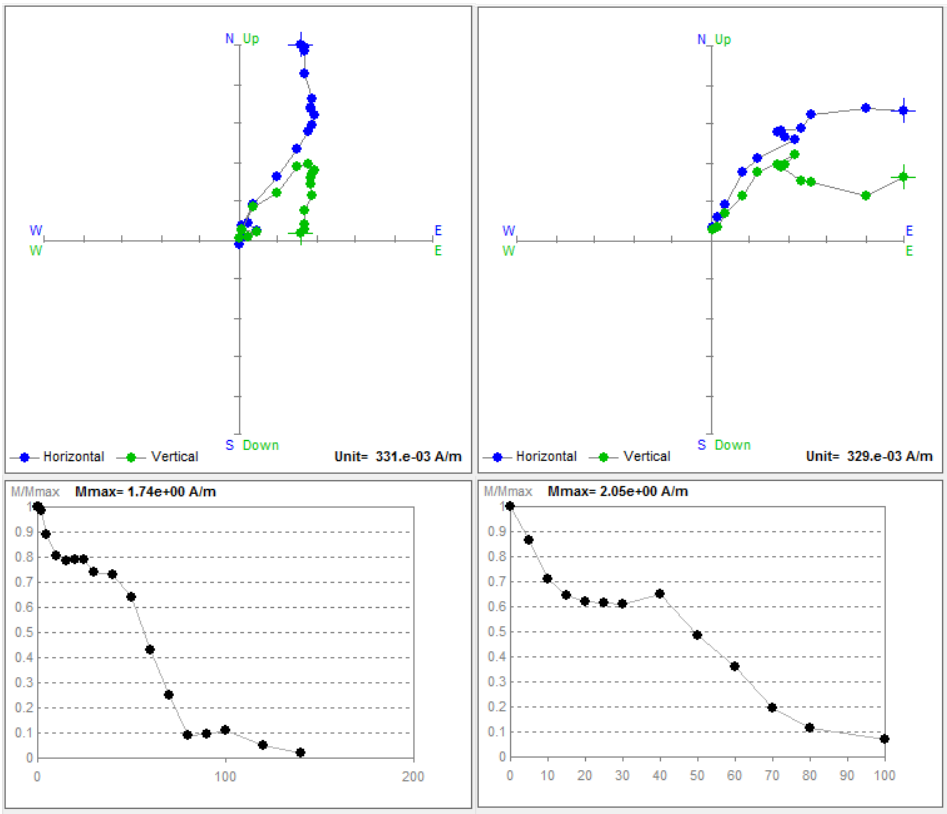

MOD39-1a MOD39-1t

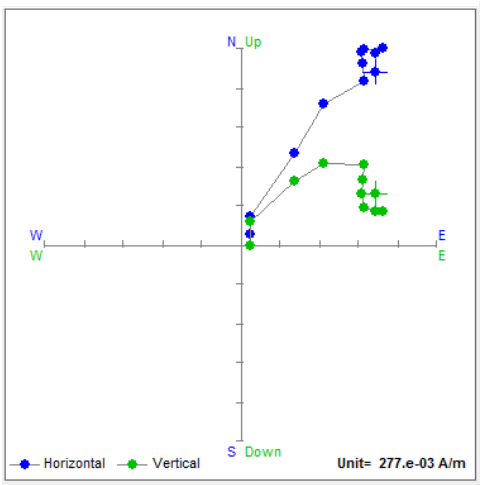

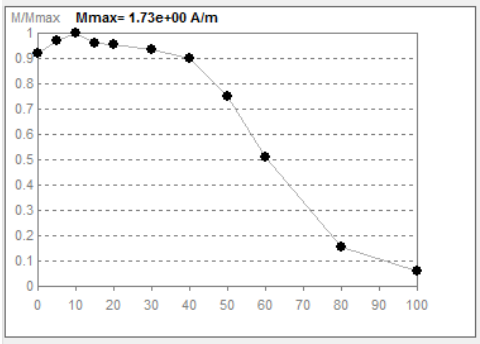

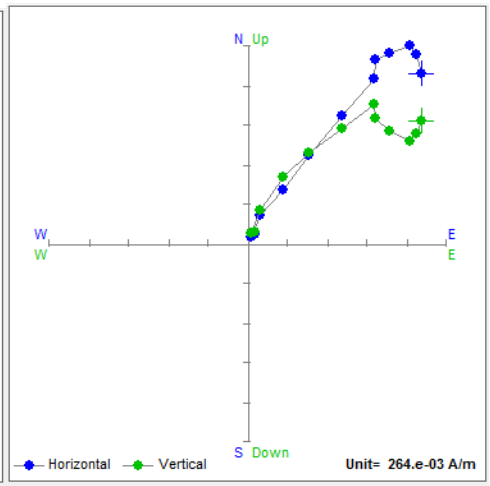

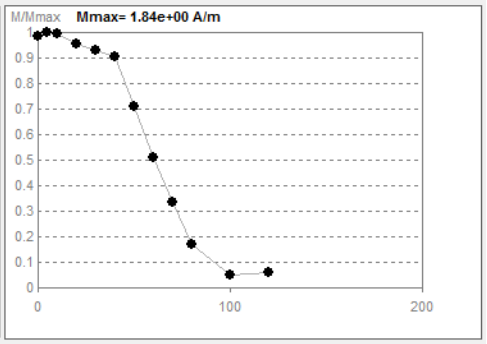

MOD39-2a MOD39-3a

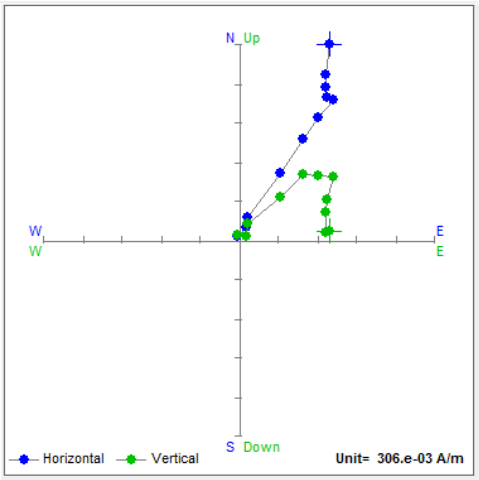

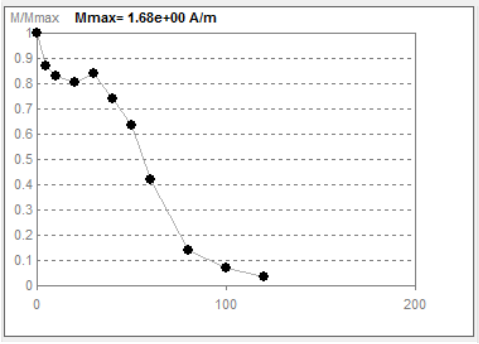

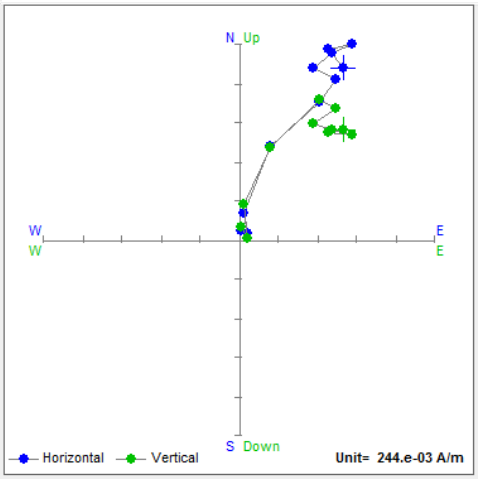

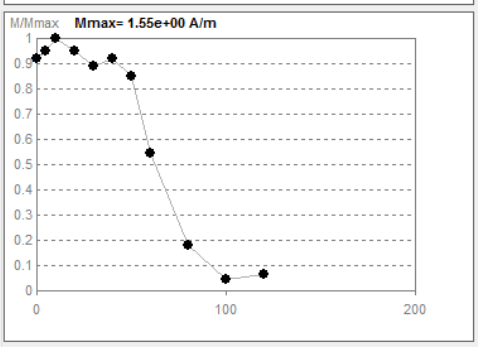

MOD39-3bb MOD39-4a

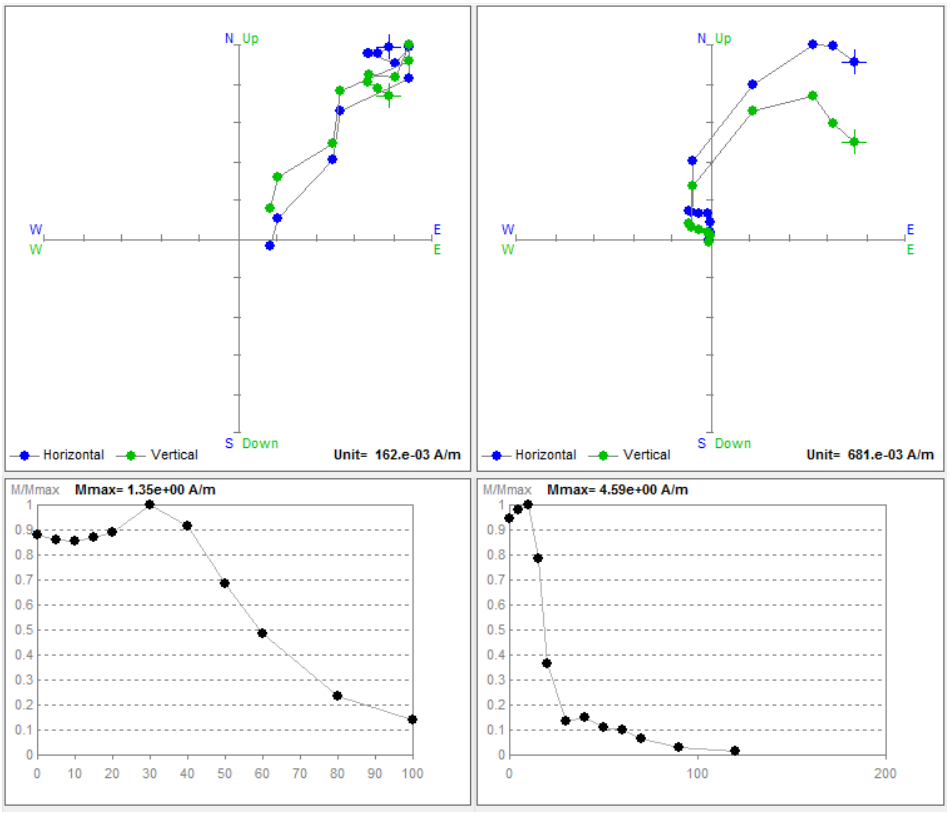

MOD39-4t MOD40-1a

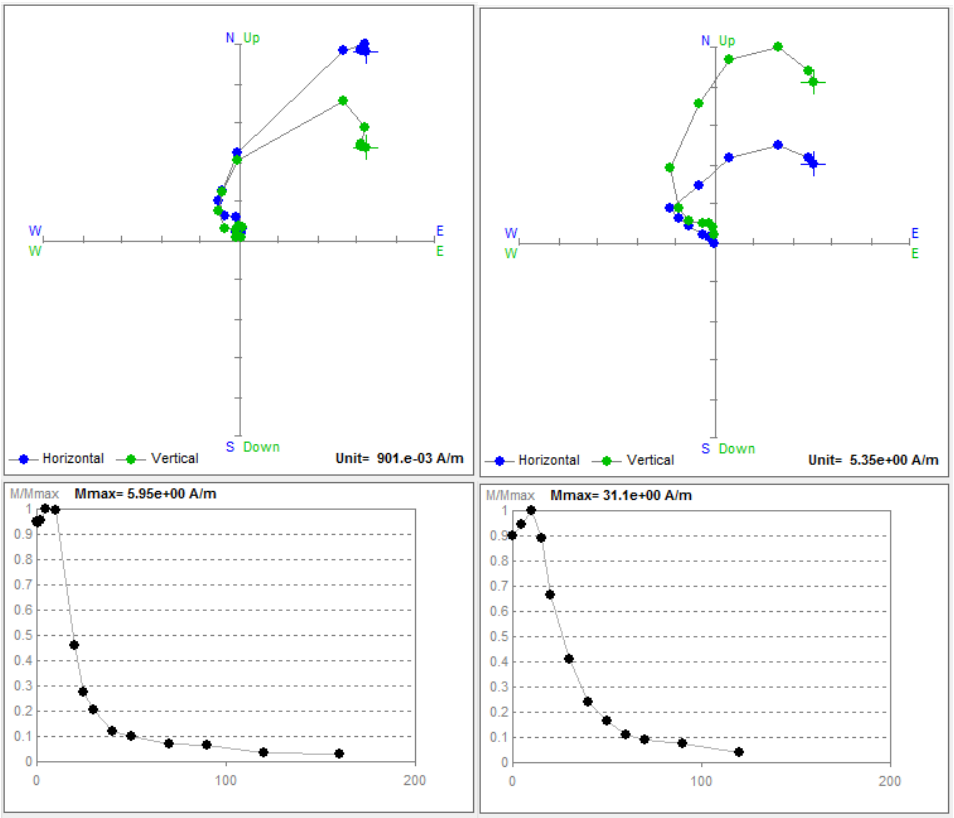

MOD40-1b MOD40-1c

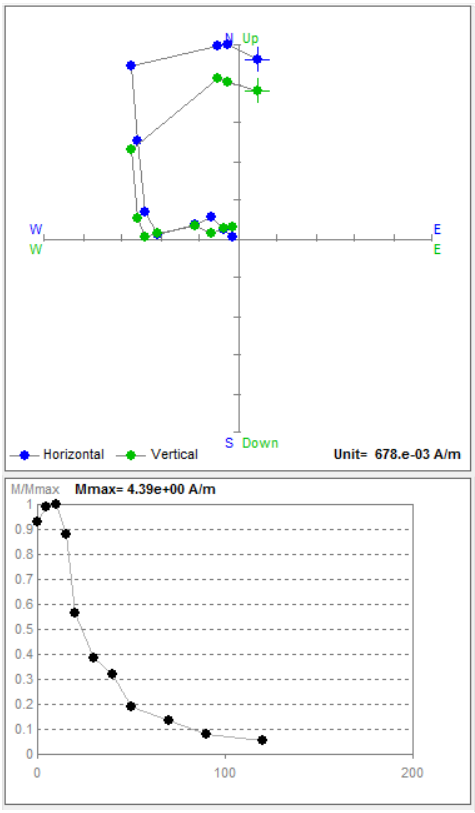

MOD40-2a

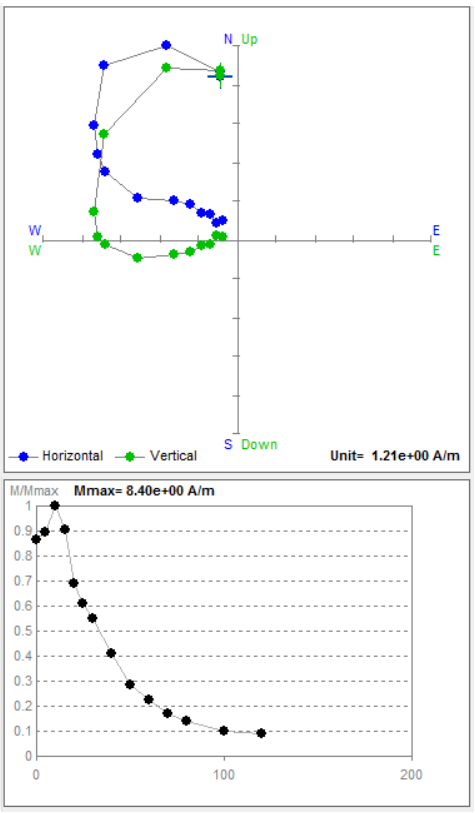

MOD40-2bb

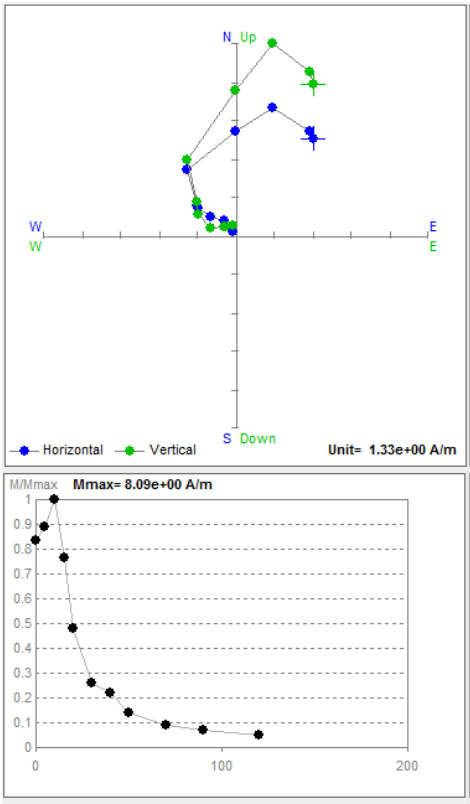

MOD40-3a

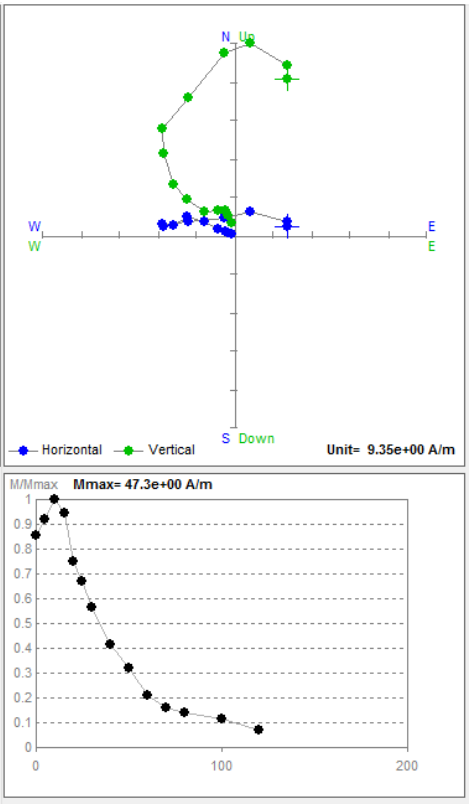

MOD40-3c

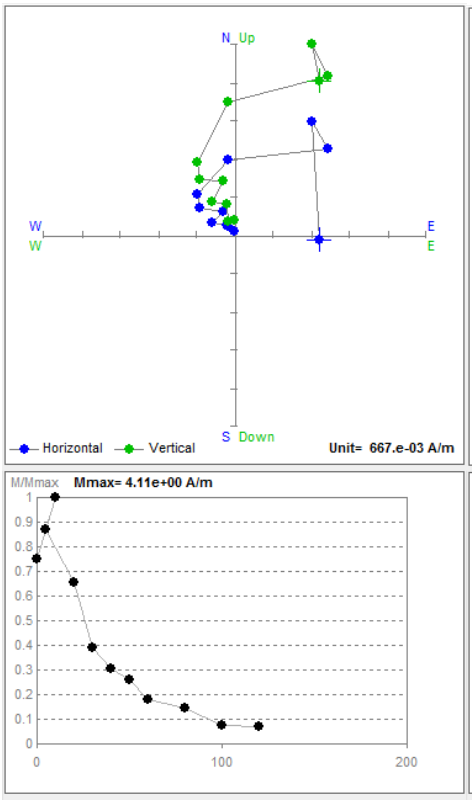

MOD41-1a

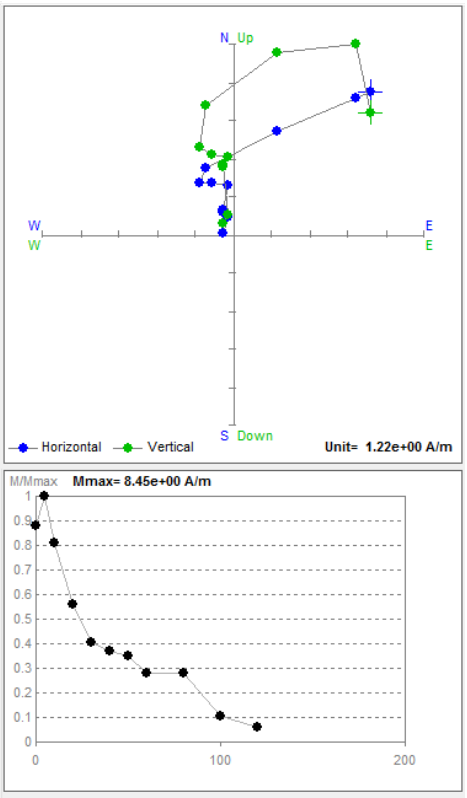

MOD41-1b

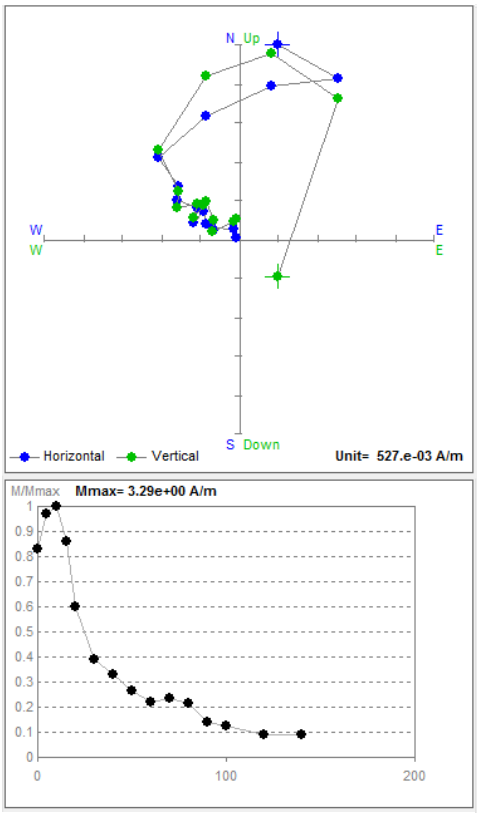

MOD41-2b

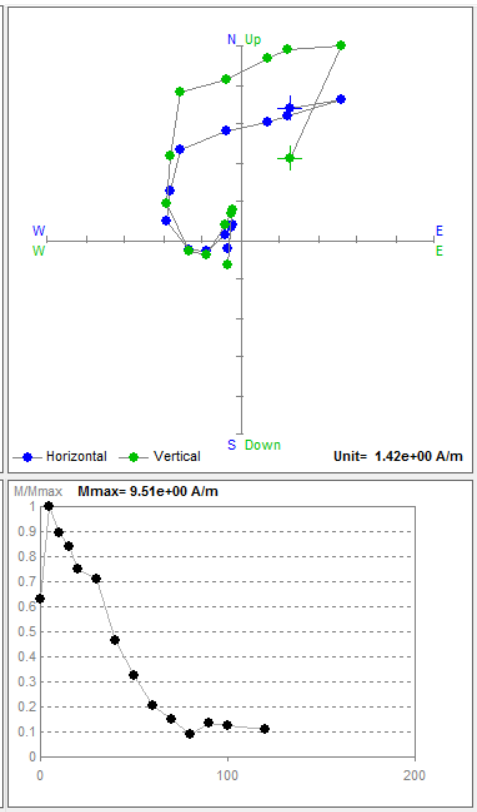

MOD41-2c

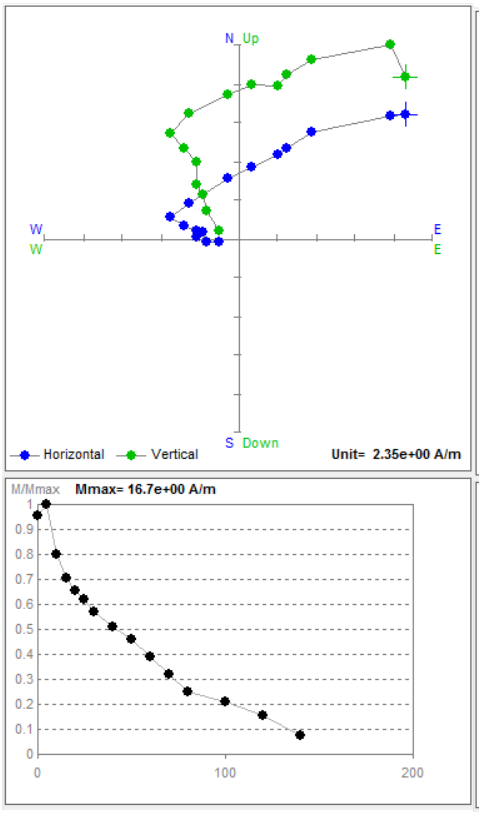

MOD41-4a

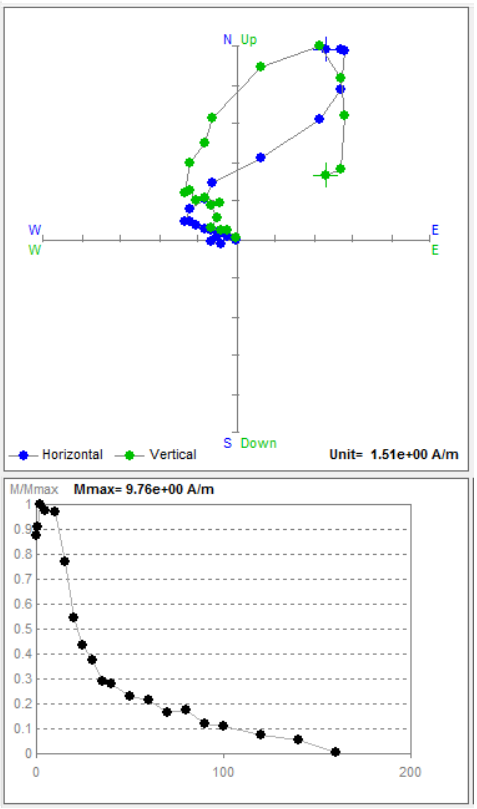

MOD41-4b

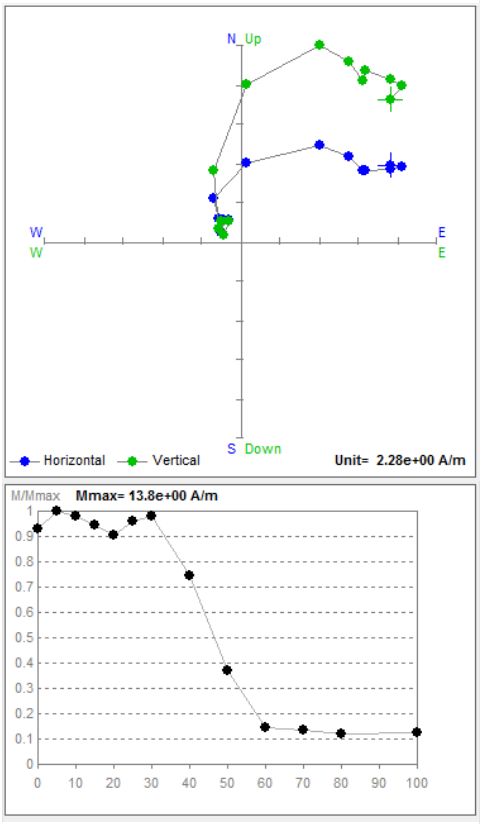

MOD41-5a

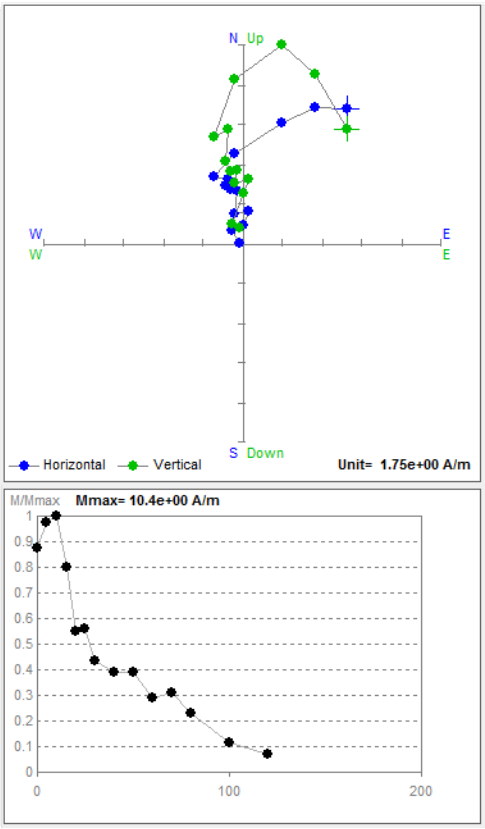

MOD41-5b

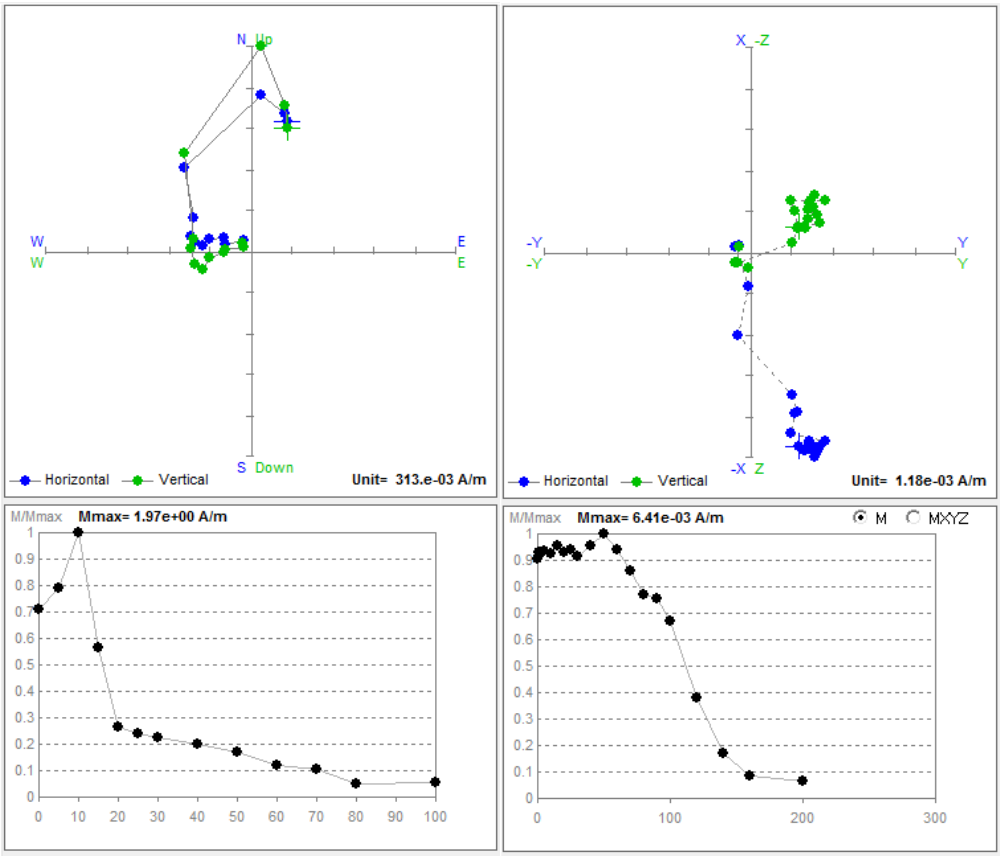

MOD41-t MODHJK-1a

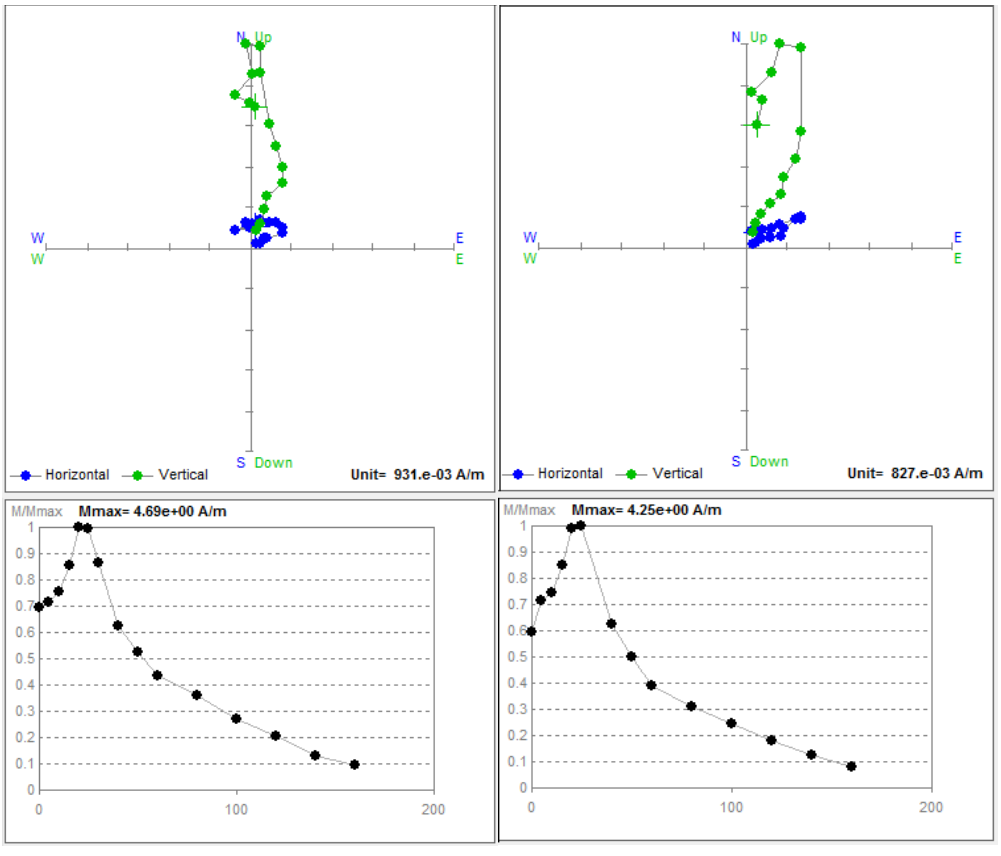

HJ002-aa HJ002-ba

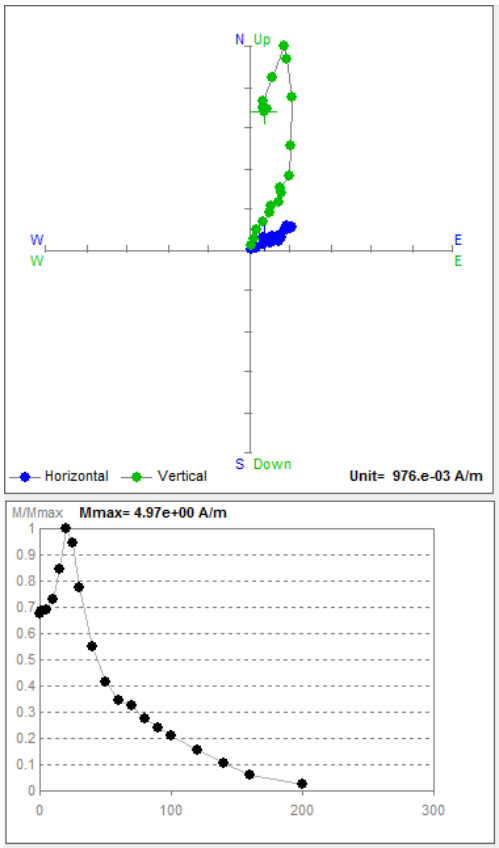

HJ002-ca

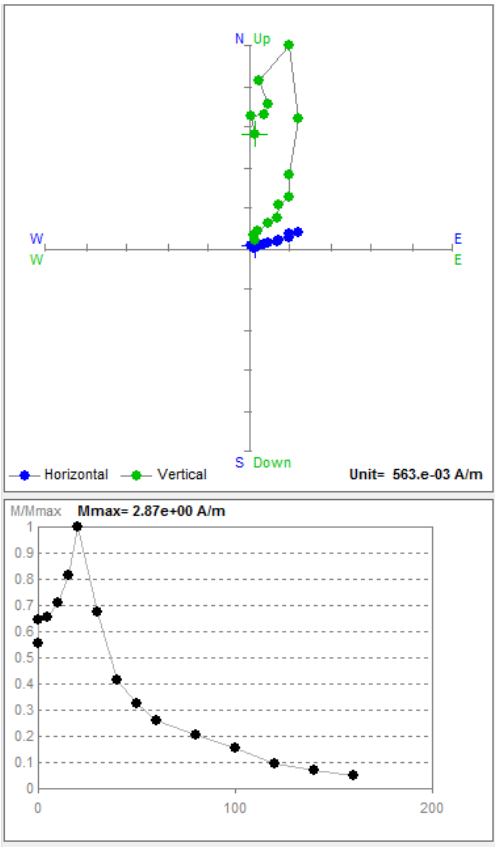

HJ002-cc

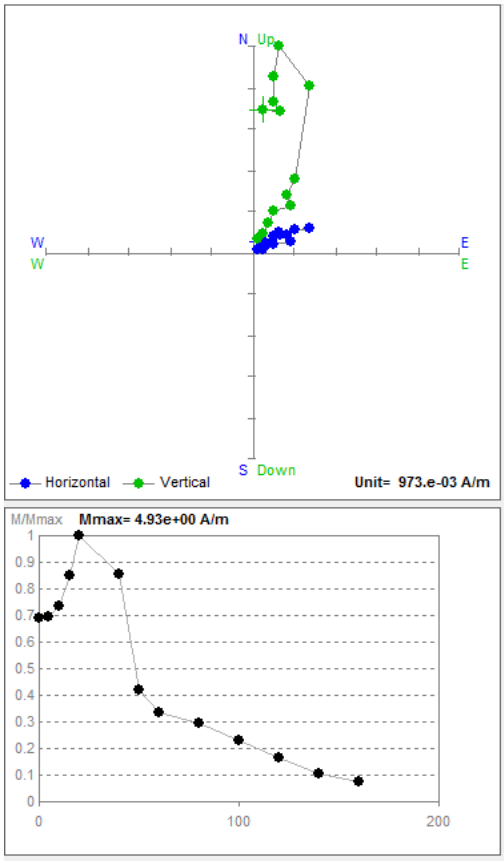

HJ002-da

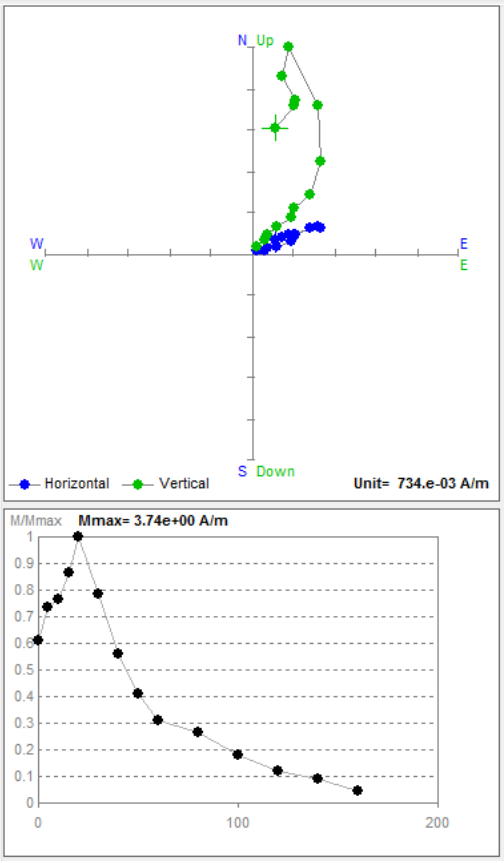

HJ002-eb

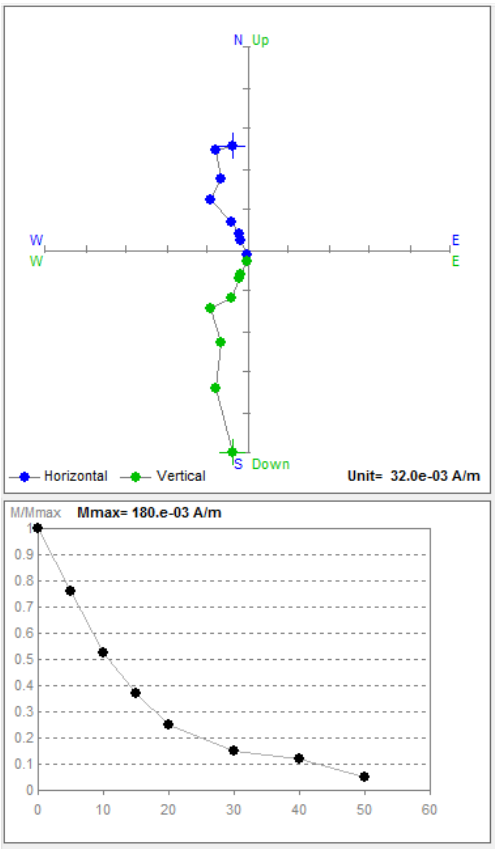
N_Up
W
W
E
E
S Down
Horizontal
Vertical
Unit= 32.0e-03 A/m
M/Mmax
Mmax= 180.e-03 A/m
1
0.9
0.8
0.7
0.6
0.5
0.4
0.3
0.2
0.1
0
0
10
20
30
40
50
60

HJ003-aa

Appendix C – Castle Meeting conference poster

Magnetic properties of highly oxidized amphibolite-facies rocks from Modum, Norway

Student presentation

Hedda Garshol Jensen, Alexander Michels, Suzanne McEnroe and Peter Robinson

Introduction: Modum lies within Mesoproterozoic basement, in the western part of the Oslo rift, Southern Norway. The area is characterized by supracrustal rocks with gabbroic intrusions, which are metamorphosed to amphibole facies. Here we focus on selected amphibolite samples. Studied thin sections show clear foliation with talc, quartz, feldspar, tourmaline and what is believed to be cordierite present in all samples. Titanohematite is present in varying amounts, commonly as discrete grains, and as small inclusions in cordierite. Studies on minerals that are remanent carriers has led to discoveries of titanohematite samples with unusual magnetic properties, such as extreme bias caused by nanoscale exsolution lamellae with their related lamellar magnetism. Titanohematite with nanoscale exsolution lamellae has been shown to be the primary source of a remanent magnetization and correlative anomalies in the area. Studied samples show signs of at least two phases, and further work will include quantifying phases to explain magnetic behavior.

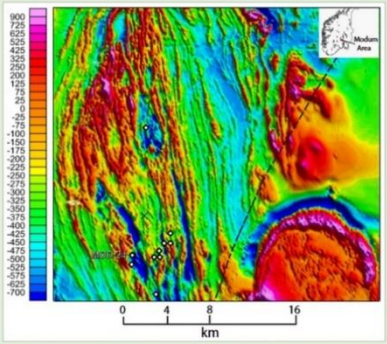

Anomaly dominated by remanence

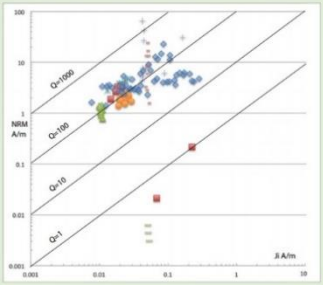

Q-plot of NRM vs induced magnetization. Mean Q-value is 91, with mostly values >10. This implies mostly remanent magnetization. Field used to calculate Ji: H=40,6 A/m.

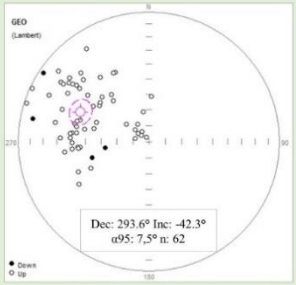

NRM directions. The NRM component, which is negative, dominates the magnetic response of the anomalies seen in the units studied here.

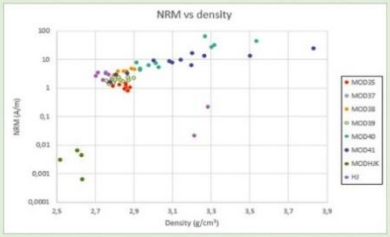

NRM vs density shows two distinct groups; low NRM for density <2.7 g/cm³ and much higher NRM for densities above 2.7 g/cm³. Density is primarily controlled by rock type, however a higher oxide content will increase the density of the sample from the same rock type.

Distribution of hematite and cordierite

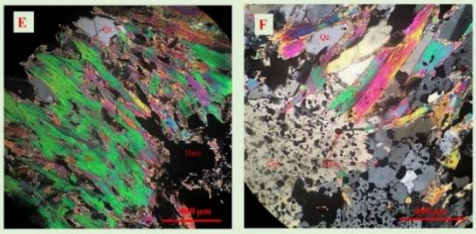

E: thin section from MOD37. This sample show stratification, with some areas with mostly cordierite and some areas with mostly talc. The titanohematite is coarse grained, located along grains of cordierite, and the platy talc makes up the foliation. F: thin section from MOD38. More cluttered than MOD37, and finer grained titanohematite as inclusions in cordierite. Difference in distribution of titanohematite gives different magnetic properties.

Titanohematite: the primary remanence carrier

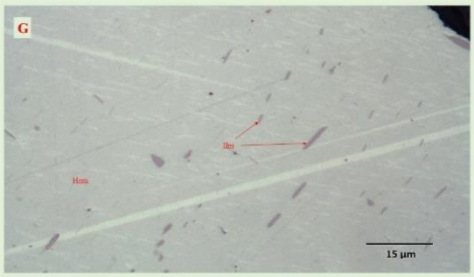

G: microphotograph from MOD39 showing hematite with ilmenite lamellae.

Demagnetization plots and hysteresis loops

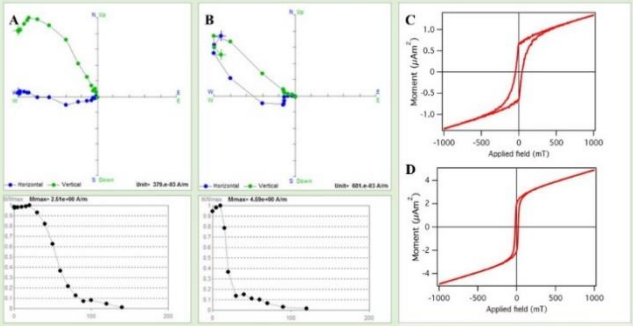

A and B: Demagnetization plots of resp. MOD37 and MOD40 clearly implies two phases. C: hysteresis loops of MOD37, the square shape is typical for titanohematite. D: hysteresis loop for MOD40, this has a more curved shape which implies other phases may be present.

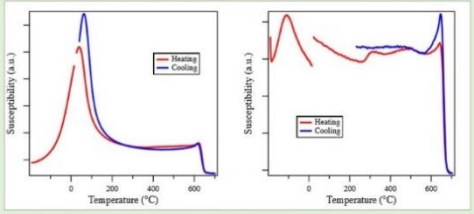

Temperature-dependent susceptibility of resp. MOD40 and MOD37 with Curie-temperature of ~640°C and ~660°C. This implies presence of titanohematite. The shape of the curves can imply multiple phases.

NTNU
Norwegian University of Science and Technology